AN EXPLANATION FOR THE UNEXPECTED DIVERSITY OF DWARF GALAXY ROTATION CURVES

by

Kyle Oman
B.Sc., University of Waterloo, 2011
M.Sc., University of Waterloo, 2013

A dissertation submitted in partial fulfillment of the
requirements for the degree of

DOCTOR OF PHILOSOPHY

in the Department of Physics and Astronomy

AN EXPLANATION FOR THE UNEXPECTED DIVERSITY OF DWARF
GALAXY ROTATION CURVES

by

Kyle Oman
B.Sc., University of Waterloo, 2011
M.Sc., University of Waterloo, 2013

Supervisory Committee

Dr. J. F. Navarro, Supervisor
(Department of Physics and Astronomy)

Dr. F. Herwig, Departmental Member
(Department of Physics and Astronomy)

Dr. F. Diacu, Outside Member
(Department of Mathematics and Statistics)

ABSTRACT

The cosmological constant + cold dark matter (ΛCDM) theory is the 'standard model' of cosmology. Encoded in it are extremely accurate descriptions of the large scale structure of the Universe, despite a very limited number of degrees of freedom. The model struggles, however, to explain some measurements on galactic and smaller scales. The shape of the dark matter distribution toward the centres of galaxies is predicted to be steeply increasing in density ('cuspy') by the theory, yet observations of the rotation curves of some galaxies suggest that it instead reaches a central density plateau (a 'core'). This discrepancy is termed the 'cusp-core problem'.

I propose a new way of quantifying this problem as a diversity in the central mass content of galaxies. This characterization does not distinguish between dark and ordinary ('baryonic') matter, but the apparent problem is so severe that the signature of the cusp-core discrepancy is still obvious. By formulating the problem in this way, several uncertain modelling steps are effectively removed from the discussion, allowing for a more narrowly focussed examination of remaining steps in the analysis.

My subsequent comparison of recent results from galaxy formation simulations and observed galaxies in the space of the baryonic Tully-Fisher relation (BTFR) reveals some galaxies with an apparent anomalously low dark matter content not only in the centre, but out to the largest measurable radii. These objects are very difficult to explain within the ΛCDM framework; the most plausible interpretation which emerges is that the effect of systematic uncertainties in modelling the kinematics in these galaxies – particularly in the estimate of their inclinations – has been substantially underestimated. This motivates a re-examination of rotation curve measurement methods.

I use a collection of simulated galaxies to demonstrate that, when these are synthetically 'observed' and modelled analogously to real galaxies, non-circular motions present in the gas discs give the appearance of cores, even though all of the simulated galaxies have central cusps. The errors are large enough to reproduce the full width of the observed scatter in rotation curve shapes. Provided the simulations produce sufficiently faithful models of real galaxies, these modelling errors could constitute a solution to the cusp-core problem within the ΛCDM paradigm. Regardless, the kinematic models must be better understood before drawing any strong cosmological conclusions.

Contents

List of Tables

List of Figures

ACKNOWLEDGEMENTS

DÉDICACE

Marie-Claire, sans qui ceci ne fut possible.

Chapter 1

Introduction

1.1 The dark matter problem

There are multiple compelling lines of evidence pointing to the fact that the bulk of the matter in the Universe is not made up of the ordinary 'baryonic' material of stars and interstellar gas, but rather of dark matter (for a review, see Bertone et al., 2005). The dark matter is thought to have been the dominant component in the regulation of the expansion of the Universe and in shaping the formation of structure during much of its history. Despite considerable efforts to detect it, the nature of the dark matter particle(s) is as yet unknown.

1.1.1 The ΛCDM model

Once the dark matter hypothesis finally gained wide acceptance (Rubin et al., 1978; Bosma, 1978; Rubin et al., 1980), more than 40 years after it was proposed (Zwicky, 1933), several models corresponding to different particle candidates and abundances were suggested. Gradually many were ruled out until a cosmologically flat model with cold dark matter (CDM) making up ~ 30 per cent of the critical density required for flatness and a cosmological constant, Λ, making up the remainder remained as the only well-developed viable model[1]. The observation of the acceleration of the expansion of the Universe (Garnavich et al., 1998; Perlmutter et al., 1999) eventually cemented the ΛCDM model as the 'standard model' of cosmology.

In CDM-type models, the particle making up the dark matter is assumed to be a massive ($\sim 100\,\mathrm{GeV}$) particle which interacts only via the gravitational force

---

[1]A concise history of the subject is given by Mo et al. (2010), Sec. 1.4.4.

and the weak force, or another force with similarly weak coupling. It is a remarkable coincidence that such a weakly interacting massive particle (WIMP), if it exists, could be produced thermally in the early Universe in exactly the amount required to make it a viable dark matter candidate (Kolb & Turner, 1990, Ch. 5) – this is often called the 'WIMP miracle'. The combination of this strong particle physics-based motivation and the ability of the ΛCDM model, with only six free paramters, to precisely satisfy several independent cosmological constraints, have led to its enduring success.

1.1.2 Successes on large scales

The crowning successes of the ΛCDM model are its various accountings for the structure of the Universe on scales larger than individual galaxies. In Sec. 1.1.3 I will outline a few areas where the theory struggles to explain phenomena on smaller scales, but first I wish to very briefly set the stage by mentioning some of the large scale successes.

The cosmic microwave background

The cosmic microwave background (CMB) radiation was emitted when the Universe cooled enough for electrons to bind to nuclei, making the Universe neutral and transparent to light. Before this, photons had a very short mean free path and were in local thermodynamic equilibrium with the surrounding plasma. As a consequence, the conditions in the plasma at the time of recombination[2] are imprinted on the spectrum of the CMB photons. In particular, fluctuations in the CMB temperature as a function of position on the sky correspond to local over- and underdensities in the matter distribution, the sites which later collapse to form galaxies or expand to form cosmic voids. The ΛCDM model, with its handful of parameters, fits extremely accurately the distribution of power in fluctuations as a function of angular scale (de Bernardis et al., 2000; Hanany et al., 2000; Halverson et al., 2002; Sievers et al., 2003; Spergel et al., 2003; Planck Collaboration et al., 2016).

The cosmic web

As perturbations in the initial density field of the Universe are amplified under the action of gravity, overdense regions collapse first along one direction, forming sheets,

---

[2]The 're-' is confusing, but is part of the usual name for this epoch of cosmic history.

then a second, forming filaments, and finally the third to form spheroidal 'haloes'. The initial density fluctuations can be measured from the CMB and evolved forward in time by means of an N-body simulation assuming the ΛCDM model and parameter values from the CMB. If members of a population of galaxies are assigned to the simulated halo distribution by a reasonable scheme and the resulting galaxy distribution is compared with galaxy redshift surveys, the resemblance is visually striking, and in quantitatively excellent agreement (e.g. the review of Springel et al., 2006).

The Ly α forest

As high-energy photons from distant quasars travel, they are redshifted by the expansion of space. At some location along their path their wavelength may correspond to the Ly α, $n = 2 \rightarrow 1$ transition of hydrogen. If at this point they happen to be passing through a cloud of cold gas, they can be absorbed and drop out of the quasar spectrum. This causes a dense series – a forest – of narrow absorption lines in the continuum spectra of quasars, each corresponding to a gas cloud at a different redshift. Gas clouds cluster along the dark matter filaments, sheets and nodes of the cosmic web, so the Ly α forest is a tracer of the large-scale structure. Comparisons between observed spectra and predictions from N-body simulations which assume the ΛCDM model reveal that the two are in excellent agreement (Weinberg et al., 2003, and references therein).

Baryon acoustic oscillations

At early times, the Universe was filled with ionized plasma and so was opaque to light. The plasma was in thermal equilibrium with the radiation field. Any perturbations of the density in this fluid propagated as acoustic waves: local compressions were amplified by gravity until the increased pressure caused the compression to stop and then reverse, and eventually the region expands enough that it is underdense and the surrounding pressure forces another collapse, etc. This process halted when the Universe cooled enough for electrons to bind to nuclei and allowed the photons stream away, causing a sudden loss of pressure support. There is a characteristic length scale for which a perturbation had time to expand exactly once before recombination, i.e. the acoustic waves completed a quarter of an oscillatory cycle. This synchronization in phase leads to an increased probability of finding overdense regions separated by a particular distance (see e.g. Hu & Dodelson, 2002, for a review). Later these

overdensities form galaxies, and the separation expected given the measured ΛCDM parameters is $\sim 150\,\mathrm{Mpc}$ at the present day. The theory therefore predicts that there should be a peak in the two-point correlation function of galaxies at this separation, which is exactly what was eventually measured by Eisenstein et al. (2005); Cole et al. (2005).

1.1.3 The small-scale crisis

Though the ΛCDM picture is broadly successful in describing the cosmology of the Universe on large scales, some observations on galactic and sub-galactic scales are difficult to reconcile with theoretical predictions. The collection of the few best known such problems: missing satellites, the too-big-to-fail problem and the cusp-core problem, have been described as constituting a crisis for the model (see Del Popolo & Le Delliou, 2017, for a recent review). In the context of these problems, the output of pure N-body simulations of structure formation are taken as the fiducial predictions of the model. These simulations do not include hydrodynamics, radiative processes or models for galaxy formation – the only physics included is gravitation acting on collisionless cold dark matter particles.

Missing satellites

N-body simulations of systems similar in mass to the Milky Way predict a very steep subhalo mass function: there should be thousands of clumps of dark matter with masses $\geq 10^6\,\mathrm{M_\odot}$ surrounding our galaxy, and more still with lower masses. These haloes are potential sites for galaxy formation, but the observed stellar mass function of satellite galaxies around the Milky Way is much shallower than the predicted halo mass function. This means that if each galaxy is assigned to a host dark matter subhalo, there are many haloes left over after all galaxies have been assigned. This mismatch has come to be known as the 'missing satellites problem' (Klypin et al., 1999; Moore et al., 1999).

The missing satellites problem can be solved either by a reduction in the expected number of small dark matter haloes, or if galaxies are somehow prevented from forming in many of the small haloes. A $7\,\mathrm{keV}$ sterile neutrino is a reasonably well-motivated particle candidate for dark matter (e.g. Boyarsky et al., 2009b,a, and references therein) which is less massive than the WIMP assumed in the CDM model. Models built around these neutrinos, or other particle candidates of similar mass, are

called warm dark matter (WDM) models. These neutrinos are dynamically hotter than WIMPs at early times[3]. One of the consequences of such a light particle is that structure formation is suppressed on small scales (Bond & Szalay, 1983), leading to a reduction in the number of predicted subhaloes in Milky Way-like systems.

Within the CDM paradigm, cosmic re-ionization has been suggested as a mechanism to prevent the formation of galaxies in small haloes (Efstathiou, 1992). As the Universe cooled, electrons in the initially fully ionized primordial plasma bonded to protons to form neutral hydrogen atoms. Stars, once they formed, were a source of ionizing radiation which eventually re-ionized most intergalactic gas. This process happened early enough that it is thought to have heated the gas and prevented it from collapsing into the (progenitors of) small subhaloes of the Milky Way, resulting in the observed deficit of satellite galaxies (Efstathiou, 1992; Sawala et al., 2016a). Heating and gas loss due to supernova explosions can also prevent these small galaxies from making more than a small first generation of stars. The details are still debated, but this seems to have emerged as an acceptable solution to the missing satellites problem within a CDM framework.

Too-big-to-fail

Even if the presumed thousands of low-mass subhaloes of the Milky Way can be prevented from forming galaxies, the number of subhaloes of sufficient mass that they would be still be expected to form stars still exceeds the number of Milky Way satellite galaxies observed to occupy such massive subhaloes (Boylan-Kolchin et al., 2011, 2012). The question is then: what is the fate of the haloes which should have been 'too big to fail' (TBTF) to form a galaxy? The same problem has also been argued to apply to nearby isolated galaxies, which also seem to fall short of the abundance of haloes predicted at relatively low masses (Papastergis et al., 2015).

These discrepancies have been attributed to several causes. Only a handful of TBTF subhaloes are expected around the Milky Way, and the number is very sensitive to the total mass of the system, which is known only within a factor of ~ 2. Assuming a Milky Way halo mass toward the low end of the distribution of recent estimates is enough to fully alleviate the problem (Wang et al., 2012; Vera-Ciro et al., 2013). Incorrect mass estimates due to dark matter 'cores' (e.g. Chan et al., 2015, and

---

[3]Hot dark matter (HDM) models refer to those where the dark matter is made of ordinary standard model neutrinos – such models have been ruled out on the grounds that HDM cannot cluster and form structures on scales $\lesssim 10\,\mathrm{Mpc}$.
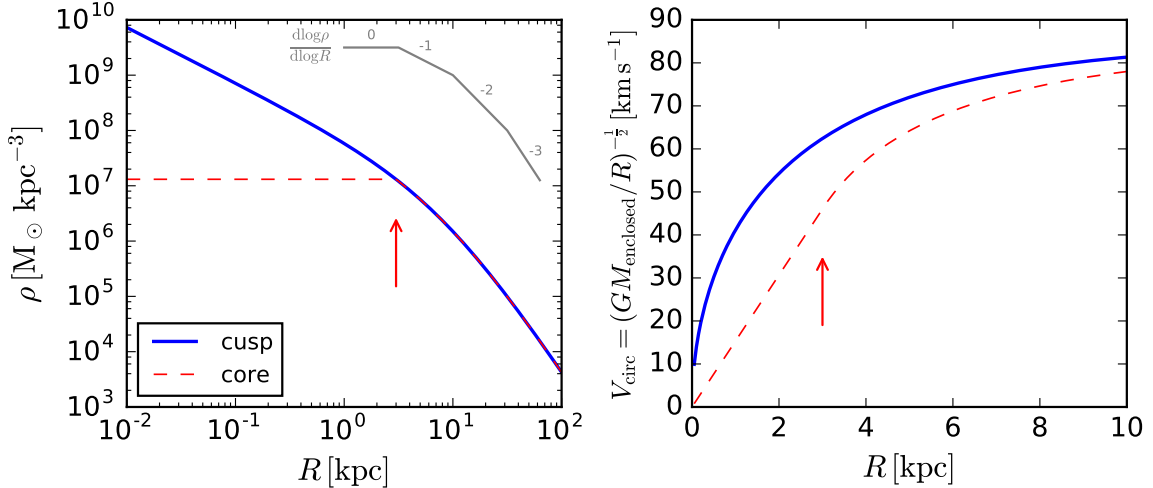
Figure 1.1: *Left:* Schematic illustration of cuspy and cored dark matter density profiles for a $10^{11}\,\mathrm{M}_\odot$ halo. The NFW density profile (blue line) has a centrally divergent, cuspy shape. The red line shows the same profile, but with a constant density 'core' imposed in the central $3\,\mathrm{kpc}$. *Right:* Circular velocity curves corresponding to the density profiles in the left panel. The core has a characteristic linear rise within the core radius, marked by the arrow.

see Sec. 1.2) and slower growth due to small amounts of mass loss at early times (Sawala et al., 2016a) have also been suggested as means to reduce the mass of the largest subhaloes and bring measurements and theory into agreement. For the TBTF problem in the field, it has also been suggested that the H I line width measurements, which are used as a proxy for the maximum circular velocity of the halo which the gas occupies, systematically underestimate the halo mass (Dutton et al., 2016). There does not yet seem to be an emerging consensus regarding a solution to the TBTF problem, but there seem to exist possible solutions within the scope of CDM theory.

1.2   The cusp-core problem

The third of the small scale crisis problems alluded to above is intimately related to the 'rotation curve diversity' which is the central theme of this thesis; it therefore deserves a more detailed discussion. In this section I will give a simple, schematic statement of the cusp-core problem, and an overview of possible paths to a solution. In Sec. 1.3 I will elaborate in more detail how the relevant observations are performed and analysed.

1.2.1 The cusp prediction

N-body simulations make a clear prediction for the internal structure of cold dark matter haloes: the spherically averaged density profile of the halo rises toward the centre, at least until the radius where any given simulation can no longer resolve smaller scales (Dubinski & Carlberg, 1991; Navarro et al., 1996b). This feature is termed a dark matter 'cusp'. Since the only physics in these simulations is gravity, which is scale-free, and the initial conditions of a CDM simulation are also scale-free, this rise is expected to continue to arbitrarily small radii, until the scale where the particle nature of the dark matter becomes important. There are a few analytic models often used to represent haloes with profiles of this form, the most common being the Hernquist (1990), NFW (Navarro et al., 1996b, 1997) and Einasto (1965) profiles. For the purposes of the cusp-core problem, these are all more or less equivalent (within some range of the parameters of each model) – the meaningful differences are at large radii which are generally not accessible observationally. For the remainder of this thesis the NFW model will be used as the fiducial cuspy halo model. The density profile of this model is:

$$\frac{\rho(R)}{\rho_0} = \left[\frac{R}{R_s} \left(1 + \frac{R}{R_s} \right)^2 \right]^{-1} \tag{1.1}$$

which goes as $\rho \propto R^{-1}$ at small radii and $\rho \propto R^{-3}$ at large radii. ρ_0 and R_s are a characteristic density and scale radius, respectively. This profile is shown by the blue solid line in Fig. 1.1. An alternate parameterization of the model replaces R_s and ρ_0 with a characteristic mass M_{200} and concentration parameter c. M_{200} is defined as the mass within a radius R_{200} within which the mean density is 200 times the critical density required for cosmological flatness ($\rho_{\rm crit} \approx 138 \, \mathrm{M_\odot \, kpc^{-3}}$ at the present day). The concentration parameter is simply $c = R_{200}/R_s$. In N-body simulations M_{200} and c are found to correlate tightly. One concise empirical description of this 'mass–concentration relation' (Neto et al., 2007) is:

$$c = 5.26 \left(\frac{M_{200}}{h^{-1} 10^{14} \, \mathrm{M_\odot}} \right)^{-0.10} \tag{1.2}$$

The combination of the NFW model and the mass-concentration relation leaves only a single free parameter, the mass of the halo.

Dark matter density is unobservable directly, but can be probed by the dynamics

of visible matter orbiting inside the halo. A useful connection between the density profile and observable dynamics is the circular velocity curve, defined in terms of the cumulative mass enclosed within each radius $M(< R)$:

$$V_{\text{circ}} = \sqrt{\frac{GM(< R)}{R}} \qquad (1.3)$$

The circular velocity curve corresponding to the NFW density profile the left panel of Fig. 1.1 is shown in the right hand panel. A useful parameter derived from the circular velocity curve is the maximum circular velocity V_{max}. Because the maximum circular velocity is a (messy) monotonic function of M_{200} it is often used as a proxy for the total mass of the halo. The relation can be expressed more concisely in terms of ρ_0 and R_s:

$$V_{\text{max}} \approx 0.465 \sqrt{4\pi G \rho_0 R_s^2} \qquad (1.4)$$

1.2.2 The core observation

The observed rotation curves of many dwarf galaxies resemble the dashed red line in the right panel of Fig. 1.1, with a characteristic linear rise in the centre, rather than the NFW circular velocity curve. A few of the many examples are shown in Appendix B. Assuming that these rotation curves are accurate tracers of the mass profile, the corresponding density profile is shown with the same line style in the left panel. The central constant density region is called a 'core'. The total mass (M_{200}) of the system is nearly unchanged – most of the mass is at large radii – and the maximum circular velocity drops only very slightly.

The left panel of Fig. 1.1 illustrates that there are two related but distinct ways to characterize the cusp-core problem. It can be understood as either a difference in the central slope of the density profile, or as a central deficit of mass. In Chapter 2 I propose a new description of the problem of the latter kind.

Before returning in the next section to the details of how these measurements are made in practice, I wish to describe briefly the five known ways the theoretical cusps might be reconciled with the observed cores. The first three involve an actual change in the distribution of dark matter, either via a process which transforms a cusp into a core, or which causes the halo to form with a core in the first place. The latter two are rather arguments that the discrepancy is a matter of how the measurements are interpreted.

1.2.3 Supernova-driven core formation

Although baryons make up at most only 17 per cent ($f_b = \Omega_{\rm b}/\Omega_{\rm m} = 0.17$) of a galactic system, gas cooling allows the baryonic distribution to collapse to high densities and become dynamically important. A gas cloud slowly collapsing in a dark matter halo causes the halo to contract without significant energy transfer between the gas and dark matter (e.g. Mo et al., 1998) – if anything, this reinforces the cusp. However, if the condensed baryons, or at least a fraction of them, are subsequently ejected from the centre rapidly, on a timescale shorter than the dynamical time, the dark matter halo receives a net energy injection which can flatten the central density profile (Navarro et al., 1996a). The effect can be compounded by repeated episodes of collapse and ejection (Read & Gilmore, 2005).

Supernova driven winds are a plausible cause of such rapid gas motions. This mechanism is explicitly seen to operate in some current galaxy formation models (for instance those of Pontzen & Governato, 2012; Brooks & Zolotov, 2014; Chan et al., 2015; Tollet et al., 2016). Other models with milder supernova feedback implementations do not form dark matter cores via this mechanism. However, they still seem able to produce galaxies which otherwise appear at least as 'realistic' as those in models which do form cores (Vogelsberger et al., 2014a; Schaller et al., 2015).

Perhaps the biggest current challenge to the supernova wind-driven core formation model is the existence of very large cores, such as that of IC 2574 which extends to $\sim 8\,\mathrm{kpc}$, to the very edge of the stellar distribution of this galaxy. Since in this picture the core is tied to a stellar process this is difficult to explain – this is discussed further in Chapters 2 & 3.

1.2.4 Clumpy infall & dynamical friction

Dynamical friction is another mechanism by which the motions of gas can affect the dark matter distribution. El-Zant et al. (2001) proposed a model in which dark matter haloes initially form with cusps, but the initial infall of gas clumps into the halo, just before the first stars are formed, injects energy into the cusp as the clumps slow via dynamical friction. This heats the central dark matter particles and flattens the density profile, and most of the gas clumps are dissipated shortly thereafter by supernova explosions. This model and later updates to it (Del Popolo, 2009) do not seem to be as widely regarded as a potentially viable solution to the cusp-core problem as the supernova-driven core formation mechanism. The reason for this is difficult

to pinpoint, but may stem from the semi-analytic rather than fully hydrodynamical nature of the model. It is also very difficult to constrain observationally because the cusp to core transformation occurs very early in the galaxy formation process and does not seem to have a clear signature which persists to the present day.

1.2.5 Modified dark matter physics

The physics of the dark matter, if it differs from the standard collisionless cold dark matter model, may also create cores. If the dark matter particle has a scattering interaction with itself, this could place a limit on the central density in dark matter haloes (Spergel & Steinhardt, 2000). In order to simultaneously satisfy observational constraints on the central dark matter density profiles of galaxy clusters and dwarf galaxies, a collisional cross section which depends on the inter-particle velocity may be required (Vogelsberger et al., 2012), though this is debated (Rocha et al., 2013). The recent development of techniques for modelling a dark matter scattering interaction within the framework of galaxy formation simulations (Vogelsberger et al., 2016) allows for fully self-consistent predictions. The initial results of Creasey et al. (2017) using this method suggest that self interacting dark matter (SIDM) may even be able to account for very large cores such as that of IC 2574.

1.2.6 Modified gravity

Underpinning the entire process of dynamical mass measurements on which the existence of the cusp-core problem is predicated is the assumption that gravity operates as described by general relativity. The dark matter problem has motivated the development of alternate theories of gravity. One of the specific objectives of the modified Newtonian dynamics (MOND) of Milgrom (1983) was to explain the galactic rotation curve measurement, in particular that the rotation curves of galaxies remain flat well beyond the edge of the visible galaxy. In this theory gravity is indistinguishable from Newtonian gravity except in the limit of very low accelerations $a \lesssim 10^{-10} \, \mathrm{m \, s^{-2}}$; the accelerations in the outskirts of galaxies are of this order. What MOND, and similar theories, predict for the inner parts of rotation curves is less clear. Lelli et al. (2016b) derived a 'radial acceleration relation' from the rotation curves and surface brightness profiles of a large sample of disc galaxies and McGaugh et al. (2016) suggest that the tightness and shape of this relation are natural predictions of MOND. However, Navarro et al. (2016) point out that some galaxies – the same which appear

to have dark matter cores – deviate significantly from the relation. It seems therefore that MOND-like theories struggle to resolve the cusp-core discrepancy. Nevertheless, testing the laws of gravity in the extreme weak field regime remains a useful and important check in validating the measurements on which the cusp-core problem is based.

1.2.7   Modelling errors

There is a long running debate around whether and when the rotation curves of galaxies can be interpreted as circular velocity curves, and consequently used to derive mass and density profiles. The systematic errors of particular concern can be split into two broad categories: (i) uncertainty regarding the basic properties and geometry of the galaxy, e.g. distance, inclination, morphology, etc. and (ii) the effects of non-circular motions in the velocity field. These parameters and their effects on kinematic modelling are described in more detail in the next section, and are central to Chapter 4. Much of the difficulty comes from the risk of confusing the observable signature of effects in the two categories. For instance, small errors in inclination and rotation velocity both strongly resemble the pattern in projection due to a quadrupole term in the velocity field (Warner et al., 1973; Schoenmakers et al., 1997), especially if the rotation curve appears to be linearly rising, as is the case for galaxies hosting a putative dark matter core.

Fortunately there are avenues both observational and theoretical to at least quantify, if not compensate for, these systematic uncertainties. Observationally, a particularly illuminating strategy is to observe multiple dynamically independent components of the same galaxy, e.g. stellar kinematics and gas kinematics (e.g. Adams et al., 2014), or gas in multiple phases[4](e.g. Swaters et al., 2003; Richards et al., 2016). On the theoretical side of things, forward modelling techniques allow for the validation of models and model assumptions on simulated systems where the correct answer is known (e.g. Rhee et al., 2004; Valenzuela et al., 2007; Kuzio de Naray & Kaufmann, 2011; Read et al., 2016; Pineda et al., 2017); the main limitation is the ability of the simulations to capture the full detail and complexity of real systems.

---

[4]The different components, especially in the case of multiple gas phases, are not *entirely* independent, but observing and comparing e.g. H I in the radio and H α in the optical at least allows for the isolation of some systematic effects.

1.3   Circular velocity and rotation curves

Because the dark matter component of a galaxy is not directly observable, its distribution must be inferred from the dynamics of the system. Indeed, dark matter was originally invoked to explain the discrepancy between the observable mass distributions and the dynamics of astrophysical systems. Making the connection explicitly, the mass distribution ρ defines a gravitational potential Φ via Poisson's equation:

$$\nabla^2\Phi = 4\pi G\rho, \tag{1.5}$$

and the potential has an associated force $\vec{F}$:

$$\vec{F} = \nabla\Phi. \tag{1.6}$$

In the absence of other forces, the kinematics of a collection of 'tracer' particles in a system are sufficient to fully specify the mass distribution, provided the system is in dynamical equilibrium, for the regions in which tracers exist. Equilibrium can be maintained if gravitational collapse is compensated by the kinematics, either by ordered (rotational) motions, disordered motions (dispersion), or a combination of the two. Tracers falling in any of these three categories can be used to attempt a measurement of the dark matter distribution in a galaxy (see, for instance, Lelli et al., 2017, for a recent analysis using all types). For tracers predominantly supported by rotational motion, the circular velocity curve:

$$V_{\mathrm{circ}}(R) = \sqrt{\frac{GM(<R)}{R}}, \tag{1.7}$$

where $M(<R)$ is the mass enclosed within radius R, is a useful proxy for the mass distribution. Provided the following conditions are satisfied, then tracer particles at radius R will have velocity $V_{\mathrm{circ}}(R)$:

1. The mass distribution is spherically symmetric.

2. Tracer particles are on circular orbits.

3. The system is in dynamical equilibrium.

4. No non-gravitational forces are acting on the tracers.

In this thesis I have taken care to distinguish between the circular velocity curve, which can be thought of as a spherically symmetric mass profile expressed in units of velocity, and the rotation curve, which is a measurement of the motions in a galaxy. The two are only equivalent if the conditions enumerated above are satisfied.

1.3.1 Dwarf galaxies

Dwarf galaxies, loosely defined as galaxies with total masses (including dark matter) of $\lesssim 10^{11} \, \mathrm{M_\odot}$ – about an order of magnitude less than the Milky Way – have several properties which make them preferable over their giant counterparts for the purposes of measuring their dark matter distribution. Foremost is that they have large mass-to-light ratios: the luminous components of the galaxy (stars, gas) form a tiny fraction of the total mass. While this is globally true for galaxies in general – the cosmic baryon fraction of $f_{\mathrm{bar}} = \Omega_{\mathrm{b}}/\Omega_{\mathrm{m}} \sim 0.17$ more or less guarantees this – for dwarf galaxies, the statement also applies locally (e.g. de Blok & McGaugh, 1996, 1997). Even within the luminous part of the galaxy, the dark matter still makes the dominant contribution to the local density.

This observation is useful for two reasons. First, it avoids the need to measure and subtract the luminous mass distribution from the total mass distribution. Instead, the luminous matter can be treated as a collection of massless tracers orbiting in a potential sourced purely by dark matter. This removes a potentially substantial contribution to the error budget in the dark mass distribution measurement. Second, dark matter haloes are thought to be approximately spherically symmetric. If the dark matter fully dominates the dynamics, this fulfills one of the criteria required for the rotation curve to equate to the circular velocity curve.

One of the main drawbacks of using dwarf galaxies in rotation curve work is that they tend to have irregular or spheroidal stellar morphology, both of which point to likely strongly non-circular orbits, in contrast to the clearly disc-shaped spiral galaxies amongst the giants. The morphology of the neutral hydrogen (H I), for those dwarfs which have any appreciable amount of it (dwarf spheroidals tend not to), however, is often disc-like. Holes, warps, lopsidedness and other irregularities are common (Holwerda et al., 2011, and subsequent papers in the same series), but in the gas, unlike for stars, hydrodynamic forces and radiative dissipation of angular momentum actively work to settle the gas into a disc. It is therefore arguably reasonable to assume that the gas is on circular orbits. I will return to this point later: departures

from circular motion will be a central theme of Chapter 4.

Of the four conditions enumerated above the dynamical equilibrium condition is probably the most difficult to quantify. In some cases, like ongoing mergers between galaxies, it is obvious that a system is out of equilibrium. All galaxies are out of equilibrium to some degree, though, and measuring the degree of departure from dynamical equilibrium is difficult using only observationally accessible quantities.

1.3.2 Pressure support corrections

Coming now to the last of the four conditions enumerated above, there are of course non-gravitational forces which act on the gas in a galactic disc. Provided these forces are small relative to the gravitational force, the equality $V_{\text{circ}} = V_{\text{rot}}$ will still approximately hold. One force which is sometimes non-negligible, particularly in the weaker gravitational environments of dwarf galaxies, is that due to a radial hydrostatic pressure gradient in the gas disc. For this particular case there is a standard diagnostic and correction[5] which can be made (e.g. Valenzuela et al., 2007; Dalcanton & Stilp, 2010; Oh et al., 2015). Conceptually, the correction is very simple: an extra term appears in Newton's second law, focussing here on the radial component in the plane of the disc:

$$\frac{V_{\text{rot}}^2}{R} = \frac{GM(<R)}{R^2} + \frac{1}{\rho}\frac{\mathrm{d}P}{\mathrm{d}R} \tag{1.8}$$

with P the hydrostatic pressure and ρ the gas density. The pressure gradient is typically negative, so the disc rotates more slowly if it is partially pressure supported. Turbulence is thought to be the dominant source of pressure in H I discs (Dalcanton & Stilp, 2010), so the pressure is related to the radial velocity dispersion σ_R as $P = \rho\sigma_R^2$. Re-arranging gives a more convenient formulation:

$$V_{\text{rot}}^2 = V_{\text{circ}}^2 + \sigma_R^2 \frac{\mathrm{d}\log(\rho\sigma_R^2)}{\mathrm{d}\log R} \tag{1.9}$$

The volume density and radial component of the velocity dispersion are not directly observable. Assuming that the vertical structure of the disc is radially invariant allows ρ to be replaced by the surface density Σ_{HI}, and further assuming that the velocity dispersion is isotropic allows σ_R to be replaced by σ, the velocity dispersion along the line of sight. This yields a formulation that is entirely in terms of observables which

---

[5]Often misleadingly called an asymmetric drift correction, see e.g. Pineda et al. (2017) for an extensive discussion.

can be used as a diagnostic or correction:

$$V_{\mathrm{rot}}^2 = V_{\mathrm{circ}}^2 + \sigma^2 \frac{\mathrm{d}\log(\Sigma_{\mathrm{HI}}\sigma^2)}{\mathrm{d}\log R} \tag{1.10}$$

1.3.3 Kinematic modelling

The rotation speed of gas in a galactic disc is not directly measurable. It must instead be estimated from spectra measured at various positions across the disc, which provide information about the distribution of velocities along the line of sight at each position. Accurate distances and the velocity components in the plane of the sky are generally inaccessible, so the task is to reconstruct the full 6 dimensional phase space description of the kinematics from measurements of only 3 of the components.

The simplest technique to measure a rotation curve is to measure a series of spectra along the geometric major axis of a galaxy, with the implicit assumption that this coincides with the kinematic major axis. This can be achieved cheaply with a long slit spectrograph. To extract velocity information a known spectral line is required; the most often used line is H α (e.g. de Blok et al., 2001; de Blok & Bosma, 2002; Swaters et al., 2003; Spekkens et al., 2005; Reyes et al., 2011; Kauffmann et al., 2015), which is both bright and usually present throughout most of the stellar disc. The velocity profile along the slit is then directly interpreted as a rotation curve, requiring only a correction for the inclination of the system: $V_{\mathrm{observed}} = V_{\mathrm{rot}}\sin(i)$. The difference between the approaching and receding sides of the disc is often used to construct a rough estimate of the systematic uncertainty in the measurement. This kind of measurement is simple and cheap, but suffers from several systematic effects which are difficult to control for. For instance, a slight misplacement of the slit so that it misses the galactic centre, or is slightly rotated relative to the kinematic major axis, will cause a systematic underestimate of the rotation curve (Swaters et al., 2003; Spekkens et al., 2005).

Much more useful information for the extraction of a rotation curve is contained in measurements which are resolved in two spatial and one spectral dimension, i.e. data cubes. Radio interferometers produce such measurements 'by default', and the 21-cm hyperfine transition of neutral hydrogen (H I) is a useful emission line at radio wavelengths. This line can usually be measured to radii well beyond the limit of the H α emission, offering a better chance of reaching the peak or flat part of the rotation curve which correlates with the total mass of the system. For many years the main

drawback of radio interferometry-based rotation curves was the poor spatial resolution of $\gtrsim 50\,\mathrm{arcsec}$ (compare to $\sim 1.5\,\mathrm{arcsec}$ for seeing-limited optical measurements), which causes a systematic underestimate of the rotation curve due to 'beam smearing' (Swaters et al., 2009, and references therein). The THINGS (Walter et al., 2008) and LITTLE THINGS (Hunter et al., 2012) surveys utilizing the Very Large Array have relatively recently changed this picture with their 6-12 arcsec resolution H I maps. While still a factor of a few shy of the spatial resolution achievable with optical spectroscopy, this is still sufficient to resolve $\sim 100\,\mathrm{pc}$ scales in nearby galaxies. The advent of optical integral field spectrographs also makes it possible to obtain high resolution 2D maps of H α emission (or other features). These are also used for rotation curve work (e.g. Kuzio de Naray et al., 2008; Adams et al., 2014; Richards et al., 2016); their main drawback is again the limited radial extent of useful optical spectral features.

Most models in current use for the extraction of rotation curves from data cubes are variations on the 'tilted ring' model of Rogstad et al. (1974). In the usual formulation the gas disc is approximated as infinitesimally thin and divided into a series of concentric annuli, or 'rings'. Each ring is characterized by its surface brightness (i.e. mass) and rotation velocity. The model allows for warps in the disc by allowing the rings to tilt, parameterized by an inclination angle relative to the observer (by convention $i = 0°$ is face-on, $i = 90°$ edge-on) and a position angle, the direction of the receding side of the kinematic major axis measured counter-clockwise from North. Each ring may also have an independent centroid and systemic velocity (bulk motion along the line of sight), though in practice these are usually fixed to a constant for all rings. There are differences in the details of the various implementations of tilted ring modelling routines. Some, for instance, add a parameter to account for the velocity dispersion of each ring (e.g. the TIRIFIC code of Józsa et al., 2007; Kamphuis et al., 2015). In most cases the inputs are the 0th and 1st moments of the data cube $F(x, y, v)$ (Schoenmakers, 1999; Krajnović et al., 2006; Spekkens & Sellwood, 2007; Józsa et al., 2007, amongst others), i.e. the surface brightness and velocity maps,

computed along the lines of[6]:

$$\Sigma(x,y) = \int F(x,y,v)\,\mathrm{d}v \tag{1.11}$$

$$\overline{V}(x,y) = \frac{\int v\,F(x,y,v)\,\mathrm{d}v}{\Sigma(x,y)} \tag{1.12}$$

If the velocity dispersion is fit, the 2nd moment (dispersion map) is also needed:

$$\sigma(x,y) = \left(\frac{\int \left(v\,F(x,y,v) - \overline{V}(x,y)\right)^2 \mathrm{d}v}{\Sigma(x,y)} \right)^{\frac{1}{2}} \tag{1.13}$$

If maps are the model inputs, then the tilted ring model is used to create a set of model maps whose residuals with respect to the input, quantified by some figure of merit. The parameter choices which minimize the residuals are then sought using an iterative technique. In some more recent implementations, such as the ^{3D}BAROLO package (Di Teodoro & Fraternali, 2015) used in Chapter 4, the input is the entire data cube. In this case the ring parameters are used to directly construct a model data cube which is subtracted from the input to yield a residual.

The parameter space of tilted ring models in general has many dimensions. Each ring has at least 3 $(V_{\mathrm{rot}}, i, \mathrm{PA})$ and up to 8 $(\sigma, \Sigma, X_0, Y_0, V_{\mathrm{sys}})$ parameters to be fit, and the number of rings varies from ~ 10 to over 100 depending on the size of the galaxy in units of the observational resolution. An additional complication is that some parameters are strongly degenerate – crucially, the inclination angle and rotation velocity are *exactly* degenerate in the case of 'solid body' rotation, i.e. $V(R) \propto R$. Some common strategies to help mitigate these issues are (i) to fit the parameters of each ring independently of the other rings, (ii) to perform an initial fit with all parameters free, then radially smooth the geometric parameters (particularly i and PA) and perform a second fit with these parameters fixed to their smoothed values and (iii) to use additional constraints such as the visible or H I morphology of the galaxy to impose strong priors on the geometric parameters (de Blok et al., 2008; Oh et al., 2011, 2015; Richards et al., 2016; Iorio et al., 2017). All of these can have potentially significant impact on the result of the model fitting.

---

[6]Depending on context, different weighting schemes are sometimes used.

1.3.4   Mass modelling

Once kinematic modelling is complete and the resulting rotation curve has been corrected for pressure support, if relevant, one more step, usually termed 'mass modelling' is required to complete a measurement of the dark matter distribution. This involves decomposing the spherically averaged total mass profile – the rotation curve – into its constituent parts: dark matter, gas and stars[7] (the latter two collectively being termed 'baryons'). The stars are often further sub-divided, if relevant, into bulge and disc components. The gas mass profile is usually estimated from the H i emission assuming a constant correction factor of 1.33–1.4 to account for the mass in helium and heavier elements. Conveniently the H i emission is almost always close to the optically thin regime, and the conversion from H i line flux to neutral hydrogen mass is straightforward and well understood (e.g. Giovanelli & Haynes, 1988). Contributions from molecular or ionized hydrogen are usually neglected. For more massive galaxies, where the stellar component usually strongly dominates the baryonic contribution, the gas is sometimes neglected entirely.

The conversion from stellar light to mass is more subtle. The mass-to-light ratio Υ is an extensively studied parameter (Courteau et al., 2014, and references therein). The best estimate value depends on the photometric filter, has several secondary systematic correlations (e.g. colour), and is generally somewhat uncertain. In the optimal scenario $3.6\,\mu$m infrared photometry is used; this is the band where the systematic uncertainty in Υ is minimized (Verheijen, 2001; Lelli et al., 2016a). As a way of quantifying the maximum possible impact of uncertainty in Υ, so-called maximum and minimum disc models are sometimes used. In the maximum disc model the largest possible Υ is chosen such that the baryonic contribution to the rotation curve nowhere exceeds the measured rotation curve. Conversely, in the minimum disc model $\Upsilon = 0$ is assumed. The combination of the two models puts conservative upper and lower limits on the dark matter mass profile.

Once the dark matter mass profile has been isolated, models corresponding to cuspy and cored dark matter haloes may be fit – some of the most commonly used are the NFW and pseudo-isothermal profiles (e.g. de Blok et al., 2001; Kuzio de Naray et al., 2008; de Blok et al., 2008; Oh et al., 2011, 2015). While this may be instructive, great care must be taken in the interpretation since the goodness of fit of each model is strongly affected by systematic effects: the extent of the rotation

---

[7]On the $\gtrsim 100\,$pc scales resolved by the observations described in Sec. 1.3.3 the central supermassive black hole is invariably dynamically insignificant.

curve, the inclination of the galaxy, the choice of radial sampling rate all play a role. These issues have recently been revisited by Pineda et al. (2017).

Another often used measure of the cusp core problem is to measure the inner slope of the dark matter density profile – cuspy haloes have central slopes $\mathrm{d}\log\rho/\mathrm{d}\log R \sim -1$, while a core corresponds to an inner slope closer to 0 (see Fig. 1.1). This measurement requires numerically computing two derivatives, one to compute $\rho(R)$ from the mass profile, and a second to measure the slope of the density profile. It furthermore relies heavily on the few most central resolution elements. Despite these difficulties, it has recently been used to claim that all sufficiently resolved galaxies in a large sample of dwarfs are strongly cored (Oh et al., 2015), and also that there is a diversity in the inner slopes spanning ∼all values between the cusped and cored cases (Adams et al., 2014).

The mass modelling process introduces many additional uncertain analysis steps after the already uncertain kinematic modelling. The new approach to quantifying the cusp-core problem I propose in Chapter 2 avoids using mass modelling entirely. This limits its applicability to dark matter dominated dwarf galaxies, but these happen to be the especially interesting cases anyway (e.g. Sec. 1.2.3).

1.4 Outline

In Chapter 2 I present a comparison of a compilation of rotation curves of galaxies across a wide range of masses and the circular velocity curves of galaxies drawn from cosmological hydrodynamical simulations. The metric used for the comparison evinces the cusp-core problem as a central mass deficit, and further highlights that the rotation curves of dwarfs, in particular, exhibit a wide diversity in their shapes at fixed V_{max}, much larger than seen in the simulations. Any satisfactory solution to the cusp-core problem must account for this diversity, in addition to the apparent existence of cores.

I switch focus in Chapter 3 away from the central mass content to the mass integrated out to the outskirts of galaxies. Most galaxies lie along a tight scaling relation between their baryonic and total mass, the baryonic Tully-Fisher relation. Some outliers with apparently anomalously low dark matter content are very difficult to explain. The most plausible explanation that emerges is that the inclinations of these galaxies have been overestimated, though this remains difficult to reconcile with error estimates reported in the literature.

Building on the conclusion of 3, that systematic errors in kinematic modelling can greatly impact the inferred properties of galaxies, in Chapter 4 I apply the same models used with observed galaxies to synthetic observations of simulated galaxies. Non-circular motions in the gas discs of the simulated galaxies, especially a quadrupolar perturbation to the azimuthal velocity field, are found to severely bias the recovered rotation curves. The end result is a diversity in rotation curve shapes strongly reminiscent of that seen in observed galaxies in Chapter 2. This is an encouraging step toward a possible solution to the cusp-core problem; whether these systematic errors can fully account for the discrepancy remains to be seen.

Chapter 5 contains concluding remarks and a summary.

1.5   Co-author contributions to published work

Chapters 2 and 3 are closely based on published articles; full references are given at the beginning of each chapter. In addition, an article closely based on Chapter 4 has been submitted for publication with the title 'Apparent cores and non-circular motions in the H I discs of simulated galaxies' and with author list as follows: Kyle A. Oman, Antonino Marasco, Julio F. Navarro, Carlos S. Frenk, Joop Schaye and Alejandro Benítez-Llambay.

Chapter 2 was written in collaboration with members of the EAGLE simulation collaboration (R. Bower, R. A. Crain, M. Furlong, M. Schaller, J. Schaye, T. Theuns) whose main contribution was the development, testing and calibration of the EAGLE galaxy formation model. The APOSTLE simulation collaboration are also co-authors (J. F. Navarro, A. Fattahi, C. S. Frenk, T. Sawala), they variously contributed by conceiving, running, managing and/or maintaining the APOSTLE suite of simulations, and offering suggestions on the methodology during ∼bi-weekly video-conferences. S. D. M. White suggested several useful improvements to the execution and presentation of the methodology. I performed all the analysis presented in the chapter myself, including assembling the compilation of observational measurements from the literature, writing routines to analyse the outputs of the APOSTLE and EAGLE simulations, and the preparation of all figures and an initial draft of the manuscript. The entire process was of course completed in close consultation with J. F. Navarro. All co-authors provided editorial input in the preparation of the final manuscript draft.

Chapter 3 was again written in collaboration with members of the APOSTLE

team (J. F. Navarro, A. Fattahi, C. S. Frenk, T. Sawala, M. Schaller). L. V. Sales was contemporaneously conducting a study using the APOSTLE simulation suite of the baryonic Tully-Fisher relation; her application of a similar methodology to similar (but distinct) questions led naturally to a collaborative effort; I am also a co-author on the article which she led. S. D. M. White again contributed a critical and useful assessment of the mehtodology. Similarly to above, I conducted all the analysis presented in the chapter, including the preparation of all figures and the initial drafting of substantial portions of the text, in close consultation with J. F. Navarro. All co-authors provided editorial input in the preparation of the final manuscript draft.

The co-authors of the article (under review) based on Chapter 4 are part of a group formed specifically to pursue the project presented in that chapter, and related work, which meets regularly by videoconference to discuss all aspects, both scientific and technical, of the work. The sole exception is A. Benítez-Llambay, who provided simulations of idealized gas discs which were useful in testing elements of the methodology. I completed all the analysis presented in the chapter myself, including the preparation of all synthetic observations, all figures, and the initial draft of the text, all in close consultation with J. F. Navarro. A. Marasco completed analysis very similar or identical to several of the steps in order to address related problems; this was very useful in checking several steps for correctness and sensitivity to details in the method. All co-authors provided editorial input in the preparation of the final manuscript.

Chapters 2 and 3 are identical to the published versions except where changes were required following the oral examination of this dissertation.

Chapter 2

The unexpected diversity of dwarf galaxy rotation curves

Abstract

We examine the circular velocity profiles of galaxies in ΛCDM cosmological hydrodynamical simulations from the EAGLE and LOCAL GROUPS projects and compare them with a compilation of observed rotation curves of galaxies spanning a wide range in mass. The shape of the circular velocity profiles of simulated galaxies varies systematically as a function of galaxy mass, but shows remarkably little variation at fixed maximum circular velocity. This is especially true for low-mass dark matter-dominated systems, reflecting the expected similarity of the underlying cold dark matter haloes. This is at odds with observed dwarf galaxies, which show a large diversity of rotation curve shapes, even at fixed maximum rotation speed. Some dwarfs have rotation curves that agree well with simulations, others do not. The latter are systems where the inferred mass enclosed in the inner regions is much lower than expected for cold dark matter haloes and include many galaxies where previous work claims the presence of a constant density 'core'. The 'cusp vs core' issue is thus better characterized as an 'inner mass deficit' problem than as a density slope mismatch.

For several galaxies the magnitude of this inner mass deficit is well in excess of that reported in recent simulations where cores result from baryon-induced fluctuations in the gravitational potential. We conclude that one or more of the following statements must be true: (i) the dark matter is more complex than envisaged by any current model; (ii) current simulations fail to reproduce the effects of baryons on the inner regions of dwarf galaxies; and/or (iii) the mass profiles of 'inner mass deficit' galaxies inferred from kinematic data are incorrect.

2.1   Introduction

Cosmological simulations have led to a detailed theoretical characterization of the clustering of dark matter on galaxy scales. It is now well established that, when baryons may be neglected, the equilibrium mass profiles of cold dark matter (CDM) haloes are approximately self-similar and can be adequately approximated by a simple formula (Navarro et al., 1996b, 1997). The 'NFW profile', as this is commonly known, has a formally divergent density 'cusp' near the centre, $\rho \propto r^{-\gamma}$, with $\gamma = 1$, and steepens gradually at larger radii. The corresponding circular velocity profile, $V_{\rm circ}(r)$, is thus relatively steep near the centre, $V_{\rm circ} \propto r^{1/2}$, in contrast with the rotation curves of some dwarf galaxies, where the inner rotation speed rises linearly with radius. The latter behaviour suggests that the dark matter density profile has a shallower inner slope than predicted by simulations, closer to a constant density 'core' rather than a steeply divergent 'cusp'. This 'cusp vs core' problem (Moore, 1994; Flores & Primack, 1994) has been known since the mid 1990s and has elicited a number of proposed solutions.

One is that the dark matter is not 'cold'. Cores can be produced in dark matter haloes by particle physics effects if the dark matter particles have specific properties that differ from those of WIMPs or axions, the standard CDM candidates. For example, phase space constraints give rise to cores in warm dark matter (WDM) haloes (e.g. Bode et al., 2001; Lovell et al., 2012), although current lower limits on WDM particle masses imply cores that are much smaller than those inferred for many dwarfs (Macciò et al., 2012a; Shao et al., 2013; Viel et al., 2013).

Alternatively, elastic collisions between particles of 'self-interacting' dark matter (SIDM; see, e.g., Spergel & Steinhardt, 2000) may create cores, provided the cross-sections are the right size. SIDM has fallen somewhat out of favour because of concerns that it may fail to account for the central dark matter density profiles of galaxy

clusters (Miralda-Escudé, 2002) or that it would lead to the dissolution of individual galaxies in clusters (Gnedin & Ostriker, 2001). However, recent work has concluded that those arguments may be countered by appealing to velocity-dependent cross sections (Vogelsberger et al., 2012) or by re-evaluating carefully the observational constraints. Indeed, Rocha et al. (2013) argue that a velocity-independent specific cross-section of order $\sigma/m \sim 0.1\,\mathrm{cm^2\,g^{-1}}$ can reproduce simultaneously dwarf and cluster observations, although this conclusion relies on a relatively uncertain extrapolation of their results to the regime of dwarfs. As a result, the situation remains unsettled. Zavala et al. (2013), for example, have recently argued that only a finely-tuned SIDM model can be reconciled with observation while Elbert et al. (2015) have concluded the opposite, although we note that the latter work is based on resimulations of only two halos of similar ($\sim 40\,\mathrm{km\,s^{-1}}$) circular velocity.

An alternative is that rotation curves may be reconciled with ΛCDM haloes by 'baryon effects' operating during the formation of the galaxy (Navarro et al., 1996a; Gnedin & Zhao, 2002; Read & Gilmore, 2005). In particular, recent simulations in which star formation occurs in a series of short bursts where dense clouds of gas are continually assembled and violently dispersed have been shown to drive potential fluctuations that can induce constant density cores at the centre of ΛCDM haloes (Mashchenko et al., 2006; Governato et al., 2010, 2012; Brook et al., 2012; Teyssier et al., 2013; Madau et al., 2014). Although there is no consensus that galaxy formation necessarily has this effect (other simulations make realistic galaxies without producing cores; see, e.g., Schaller et al., 2015, and our discussion below), there is growing consensus that the inner dark matter profiles can, in principle, be reshaped during the formation of a galaxy, even a dark matter-dominated one, in a manner that may depend on its merger history (see, e.g., Di Cintio et al., 2014; Oñorbe et al., 2015). 'Baryon-induced' cores in CDM halos would be difficult to distinguish from those produced by other effects, such as collisional effects in the case of SIDM (see, e.g., Vogelsberger et al., 2014b; Fry et al., 2015), complicating matters further.

Finally, it has been argued that a critical reappraisal of the actual constraints placed on the inner dark matter density slope by observations might be needed, citing concerns about complexities such as non-circular motions (Swaters et al., 2003), instrumental smearing effects (Swaters et al., 2003; van den Bosch et al., 2000), and/or departures from axisymmetry (Hayashi et al., 2004), all of which may complicate the relation between the observational data and the underlying gravitational potential. The advent of two-dimensional observational surveys with better sensitivity and an-
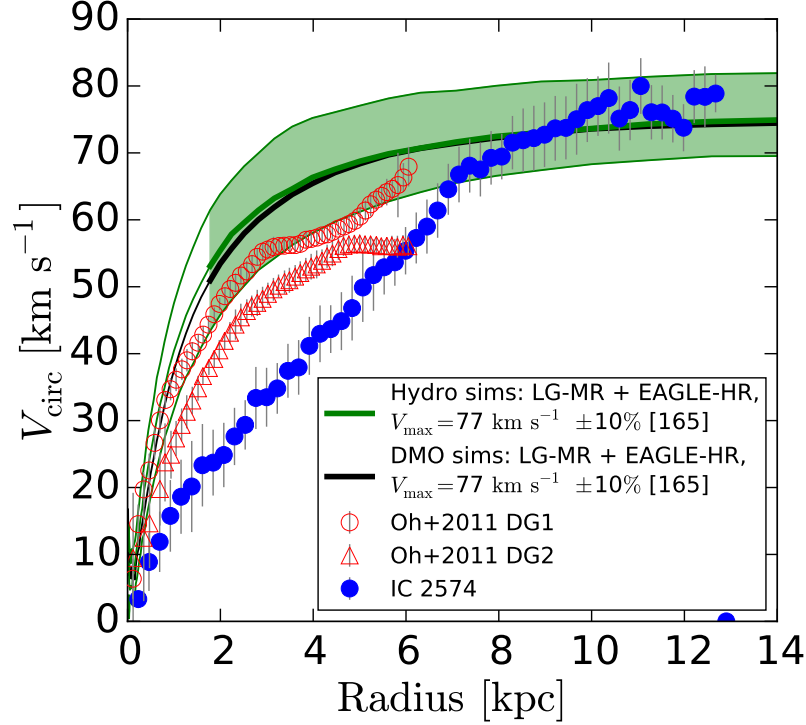
Figure 2.1: Rotation curves of IC 2574 (filled circles) and of the simulated galaxies DG1 (open circles) and DG2 (open triangles), taken from Oh et al. (2011). The green line shows the median circular velocity curve of all galaxies from our LG-MR and EAGLE-HR simulations (see Sec. 2.2.1) with $V_{max} = 77$ km s$^{-1} \pm 10$ per cent, matching the value of V_{max} of IC 2574. The shaded area indicates the 10th–90th percentile range at each radius. The lines become thinner and the shading stops inside the average convergence radius, computed following the prescription of Power et al. (2003). The numbers in square brackets in the legend are the numbers of galaxies/haloes that contribute to that velocity bin. The solid black line is the median circular velocity profile of haloes of the same V_{max}, identified in our dark matter-only simulations.

gular resolution have allayed some of these earlier concerns (e.g., Simon et al., 2003; de Blok et al., 2008; Kuzio de Naray et al., 2008; Oh et al., 2011; Adams et al., 2014; Oh et al., 2015), and have led to the view that reliable determination of the inner slope of the dark matter density profile is indeed possible.

Some questions, however, remain. Adams et al. (2014), for example, report inner slopes as steep as $\gamma = 0.67 \pm 0.10$ for a sample of seven nearby dwarfs, whereas Oh et al. (2011) report much shallower slopes ($\gamma = 0.29 \pm 0.07$) for seven dwarfs selected from the THINGS survey (Walter et al., 2008). Whether these discrepancies reflect a genuine physical difference between the galaxies in each of those samples, or a systematic difference in the modeling of the observational data, is still unclear. What is clear is that the inferred slopes are highly sensitive to how the mass of the baryonic population is modeled as well as to how the inevitable presence of noncircular motions near the centre is accounted for.

The case of NGC 2976 offers a sobering example: when inner kinematic peculiarities in the gas are ignored a nearly constant density core is inferred (Simon et al., 2003), while a much steeper slope is inferred from Jeans modeling of stellar tracers (Adams et al., 2012). Although the disagreement can be resolved once the non-circular motions are accounted for and the total mass of the stellar component is better constrained (Adams et al., 2014), this example illustrates the difficulty of inferring γ, even when quality multi-tracer data at high resolution are available.

A further drawback of focusing the discussion on the central value of γ is that it risks missing an important dimension of the problem, which concerns the total mass enclosed within the inner regions of a galaxy. This may be illustrated by the case of IC 2574, one of seven systems whose rotation curves were compared by Oh et al. (2011) to simulated galaxies where baryon-induced fluctuations had flattened the dark matter cusp (Governato et al., 2010). Oh et al. conclude that the simulated galaxies have 'haloes with a central mass distribution similar to that observed in nearby dwarf galaxies', a conclusion based on the similarity of the innermost values of γ.

Although the value of γ in the inner $\sim 1\,\mathrm{kpc}$ of these systems might be similar, the full circular velocity profiles of IC 2574 and simulated galaxies are actually very different. We show this in Fig. 2.1, where we plot the circular velocity profile of IC 2574 (filled circles) with that of DG1 (open circles) and DG2 (open triangles), the two simulated galaxies from the Oh et al. study. The simulated galaxies show a clear excess of mass in the inner regions compared to IC 2574, despite the 'cores' in the dark matter carved out by baryons. The reason for the discrepancy is that these
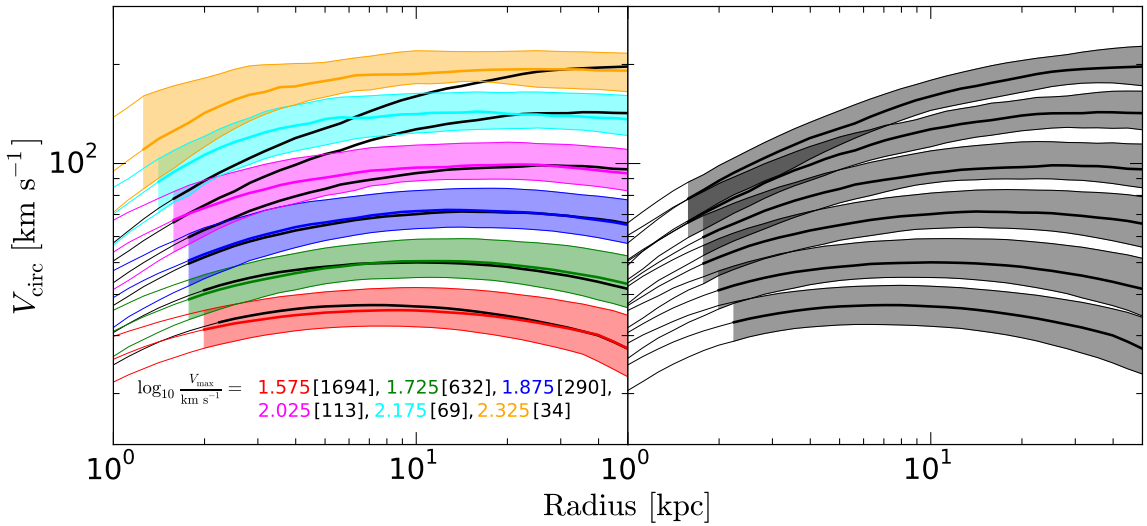
Figure 2.2: Circular velocity curves of simulated galaxies in the EAGLE-HR and LG-MR simulations, which have similar mass and force resolution. The left panel shows the results for hydrodynamical simulations; the right panel shows results for the corresponding dark matter-only (DMO) runs. Systems are grouped according to their maximum circular velocity in bins of 0.15-dex width as listed in the legend. The number of systems in each bin is also listed in the legend, in square brackets. Solid curves indicate the median circular velocity curve for galaxies in each bin; the shaded areas show the 10th–90th percentile range. The curves become thinner line and shading stops inside the average convergence radius, computed for each bin using the prescription of Power et al. (2003). The solid black curves are the same in both panels, and indicate the median circular velocity curves in the DMO simulations.

cores are small, and only affect the inner kpc, whereas IC 2574 shows a linearly-rising rotation curve out to $\sim 8\,\text{kpc}$. The 'baryon-induced' cores in these simulations are clearly too small to reconcile CDM with rotation curves of galaxies like IC 2574, so the reported agreement between observation and simulation is, in this case, illusory.

The above discussion demonstrates that resolving the 'cusp vs core' problem requires more than just matching the innermost values of γ. Even if baryon effects are able to flatten the innermost value of γ to values consistent with observed estimates (see, e.g., fig. 2 in Pontzen & Governato, 2014, for a comparison at 500 pc from the centre), this is not enough to ensure that simulated rotation curves agree with observation. We argue therefore for a reassessment of the 'cusp vs core' controversy where full circular velocity profiles of observed galaxies are directly compared with the results of cosmological hydrodynamical simulations. This has only become possible very recently, given the advent of cosmological hydrodynamical simulations able to produce a realistic galaxy population and, presumably, also realistic rotation curves (see, e.g., Vogelsberger et al., 2014a; Schaye et al., 2015).

The analysis we advocate here, which extends to lower masses that of Schaller et al. (2015), has a number of advantages. One is that the inner regions, which are difficult to observe *and* to simulate, are less emphasized in the comparison. The second is that it makes full use of the predictive power of the ΛCDM paradigm. Earlier work had left considerable room for discussion because of uncertainties, for example, in the normalization of the NFW mass-concentration relation, which determines the actual density profile of a halo of given mass. That debate has now been settled: the cosmological parameters are known to exquisite accuracy (see, e.g., Planck Collaboration et al., 2016), and large cosmological simulations with excellent resolution have characterized conclusively the mass-concentration relation, its normalization, and scatter (see, e.g., Neto et al., 2007; Duffy et al., 2008; Macciò et al., 2008; Zhao et al., 2009; Prada et al., 2012; Ludlow et al., 2014). As a result, simulated galaxies can now be compared directly with observations without need for rescalings or other adjustments.

We adopt this view here by considering the circular velocity profiles of galaxies selected from the EAGLE and LOCAL GROUPS simulation projects. The simulated galaxies cover a wide range of maximum circular velocity, from 25 to $250\,\text{km s}^{-1}$, and are compared with data compiled from the literature for galaxies that span a similar range in maximum rotation velocity. We begin by presenting the simulated curves in Sec. 2.2 and the observed compilation in Sec. 2.3. We then compare them and discuss

our results in Sec. 2.4, before summarizing our main conclusions in Sec. 2.5.

2.2 Circular Velocity Profiles of Simulated Galaxies

We discuss here the circular velocity curves of galaxies selected from the EAGLE (Schaye et al., 2015; Crain et al., 2015) and LOCAL GROUPS (Sawala et al., 2015) simulation projects. EAGLE is calibrated to reproduce, in a cosmological volume, the observed population of galaxies, including their abundance as a function of galaxy mass and their typical size. LOCAL GROUPS simulates volumes tailored to match the Local Group environment with the same physics as EAGLE but at higher numerical resolution. We refer the interested reader to the above references for details, and provide here only a brief summary of the parameters most relevant to our analysis.

2.2.1 The numerical simulations

The EAGLE simulations

The EAGLE project is a suite of cosmological hydrodynamical simulations run with a substantially modified version of the P-GADGET3 code, itself a descendent of the publicly available GADGET2 (Springel, 2005). In this work we use only the highest-resolution realization in the suite, which we denote EAGLE-HR (Ref-L025N0752[1] in the nomenclature of Schaye et al., 2015). This simulation has a cube side length of 25 comoving Mpc; 752^3 dark matter particles each of mass $1.21 \times 10^6 \, M_\odot$; the same number of gas particles each of mass $2.26 \times 10^5 \, M_\odot$; and a Plummer-equivalent gravitational softening length of 350 proper pc (switching to comoving above redshift 2.8). The cosmology adopted is that of the Planck Collaboration (2014), with $\Omega_m = 0.307$, $\Omega_\Lambda = 0.693$, $\Omega_b = 0.04825$, $h = 0.6777$ and $\sigma_8 = 0.8288$. EAGLE uses the pressure-entropy formulation of smoothed particle hydrodynamics (Hopkins, 2013), and includes subgrid models for radiative cooling, star formation, stellar and chemical enrichment, energetic stellar feedback, black hole accretion and mergers, and AGN feedback.

---

[1]Though the fiducial EAGLE model for this box size and resolution is Recal-L025N0752, we use the Ref-L025N0752 model because it more closely matches the subgrid physics used in the LOCAL GROUPS simulations.
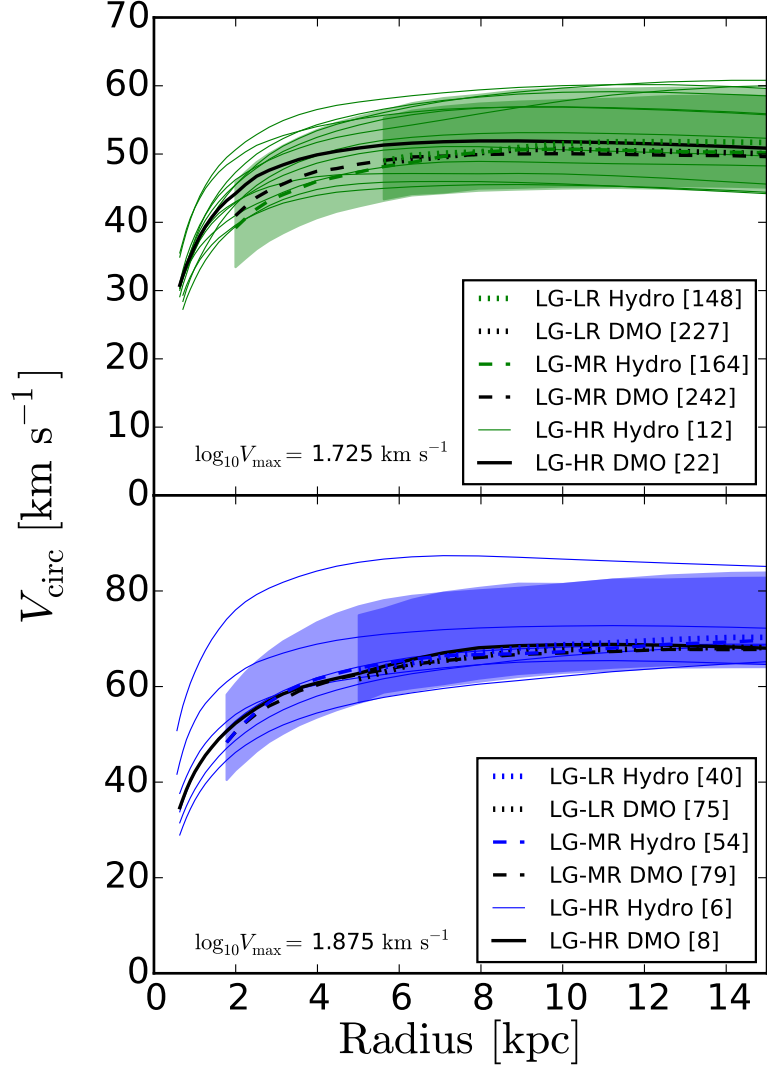
Figure 2.3: As Fig. 2.2, but for only two velocity bins, and shown in linear units. The total number of galaxies in each bin are listed in the legend. The dotted lines correspond to galaxies in the low-resolution LG-LR simulations, shown only down to their convergence radii. The dashed line shows the same, but for galaxies in the medium resolution LG-MR simulations. Thin solid curves correspond to individual systems in the high-resolution LG-HR simulations. Only two of the twelve LG volumes have been simulated at high resolution, hence the relatively small number of individual curves in each panel. The black lines show the median circular velocity profile for dark matter-only simulations.

Table 2.1: Summary of the key parameters of the EAGLE and LOCAL GROUPS simulations used in this work. Details of the cosmological parameters are available in Komatsu et al. (2011, WMAP7) and Planck Collaboration (2014, Planck13).

Simulation	Particle Masses ($M_\odot$)		Max Softening Length (pc)	Cosmology
	DM	Gas		
EAGLE-HR	1.2×10^6	2.3×10^5	350	Planck13
LG-LR	7.3×10^6	1.5×10^6	712	WMAP7
LG-MR	5.9×10^5	1.3×10^5	308	WMAP7
LG-HR	5.0×10^4	1.0×10^4	134	WMAP7

The LOCAL GROUPS simulations

The LOCAL GROUPS project is a suite of zoom-in hydrodynamical simulations of regions selected from cosmological dark matter-only simulations to contain two haloes with approximately the masses and dynamics of the Milky Way and M31, and no other nearby large structures (Fattahi et al., 2016). LOCAL GROUPS uses the same code and physics as the 'Ref' EAGLE simulations. The same volumes are simulated at three different resolution levels, which we denote LR-LR, LG-MR and LG-HR for low, medium and high resolution, respectively. Each resolution level is separated by a factor of ~ 10 in particle mass and a factor of ~ 2 in force resolution.

Table 2.1 summarizes the particle masses and softening lengths of each resolution level. We note that the LG-MR resolution level corresponds closely to EAGLE-HR. There are 12 volumes, all of which have been simulated at LR-LR and LG-MR resolution levels. Only volumes 1 and 4 have been simulated at high resolution. For each hydrodynamical simulation there is also a corresponding dark matter-only (DMO) simulation of the same region at the same resolution. The WMAP7 cosmological parameters (Komatsu et al., 2011) are used in LOCAL GROUPS[2], with $\Omega_m = 0.2727$, $\Omega_\Lambda = 0.728$, $\Omega_b = 0.04557$, $h = 0.702$ and $\sigma_8 = 0.807$.

The LOCAL GROUPS simulation suite produces realistic Local Group-like environments, reproducing the stellar mass function of Milky Way and M31 satellites, and that of Local Group dwarf galaxies (Sawala et al., 2016a) using the same calibration parameter choices as the EAGLE-Ref simulations.

---

[2]The differences between the cosmological parameters used in the EAGLE and LOCAL GROUPS projects are very small and of little consequence to this study.

Halo finding

Structures are identified in our simulations using the SUBFIND algorithm (Springel et al., 2001; Dolag et al., 2009). Particles are first grouped into friends-of-friends (FoF) haloes by linking together dark matter particles separated by less than 0.2 times the mean interparticle spacing; gas and star particles are assigned to the same FoF halo as their nearest dark matter particle. Substructures are then separated along saddle points in the density distribution; in this step dark matter, gas and star particles are treated as a single distribution of mass. Finally, particles that are not gravitationally bound to the substructures are removed. The result is a collection of substructures termed 'subhaloes', each typically corresponding to a single galaxy.

2.2.2 Circular velocity curves

The circular velocity profiles of simulated galaxies, $V_{\mathrm{circ}}(r) = (GM(<r)/r)^{1/2}$, where $M(<r)$ is the mass enclosed within radius r, are shown in the left panel of Fig. 2.2. Here we have gathered all 'central' galaxies (i.e. excluding satellites) in the 12 LG-MR simulations, together with all centrals in the EAGLE-HR simulation, and binned them according to their maximum circular velocity, V_{max}. We adopted bins of 0.15-dex width, centred at $\log_{10}(V_{\mathrm{max}}/\mathrm{km\,s^{-1}}) = 1.575, 1.725, 1.875, 2.025, 2.175, 2.325$, and show the median rotation curve for galaxies in each bin with solid lines. The shaded areas indicate, at each radius, the 10th and 90th percentile velocity for all galaxies in each bin. The number of galaxies in each bin is listed in the legend.

This figure illustrates two important points. One is that the shapes of the circular velocity curves of ΛCDM galaxies are a strong function of the maximum circular velocity of the system. Indeed, once V_{max} is specified, the circular velocity profile of a system is very well constrained at all radii that are resolved[3] by the simulations. The second point is that, in general, circular velocity curves of systems with substantially different V_{max} do not cross, so that in principle a well measured circular velocity at almost any radius may be translated into an excellent constraint on V_{max}.

These characteristics of the circular velocity curves are largely a reflection of the self-similar nature of ΛCDM haloes, modified by the baryonic component. This may be seen in the right panel of Fig. 2.2, which is analogous to that in the left, but for

---

[3]We adopt in all cases the 'convergence radius' introduced by Power et al. (2003), as computed from the DMO simulations. This radius marks the point where curves turn thinner and the shading stops in all figures.

systems identified in dark matter-only simulations of the same EAGLE and LOCAL GROUPS volumes. (The solid black lines are the same in both panels and indicate the median rotation curves in the DMO simulations.) As discussed by Schaller et al. (2015), the effects of baryons are mainly discernible in systems with $V_{\mathrm{max}} > 60\,\mathrm{km\,s^{-1}}$. In those systems, the assembly of the baryonic component of the galaxy leads to an increase in mass that tends to flatten the $V_{\mathrm{circ}}(r)$ profile in the inner few kpc.

In systems with $V_{\mathrm{max}} < 60\,\mathrm{km\,s^{-1}}$, on the other hand, the galaxy formation 'efficiency' is very low, and the baryonic mass of the central galaxy has, in general, a negligible effect on the circular velocity curve, even in the inner regions. Our simulations thus show little evidence for the formation of a constant-density 'core' near the centre of dwarf galaxies, suggesting that the dark matter 'core creation' mechanism discussed by Pontzen & Governato (2014) is not a general result of ΛCDM simulations that produce realistic galaxy populations, but rather a consequence of particular algorithmic choices adopted to simulate star formation and feedback.

Indeed, simulations that produce 'cores' generally adopt a high density threshold for star formation ($n_H \gtrsim 100\,\mathrm{cm^{-3}}$, e.g. Governato et al., 2010) that results in micro bursts of star formation concentrated in highly compact gas clouds that can be rapidly dispersed by feedback. This mode of star formation is not present in our simulations, which adopt a lower effective star formation threshold ($n_H \gtrsim 0.1\,\mathrm{cm^{-3}}\,(Z/0.002)^{-0.64}$, depending on the metallicity Z and motivated by models of the H I–H$_2$ transition; Schaye, 2004) because we do not attempt to model a cold ($T \ll 10^4$ K) insterstellar gas phase. Our simulations thus allow star formation to occur throughout the rotationally-supported gaseous disk of a galaxy, limiting the sudden fluctuations in the gravitational potential on small scales.

Although we do not see obvious evidence for constant density cores in the circular velocity profiles, we do find $\sim 1\,\mathrm{kpc}$ cores in the dark matter density profile of some galaxies with $V_{\mathrm{max}} \gtrsim 100\,\mathrm{km\,s^{-1}}$. These cores are *only* present in the dark matter – any dark mass displaced is actually replaced by baryons so that the net result is typically an overall increase in the total mass in the inner regions and a steepening of the potential. As a result, these cores canonot explain the linearly-rising rotation curves of dwarf galaxies, and are of little consequence to the rest of our analysis.

Fig. 2.3 offers evidence that the lack of 'cores' in the *total* mass profiles in our simulations is not a result of insufficient numerical resolution. Here we show, in linear units, the circular velocity profiles of LOCAL GROUPS galaxies in two bins of V_{max}, simulated at three different numerical resolutions (LG-HR, LG-MR, and LG-LR; see

Sec. 2.2.1). As in Fig. 2.2, the shaded regions in Fig. 2.3 show the 10th–90th percentile range spanned by the $V_{\text{circ}}(r)$ curves in each bin, for the medium-resolution (MR) and low-resolution (LR) simulations. The thin lines in Fig. 2.3 correspond to individual systems identified in the high-resolution (HR) version of the same simulations. Fig. 2.3 shows that, at all well-resolved radii, the circular velocity profiles are insensitive to numerical resolution, despite the fact that the LG simulation series span a factor of $12^2 = 144$ in particle mass and of more than ~ 5 in force resolution.

We emphasize that, although our simulations do not form 'cores', they do produce galaxies whose abundance, structural properties, and evolution seem in good accord with observational constraints (see, e.g., Schaye et al., 2015; Sawala et al., 2016a; Furlong et al., 2015; Schaller et al., 2015). The formation of dark matter 'cores' thus does not appear to be a requisite ingredient of galaxy formation simulations that successfully reproduce the structural properties of the observed galaxy population, at least for galaxies with stellar masses $M_\star \gtrsim 10^9 \, \text{M}_\odot$.

2.3   Observed Rotation Curves

Our sample of galaxy rotation curves is compiled from several literature sources. We describe the sources of our compilation in detail in Sec. A, and list some key properties of the individual rotation curves that we use in our analysis in Table A.1. Our compilation retains only recent data sets (i.e., published after 2001), and favours, where possible, data sets based on two-dimensional velocity fields, such as the integral-field optical data sets of Kuzio de Naray et al. (2008); or the high-resolution H I datacubes from Oh et al. (2015). For more massive galaxies, we supplement our compilation with the long-slit rotation curves of Reyes et al. (2011)[4] and Kauffmann et al. (2015). Although our data set is by no means complete, it contains 304 rotation curves (and an additional 189 from Reyes et al., 2011) spanning a wide range of V_{max}, from 21 to $350 \, \text{km} \, \text{s}^{-1}$. It also contains the majority of the dwarf galaxies that have been used in the literature to illustrate the 'cusp vs core' problem.

We assume throughout our analysis that the published rotation curves (which have been corrected, in most cases, for inclination effects, asymmetric drift, and non circular motions) provide a fair approximation to the circular velocity profiles of galaxies in our sample and hereafter refer to both as 'V_{circ}'. We note that this is a

---

[4]Full rotation curves were not available, we use instead the published parameters of fits to their rotation curves.

strong assumption which may fail for a number of dwarf systems where the observed galaxy is clearly highly irregular.

2.4 Observed vs Simulated Rotation Curves

2.4.1 The similarity of simulated circular velocity curves

The general properties of the rotation curves of simulated galaxies shown in Fig. 2.2 are in reasonable agreement with those of observed galaxies, thus extending the agreement between EAGLE and observations noted by Schaller et al. (2015, e.g. their fig. 6) for $V_{max} > 100 \, \mathrm{km \, s^{-1}}$ to lower mass systems. Circular velocities tend to rise sharply and stay flat in massive galaxies, but to rise more slowly in dwarf systems, where baryons play a less important role.

The agreement is not just qualitative. This may be seen in Fig. 2.4, where we compare directly the rotation curves of four galaxies of different circular velocity with the simulation results. The comparison is made with simulated systems whose maximum circular velocity matches, within 10 per cent, that of the observed galaxy, without any rescaling. The match in V_{max} ensures as well that the baryonic masses of simulated and observed galaxies are comparable, since the simulated systems satisfy the observed baryonic Tully-Fisher relation (Sales et al., 2017). We repeat one of the examples in Fig. 2.5, NGC 1560, to show a comparison with individual circular velocity curves drawn from the simulations. This galaxy follows the broad trend seen in simulations for object of comparable maximum circular velocity, however no individual curve is a precise match to the shape of the curve for NGC 1560.

The excellent agreement shown in Fig. 2.4 is meant to illustrate a more general point: the rotation curves of *many* galaxies, dwarfs included, are actually consistent with ΛCDM predictions. This is important to emphasize, since it is often thought that ΛCDM rotation curves are in conflict with data for *all* or *a majority* of galaxies, especially dwarfs.

2.4.2 The diversity of observed rotation curves

Actually, the main difference between simulated and observed rotation curves is the great *diversity* of the latter (especially for dwarfs), which is unexpected according to our results. We illustrate this in Fig. 2.6, where the rotation curves of four different
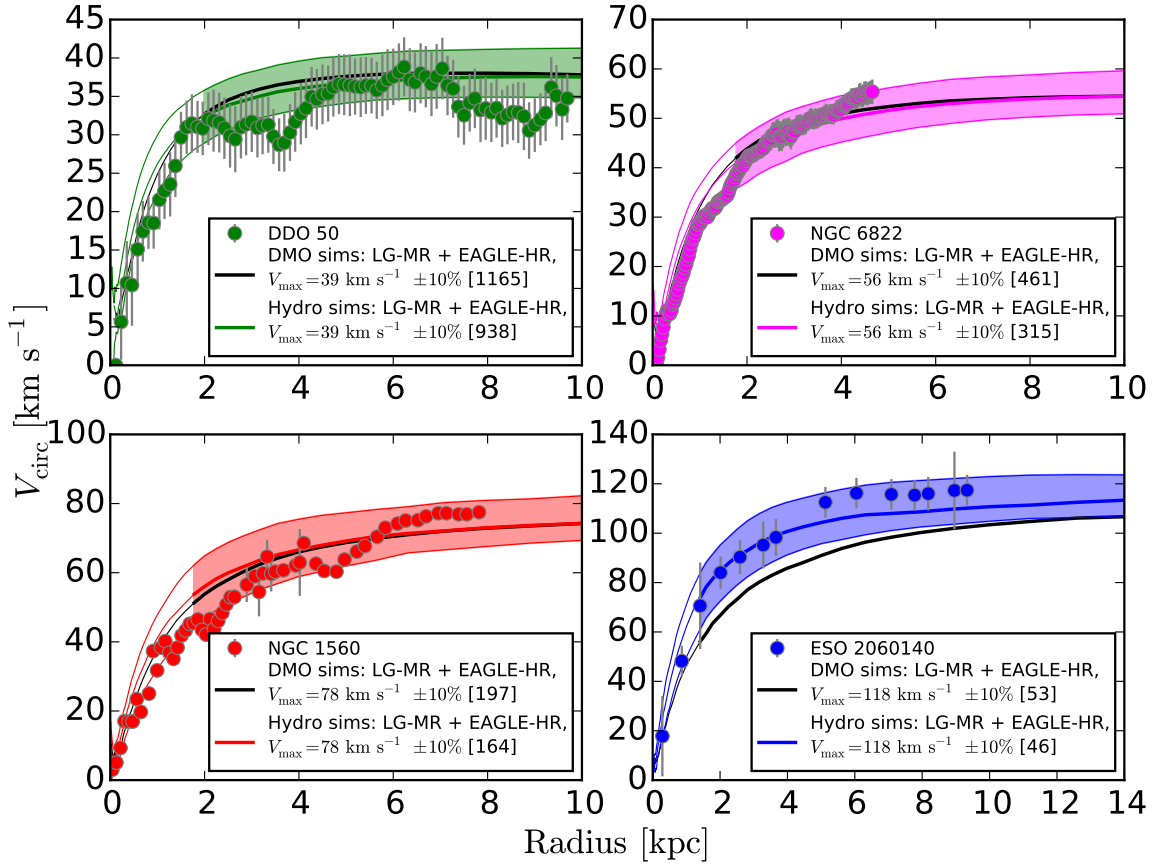
Figure 2.4: Four examples of galaxies in our sample with rotation curves that are in good agreement with the circular velocity curves of our ΛCDM hydrodynamical simulations. The four galaxies have been chosen to span a wide range in maximum circular velocity, from ~ 30 (top left) to $\sim 120\,\mathrm{km\,s^{-1}}$ (bottom right). As in Fig. 2.2, the solid curves and shaded areas show the median (and 10th–90th percentile range) of all simulated galaxies in 20 per cent-width bins centred at the maximum circular velocity of the galaxy in each panel (see legend). The solid black curve corresponds to the median circular velocity curve of our DMO simulations.
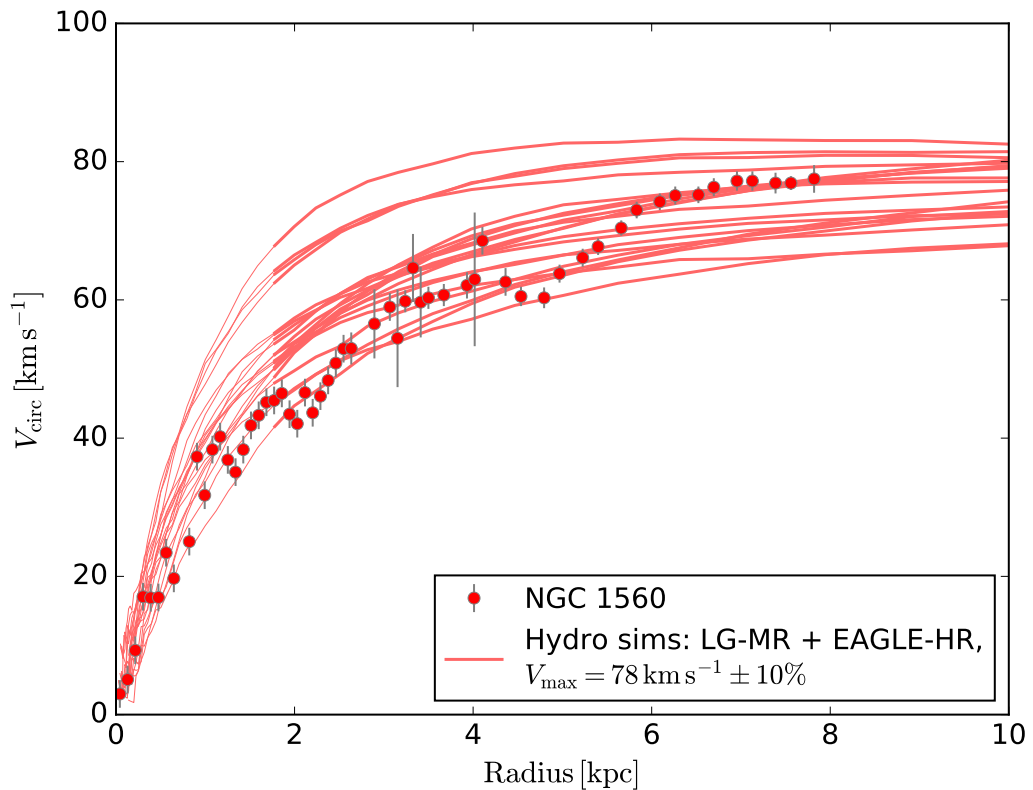
Figure 2.5: Rotation curve of NGC 1560 (symbols), as in lower left panel of Fig 2.4, compared with 20 individual simulated rotation curves randomly selected from the set of systems with $V_{max} = 78\,\mathrm{km\,s^{-1}} \pm 10$ per cent, from simulations including full hydrodynamics and galaxy formation modelling.

dwarf galaxies of similar maximum circular velocity are compared with simulated galaxies of matching V_{max}.

The four galaxies in this figure have been selected to illustrate the large diversity of rotation curve shapes at fixed V_{max}. According to the baryonic Tully-Fisher relation (McGaugh, 2012), these four galaxies have similar total baryonic masses, so the differences in rotation curve shape must be due to either systematic variations in the spatial distribution of the baryons, or to varying amounts of dark matter.

The baryon distribution is at least partly responsible, since it is well documented that high-surface brightness galaxies have more steeply rising rotation curves than low-surface brightness systems (see, e.g., McGaugh & de Blok, 1998; Swaters et al., 2009, and references therein). Quantitatively, however, the differences cannot be fully ascribed to baryons (see below), so the diversity seen in Fig. 2.6 reflects large systematic variations in the inner dark matter content as well.

2.4.3   The challenge to ΛCDM

The comparison between observed and simulated rotation curves thus highlights two challenges to ΛCDM. One is to understand the origin of the *diversity* at fixed V_{max}, especially in dwarf galaxies, which tend to be dark matter dominated. These are all galaxies that form in similar halos, have approximately the same baryonic mass, and similar morphologies. Some diversity induced by differences in the distribution of the baryonic component is expected, but clearly the observed diversity is much greater than in our simulations.

The second, and more worrying, concern is the *inner mass deficit* that some of these galaxies seem to exhibit relative to the ΛCDM simulation predictions. Indeed, except for UGC 5721, all of the galaxies shown in Fig. 2.6 have *less* mass in the inner 8 kpc than expected not only from our hydro simulations (shaded coloured regions) but also from a ΛCDM halo *alone* (solid black lines). Systems like UGC 11707 seem marginally consistent, and could perhaps be interpreted as outliers, but cases like IC 2574, or LSB F583-1 are too extreme to be accommodated by our model without significant change.

The mass deficit we highlight here has been noted before in the context of the 'cusp vs core' debate (see, e.g., McGaugh et al., 2007, and references therein). Indeed, if constant density 'cores' were imposed on the dark matter it would be relatively straightforward to reproduce the data shown in Fig. 2.6. Such cores, however, would
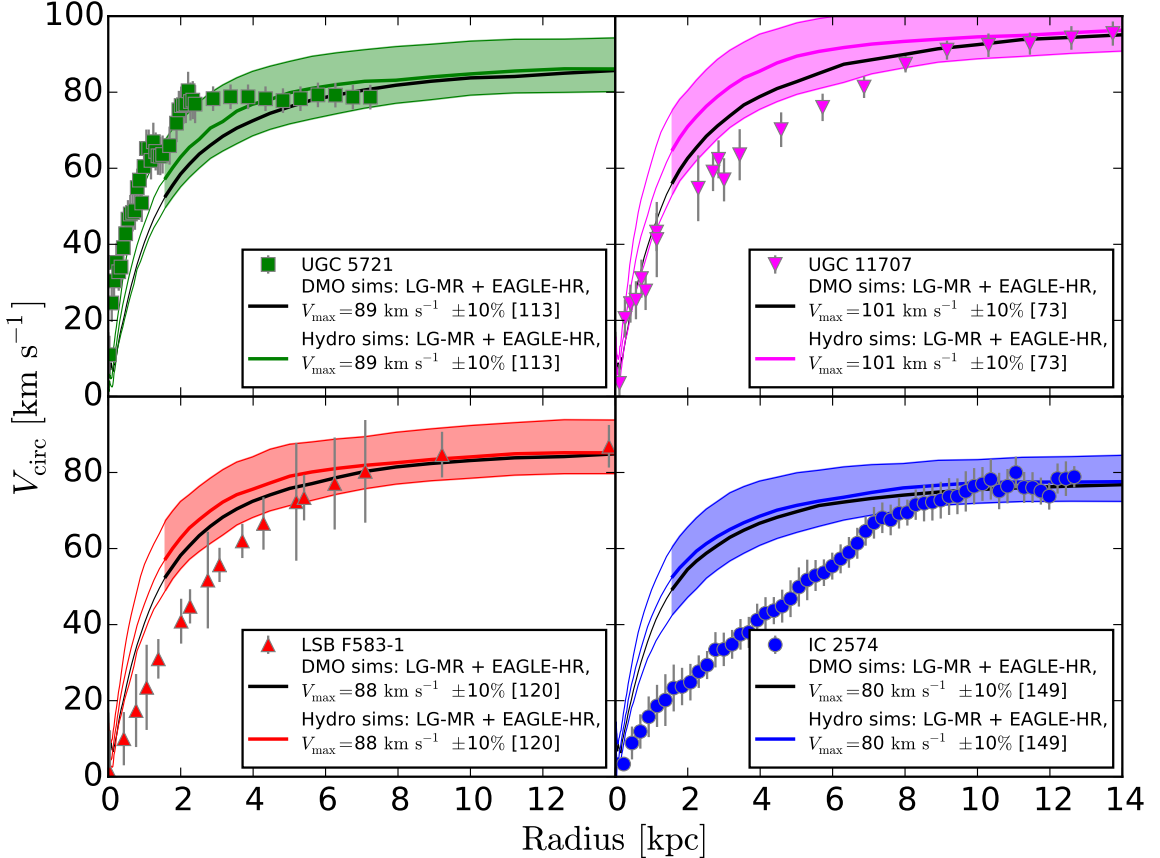
Figure 2.6: Rotation curves of four dwarf irregular galaxies of approximately the same maximum rotation speed (~ 80–$100\,\mathrm{km\,s^{-1}}$) and galaxy mass, chosen to illustrate the diversity of rotation curve shape at *given* V_{max}. As in previous figures, coloured solid curves and shaded areas correspond to the median (and 10th–90th percentile) circular velocity curve of simulated galaxies matching (within 10 per cent) the maximum circular velocity of each galaxy. Note that the observed rotation curves exhibit a much wider diversity than seen in the EAGLE and LOCAL GROUPS simulations, from galaxies like UGC 5721, which are consistent with our simulations, to galaxies like IC 2574, which show a much more slowly rising rotation curve compared with simulations, either hydrodynamical (coloured lines) or dark matter-only (black lines).

need to vary from galaxy to galaxy, *even at fixed halo mass and galaxy mass*. Indeed, a core at least as large as $\sim 5\,\mathrm{kpc}$ would be needed to explain the fact that the rotation curve of IC 2574 rises linearly out to $\sim 8\,\mathrm{kpc}$, but ought to be much smaller in LSB F583-1 and even smaller, if at all present, in UGC 5721.

2.4.4   The challenge to baryon-induced core formation

The diversity of observed rotation curves presents a challenge not only to our simulations, but also to the baryon-induced 'core' creation mechanism: why would baryons carve out cores so different in galaxies that are so similar in terms of morphology, halo mass, and galaxy mass? Further, we would expect the dark matter to be most affected in systems where baryons play a more important role in the potential, such as high-surface brightness galaxies, whereas observations seem to suggest the opposite trend.

A second challenge concerns the magnitude of the effect needed to create a core as large as that inferred, for example, for IC 2574. Published simulations where baryon effects create cores tend to have overall a modest effect on the total inner mass profile of the galaxy. One example is provided in Fig. 2.1; although baryons have carved a $\sim 1\,\mathrm{kpc}$ core in the dark matter halo in the simulated galaxy DG1, the total inner mass profile is actually quite similar to what is expected for galaxies of that circular velocity in our simulations (green-shaded region), which do not produce cores. This is because, to first order, the baryons that displace the dark matter to create a core take its place, leading to modest net changes in the total mass profile.

In other words, 'flattening the dark matter cusp' is not enough to explain galaxies like IC 2574. A *net removal* of large amounts of mass from the inner regions is needed to reconcile such galaxies with ΛCDM, at least if we equate the measured rotation curve with the circular velocity curve. In the case of IC 2574, at least $\sim 2.5 \times 10^9\,\mathrm{M_\odot}$ seem to have been expelled from the inner $\sim 5\,\mathrm{kpc}$; more than the total baryonic mass of the galaxy. It seems unlikely that baryon-induced fluctuations can cause an effect this large.

2.4.5   The challenge to alternative dark matter models

Finally, we note that the diversity of rotation curves illustrated in Fig. 2.6 disfavours solutions that rely solely on modifying the physical nature of the dark matter. Cores can indeed be produced if the dark matter is SIDM or WDM but, in this case, we
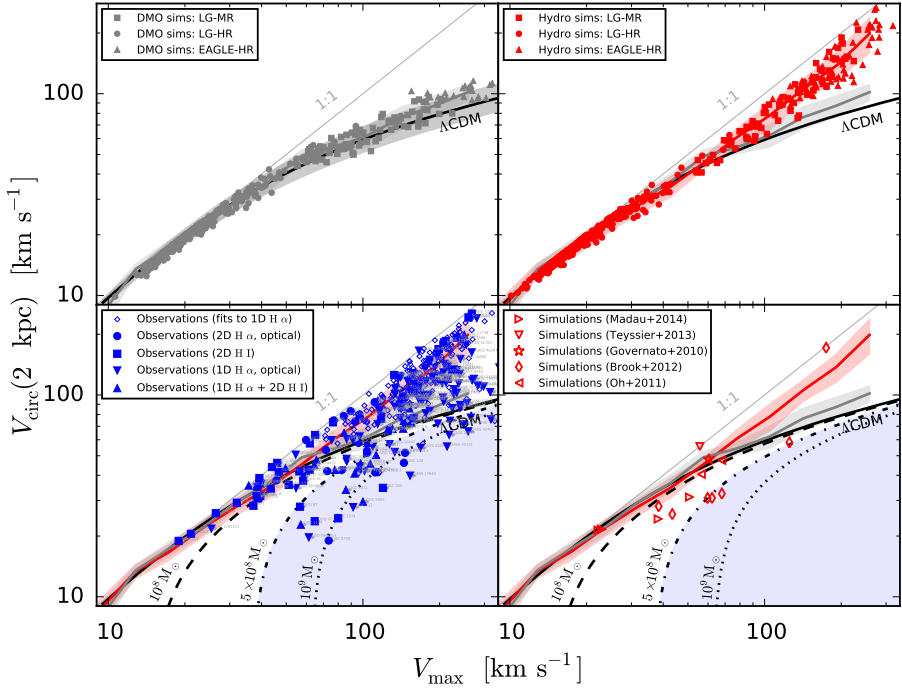
Figure 2.7: Circular velocity at $r = 2\,\mathrm{kpc}$ vs the maximum circular velocity, $V_{\max}$, for observed and simulated galaxies. For observed galaxies we use the maximum rotation speed as an estimate of $V_{\max}$, and the rotation speed measured at $2\,\mathrm{kpc}$ for $V_{\mathrm{circ}}(2\,\mathrm{kpc})$. We show only simulated systems for which the convergence radius is less than $2\,\mathrm{kpc}$, and observed galaxies for which the nominal angular resolution of the data is better than the angle subtended by $2\,\mathrm{kpc}$ at the galaxy's distance. *Top-left:* Results for dark matter-only simulations (grey points), together with the correlation expected for NFW haloes of average concentration (solid black line). The thick gray line traces the mean $V_{\mathrm{circ}}(2\,\mathrm{kpc})$ as a function of $V_{\max}$, whereas the shaded areas show the standard deviation. *Top-right:* As the top-left panel, but for simulated galaxies in the LOCAL GROUPS and EAGLE cosmological hydrodynamical simulations (red symbols). See the legend for details about each symbol type. The grey line and grey shaded region repeat the DMO correlation in the top-left panel, the red line and shaded region are analogous for the hydrodynamical simulations. *Bottom-left:* Observed galaxies (small text labels identify individual objects). The different symbols show the different tracers observed (H I, H α, other features in the optical) and whether the observations are in 1 dimension (1D, e.g. long slit spectroscopy) or 2 dimensions (2D, e.g. radio interferometry, integral field spectroscopy). Solid lines and shaded regions are as in the top right panel. Note the large variation in $V_{\mathrm{circ}}(2\,\mathrm{kpc})$ at fixed $V_{\max}$ compared with the simulation results. The dotted, dashed and dot-dashed lines indicate the changes in $V_{\mathrm{circ}}(2\,\mathrm{kpc})$ induced by removing a fixed amount of mass from the inner $2\,\mathrm{kpc}$ of ΛCDM haloes, as labelled. The blue-shaded region highlights systems with an inner $2\,\mathrm{kpc}$ mass deficit exceeding $5 \times 10^8 \mathrm{M}_\odot$. *Bottom-right:* Results of recent simulations that report the formation of cores in the dark matter profiles of ΛCDM haloes. These cores lead to a slight reduction in the value of $V_{\mathrm{circ}}(2\,\mathrm{kpc})$ relative to those in our simulations, but the changes are insufficient to explain the full range of values spanned by the observational data. The dotted lines and dashed lines are as in the bottom-left panel, for ease of comparison.

would expect *all* galaxies to have cores and, in particular, galaxies of similar mass or velocity to have cores of similar size. Available simulation data are sparse but suggest that the scatter in structural properties at fixed halo mass is no larger for alternative dark matter models than for ΛCDM (e.g. Rocha et al., 2013; Lovell et al., 2014, for SIDM and WDM respectively). This is in disagreement with rotation curve data and suggests that a mechanism unrelated to the nature of the dark matter must be invoked to explain the rotation curve shapes.

2.4.6 The 'inner mass deficit' problem

The prevalence of the 'inner mass deficit' problem discussed above may be characterized by comparing the inner circular velocities of observed galaxies with those of ΛCDM galaxies of matching $V_{\max}$. We show this in Fig. 2.7, where we use our ΛCDM simulations, as well as the compiled rotation curve data, to plot the circular velocity at 2 kpc against the maximum measured rotation speed, $V_{\max}$. Where data do not exist at exactly 2 kpc, we interpolate linearly between nearby data points. We choose a fixed physical radius of 2 kpc to characterize the inner mass profile because it is the minimum radius that is well resolved in all of our simulations for systems in the mass range of interest here. It is also a radius that is well resolved in all observed galaxies included in our compilation.

The grey symbols in the top left panel of Fig. 2.7 show the results of our DMO simulations. The tight correlation between these quantities in the DMO case is a direct consequence of the nearly self-similar nature of ΛCDM haloes: once the cosmological parameters are specified, the circular velocity at 2 kpc may be used to predict $V_{\max}$, and vice versa. Variations in environment, shape and formation history result in some scatter, but overall this is quite small. For given $V_{\max}$, the circular velocity at 2 kpc has a standard deviation of only ~ 0.1 dex. Our results are in good agreement with earlier DMO simulation work. The solid black line (and shaded region) in the figure indicates the expected correlation (plus 1-σ scatter) for NFW haloes with the mass-concentration relation corresponding to the cosmological parameters adopted in our simulations (Ludlow et al., 2014). Note that the simulated data approach the 1:1 line for $V_{\max} < 30 \, \mathrm{km \, s^{-1}}$: this is because those halos are intrinsically small; the radius where circular velocity profiles peak decreases steadily with decreasing circular velocity, from 4.6 kpc to 1.9 kpc when $V_{\max}$ decreases from 30 to 15 $\mathrm{km \, s^{-1}}$.

The inclusion of baryons modifies these correlations, as shown by the red symbols

in the top-right panel of Fig. 2.7, which show results for our hydrodynamical simula-tions. The main result of including baryons is to shift the expected correlation toward higher values of $V_{\rm circ}(2\ {\rm kpc})$ for galaxies with $V_{\rm max} \gtrsim 60\,{\rm km\,s^{-1}}$. This is not surpris-ing: the assembly of the luminous galaxy adds mass to the central few kiloparsecs and raises the circular velocity there. A tight relation between $V_{\rm max}$ and $V_{\rm circ}(2\ {\rm kpc})$ remains, however: the scatter increases only slightly, to at most ~ 0.15 dex (standard deviation).

Observed galaxies are shown in the bottom-left panel of Fig. 2.7. The diversity of rotation curves alluded to above is clearly seen here. At $V_{\rm max} \sim 70\,{\rm km\,s^{-1}}$, for exam-ple, the rotation speed at $2\,{\rm kpc}$ of observed galaxies spans more than a factor of ~ 4, or about a factor of ~ 16 in enclosed mass. Some of those galaxies, like DDO 168 have ro-tation speeds at $2\,{\rm kpc}$ comparable to the maximum ($V_{\rm max} \sim 62\,{\rm km\,s^{-1}}$, $V_{\rm circ}(2\ {\rm kpc}) \sim 58\,{\rm km\,s^{-1}}$), which indicates an enclosed mass of $\sim 2.3 \times 10^9\,{\rm M_\odot}$, or about twice as much as the *total* baryonic mass of the galaxy, according to the baryonic Tully-Fisher relation; $M_{\rm bar}/{\rm M_\odot} = 102.3\,(V_{\rm max}/\,{\rm km\,s^{-1}})^{3.82}$ (McGaugh, 2012). At the other ex-treme, galaxies like UGC 5750 ($V_{\rm max} \gtrsim 73\,{\rm km\,s^{-1}}$) [5] have rotation speeds at $2\,{\rm kpc}$ of just $\sim 20\,{\rm km\,s^{-1}}$, corresponding to an enclosed mass of only $\sim 2 \times 10^8\,{\rm M_\odot}$, or just about 10 per cent of its total baryonic mass.

Within their diversity, many observed galaxies actually have rotation curves that agree with ΛCDM, and fall well within the region of parameter space expected from our simulations (shown by the red-shaded area in this panel). Others do not. Galaxies *below* the solid gray line (which indicates the average DMO results in all panels) have less mass within $2\,{\rm kpc}$ than expected from a DMO simulation: if rotation velocities faithfully represent the circular velocity at this radius, then some of the central mass must have been displaced.

The dotted, dot-dashed, and dashed lines in the bottom panels of Fig. 2.7 quantify this effect. They indicate the result of removing a fixed amount of mass, as labelled, from the inner $2\,{\rm kpc}$ of NFW halos on the ΛCDM correlation (solid black line). Galaxies in the light blue-shaded area below the dot-dashed curve, in particular, have a mass deficit in the inner $2\,{\rm kpc}$ of more than $5 \times 10^8 {\rm M_\odot}$ compared with a typical ΛCDM halo. For DDO 87 ($V_{\rm max} \gtrsim 57\,{\rm km\,s^{-1}}$, $V_{\rm circ}(2\ {\rm kpc}) \sim 28\,{\rm km\,s^{-1}}$), for example, a galaxy that falls close to the dot-dashed line, this implies a total mass

---

[5] A rightward arrow is used in the bottom left panel of Fig. 2.7 to indicate cases where the rotation curve is still rising at the outermost radius measured – the maximum observed rotation speed may therefore underestimate $V_{\rm max}$.

deficit in the inner $2\,\mathrm{kpc}$ comparable to its total baryonic mass, as estimated from the baryonic Tully-Fisher relation. Indeed, several galaxies in our compilation have apparently expelled from the inner $2\,\mathrm{kpc}$ a mass comparable to or larger than their total baryonic mass.

Published simulations that report baryon-induced 'cores' seem unable to match these results. We show this in the bottom-right panel of Fig. 2.7, where the different open symbols show the results of simulations for which the formation of a 'core' in the dark matter has been reported. A few trends seem clear. Although 'core' formation alleviates the problem in some cases by bringing down the velocities at $2\,\mathrm{kpc}$, the effect is generally small; indeed, no 'cored' galaxies lie well inside the blue shaded area that characterizes systems with a mass deficit larger than $5 \times 10^8 \mathrm{M}_\odot$ in the inner $2\,\mathrm{kpc}$.

Further, core creation – or inner mass removal – seems ineffective in galaxies with $V_{\mathrm{max}} > 100\,\mathrm{km\,s^{-1}}$. Observations, on the other hand, show sizeable 'inner mass deficits' even in galaxies with maximum rotation velocities well above $100\,\mathrm{km\,s^{-1}}$. This may be a problem for 'baryon-induced' core formation, since it has been argued that the potential well might be too deep[6] in such systems for baryons to create a sizeable core (Brook et al., 2012). We note, however, that this conclusion is based only on two systems (see bottom-right panel of Fig. 2.7), and that none of those simulations include AGN feedback. It remains to be seen whether further simulation work will be able to produce inner mass deficits as large as observed in some of these massive galaxies.

With these caveats in mind, we conclude that none of the mechanisms proposed so far to explain the apparent presence of cores in dwarf galaxies has been able to fully account for their inner mass deficits and for the observed diversity of their rotation curves.

2.5   Summary and conclusions

We have used circular velocity curves from recent cosmological hydrodynamical simulations of galaxy formation in a ΛCDM universe, taken from the EAGLE and LOCAL GROUPS projects, to investigate the rotation curves of galaxies and reassess the 'cusp

---

[6]We note that Macciò et al. (2012b) report the creation of cores in more massive systems, but since these authors do not show the circular velocity profiles, we have been unable to add their results to our plot.

vs core' controversy.

The circular velocity curves of simulated galaxies vary systematically as a function of their maximum circular velocity (V_{max}), but show little variation for given V_{max}. Observed rotation curves, on the other hand, show great diversity, even at fixed V_{max}, especially for dwarf galaxies. At any given maximum rotation speed, some have shapes that are consistent with the simulation predictions, others do not. Deviant galaxies typically have much lower circular velocities in the inner regions than expected in ΛCDM from the dark matter halo *alone*. This apparent inner mass deficit varies from galaxy to galaxy, even at fixed galaxy mass, and can exceed, within ~ 2 kpc, the total baryonic mass of a galaxy.

Although this inner mass deficit may also be interpreted as evidence for a 'core' in the dark matter profile, we argue that characterizing the problem as an inner mass deficit is more robust, since it allows simulations to be compared directly with data without relying on uncertain decomposition of the dark matter and baryonic contributions to the central mass profile, or estimating dark matter density slopes in the innermost regions, where uncertainties in observations and simulations are largest.

Models that attempt to reconcile rotation curves with ΛCDM by carving 'cores' in the dark matter through baryon-induced gravitational fluctuations offer no natural explanation for the large dispersion in the values of the observed mass deficit. Nor do they seem able, at least according to published simulations, to account quantitatively for the largest mass deficits observed.

The diversity of observed rotation curves is also unexpected in alternative dark matter scenarios, substantially diminishing their appeal. This is because modifying the nature of dark matter may produce cores in dark haloes, but such cores would all be of similar size at given mass scale, unlike what is inferred from rotation curves.

Finally, it may be that dynamical inferences from available kinematic data need to be reevaluated. Many of the galaxies that show the largest mass deficits (or the strongest evidence for a 'core') appear highly irregular. Complexities such as non-circular and random motions, instrumental smearing and sampling effects, and/or departures from axisymmetry and coplanarity can substantially complicate the reconstruction of circular velocity profiles from the observed kinematics. The magnitude of the effect needed to reconcile ΛCDM with the data shown in Fig. 2.7 seem too large, however, to be due wholly to such uncertainties.

We conclude that present rotation curve data support neither a revision of the nature of dark matter, nor current models for 'core formation' in galaxies formed in

ΛCDM universe. The mystery of the inner rotation curves of galaxies thus remains unsolved.

Chapter 3

Missing dark matter in dwarf galaxies?

Abstract

We use cosmological hydrodynamical simulations of the APOSTLE project along with high-quality rotation curve observations to examine the fraction of baryons in ΛCDM haloes that collect into galaxies. This 'galaxy formation efficiency' correlates strongly and with little scatter with halo mass, dropping steadily towards dwarf galaxies. The baryonic mass of a galaxy may thus be used to place a lower limit on total halo mass and, consequently, on its asymptotic maximum circular velocity. A number of observed dwarfs seem to violate this constraint, having baryonic masses up to ten times higher than expected from their rotation speeds, or, alternatively, rotating at only half the speed expected for their mass. Taking the data at face value, either these systems have formed galaxies with extraordinary efficiency – highly unlikely given their shallow potential wells – or their dark matter content is much lower than expected from ΛCDM haloes. This 'missing dark matter' is reminiscent of the inner mass deficit of galaxies with slowly-rising rotation curves, but cannot be explained away by star formation-induced 'cores' in the dark mass profile, since the anomalous deficit applies to regions larger than the luminous galaxies themselves. We argue that

explaining the structure of these galaxies would require either substantial modification of the standard ΛCDM paradigm or else significant revision to the uncertainties in their inferred mass profiles, which should be much larger than reported. Systematic errors in inclination may provide a simple resolution to what would otherwise be a rather intractable problem for the current paradigm.

3.1 Introduction

The baryon content of the Universe is one of the best known parameters of the present cosmological paradigm, and is well constrained by a variety of independent observations, ranging from the cosmic abundance of the light elements (e.g., Steigman, 2007) to the fluctuations in the cosmic microwave background radiation (e.g., Hu & Sugiyama, 1995; Planck Collaboration et al., 2016). It is now widely accepted that the Universe has critical density ($\Omega \approx 1$) and that matter makes up ~ 31 per cent of the total matter-energy density ($\Omega_{\rm M} \sim 0.31$), with baryons contributing only a modest fraction ($f_{\rm bar} = \Omega_{\rm b}/\Omega_{\rm M} \sim 0.17$, Planck Collaboration et al., 2016).

Only a fraction of the Universe's baryons are at present locked up within the luminous regions of galaxies: current estimates of this quantity are in the range ~ 6–10 per cent (see, e.g., Madau & Dickinson, 2014). Galaxy formation has thus been a very inefficient process; most of the available baryons have been prevented (or pre-empted) from condensing into galaxies, presumably by cosmic reionization and by the feedback effect of the energetic output of evolving stars and active galactic nuclei.

A simple quantitative estimate of the resulting galaxy formation efficiency – which we define hereafter as $f_{\rm eff} = M_{\rm bar}/(f_{\rm bar}\, M_{200})$, i.e., the ratio between the baryonic mass of a galaxy, $M_{\rm bar}$, to the theoretical maximum consistent with the virial[1] mass of its host halo (White et al., 1993) – may be obtained by 'abundance matching' modelling of the galaxy population. These models indicate that the mean galaxy formation efficiency should be low in haloes of all masses, peaking at ~ 18 per cent in galaxies of stellar mass of order $3 \times 10^{10}\,{\rm M}_\odot$ and decreasing steeply toward higher and lower masses (see, e.g., Behroozi et al., 2013, and references therein).

The Milky Way sits near the peak of this relation and, at $f_{\rm eff} \sim 0.2$ (for a baryonic mass of order $\sim 5 \times 10^{10}$ and a virial mass of $1.5 \times 10^{12}\,{\rm M}_\odot$, Rix & Bovy, 2013; Wang

---

[1]We define the virial mass, M_{200}, as that enclosed by a sphere of mean density 200 times the critical density of the Universe, $\rho_{\rm crit} = 3H^2/8\pi G$. Virial quantities are defined at that radius, and are identified by a '200' subscript.

et al., 2015), it is considered something of an outlier where galaxy formation has proceeded particularly efficiently. Galaxy formation is expected to be *much* less efficient in fainter systems due to the enhanced feedback effects on shallower potential wells (Larson, 1974; White & Rees, 1978; Efstathiou, 1992; Bullock et al., 2000; Benson et al., 2002), dropping down to essentially zero in haloes with virial masses below $\sim 10^9 \, \mathrm{M_\odot}$ (Sawala et al., 2016b).

The steady decline of f_{eff} with decreasing halo mass is now recognized as one of the basic ingredients of galaxy formation models in the Lambda-Cold Dark Matter (ΛCDM) paradigm, since it serves to reconcile the steeply-rising low-mass end of the CDM halo mass function with the relatively shallow faint-end of the galaxy stellar mass function (White & Frenk, 1991). Assuming that the scatter in the galaxy mass–halo mass relation remains relatively small at low mass, the baryonic mass of a galaxy thus imposes a fairly strict lower limit on the mass of the halo it inhabits and, given the self-similar nature of CDM halo structure (Navarro et al., 1997), on its asymptotic maximum circular velocity. This basic prediction could in principle be readily verified by analysing galaxies where high-quality estimates of their baryonic masses and rotation speeds are available.

A few issues must be considered, however, when attempting such a comparison. Observational estimates of baryonic masses include the contributions of stars and atomic/molecular gas, and are subject to uncertainties in the mass-to-light ratio of the stellar component; in the conversion from neutral hydrogen to total gaseous mass; and in the distance to each individual galaxy (well-studied dwarfs are usually too close for redshift-based distance estimates to be accurate). Another problem is the short radial extent of rotation curves, which in many cases are still rising at the outermost point and, therefore, do not constrain the maximum circular velocity of the system. Finally, observations measure gas velocity fields, which are usually translated into estimates of *circular* velocity curves to probe the underlying gravitational potential. This translation includes corrections for inclination, asymmetric drift, non-axisymmetric and random motions, and instrumental limitations which must be carefully taken into account, especially in dwarf galaxies, many of which are notorious for their irregular morphology.

The theoretical modelling introduces additional uncertainties. A large scatter in galaxy formation efficiency in low-mass haloes might be expected given the sharp decline in f_{eff} required as haloes approach the mass below which galaxies fail to form (Ferrero et al., 2012). In addition, baryons may alter the structure of the dark

halo, creating cores that reduce the central density and depress systematically local estimates of the circular velocity (Navarro et al., 1996a; Mashchenko et al., 2006; Pontzen & Governato, 2014).

The observational issues may be addressed by selecting for analysis a galaxy sample with well-calibrated distances, good photometry in multiple passbands, and rotation curves that provide estimates of the circular velocity well beyond the radius that contains the majority of the stars in a galaxy. We therefore focus here on some of the best studied nearby galaxies, including those from (i) the THINGS (Walter et al., 2008) and LITTLE THINGS (Hunter et al., 2012) surveys; (ii) six dwarfs with exquisite multiwavelength data from Adams et al. (2014), as well as (iii) those included in the baryonic Tully-Fisher compilation of McGaugh (2012). The 77 selected galaxies span nearly four decades in baryonic mass, $10^7 < M_{bar}/M_\odot < 10^{11}$, and roughly a decade in maximum rotation speed, $20 < V_{rot}^{max}/km\,s^{-1} < 200$.

We address the theoretical modelling issues by using results from some of the latest ΛCDM cosmological hydrodynamical simulations of galaxy formation. We use, in particular, results from the APOSTLE[2] suite of simulations (Fattahi et al., 2016), which uses the same code developed for the EAGLE project (Schaye et al., 2015; Crain et al., 2015). This code, based on P-GADGET3, a descendent of the GADGET2 code (Springel, 2005), has been shown to reproduce the galaxy size and stellar mass functions in a cosmological volume as well as the abundance and properties of dwarf galaxies and satellite systems in the Local Group (Sawala et al., 2016a). These simulations thus provide realistic estimates of the dependence of galaxy formation efficiency on halo mass, as well as its scatter.

Dark matter cores do not develop in dwarfs in the APOSTLE simulations, presumably as a result of choices made when implementing subgrid physics in EAGLE (Schaller et al., 2015; Oman et al., 2015). These choices are effective at preventing the artificial fragmentation of gaseous disks, but also limit the magnitude of fluctuations in the gravitational potential that result from the assembly and dispersal of dense star-forming gas clouds. The latter, according to recent work, might lead to the formation of cores in the dark matter (Pontzen & Governato, 2014). We therefore supplement our analysis with results from the literature where 'baryon-induced cores' have been reported (Brook et al., 2012; Chan et al., 2015; Santos-Santos et al., 2016).

---

[2]APOSTLE stands for 'A Project Of Simulating The Local Environment', a suite of 12 volumes selected from a large cosmological box to match the main properties of the Local Group of Galaxies and its immediate surroundings.

Like APOSTLE, other simulations have also attempted to reproduce the Local Group environment and kinematics, notably those from the CLUES project (Gottlöber et al., 2010) and from the ELVIS project (Garrison-Kimmel et al., 2014). We do not include their results here, however, mainly because (i) ELVIS consists of runs that follow solely the dark matter component, and because (ii) the feedback algorithm adopted in CLUES is too weak to prevent excessive star formation in low mass haloes, leading to an unrealistic number of masive dwarfs (see, e.g., Benítez-Llambay et al., 2013).

We begin by describing the simulated (Sec. 3.2) and observed (Sec. 3.3) galaxy samples. We then analyse (Sec. 3.4) the baryon content and galaxy formation efficiency of APOSTLE galaxies and establish their correlations with halo mass/circular velocity. These relations are compared with our observed galaxy sample, an exercise that yields a number of outliers for which there are no counterparts in the simulations. Particularly interesting are outliers inferred to have exceptionally high galaxy formation efficiency, or, alternatively, to rotate far too slowly for their baryonic mass, presumably because they are anomalously deficient in dark matter. Neither possibility finds a natural explanation in current simulations of dwarf galaxy formation. We examine in Sec. 3.5 the possibility that this issue is related to the question of cores inferred in the inner rotation curves of some dwarf galaxies, and whether errors in the rotation curve modelling could be the source of the observed anomalies. We conclude in Sec. 3.6 with a brief summary and discussion of the implications of these puzzling systems for our understanding of dwarf galaxy formation in a ΛCDM universe.

3.2 The APOSTLE project

3.2.1 The numerical simulations

We select galaxies from the APOSTLE suite of zoom-in hydrodynamical simulations. These follow a total of 12 volumes specifically selected from a cosmological dark matter-only simulation to contain two haloes with approximately the masses and dynamics of the Milky Way and M 31, and no other nearby large structures (for details, see Fattahi et al., 2016; Sawala et al., 2016a).

APOSTLE uses the same code and physics as the 'Ref' EAGLE simulations described by Schaye et al. (2015). EAGLE uses the pressure-entropy formulation of smoothed particle hydrodynamics (Hopkins, 2013) and the ANARCHY collection of

Table 3.1: Summary of the key parameters of the APOSTLE simulations used in this work. Particle masses vary by up to a factor of 2 between volumes at a fixed resolution 'level'; the median values below are indicative only (see Fattahi et al., 2016, for full details). Details of the *WMAP7* cosmological parameters used in the simulations are available in Komatsu et al. (2011).

| Simulation | Particle masses ($M_\odot$) | | Max softening length (pc) |
	DM	Gas	
AP-L3	7.3×10^6	1.5×10^6	711
AP-L2	5.8×10^5	1.2×10^5	307
AP-L1	3.6×10^4	7.4×10^3	134

numerical methods (Dalla Vecchia et al., in preparation; for a brief description see Schaye et al. 2015). It includes subgrid models for radiative cooling (Wiersma et al., 2009a), star formation (Schaye, 2004; Schaye & Dalla Vecchia, 2008), stellar and chemical enrichment (Wiersma et al., 2009b), energetic stellar feedback (Dalla Vecchia & Schaye, 2012), and cosmic reionization (Haardt & Madau, 2001; Wiersma et al., 2009b), and is calibrated to reproduce the galaxy stellar mass function and size distribution for galaxies of $M_* > 10^8 \, M_\odot$ (Crain et al., 2015).

The APOSTLE volumes are simulated at three different resolution levels which we denote AP-L1, AP-L2 and AP-L3 in order of decreasing resolution. Each resolution level is separated by a factor of ~ 10 in particle mass and a factor of ~ 2 in force resolution. All 12 volumes have been simulated at AP-L2 and AP-L3 resolution levels, but only volumes 1 and 4 have been simulated at AP-L1 resolution. APOSTLE assumes *WMAP7* (Komatsu et al., 2011) cosmological parameters: $\Omega_M = 0.2727$, $\Omega_\Lambda = 0.728$, $\Omega_b = 0.04557$, $h = 0.702$ and $\sigma_8 = 0.807$. Table 3.1 summarizes the particle masses and softening lengths of each resolution level.

3.2.2 The simulated galaxy sample

Galaxies are identified in APOSTLE using the SUBFIND algorithm (Springel et al., 2001; Dolag et al., 2009). Particles are first grouped into friends-of-friends (FoF) haloes by linking together dark matter particles separated by less than 0.2 times the mean inter-particle spacing (Davis et al., 1985); gas and star particles are assigned to the same FoF halo as their nearest dark matter particle within the linking length. Substructures are then separated along saddle points in the density distribution; in

this step, dark matter, gas and star particles are treated as a single distribution of mass. Finally, particles that are not gravitationally bound to the substructures are removed.

We retain for analysis the main (central) galaxy of each separate FoF halo; this excludes by construction satellites of more massive systems and are best identified with 'isolated' field galaxies. For each of these galaxies we measure the virial mass of its surrounding halo, M_{200}, as well as its baryonic mass, $M_{\rm bar}$, which we identify with the total mass of baryons within the galactic radius, $r_{\rm gal} = 0.15\,r_{200}$. This definition includes the great majority of stars and cold gas within the halo virial radius.

We shall consider two characteristic circular velocities for each galaxy in our analysis: (i) the maximum circular velocity, $V_{\rm max}$, measured within the virial radius; and (ii) the velocity at the outskirts of the luminous galaxy, which we identify with the circular velocity at twice the stellar half-mass radius, $V_{\rm circ}(2\,r_h^{st})$. For simplicity, we estimate all circular velocities using the total enclosed mass, assuming spherical symmetry; i.e., $V_{\rm circ}^2(r) = GM(<r)/r$.

We use the three APOSTLE resolution levels to determine which simulated galaxies are sufficiently resolved to measure baryonic masses and circular velocities. We retain AP-L1 galaxies with $V_{\rm circ}^{\rm max} > 26\,{\rm km\,s^{-1}}$, AP-L2 galaxies with $V_{\rm circ}^{\rm max} > 56\,{\rm km\,s^{-1}}$ and AP-L3 galaxies with $V_{\rm circ}^{\rm max} > 120\,{\rm km\,s^{-1}}$ in our sample. These cuts correspond to virial masses of $\gtrsim 3 \times 10^9$, 3×10^{10} and $3 \times 10^{11}\,{\rm M_\odot}$, respectively, or a particle count $\gtrsim 5 \times 10^4$. All circular velocities used in our analysis are well resolved according to the criterion of Power et al. (2003).

3.3 The observed galaxy sample

Our observed galaxy sample has been drawn from several heterogeneous sources, placing an emphasis on galaxies with good estimates of their baryonic masses and high-quality rotation curves derived from 2D velocity fields. This is a subset of the compilation of rotation curves presented in Oman et al. (2015), and contains galaxies taken from the sources listed below. We take baryonic masses directly from the listed sources[3], and adopt their published circular velocity estimates, which are based on folded rotation curves corrected for inclination, asymmetric drift, and instrumental effects. No further processing of these data has been attempted. The properties of

---

[3]We have adopted $M_{\rm gas}/M_{\rm HI} = 1.4$ to account for the gas mass in Helium and heavy elements.

galaxies in our compilation that have rotation curves extending to at least twice their stellar half mass radius (see Sec. 3.5.2) are summarized in Table 3.2. Below, we briefly discuss each of these datasets.

3.3.1 THINGS and LITTLE THINGS

Rotation curves for 44 galaxies in the THINGS and LITTLE THINGS surveys were published by de Blok et al. (2008), Oh et al. (2011) and Oh et al. (2015). These galaxies span a wide range of masses, with maximum circular velocities between ~ 20 and $\sim 400\,\mathrm{km\,s^{-1}}$. The surveys obtained H I data cubes using the NRAO Very Large Array with angular resolutions of 12 (THINGS) and 6 (LITTLE THINGS) arcsec, making them some of the most finely spatially resolved H I rotation curves available. The rotation curves were constructed from the velocity fields using a tilted-ring model (Rogstad et al., 1974; Kamphuis et al., 2015), corrected for inclination, and asymmetric drift when necessary. A few galaxies are analysed in multiple publications; in these cases we use only the most recent analysis. H I masses are derived from the THINGS and LITTLE THINGS data by Walter et al. (2008) and Oh et al. (2015), respectively.

Stellar masses are estimated by fitting stellar population spectral energy density models to Spitzer IRAC $3.6\,\mu$m observations (Hunter & Elmegreen, 2006). We use the disk scale lengths reported in Hunter et al. (2012) to estimate r_h^{st} for LITTLE THINGS galaxies – for an exponential profile the half mass radius is related to the scale length, r_d, as $r_h^{st} \approx 1.68\,r_d$. For the THINGS sample, no scale lengths are reported, but the contribution of stars to the circular velocity is shown as a function of radius. We therefore assume an exponential disk profile and estimate a scale length from the position of the peak of the contribution of the stellar component of each galaxy (Binney & Tremaine, 2008, Sec. 2.6.1b).

3.3.2 Adams et al. (2014)

Adams et al. (2014) present a sample of 7 rotation curves of galaxies with maximum circular velocities of $\sim 100\,\mathrm{km\,s^{-1}}$. The velocity fields were measured with the VIRUS-W integral field spectrograph on the 2.7-m Harlan J. Smith Telescope at McDonald Observatory with an angular resolution of 3.1 arcsec. The authors analyse separately absorption lines, tracing the stellar velocity field, and H β, O III 4959 Å and O III 5007 Å emission, tracing the gas velocity field. Using a tilted-ring model,

two independent rotation curves, one for each velocity field, were constructed for each galaxy. In most cases the two curves are in good agreement. We use the gas emission based curves in our analysis, and note that using the stellar absorption based curves would not change anything substantial in our analysis. We use the disk scale lengths reported by the authors to estimate r_h^{st}, and the H I masses they quote from Paturel et al. (2003). We use the stellar masses they derive by modelling the gas rotation curves, which are better constrained than those derived by modelling the stellar rotation curves (see, e.g., their fig. 13).

3.3.3   McGaugh (2012)

We use the compilation of 47 galaxies of McGaugh (2012) to supplement our own compilation. It provides self-consistent estimates of the height of the flat portion of the rotation curve (which we consider equivalent to $V_{\mathrm{rot}}^{\mathrm{max}}$ in our notation), stellar masses, and gas masses. The gas masses assume $M_{\mathrm{gas}}/M_{\mathrm{HI}} = 1.33$; we increase the gas masses by ~ 5 per cent for consistency with the rest of our compilation. We remove 7 galaxies already included in our compilation from the THINGS survey and one duplicate entry (UGC 4115 a.k.a. LSB D631-7). The majority of the remaining galaxies do not have high quality rotation curve measurements that are readily available, so we only use these data in our baryonic Tully-Fisher and f_{eff} analysis below.

Table 3.2: Summary of properties for galaxies with rotation curves extending to at least $2r_h^{st}$, ordered by $V_{\mathrm{rot}}(2r_h^{st})$, i.e. left-to-right in Fig. 3.4. Columns: **(1)** galaxy name used by reference in (2); **(2)** rotation curve source; **(3)** distance as given by reference in (2); **(4)** inclination as given by reference in (2); **(5)** stellar half mass radius estimated as described in Sec. 3.3; **(6)** maximum measured rotation velocity; **(7)** measured rotation velocity at twice the stellar half mass radius; **(8)** stellar mass as given by reference in (2); **(9)** baryonic mass assuming stellar mass in (7) and $M_{\mathrm{gas}}/M_{\mathrm{HI}} = 1.4$; **(10)** galaxy formation efficiency as shown in Fig. 3.2.

Galaxy	Ref.	D	i	r_h^{st}	$V_{\mathrm{rot}}^{\max}$	$V_{\mathrm{rot}}(2r_h^{st})$	M_*	M_{bar}	f_{eff}
		[Mpc]	[°]	[kpc]	[km s^{-1}]	[km s^{-1}]	[M$_\odot$]	[M$_\odot$]	
IC 1613	Oh et al. (2015)	0.7	48	0.97	21.1	19.3	2.88×10^7	8.77×10^7	36.4%
NGC 1569	Oh et al. (2015)	3.4	69	0.64	39.3	23.0	3.63×10^8	5.67×10^8	34.2%
CVnIdwA	Oh et al. (2015)	3.6	66	0.96	26.4	24.1	4.90×10^6	3.37×10^7	7.0%
DDO 43	Oh et al. (2015)	7.8	41	0.69	38.3	25.6	—	2.34×10^8	15.3%
UGC 8508	Oh et al. (2015)	2.6	82	0.45	46.1	26.0	7.76×10^6	1.98×10^7	0.7%
DDO 50	Oh et al. (2015)	3.4	50	1.85	38.8	29.0	1.07×10^8	1.43×10^9	88.9%
Haro 29	Oh et al. (2015)	5.9	61	0.49	43.5	33.1	1.45×10^7	1.08×10^8	4.7%
DDO 70	Oh et al. (2015)	1.3	50	0.81	43.9	33.7	1.95×10^7	5.75×10^7	2.4%
LSB F564-V3	Oh et al. (2015)	8.7	56	0.89	39.2	33.8	—	4.37×10^7	2.6%
WLM	Oh et al. (2015)	1.0	74	0.96	38.5	34.3	1.62×10^7	9.57×10^7	6.1%
DDO 154	Oh et al. (2015)	3.7	68	0.99	51.1	35.9	8.32×10^6	3.63×10^8	9.6%
DDO 126	Oh et al. (2015)	4.9	65	1.46	38.7	38.7	1.62×10^7	1.78×10^8	11.2%
Haro 36	Oh et al. (2015)	9.3	70	1.16	58.2	39.5	—	1.12×10^8	2.0%
DDO 87	Oh et al. (2015)	7.7	56	2.20	56.6	44.4	3.24×10^7	3.21×10^8	6.2%
NGC 2366	Oh et al. (2015)	3.4	63	2.28	59.8	55.5	6.92×10^7	1.14×10^9	18.6%

Galaxy	Ref.	D	i	r_h^{st}	$V_{\rm rot}^{\rm max}$	$V_{\rm rot}(2r_h^{st})$	M_*	$M_{\rm bar}$	$f_{\rm eff}$
		[Mpc]	[°]	[kpc]	[km s^{-1}]	[km s^{-1}]	[M$_\odot$]	[M$_\odot$]	
DDO 47	Oh et al. (2015)	5.2	46	2.30	64.7	60.1	—	4.68×10^8	6.0%
DDO 52	Oh et al. (2015)	10.3	43	2.18	61.7	60.5	5.37×10^7	3.85×10^8	5.7%
DDO 168	Oh et al. (2015)	4.3	46	1.38	61.9	60.5	5.89×10^7	3.16×10^8	4.6%
NGC 5204	Adams et al. (2014)	3.2	47	0.79	89.4	76.2	2.51×10^8	5.33×10^8	2.5%
IC 2574	Oh et al. (2011)	4.0	55	5.23	80.0	78.2	1.02×10^9	2.84×10^9	18.7%
NGC 2552	Adams et al. (2014)	11.4	53	3.23	96.1	95.7	1.26×10^9	2.17×10^9	8.1%
UGC 11707	Adams et al. (2014)	15.0	73	3.69	103.7	96.7	1.20×10^9	3.20×10^9	9.3%
NGC 7793	Oh et al. (2011)	3.9	50	2.65	117.9	114.1	2.75×10^9	3.98×10^9	7.8%
NGC 2403	Oh et al. (2011)	3.2	63	2.40	143.9	122.7	5.13×10^9	8.76×10^9	9.2%
NGC 3621	Oh et al. (2011)	6.6	65	3.83	159.2	139.6	1.58×10^{10}	2.58×10^{10}	19.9%
NGC 4736	Oh et al. (2011)	4.7	41	2.62	198.3	153.1	2.00×10^{10}	2.05×10^{10}	8.0%
NGC 3198	Oh et al. (2011)	13.8	72	5.60	158.7	153.4	2.51×10^{10}	3.92×10^{10}	30.5%
NGC 6946	Oh et al. (2011)	5.9	33	5.34	224.3	195.3	6.31×10^{10}	6.89×10^{10}	18.2%

3.4 Galaxy baryonic mass and dark halo mass

3.4.1 The baryonic Tully-Fisher relation

For dark matter-dominated galaxies, the most reliable measure of virial mass is their asymptotic maximum rotation velocity. We therefore begin our analysis by presenting, in Fig. 3.1, the baryonic mass of APOSTLE galaxies (small red symbols) as a function of the maximum circular velocity, $V_{\mathrm{circ}}^{\mathrm{max}}$, measured within the virial radius. This figure combines results from the three APOSTLE resolution levels, using only those galaxies whose relevant properties are well resolved (see Sec. 3.2).

Baryonic mass correlates strongly and with little scatter with $V_{\mathrm{circ}}^{\mathrm{max}}$ in simulated galaxies; indeed, the dispersion about the fit[4] shown by the thick solid line is only 0.33 dex in mass, or 0.08 dex in velocity. This baryonic Tully-Fisher (BTF) relation is, on average, in remarkable agreement with that of the observed galaxy sample (open black squares), for which we adopt the maximum speed reached by the rotation[5] curve of a galaxy, $V_{\mathrm{rot}}^{\mathrm{max}}$.

The agreement is encouraging, especially since the APOSTLE simulations use the same code as the EAGLE project, which was calibrated to reproduce the observed number and size of galaxies of stellar mass larger than $\sim 10^8 \, \mathrm{M}_\odot$ as a function of stellar mass. Fig. 3.1 thus shows that ΛCDM simulations that match those constraints also reproduce both the zero-point and velocity scaling of the BTF relation without further calibration.

One difference, however, seems clear: the scatter in the observed BTF relation appears to increase toward less massive objects, exceeding the rather narrow dispersion about the median trend of the APOSTLE galaxies (see Papastergis & Shankar, 2016, for a similar conclusion). We shall discuss the faint end of the simulated BTF relation in a companion paper (Sales et al., 2017), and focus here on the origin and cosmological significance of the outliers to the BTF relation seen in Fig. 3.1. Although the existence of such outliers has in the past been regarded with scepticism and ascribed to inferior data, the situation has now changed, and a number of authors

---

[4]The functional form of the fit shown in Fig. 3.1 is $M_{\mathrm{bar}}/\mathrm{M}_\odot = 5.12 \times 10^9 \, \nu^{3.08} \exp(-0.16\nu^{-2.43})$, where ν is the maximum circular velocity expressed in units of $100 \, \mathrm{km\,s}^{-1}$.

[5]On a technical note, for observed galaxies we actually use the maximum circular velocity estimated from 2D velocity fields as provided by the authors, which typically correct rotation speeds for inclination, asymmetric drift, and instrumental effects. We distinguish these from circular velocities of simulated galaxies, which are estimated directly from the enclosed mass profile, $V_{\mathrm{circ}}^2(r) = GM(<r)/r$.
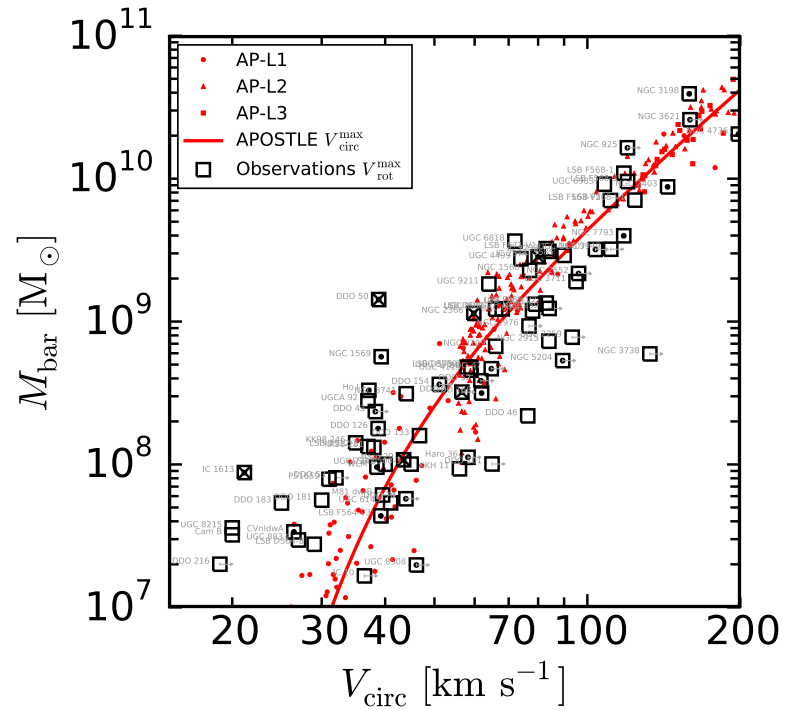
Figure 3.1: Baryonic masses of simulated galaxies, $M_{\rm bar}$, as a function of their maximum circular velocity in the APOSTLE simulations (red symbols). Galaxy masses are measured within the galactic radius, defined as $r_{\rm gal} = 0.15\, r_{200}$. The thick red solid line shows a fit to the velocity dependence of the median $M_{\rm bar}$ in the simulations. Observed galaxies labelled by their name are shown with open squares and use the maximum measured rotation speed of each galaxy and their baryonic masses, taken from the literature (see Sec. 3.3 for details on the sample). Squares containing dots correspond to galaxies with rotation curves extending out to at least twice the stellar half-mass radius (see Sec. 3.5.2 and Fig. 3.4). Squares with crosses highlight the galaxies whose rotation curves are shown in Fig. 3.3.

have argued that the scatter in the BTF relation genuinely increases toward fainter objects (see, e.g., Geha et al., 2006; Trachternach et al., 2009). The scatter in the *inclination-corrected* velocities of observed galaxies shown in Fig. 3.1 increases from ~ 0.08 dex to ~ 0.17 dex above/below a baryonic mass of $2 \times 10^9 \, \mathrm{M_\odot}$. This is much greater than the circular velocity scatter of simulated galaxies, which is 0.04 dex and 0.05 dex, respectively, above/below the same baryonic mass.

3.4.2 Galaxy formation efficiency

Examples of BTF outliers – two of the galaxies highlighted with crosses in Figs. 3.1, 3.2 and 3.4 – are provided by DDO 50 ($M_{\mathrm{bar}} = 1.43 \times 10^9 \, \mathrm{M_\odot}$, $V_{\mathrm{rot}}^{\max} = 38.8 \, \mathrm{km \, s^{-1}}$) and IC 1613 ($M_{\mathrm{bar}} = 8.77 \times 10^8 \, \mathrm{M_\odot}$, $V_{\mathrm{rot}}^{\max} = 19.3 \, \mathrm{km \, s^{-1}}$), two nearby dwarf galaxies that have been comprehensively studied as part of the LITTLE THINGS survey. These are systems whose baryonic masses are much higher than expected for their velocities or, equivalently, whose measured velocities are much lower than expected for their mass.

This may be seen in Fig. 3.2, where we show f_{eff} as a function of $V_{\mathrm{circ}}^{\max}$ for APOSTLE galaxies compared with observations. For the latter we plot the maximum observed rotation velocity, and estimate f_{eff} using the best-fitting relation between virial mass and maximum circular velocity derived from the simulations: $M_{200}/\mathrm{M_\odot} = 1.074 \times 10^5 (V_{\max}/\mathrm{km \, s^{-1}})^{3.115}$. As expected from the discussion in Sec. 3.1, f_{eff} peaks at ~ 15 per cent for circular velocities comparable to the Milky Way ($\sim 200 \, \mathrm{km \, s^{-1}}$) but declines precipitously[6] toward lower masses, dipping to less than 1 per cent for haloes below $30 \, \mathrm{km \, s^{-1}}$. If the rotation velocities of DDO 50 and IC 1613 trace reliably the maximum circular velocity of their dark matter haloes then these outliers would correspond to systems where the galaxy formation efficiency, f_{eff}, is extraordinarily high, at 89 per cent and 36 per cent, respectively, despite their low rotation speeds.

Those two galaxies are not the only outliers from the trend predicted by the numerical simulations. There are also systems that fall well *below* the solid red curve in Fig. 3.2 and correspond to systems with unexpectedly high rotation velocities for their mass. There are three broad scenarios that could explain these outliers.

---

[6]The EAGLE hydrodynamics model used in APOSTLE does not include a cold gas phase and therefore does not model molecular hydrogen cooling. This artificially suppresses star formation in small haloes before cosmic reionization, so some of the dwarfs in our simulations have unrealistically low stellar masses – the decline in f_{eff} may be slightly less abrupt than our results suggest.
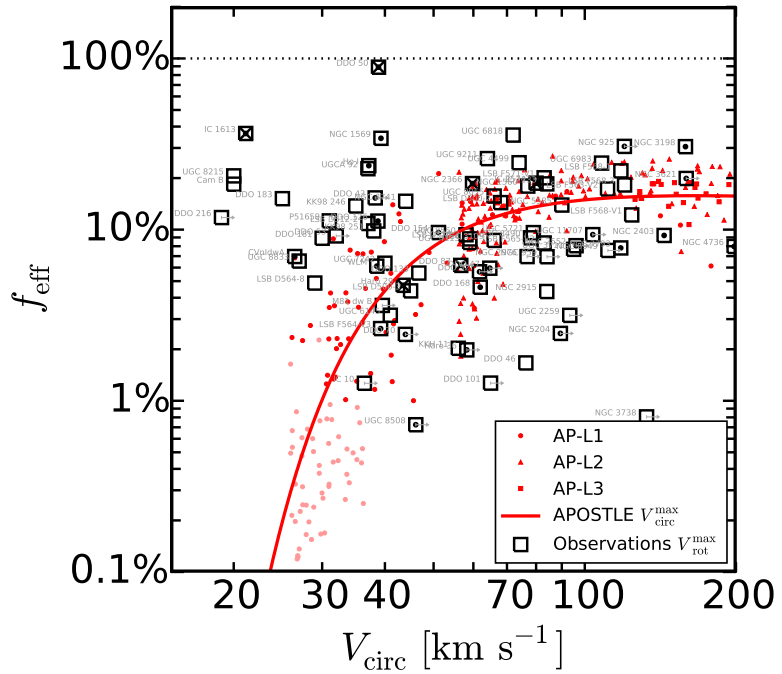
Figure 3.2: Galaxy formation efficiency, $f_{\mathrm{eff}} = M_{\mathrm{bar}}/(f_{\mathrm{bar}}\, M_{200})$, as a function of maximum circular velocity. Symbols are as in Fig. 3.1; small red symbols correspond to APOSTLE simulated galaxies (pale symbols have $M_{\mathrm{bar}} < 10^7\,\mathrm{M}_\odot$ and so do not appear in Fig. 3.1); open squares are observed galaxies. Note that f_{eff} in a simulated galaxy never exceeds 30 per cent, but that a number of outliers with anomalously high galaxy formation efficiencies are seen in the observed sample.

They may be systems with unusually low galaxy formation efficiency, perhaps as a result of heating by ionizing background radiation, of particularly effective stellar feedback following a strong past starburst, or of environmental effects such as cosmic web stripping (Benítez-Llambay et al., 2013). They may also be galaxies where the baryonic component is heavily concentrated and dominates the potential in the central regions, raising the local circular velocity above the halo asymptotic value. This scenario does not arise in APOSTLE, since the equation of state chosen for the star-forming gas imposes a minimum size for the stellar component of dwarfs (see, e.g., the discussion in Sec. 4.1.2 of Crain et al., 2015). All APOSTLE dwarfs are dark matter dominated; heavily concentrated, high-surface brightness dwarfs such as, e.g., M 32, are absent from the simulated sample.

Outliers well *above* the thick solid line in Fig. 3.2, like DDO 50 and IC 1613, are more difficult to explain. The increase in scatter in $f_{\rm eff}$ toward lower masses seen in the simulations does not seem to help, since it mainly adds galaxies with small efficiencies. Indeed, we find *no* simulated galaxy where the efficiency exceeds 27 per cent over the whole halo mass range spanned by the simulations. DDO 50, on the other hand, is so massive that over 90 per cent of its available baryons must have been able to cool and assemble at the centre of the halo. This corresponds to roughly 25 times the average efficiency expected for its circular velocity. The discrepancy is even more dramatic for IC 1613, whose estimated efficiency is ~ 40 per cent – the simulation average for its velocity is much less than 1 per cent.

Galaxies like DDO 50 and IC 1613 are therefore genuinely puzzling systems for which we find no counterparts in the APOSTLE simulations. If ΛCDM is the correct structure formation model, then such galaxies indicate that either (i) the simulations are at fault, perhaps grossly underestimating the mean efficiency and scatter in low-mass halos, or that (ii) the observed velocities of faint galaxies are not accurate indicators of the mass of their surrounding halos.

We are not aware of *any* ΛCDM-motivated model of galaxy formation (semi-analytic or numerical) that can accommodate mean efficiencies as high as those shown in Fig. 3.2 for galaxies with maximum rotation speeds in the range 20-40 $\rm km\,s^{-1}$ without dramatically overpredicting the number of dwarfs. If galaxies as massive as $\sim 10^7\,{\rm M_\odot}$ could indeed form in $\sim 20\,\rm km\,s^{-1}$ halos, then we would expect about 200 at least as massive within 2 Mpc of the Local Group barycenter (see, e.g., Fig. 4 in Sawala et al., 2016a) when, in fact, there are only ~ 20 such galaxies in such volume. It is also clear from Fig. 3.2 that the disagreement would be much easier to explain

if velocities rather than efficiencies were systematically affected, since a factor of two shift in velocity implies a change in inferred efficiency of nearly an order of magnitude. We explore this possibility further below.

3.5 Rotation curves and halo masses

3.5.1 Rising rotation curves?

Could the maximum rotation velocity somehow underestimate the asymptotic circular velocity of its surrounding halo? This would be the case, for example, for a galaxy with a rotation curve that is still rising at its last measured point, but it does not apply to either one of the two outliers highlighted above. Indeed, the rotation curves of both DDO 50 and IC 1613 show clear signs of having reached their maximum values (see top panels of Fig. 3.3). That of DDO 50 is a particularly good example, rising quickly to reach its peak and staying flat between 2 and 10 kpc.

3.5.2 The effects of baryon-induced dark matter 'cores'

Another possibility is that baryons might have carved a 'core' in the dark matter, thus reducing its central density and, consequently, the circular velocity in the central regions. This creates an inner deficit of dark matter compared with cuspy CDM haloes, which are well approximated by the NFW profile (Navarro et al., 1996b, 1997). The characteristic signature of this effect is a rotation curve that rises more gradually near the centre than the sharp rise expected for an NFW profile.

We examine this possibility in Fig. 3.4, where we show again the baryonic Tully-Fisher relation but using, for both simulated and observed galaxies, the circular velocity at the outskirts of the luminous galaxy – i.e., at twice the stellar half-mass radius, $V_{\rm rot}(2\,r_h^{st})$ – rather than its maximum attained value. This choice is useful because velocities measured as far from the centre as $\sim 2\,r_h^{st}$ should also be largely unaffected by the presence of a possible baryon-induced core. This is because, at least for the core formation mechanism discussed by Pontzen & Governato (2014), the effects of baryons on the dark matter mass profile is largely limited to the regions of a galaxy where stars form.

This is confirmed by the connected symbols in Fig. 3.4, which indicate results for 22 simulated galaxies where a baryon-induced core in the dark matter has been
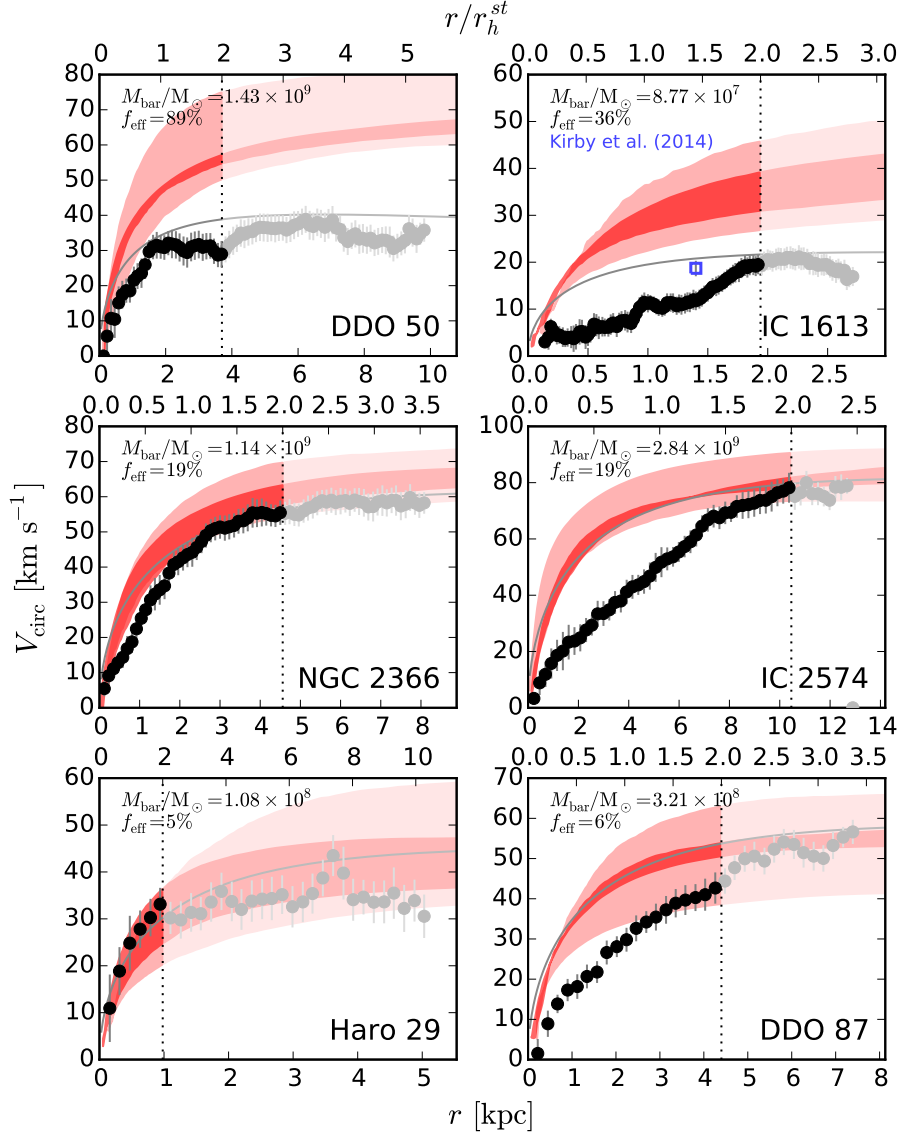
Figure 3.3: Examples of galaxies with rotation curves that extend beyond twice the stellar half-mass radius, r_h^{st}. These six galaxies are marked with a cross in Figs. 3.1–3.4. In each panel the horizontal axis shows the radius in units of kpc (bottom axis scale) and stellar half-mass radius, r_h^{st} (top axis scale). Thin grey lines show, for reference, the ΛCDM (NFW) circular velocity profiles of haloes that match the observed maximum rotation speed of each galaxy. The dark and light red-shaded areas indicate the interquartile and full range, respectively, of V_{circ} profiles of the 12 simulated galaxies whose baryonic masses most closely match that of the galaxy shown in each panel. We highlight the region that contains most of the stars in each galaxy (i.e., $r < 2\,r_h^{st}$) with a darker tint. Outside this radius, baryons are not expected to be able to modify the dark matter profile. The top two galaxies are examples of outliers in the velocity-mass relation: these galaxies are anomalously deficient in dark matter (given their baryonic mass). The bottom four galaxies have 'normal' galaxy formation efficiency parameters but differ in their inner circular velocity profiles. Those in the left column have rotation curve shapes largely consistent with ΛCDM haloes of matching maximum velocity. Those on the right show the inner deficit of dark matter at the stellar half-mass radius that is usually associated with a core. For IC 1613 (top right), an independent estimate of the mass in the inner 1.4 kpc by Kirby et al. (2014) is shown with an open blue symbol.
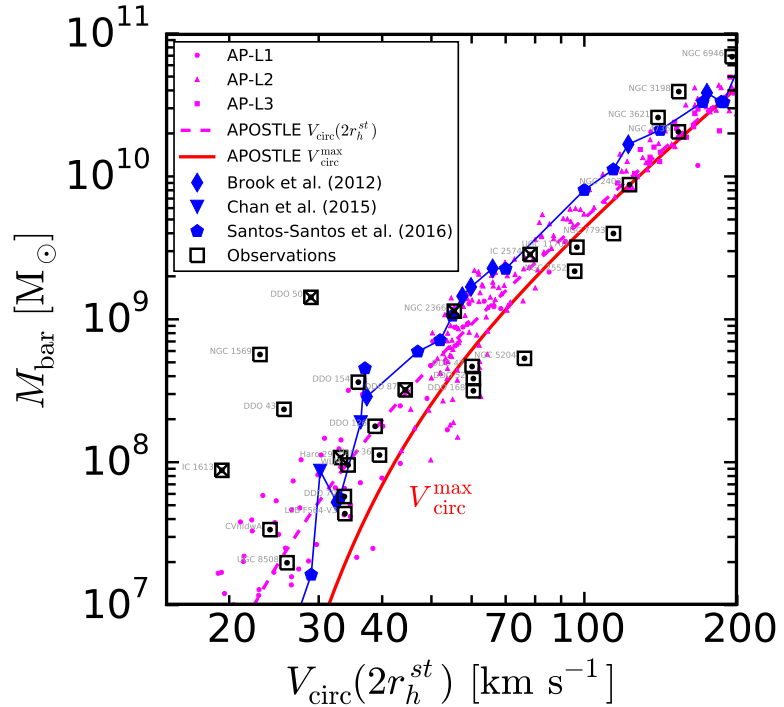
Figure 3.4: As Fig. 3.1, but for the circular velocity, $V_{\rm circ}(2r_h^{st})$, estimated at twice the stellar half-mass radius. The magenta small filled symbols and thick dashed line correspond to APOSTLE simulated galaxies. The thick red solid line indicates, as in Fig. 3.1, the results for the maximum circular velocity, and is included for reference only. Open squares correspond to all galaxies in our observed sample where the rotation curve extends at least as far as $2r_h^{st}$. The larger blue solid symbols (connected by a thin line) are individual simulated galaxies where the formation of a core in the central dark matter distribution has been reported.

reported in the literature (these have been selected from Brook et al., 2012; Santos-Santos et al., 2016; Chan et al., 2015). The magenta symbols in the same figure show the results for APOSTLE galaxies, which show no evidence for a core (Schaller et al., 2015; Oman et al., 2015). As may be seen from the slight shift between the connected line and the magenta dashed line, cores induce a slight reduction in the circular velocity at $2\,r_h^{st}$, but the changes do not exceed 20 per cent relative to APOSTLE, even for the most extreme examples. Galaxies like DDO 50 or IC 1613 are still extreme outliers that remain unaccounted for, even in simulations with cores.

3.5.3 Missing dark matter?

Rather than anomalously baryon rich, galaxies like DDO 50, IC 1613 (the leftmost outliers in Fig. 3.4) could alternatively be considered as anomalously low in their dark matter content. These galaxies would then have low circular velocities because they would be 'missing dark matter', a result reminiscent of the inner deficit of cold dark matter that characterizes dwarfs where a core has been inferred from their inner rotation curves (for a full discussion, see Oman et al., 2015). From this perspective, galaxies like the four aforementioned outliers would be simply systems where the dark mass deficit is not restricted to the inner regions but rather applies to the whole radial extent of the luminous galaxy, and beyond.

This is illustrated in the top two panels of Fig. 3.3, where we compare the rotation curves of DDO 50 and IC 1613 with the circular velocity profiles of APOSTLE galaxies of matching $M_{\rm bar}$, which are shown bracketed by the red shaded areas. These two systems are clearly missing dark matter from the entire body of the galaxy if their galaxy formation efficiency is comparable to that in simulations. The differences are not subtle. For DDO 50, the comparison implies a total deficit of roughly $\sim 8 \times 10^9\,{\rm M_\odot}$ from the inner 10 kpc, almost an order of magnitude greater than the baryonic mass of the galaxy itself.

The case of DDO 50 and IC 1613 also illustrates that unusually high galaxy formation efficiencies do not occur solely in galaxies with slowly-rising rotation curves, where the presence of a core in the central dark matter distribution might be suspected. This may be seen by considering the thin grey lines in Fig. 3.3, which indicate the expected mass profiles of ΛCDM haloes (i.e., NFW profiles with average concentration for that cosmology, see, e.g., Ludlow et al., 2014) chosen to match the observed maximum rotation velocity. IC 1613 shows clearly the inner mass deficit ascribed to a core: at $r = r_h^{st} \sim 1$ kpc, the predicted circular velocity exceeds the measured value by nearly a factor of 2. On the other hand, DDO 50 shows no evidence for a prominent core; its rotation curve rises sharply and flattens out just as expected for a ΛCDM halo.

The other four galaxies shown in Fig. 3.3 provide further examples of the disconnect between inner cores and galaxy formation efficiency. These galaxies have been chosen to span a wide range in $f_{\rm eff}$, decreasing from top to bottom. Those on the right have rotation curves with clear signs of an inner core, whereas those on the left are reasonably well fit by cuspy NFW profiles (thin grey lines) over their full radial

extent. The rotation curves of all galaxies in our sample where the rotation curve extends to at least $2r_h^{st}$ are shown in Sec. B.

The anomalies in the galaxy formation efficiency highlighted above thus seem to occur regardless of the inferred presence of a core. In the context of ΛCDM this implies that a mechanism that allows the galaxy formation efficiency in dwarfs to vary wildly at fixed halo mass is needed in order to understand these observations. It also implies that it is unlikely that these two puzzles can be explained away by a single mechanism, such as baryon-induced cores in the central structure of dark haloes. Resolving these puzzles would thus seem to require the inclusion of some additional physics still missing from simulations of dwarf galaxy formation in ΛCDM.

3.5.4 Observational and modelling uncertainties

Before entertaining more far-fetched explanations of the puzzles discussed above, we explore a few more prosaic possibilities. These include the possibility that (i) erroneous galaxy distances have led to substantial overestimation of their baryonic masses (which scale with the assumed distance squared); (ii) that some of the dark matter has been tidally stripped by interaction with a more massive neighbour; and (iii) that the inclination of the galaxies has been overestimated, leading to substantial underestimation of their true rotation speeds.

A thorough analysis of these possible explanations for the full observed sample is beyond the scope of this paper, but we have checked whether such concerns apply to DDO 50 and IC 1613, two clear outliers from the relations discussed above.

Distances

The distances to both galaxies seem quite secure: both have distances measured using multiple precise estimators. The apparent luminosity of Cepheids in DDO 50 yields a distance estimate of 3.05 ± 0.21 Mpc (Hoessel et al., 1998), and *Hubble Space Telescope* (*HST*) photometry gives a tip of the red giant branch (TRGB) distance estimate of 3.38 ± 0.05 Mpc (Dalcanton et al., 2009). IC 1613 has similarly high-quality data, with *HST*-based Cepheid and TRGB distance estimates of 0.77 ± 0.04 and 0.71 ± 0.06 Mpc, respectively (Ferrarese et al., 2000). These distances are in good agreement with those assumed by Oh et al. (2015, 3.4 Mpc for DDO 50 and 0.7 Mpc for IC 1613). The errors in the distances required to reconcile the baryonic masses of these galaxies with our BTF relation are extreme. For instance, to reduce

the inferred mass of DDO 50 by the order of magnitude needed to make it plausibly consistent with our simulation results would imply a distance of only 1.1 Mpc.

Stripping

It also seems improbable that either DDO 50 or IC 1613 have undergone any substantial dark matter stripping due to a tidal interaction with a massive neighbour. According to the catalogue of nearby galaxies compiled by Tully et al. (2009), the nearest brighter galaxy to DDO 50 is NGC 2403 at a separation of $373\,\mathrm{kpc}$. IC 1613 is similarly isolated, with no galaxies brighter than itself closer than M 33, at a separation of $449\,\mathrm{kpc}$.

Inclination effects

Of the effects considered in this section, the estimates of the inclinations of DDO 50 and IC 1613 are perhaps the least secure, although the errors necessary to bring the galaxies into agreement with our predicted efficiencies are much larger than the uncertainties quoted in the literature.

It is well known that rotation curve analyses of galaxies with $i \lesssim 40°$ are compromised by the difficulty of deriving robust inclinations solely from the kinematic data (see, e.g., Begeman, 1989; Oh et al., 2011). Even if a minimum inclination is adopted this might still fail to exclude problematic low-inclination galaxies if their kinematic inclinations somehow suggest much larger values (e.g. Read et al., 2016).

The mean inclination of DDO 50 (also known as Holmberg II) derived in the tilted-ring analysis of Oh et al. (2015) is $49°.7 \pm 6°.0$, a relatively high value consistent with that inferred by Bureau & Carignan (2002) from independent, lower-resolution data, and with the $\sim 47°$ inclination estimated from the shape of the galaxy in the V-band (Hunter et al., 2012). The true inclination would need to be of order $20°$ for consistency with our simulation results, implying a correction of order $\sim 30°$, much larger than the quoted uncertainty. Such a low inclination (and hence much larger rotation velocities) has been argued for by Gentile et al. (2012, see also Sánchez-Salcedo et al. 2014) after re-analysing the data for DDO 50 presented by Oh et al. (2011). The Gentile et al. analysis focuses on the low ellipticity of the outer regions of the HI disk, and was motivated by an attempt to reconcile DDO 50 with the predictions of Modified Newtonian Dynamics (MOND).

More recent evaluation of the same data by Oh et al. (2015), however, appears to
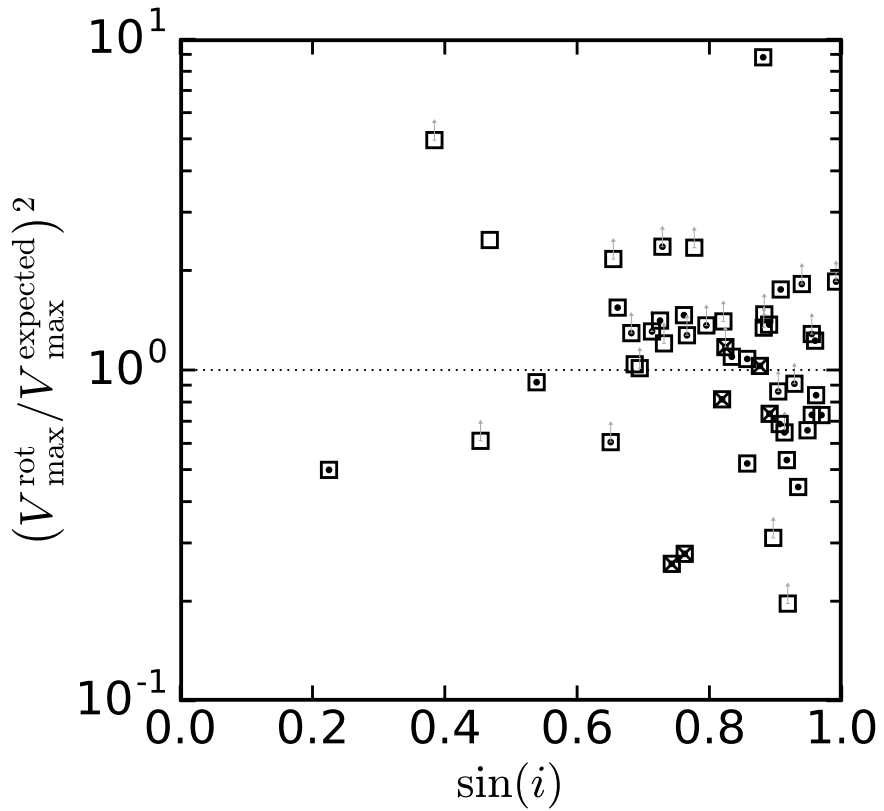
Figure 3.5: 'Mass discrepancy', i.e. the squared fractional horizontal offset from the curve in Fig. 3.1, as a function of the sin of the inclination angle for a subset of the compilation described in Sec. 3.3: the McGaugh (2012) has been omitted since it does not include inclination estimates. There is no clear preference for 'missing dark matter' galaxies to have large inclination corrections (small $\sin(i)$).

confirm the original inclination estimate, although some oddities remain. These are clearly illustrated by the disk-halo decomposition analysis shown in their fig. A.15. Note, for example, the *decreasing* importance of the dark matter with increasing radius, a result that runs counter the established trend for most galaxies. Indeed, at the outermost radius, where dark matter is usually most prominent, the gas contribution accounts almost fully for the observed velocity and the cumulative dark matter contribution is negligible. These unusual properties cast severe doubts on the robustness of the circular velocities derived for DDO 50.

The inclination of IC 1613 is also suspect. In their tilted-ring analysis, Oh et al. (2015) derive a mean kinematic inclination of $48° \pm 0°$. This result, together with the small error quoted, are difficult to reconcile with the fact that, when they allow the inclination to be a free parameter those of individual rings scatter widely between $15°$ and $85°$. Indeed, the rotation curve shown in Fig. 3.3 for IC 1613 assumes an inclination of $35°$; this is probably a compromise choice by the authors which, however, is not justified further.

An inclination of $\sim 20°$ would be sufficient to bring IC 1613 within the scatter of our simulated BTF relation by raising its rotation velocity from ~ 20 to $\sim 30\,\mathrm{km\,s^{-1}}$. It is difficult to assess whether this is plausible. The geometric inclination obtained from the V-band shape of IC 1613 is estimated at $37°.9$ (Hunter et al., 2012), close to the final value adopted by Oh et al.. On the other hand, an independent estimate of the circular velocity at $\sim 1.4\,\mathrm{kpc}$ may be obtained using the velocity dispersion and half-light radius of the galaxy (Kirby et al., 2014): this technique is insensitive to inclination and gives $18.7^{+1.7}_{-1.6}\,\mathrm{km\,s^{-1}}$ suggesting that the circular velocity curve of Oh et al. should indeed be revised upwards by ~ 50 per cent (see open blue symbol in the top-right panel of Fig. 3.3).

If inclination errors are responsible for 'missing dark matter' galaxies, we might expect such galaxies to be subject to large inclination corrections ($\propto 1/\sin(i)$). We explore this idea in Fig. 3.5. While some galaxies with anomanously low rotation speed are subject to larger inclination corrections relative to the rest of our chosen sample, others are subject to rather modest corrections, and there does not seem to be any significant increase in scatter toward lower inclination angles. Further interpretation is difficult due to the heterogenous nature of the sample selection – there is a strong, but difficult to quantify, bias toward more inclined systems.

The preceding discussion, albeit inconclusive for DDO 50, IC 1613, and the observed sample as a whole, illustrates that inclination error estimates, as well as de-

generacies in the algorithms used to map the circular velocity of a galaxy from 2D velocity fields, should be carefully reviewed and critically examined. One final example makes this point quite clear: NGC 3738 is also an extreme BTF outlier[7], but on the *opposite* side of the relation shown in Fig. 3.1. This is a case where the rotation speed is twice as high as expected for its baryonic mass and it could even be higher, since its rotation curve appears to still be rising at the outermost measured point. Taken at face value, this would imply an extremely *low* galaxy formation efficiency ($f_{\rm eff} \sim 1$ per cent, see Fig. 3.2), perhaps signalling unusually efficient feedback or environmental effects. Or an inclination error. NGC 3738 is a nearly face-on galaxy[8] with a reported mean inclination of $22°.6 \pm 0°.1$ (Oh et al., 2015). The rotation curve is derived using an inclination fixed at this mean value, but the inclinations preferred by the initial tilted ring fit with inclination as a free parameter vary between $10°$ and $70°$. If the inclination were instead about $20°$ larger than the reported mean, NGC 3738 would lie within the scatter of the results of our simulations.

3.6 Summary and Conclusions

We have analysed the baryonic masses and circular velocities of a sample of galaxies with excellent photometric data and high-quality H I observations and compared them with the results of recent ΛCDM cosmological hydrodynamical simulations from the APOSTLE project. The simulations used the same code developed for the EAGLE project, where the subgrid feedback physics modules have been calibrated to match the galaxy stellar mass function and stellar size distribution of galaxies more massive than the great majority of those studied in this paper.

Our main conclusions may be summarized as follows.

- The correlation between maximum circular velocity and baryonic mass (the 'baryonic Tully-Fisher', or BTF relation) of simulated galaxies reproduces well the zero-point and velocity scaling of observed galaxies in the range $(30, 200)\,{\rm km\,s^{-1}}$. This implies that ΛCDM galaxies of the right size and mass can match naturally the main trends of the BTF relation without further tuning.

- The sizeable scatter in the observed BTF relation at the faint end, on the other

---

[7]NGC 3738 is the farthest right outlier in Fig. 3.1, at $M_{\rm bar} = 5.9 \times 10^8\,{\rm M_\odot}$, $V_{\rm rot}^{\rm max} \sim 133\,{\rm km\,s^{-1}}$. It is not included in Table 3.2 because of the short radial extent of its available rotation curve.

[8]On these grounds it could be argued that this galaxy is unsuitable for a tilted-ring analysis.

hand, is at odds with the tight relation predicted by our simulations. Particularly challenging are dwarf galaxies, where—taking the data at face value—high baryonic masses and low rotation velocities imply halo masses so low that the inferred efficiency of galaxy formation is extraordinarily high (up to nearly 100 per cent). We find *no* counterparts to such galaxies in APOSTLE.

- Alternately, these could be systems with anomalously low dark matter content. We demonstrate that this 'missing dark matter' cannot be ascribed to the presence of a core, since the mass deficit extends over the whole luminous radius of the affected galaxies, and beyond. Furthermore, 'missing dark matter' galaxies include several examples where the rotation curves do not suggest a core, and viceversa.

- No model of galaxy formation that we are aware of can reconcile these 'missing dark matter' systems with ΛCDM; if such observations hold, they would signal the need for radical modification in our understanding of dwarf galaxy formation in ΛCDM.

- Close examination of the data, however, suggest a more plausible explanation, where outliers to our simulated BTF are simply nearly face-on galaxies where the inclinations have been overestimated, and the inclination errors have been substantially underestimated.

If inclination errors are truly responsible for the outliers from the BTF relation, then the *outer* dark mass deficits of 'missing dark matter' galaxies and the *inner* mass deficits (usually ascribed to 'cores') explored in Oman et al. (2015) may just be two manifestations of the shortcomings of 'tilted-ring' models that attempt to extract the circular velocity profile from gas velocity fields, especially in dwarf irregular galaxies. Continued efforts to understand the limitations of such models, especially using mock observations of realistic simulations of dwarf irregulars, where model output and known input can be compared directly, will be critical to making real progress in confirming or refuting this explanation.

This discussion suggests that caution must be exercised when comparing the mass measurements of dwarf galaxies with simulation results. BTF outliers have featured in discussions of the 'too-big-to-fail' problem and of the 'core-cusp' issue (Boylan-Kolchin et al., 2012; Garrison-Kimmel et al., 2014; Papastergis et al., 2015; Flores & Primack, 1994; Moore, 1994; Pontzen & Governato, 2014). If the cases of DDO 50

and IC 1613 are any guide, their mass profiles might be much more uncertain than the quoted errors would suggest.

This note of caution applies not only to mass profiles inferred from gas velocity fields, but also to Jeans-estimates of the mass enclosed within the stellar half-mass radius based on stellar velocity dispersions (Walker et al., 2009; Wolf et al., 2010). A recent analysis by Campbell et al. (2017) shows that the precision of such estimators is no better than ~ 20 per cent, even when the errors in the half-mass radii and velocity dispersions are significantly smaller. Increased errors would substantially alleviate many of the perceived problems of ΛCDM on dwarf-galaxy scales.

On the other hand, should future data/analysis confirm the existence of BTF outliers like the ones discussed above, the severity of the 'missing dark matter' problem, together with the apparent failure of 'baryon physics' to solve it, might motivate the consideration of more radical solutions. One worth highlighting is that the diversity may reflect some intrinsic particle-physics property of the dark matter. This is the case of 'self-interacting' dark matter, where, it has been argued, sizeable dispersion in the inner regions of dark matter haloes of given mass may result from scatter in their assembly history (see, e.g., Kaplinghat et al., 2016, and references therein). No detailed simulations of this process are available yet on dwarf galaxy scales, but it is certainly a possibility that needs to be developed further.

It remains to be seen whether the 'missing dark matter' problem points to 'missing physics' or 'modelling misses'. Regardless, we are hopeful that the puzzles outlined above will be profitably used to help guide future developments in our understanding of dwarf galaxy formation.

Chapter 4

Apparent cores and non-circular motions in the H I discs of simulated galaxies

Abstract

We derive the rotation curves of simulated disc galaxies from the APOSTLE suite of ΛCDM cosmological hydrodynamical simulations with velocities in the range $60 < V_{\mathrm{max}}/\mathrm{km\,s}^{-1} < 120$. These galaxies compare favourably with those in surveys of quiescent disks such as THINGS and LITTLE THINGS in terms of H I content and radius, as well as of various measures of kinematic properties and asymmetries. Our procedure analyzes synthetic H I observations using the same kind of tilted-ring model applied to interferometric H I data cubes of nearby galaxies. The modelling generally results in a large diversity of rotation curves for *each individual galaxy*, depending on the orientation of the chosen line of sight. These variations arise due to non-circular motions in the gas, in particular strong bisymmetric ($m = 2$) fluctuations in the azimuthal gas velocity field which the tilted-ring model is ill-suited to account for. These perturbations are difficult to detect in model residuals, where they may be effectively masked by combinations of the freely varying fit parameters of each ring. Still, we show that they are clearly present in DDO 47 and DDO 87, two galaxies with slowly-rising rotation curves in apparent conflict with ΛCDM predictions. Rotation curves derived using modelling procedures unable to account for non-circular motions are likely to underestimate, sometimes significantly, the circular velocity in the inner regions. This risks being misinterpreted as evidence for nonexistent cores in the dark

matter. The extent to which these findings affect galaxies with an apparent 'core' should be investigated in detail before such cores may be used as dependable evidence against the predictions of the ΛCDM paradigm.

4.1 Introduction

There are several lines of evidence pointing to the existence of an as yet elusive dark matter which is five times more abundant in the Universe on average than baryons (see Bertone et al., 2005, for a review). Despite the lack of a plausible particle candidate, the ΛCDM cosmological theory has been remarkably successful in describing the large scale structure of the Universe (Springel et al., 2006), and the parameters of the model are now known to exquisite precision (Planck Collaboration et al., 2016). Much attention has now turned to galactic scales where several conflicts between theoretical predictions and measurements have been recently been claimed. There is ongoing debate regarding the solutions to these 'small scale problems', reviewed by Del Popolo & Le Delliou (2017), in particular around whether theoretical or observational shortcomings are to blame in each case.

One such small scale discrepancy is the 'cusp-core problem' (Flores & Primack, 1994; Moore, 1994, and see de Blok, 2010 for a review) which contrasts the steeply rising central density profiles of dark matter haloes (cusps) predicted by N-body simulations and the inference from, in particular, galactic rotation curves that some galaxies have centrally flat dark matter density profiles (cores). There have been numerous attempts to explain the origin of cores by appealing to baryonic physics which couple gravitationally to the dark matter distribution (Navarro et al., 1996a; Read & Gilmore, 2005; Mashchenko et al., 2006, 2008; Pasetto et al., 2010; Governato et al., 2012; Macciò et al., 2012b; Pontzen & Governato, 2012; Teyssier et al., 2013; Brooks & Zolotov, 2014; Madau et al., 2014; Ogiya & Mori, 2014; Pontzen & Governato, 2014; Chan et al., 2015; Oñorbe et al., 2015), dynamical friction from accreted objects (El-Zant et al., 2001, 2004; Romano-Díaz et al., 2008; Johansson et al., 2009; Cole et al., 2011; Del Popolo & Pace, 2016), and non-standard dark matter physics (Spergel & Steinhardt, 2000; Bode et al., 2001; Alcubierre et al., 2002; Lovell et al., 2012; Zavala et al., 2013; Elbert et al., 2015). Alternately, rotation curve measurements may be interpreted in terms of modifications to the laws of gravity (Milgrom, 1983; Sanders, 1990; Gentile et al., 2011; Kroupa, 2012; Wu & Kroupa, 2015; McGaugh et al., 2016). So far, no single explanation has proved entirely satisfactory.

The observational evidence for dark matter cores has also repeatedly been called into question. Many earlier concerns such as 'beam smearing' (van den Bosch & Swaters, 2001; de Blok & Bosma, 2002; Swaters et al., 2009), and slit misalignment and mis-centering (Swaters et al., 2003; Spekkens et al., 2005) have largely been laid to rest with the advent of optical IFU and high resolution interferometric H I surveys (Walter et al., 2008; Kuzio de Naray et al., 2008; Hunter et al., 2012; Adams et al., 2014; Richards et al., 2016). Others, such as the importance of holes in the gas distribution (Read et al., 2016), halo shape (Dutton et al., 2005; Hayashi & Navarro, 2006; Kuzio de Naray et al., 2009), and non-circular motions (de Blok et al., 2003; Rhee et al., 2004; Simon et al., 2005; Spekkens & Sellwood, 2007; Trachternach et al., 2008; Oh et al., 2008; Kuzio de Naray & Kaufmann, 2011; Oh et al., 2015) are still debated.

An important additional constraint on possible solutions to the cusp-core problem is that not every galaxy appears to host a core. This has been highlighted as a scatter in the central slope of the dark matter density profile (Simon et al., 2005; Adams et al., 2014) and in the shapes of rotation curves (Oman et al., 2015). There have been proposed explanations for the rotation curve shape diversity in terms of the scatter in other galactic properties (Sancisi, 2004; Swaters et al., 2012; Lelli et al., 2013), as an effect of stellar feedback (Brook, 2015) and via the coupled effects of a dark matter self-scattering process and stellar feedback (Creasey et al., 2017). In this study we revisit the topic of non-circular motions present in galactic discs as an arguably simpler origin of the observed diversity.

We are hardly the first to suggest that non-circular motions, especially $m = 2$ harmonic distortions of the 3D velocity field, can substantially impact the rotation curve modelling process. The work of Schoenmakers et al. (1997) was amongst the first to elaborate in detail the signature in projection of the various harmonic modes, and in particular that a harmonic of order m in the (3D) velocity field gives rise to patterns of order $m \pm 1$ in projection. They also noted that, under the epicyclic assumption assumed in deriving their results, the geometric parameters (systemic velocity, centroid, inclination, position angle, and combinations thereof) are degenerate with various harmonic modes, and the two cannot be decoupled, e.g. by iterating toward a solution.

Rhee et al. (2004) discuss the kinematic modelling of a simulated system (their 'Model I') with a bar, using a methodology very similar to our own. The bar in question constitutes a relatively strong perturbation to the system, enough to drive

down the mean rotation velocity substantially. They find that the rotation curve they measure for the system depends sensitively on the orientation of the bar, with the apparent rotation falling far below the circular velocity of the system when the bar is aligned along the major axis of the galaxy in projection. They also note that even very small systematic errors in the velocity, on the order of 10 per cent, are enough to cause large changes in common metric of the cusp-core problem: the corresponding change to the inferred density is of order 20 per cent, and the logarithmic slope of the density profile changes by 0.35.

A similar cautionary tale, that non-circular motions which appear small in projection may be much more important than is apparent, is told by Valenzuela et al. (2007). Similarly to Rhee et al. (2004), they construct synthetic observations of simulations of isolated galaxies set up initially in equilibrium. They focus in particular on modelling NGC 3109 and NGC 6822, which both have slowly rising rotation curves, and argue that in both cases the cause is the presence of a bar or bar-like pattern. They also speculate that similar departures from axisymmetry are responsible for such extreme peculiar galaxies as IC 2574, the LMC, and DDO 47.

Whereas all prior techniques were, at best, able to account for non-circular motions which are small compared to the circular velocity at the same radius, Spekkens & Sellwood (2007) proposed a fundamentally novel approach which explicitly assumes the underlying gravitational potential is non-axisymmetric, with a bar-like distortion, and can model even large departures from circular motion at the cost of losing the ability to trace radial variations in inclination and position angle (warps). They point out that a bar-like perturbation to the potential gives rise, in addition to an azimuthal $m = 2$ mode, also to an $m = 2$ mode in the radial velocity of the gas. In an equilibrium system, the phase of the two patterns are offset by $45°$. In projection, the two patterns are found to always at least partially cancel each other. In particular, when the bar is oriented along the kinematic major axis, the two patterns cancel exactly (if they have the same amplitude), making them impossible to detect.

With numerical models of galaxies increasingly resembling the systems they purport to simulate, it is a useful and often illuminating exercise to 'observe' the simulations and analyse them on even footing with analogous observed data. When such techniques are applied to the question of rotation curves, a recurring theme emerges: Rhee et al. (2004); Valenzuela et al. (2007); Spekkens & Sellwood (2007); Read et al. (2016); Pineda et al. (2017) all find that when they 'observe' their simulated galaxies,

which all have intrinsic dark matter cusps[1], they frequently erroneously infer the presence of dark matter cores. This conclusion is not quite unanimous (Kuzio de Naray & Kaufmann, 2011), and a cogent criticism can be made that such comparisons have so far been rather limited in scope (e.g. Bosma, 2017).

Current galaxy formation models as implemented in cosmological simulations now successfully reproduce several fundamental scaling relations for galaxies (e.g. Vogelsberger et al., 2014a; Schaye et al., 2015). We make use of one such model, applied in the APOSTLE suite of simulations (Sawala et al., 2016a; Fattahi et al., 2016), which provides us an unbiased (volume limited), large sample of model dwarf galaxies ideally suited to a cusp-core study. All galaxies in this model have cuspy dark matter profiles (Oman et al., 2015; Schaller et al., 2015), yet when we extract synthetic 'observations' of their H I gas kinematics and apply the same kinematic modelling process routinely used with observed galaxies we find as large a diversity in rotation curve shapes as is seen in real galaxies.

4.2   Simulations

4.2.1   The APOSTLE simulations

The APOSTLE[2] simulation suite comprises 12 volumes selected from a cosmological N-body simulation resimulated using the zoom-in technique (Power et al., 2003; Jenkins, 2013) with the full hydrodynamics and galaxy formation treatment of the 'Ref' model of the EAGLE project (Schaye et al., 2015). The regions are selected to resemble the Local Group of galaxies in terms of the mass, separation and kinematics of two haloes analogous to the Milky Way and M 31, and the absence of any nearby more massive systems. Full details of the simulation setup and target selection are available in Sawala et al. (2016a); Fattahi et al. (2016); we summarize a few key points here.

EAGLE, and by extension APOSTLE, use the pressure-entropy formulation of smoothed particle hydrodynamics (Hopkins, 2013) and the numerical methods from the ANARCHY module [Dalla Vecchia et al. (in preparation); see Schaye et al., 2015 for a short summary]. The galaxy formation model includes subgrid recipes for radiative

---

[1]The many simulations which produce bona fide dark matter cores are of little use in this context – most systematic effects seem to cause an underestimate of the rotation curve. The relevant question is therefore whether dark matter cusps may be mistaken for cores, but *not* vice versa.

[2]A Project Of Simulating The Local Environment.

cooling (Wiersma et al., 2009a), star formation (Schaye, 2004; Schaye & Dalla Vecchia, 2008), stellar and chemical enrichment (Wiersma et al., 2009b), energetic stellar feedback (Dalla Vecchia & Schaye, 2012), and cosmic reionization (Haardt & Madau, 2001; Wiersma et al., 2009b). The model is calibrated to reproduce the galaxy stellar mass function and size distribution of $M_\star > 10^8 \, \mathrm{M_\odot}$ galaxies at $z = 0$ (Crain et al., 2015).

The APOSTLE suite is simulated at three resolution levels, labelled AP-L3 (similar to the fiducial resolution of the EAGLE project), AP-L2 (similar to the 'high resolution' realizations from EAGLE) and AP-L1. Each resolution level represents an increase by a factor of ~ 10 in mass and ~ 2 in force softening over the next lowest level. Typical values, which vary slightly from volume to volume, are shown in Table 4.1. All 12 volumes have been simulated at AP-L2 and AP-L3 resolution, but only 5 volumes: V1, V4, V6, V10 & V11 have thus far been simulated at AP-L1. APOSTLE assumes the *WMAP7* cosmological parameters (Komatsu et al., 2011): $\Omega_\mathrm{m} = 0.2727$, $\Omega_\Lambda = 0.728$, $\Omega_\mathrm{b} = 0.04557$, $h = 0.702$, $\sigma_8 = 0.807$.

The SUBFIND algorithm (Springel et al., 2001; Dolag et al., 2009) is used to identify structures and galaxies in the APOSTLE volumes. Particles are grouped into friend-of-friends (FoF) haloes by iteratively linking particles separated by at most $0.2\times$ the mean interparticle separation (Davis et al., 1985); gas and star particles are attached to the same FoF halo as their nearest dark matter particle. Saddle points in the density distribution are used to separate substructures, and particles which are not gravitationally bound to substructures are removed. The end result is a collection of FoF groups each containing at least one 'subhalo'; the most subhalo in each group is termed the 'central' galaxy, others are 'satellites'. In this analysis we focus exclusively on central objects as satellites are subject to additional dynamical processes which complicate their treatment.

We label our simulated galaxies according to the resolution level, volume number, FoF group and subgroup, so for instance AP-L1-V1-8-0 corresponds to resolution AP-L1, volume V1, FoF group 8 and subgroup 0 (the central object). We focus primarily on the AP-L1 resolution. At this resolution level the circular velocity curves of our galaxies of interest (defined below) are numerically converged at all radii $\gtrsim 700 \, \mathrm{pc}$, as defined by the criterion of Power et al. (2003, for further details pertaining to the numerical convergence of the APOSTLE simulations see Oman et al., 2015; Campbell et al., 2017).

Table 4.1: Summary of the key parameters of the APOSTLE simulations used in this work. Particle masses vary by up to a factor of 2 between volumes at a fixed resolution 'level'; the median values below are indicative only (see Fattahi et al., 2016, for full details). Details of the *WMAP7* cosmological parameters used in the simulations are available in Komatsu et al. (2011).

	Particle masses ($M_\odot$)		Max softening
Simulation	DM	Gas	length (pc)
AP-L3	7.3×10^6	1.5×10^6	711
AP-L2	5.8×10^5	1.2×10^5	307
AP-L1	3.6×10^4	7.4×10^3	134

4.2.2 Sample selection

We select galaxies from the APOSTLE simulations for further consideration based on two criteria. First, as noted above, we restrict ourselves to the highest AP-L1 resolution level so that the central regions of the galaxies, which are of particular interest in the context of the cusp-core problem, are sufficiently well resolved. Second, we choose galaxies in the interval $60 < V_{\mathrm{max}}/\mathrm{km\,s^{-1}} < 120$, where $V_{\mathrm{max}} = \max(V_{\mathrm{circ}}(R)) = \max(\sqrt{GM(<R)/R})$. The lower bound ensures that the gas distribution of the galaxies is well-sampled ($\gtrsim 10^4$ gas particles contributing to the H I distribution of each galaxy) and that the necessary corrections for pressure support are small (see Sec. 4.3.3). The upper bound ensures that the galaxies are dynamically dominated by dark matter so that the gas rotation curve is in principle fixed directly by the circular velocity curve of the halo.

In Fig. 4.1 we show where the simulated APOSTLE galaxies (small black points) and in particular those we select for further analysis (large black points) lie on three key scaling relations. For comparison, we also plot data from the Spitzer Photometry and Accurate Rotation Curves (SPARC) database (Lelli et al., 2016a) and the THINGS (Walter et al., 2008; de Blok et al., 2008; Oh et al., 2011) and LITTLE THINGS (Hunter et al., 2012; Oh et al., 2015) surveys. In the left panel we show the baryonic Tully-Fisher relation (BTFR). The quantity plotted on the horizontal axis varies by dataset: for the APOSTLE galaxies we show the maximum of the circular velocity curve $V_{\mathrm{circ}}(R) = \sqrt{GM(<R)/R}$, for the SPARC galaxies we show the asymptotically flat rotation velocity, and for the THINGS & LITTLE THINGS galaxies we show the maximum of the rotation curve. For the pupose of showing that our models are a reasonable match to the BTFR, we assume that all these quantities are equivalent and trace the maximum circular velocity of the halo. The baryonic masses are in all cases calculated as $M_{\mathrm{bar}} = M_\star + 1.4 M_{\mathrm{HI}}$. For the APOSTLE galaxies, V_{max} is the maximum of the circular velocity curve $V_{\mathrm{circ}} = \sqrt{GM(<R)/R}$, and our selection in V_{max} is highlighted by the shaded vertical band. The simulated galaxies are in broad agreement with the observed BTFR; for an in depth discussion see Sales et al. (2017); Oman et al. (2016).

The middle panel shows the H I mass – stellar mass relation. The simulated galaxies once again lie comfortably within the scatter in the observed relation. In the right panel we show the H I mass – size relation, where the size is defined as the radius at which the H I surface density, Σ_{HI}, drops below $1\,\mathrm{M_\odot\,pc^{-2}}$ ($\approx 10^{20}\,\mathrm{atoms\,cm^{-2}}$).
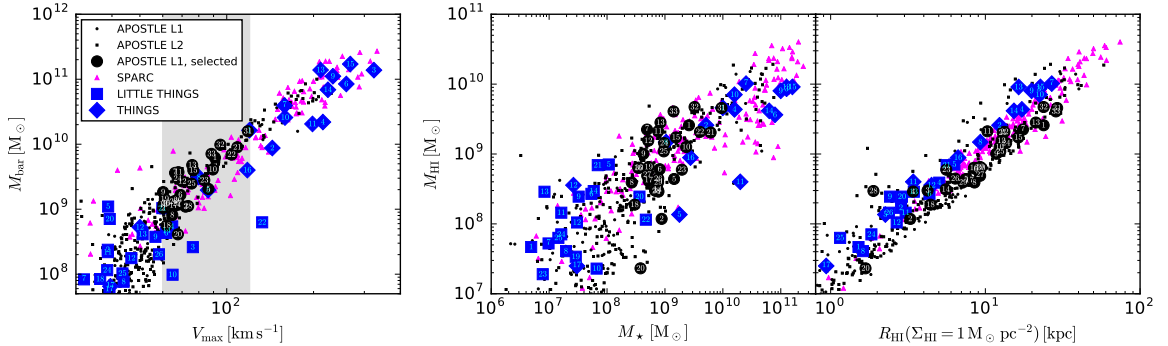
Figure 4.1: *Left:* Baryonic Tully-Fisher relation (BTFR) for APOSTLE galaxies at resolution AP-L1 (black circles) and AP-L2 (black squares). For comparison we also show the BTFR for the SPARC sample of galaxies (magenta triangles) and the THINGS (blue squares, numbering corresponds to Table C.2) and LITTLE THINGS (blue diamonds, see also Table C.2) galaxies. In all cases we assume $M_{gas} = 1.4 M_{HI}$. All AP-L1 galaxies in the range $60 < V_{max}/\mathrm{km\,s^{-1}} < 120$ are selected for further analysis and shown with larger, numbered symbols (see Table C.1). *Centre:* H I mass – stellar mass relation, symbols and numbering are as in the left panel. *Right:* H I mass–size relation. Sizes are defined as the radius where the H I surface density drops to $1\,\mathrm{M_\odot\,pc^{-2}}$. Symbols and numbering are as in the left panel.

The APOSTLE galaxies are slightly offset to larger sizes, and consequently somewhat lower Σ_{HI}. The effect is small, and depends somewhat on the (arbitrary) choice of threshold surface density. This slight offset in size has little impact on our conclusions below.

4.2.3   Creation of synthetic H I data cubes

For each simulated galaxy in our selection, we proceed as follows to carry out a synthetic H I observation. All gas particles in the friends-of-friends group of the subhalo of interest are selected, ensuring that gravitationally unbound gas particles and substructure are also included in the image. The H I mass fraction of each particle is calculated following the prescription of Rahmati et al. (2013), and includes an additional correction for the molecular gas fraciton (Blitz & Rosolowsky, 2006). The coordinate system is centred on the potential minimum of the target subhalo, and the z-axis is defined along the direction of the $\vec{L}$ angular momentum vector of the H I gas disc. A viewing angle inclined by $60°$ relative to the z-axis is chosen (the azimuthal orientation is random). Each galaxy is placed in the Hubble flow at a nominal distance of $3.657\,\mathrm{Mpc}$, similar to the average distance of $3.7\,\mathrm{Mpc}$ of galaxies in

the LITTLE THINGS sample (Hunter et al., 2012). We choose an arbitrary position on the sky at $(0^\mathrm{h}\,0^\mathrm{m}\,0.0^\mathrm{s}, +10°\,0'\,0.0'')$. We adopt an 'observing setup' similar to that used in the LITTLE THINGS survey, with a 6 arcsec circular gaussian beam and 1024^2 pixels spaced 3 arcsec apart, yielding an effective physical resolution (FWHM) of 250 pc. We use a velocity channel spacing of $4\,\mathrm{km\,s^{-1}}$ and enough channels to comfortably accomodate all of the galactic emission.

The particles are spatially smoothed with the C^2 Wendland (1995) smoothing kernel used in the EAGLE model (Crain et al., 2015). The integral of the kernel over each pixel is approximated by the value at the pixel centre. Provided the pixel size is $\leq \frac{1}{2}$ the smoothing length, this approximation is accurate to within less than 1 per cent; we explicitly check that this condition is satisfied. We also check that omitting this smoothing step does not significantly change our main results. In the velocity direction, the 21 cm emission is modeled with a gaussian line profile centred at the particle velocity and a fixed width of $7\,\mathrm{km\,s^{-1}}$, which models the (unresolved) thermal broadening of the H I line (e.g. Pineda et al., 2017). Our main results are insensitive to the precise width we choose for the line, provided it is $\lesssim 12\,\mathrm{km\,s^{-1}}$, because the integrated H I profile is dominated by the dispersion in the particle velocities. Each particle contributes flux proportionally to its H I mass. Finally, the synthetic data cube is convolved along the spatial axes with the 'beam', implemented as a 6 arcsec circular gaussian kernel. The completed cube is saved in the FITS format (Pence et al., 2010) with appropriate header information.

In Fig. 4.2 we illustrate the synthetic observations of three of our simulated galaxies by their first three moment maps. In the left column we show the surface density (0th moment) maps. The red contour marks the $\log_{10}(\Sigma_\mathrm{HI}/\mathrm{atoms\,cm^{-2}}) = 19.5$ isodensity contour. This is about 0.5 dex deeper than the typical limiting depth of observations in the THINGS and LITTLE THINGS surveys of $\sim 10^{20}\,\mathrm{atoms\,cm^{-2}}$, however we note that galaxies in our sample are slightly larger, offset by $\sim 0.2\,\mathrm{dex}$ in the M_HI–R_HI, which drives down their typical surface densities. In light of this, we find that a slightly deeper nominal limiting column density allows for more reasonable comparisons than a strict cut at $10^{20}\,\mathrm{atoms\,cm^{-2}}$. In the centre column we show the velocity (1st moment) maps[3], and in the right column the velocity dispersion (2nd moment) maps.

---

[3]We use intensity weighted mean (IWM) velocity fields. The choice of velocity field type can have a significant impact on the fit rotation curve for techniques that model the velocity field directly (de Blok et al., 2008); because $^\mathrm{3D}$BAROLO instead models the data cube, for our purposes the choice of velocity field impacts only the visualization of the data.
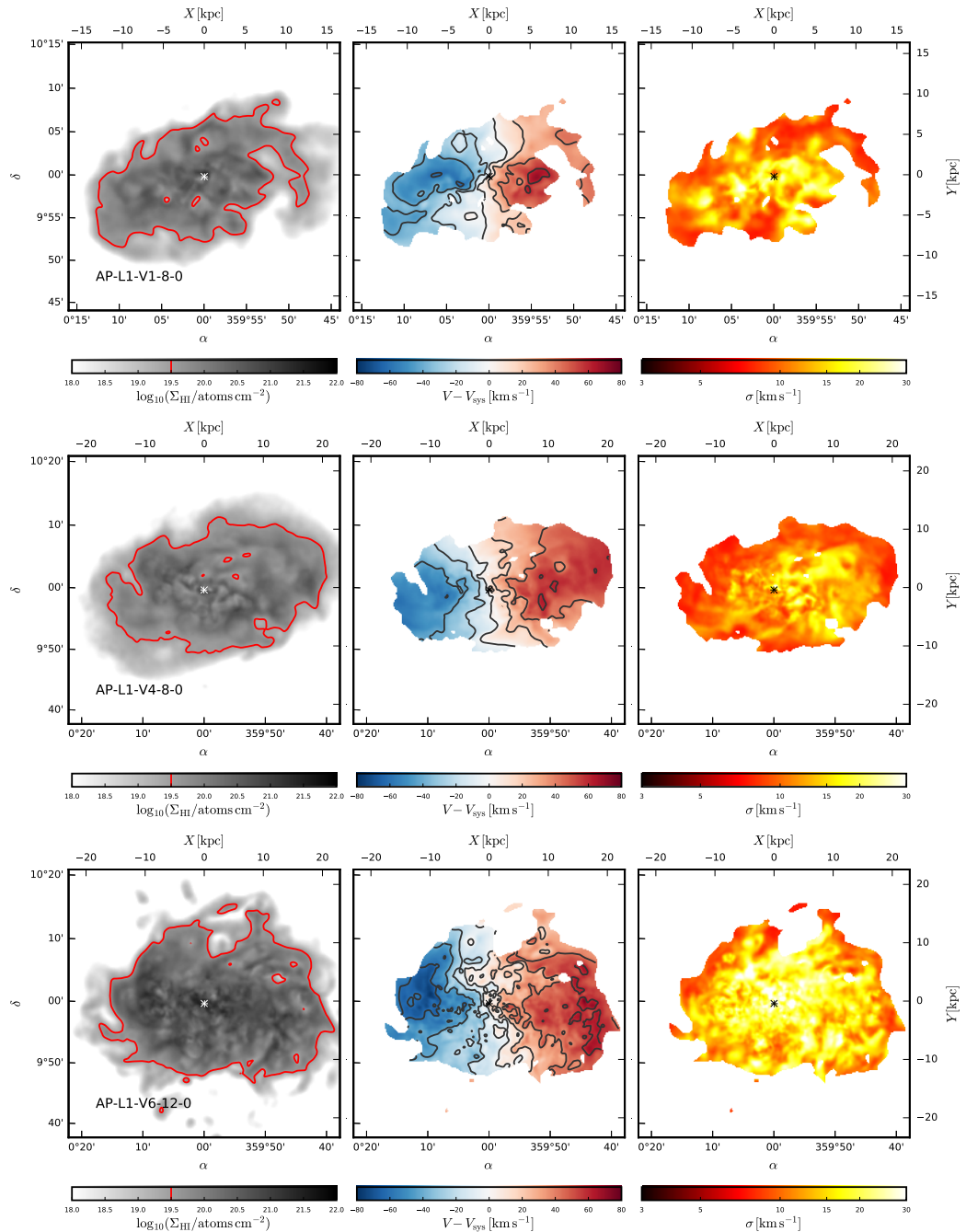
Figure 4.2: 0th moment (surface density, left column), 1st moment (flux-weighted mean velocity, centre column) and 2nd moment (flux-weighted vel ocity dispersion, right column) maps for three objects in our sample of APOSTLE galaxies. The galaxies are placed at an arbitrary sky position at a distance of 3.657 Mpc, inclination of $60°$ and position angle of $270°$, where the angular momentum vector of the H I disc is taken as the reference direction. The 1st and 2nd moment maps are masked to show only pixels where the surface density exceeds $10^{19.5}$ atoms cm^{-2}. Contours on the 1st moment map correspond to the tick locations on the colour bar. The '$\times$' marks the location of the potential minimum, which is well-traced by the peak of the stellar distribution, marked '+'.

4.2.4 Kinematic properties of simulated galaxies

Before examining the synthetic data cubes in further detail, we turn our attention for a moment to the kinematic properties of the simulated galaxies as measured directly from the simulation particle properties. In the top row of Fig. 4.3 we compare the circular velocity curves (heavy black lines) derived from the total mass profiles of three APOSTLE galaxies with the H I mass-weighted mean rotation velocity (thin gray lines) corrected for pressure support (thick gray lines, see Sec. 4.3.3). One of the underlying assumption in the mass modelling of galaxies via rotation curve measurements is that the rotational and pressure support of the gas balance the central gravitational force, i.e. that the system is in dynamical equilibrium. Galaxies AP-L1-V1-8-0 and AP-L1-V4-0 seem, within reason, to be in equilibrium. AP-L1-V6-12-0, on the other hand, has a gas disc which appears kinematically disturbed, rotating significantly slower in the central regions than would be expected from the circular velocity curve. Some real galaxies are also similarly disturbed (e.g. mergers) and are typically not considered in mass modelling studies. We adopt a simple criterion, that the pressure-corrected gas rotation speed match the circular velocity to within 15 per cent at $2\,\mathrm{kpc}$, to flag such galaxies, and focus most of the discussion below on the remaining 14 galaxies in our sample. We also show the H I velocity dispersion (second row) and H I surface density (third row) profiles of the same galaxies.

Returning now to the data cubes, we show in Fig. 4.4 three simple metrics characterizing the kinematics of our galaxies. These are not 'standard' measurements, but we have obtained the publically available moment maps[4] of the galaxies in the THINGS and LITTLE THINGS surveys and make identical measurements. The observational maps are provided cleaned of noise, with low signal-to-noise pixels masked out. We mimic this approximately by masking our kinematic maps when the H I column density drops below $10^{19.5}\,\mathrm{atoms\,cm^{-2}}$ (illustrated in Fig. 4.2), which is slightly deeper than the typical limiting column density in the aforementioned surveys to compensate the fact that H I discs in APOSTLE are somewhat larger than those of real galaxies.

In the left panel we show the median velocity dispersion along the line of sight (i.e. median of all un-masked pixels in the 2nd moment map) against the total H I mass. Points for APOSTLE galaxies which we have flagged as kinematically disturbed are shaded gray. The simulated galaxies have typically slightly larger velocity dispersions

---

[4]We use the 'natural weighted', not the 'robust weighted', maps.
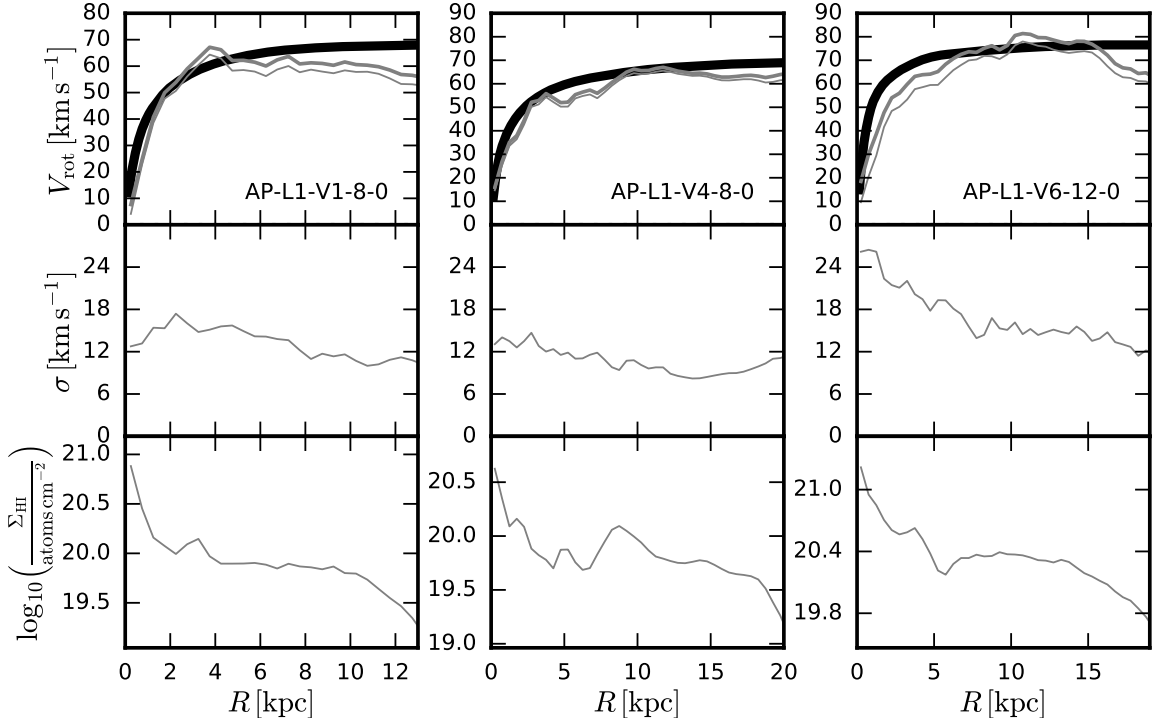
Figure 4.3: *First row:* Circular velocity curves (heavy black lines) and mean azimuthal velocity of H I gas (thin gray lines) for three of the simulated galaxies in our sample. The gas rotation velocity corrected for pressure support (see Sec. 4.3.3) is shown with the thick gray line. Because we have chosen our sample to have relatively large $V_{\max} > 60 \, \mathrm{km \, s^{-1}}$, such corrections are typically quite small. We flag galaxies in which the pressure-corrected velocity at $2 \, \mathrm{kpc}$ differs from the circular velocity by more than 15 per cent, such as AP-L1-V6-12-0, as kinematically disturbed. *Second row:* H I velocity dispersion profiles for the same galaxies, including both the thermal (sub-particle) and inter-particle contributions to the velocity dispersion, and calculated as $1/\sqrt{3}$ of the 3D velocity dispersion at each radius. *Third row:* H I surface density profiles for the same galaxies. The plot is truncated at the radius enclosing 90 per cent of the H I mass, which is typically very close to the radius where the surface density drops below our nominal limiting Σ_{HI} depth of $10^{19.5} \, \mathrm{atoms \, cm^{-2}}$.

(~ 10–$15\,\mathrm{km\,s^{-1}}$) than observed galaxies (~ 7–$10\,\mathrm{km\,s^{-1}}$), though there are several outliers in the observed distribution. The simulated galaxies are still dominantly rotationally supported; the only consequence of the increased velocity dispersion we note is slightly larger pressure support corrections (Sec. 4.3.3).

The middle and right panels both show measurements intended to quantify the symmetry of the 1$^{\text{st}}$ moment maps (velocity field). In the middle panel we use a residual map created by rotating the velocity field 180° about the centre and subtracting from the un-rotated field (with a change of sign such that in the perfectly symmetric case the residual is everywhere zero). We plot the rms width of the distribution of pixel values in this residual against the absolute value of the mean of the same distribution – this measurement is illustrated in Fig. C.1. The mean quantifies whether there is an offset in the average velocity of the approaching and receding sides of the galaxy, whereas the width quantifies more local asymmetries. (Where the mean is $< 1\,\mathrm{km\,s^{-1}}$ we plot the point at $1\,\mathrm{km\,s^{-1}}$.) The measurements of the observed and simulated galaxies essentially overlap in this space, particularly if the kinematically disturbed simulated galaxies are ignored (we plot only those THINGS and LITTLE THINGS galaxies which were selected for mass modelling by the survey team). The simulated galaxies are also more massive than most of the LITTLE THINGS galaxies (squares, which lie somewhat left of and below the diamonds for the more massive THINGS galaxies, on average), and since the measurements have dimensions $\mathrm{km\,s^{-1}}$ it is to be expected that there is a trend with mass, though we do not plot this explicitly.

In the right panel we plot a measure of the residual produced by subtracting a very simple kinematic model: the rms deviation from 0 of the velocity distribution of the residuals as a function of the H$\,$I mass. We select a single inclination, position angle and systemic velocity for each galaxy: $(i, \mathrm{PA}, V_{\mathrm{sys}}) = (60°, 270°, 257.5\,\mathrm{km\,s^{-1}})$ for APOSTLE galaxies, and the values listed in Table C.2 for observed galaxies. In a series of concentric rings defined by these parameters, we fit the function:

$$V(\phi) = V_{\mathrm{sys}} + V_0 \cos(\phi - \phi_0) \qquad (4.1)$$

where V_0 and ϕ_0 are free parameters, to remove the overall rotation[5]. This procedure is

---

[5]The freedom in ϕ_0 means that, strictly speaking, we are not removing a pure rotation field. This allows, however, to compensate for small variations in the kinematic major axis as a function of radius without the added complexity of rings with independent geometric parameters. We recall that the purpose of this measurement is to compare synthetic and real data cubes, and the measurement is made identically in both cases.
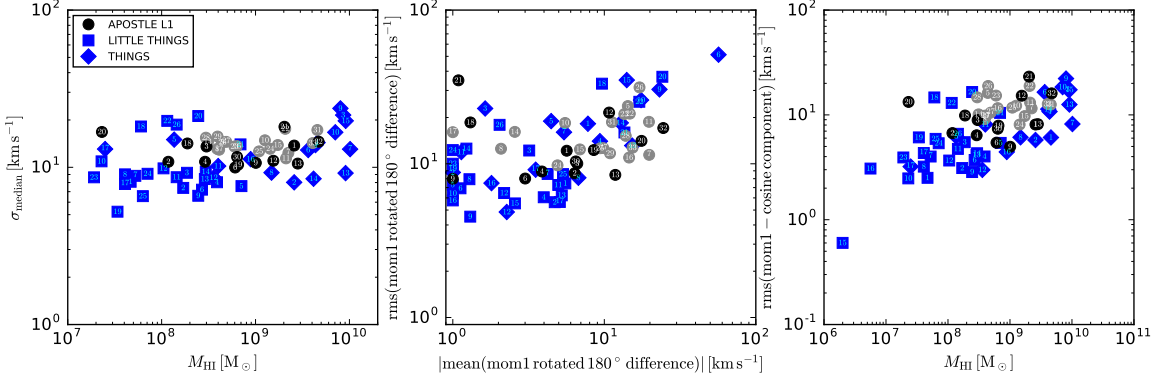
Figure 4.4: Diagnostics comparing the kinematics of observed and simulated galaxies. *Left:* Median velocity dispersion as measured along the line of sight as a function of H I mass. For the APOSTLE galaxies, the median is calculated across all pixels with $\log_{10}(\Sigma_{\mathrm{HI}}/\mathrm{atoms\,cm^{-2}}) > 19.5$; for the THINGS and LITTLE THINGS galaxies it is computed across all pixels in the S/N masked second moment map. Gray symbols correspond to galaxies which we flag as kinematically disturbed (see Fig. 4.3 and Sec. 4.2.4). *Centre:* As a measure of the symmetry of the velocity field, the first moment (mean velocity field) of each data cube is rotated 180° about its centre and subtracted from itself (with a sign change); here we plot the rms against the absolute mean offset from 0 of the pixels. Pixels which overlap a pixel with no velocity detection after rotation are discarded. See Fig. C.1 and Appendix C.2 for an illustration and further explanation of these measurements. *Right:* As another measure of the symmetry of the velocity field we construct a very simple kinematic model by fitting a cosine to the velocity field in a series of rings of constant inclination and position angle. The model is subtracted from the data and we plot here the rms about 0 of the residual against the H I mass for each galaxy. See Fig. C.2 and Appendix C.2 for an illustration and further explanation of this measurement.

further illustrated in Fig. C.2. Once again we find that the measurements of synthetic and real data cubes broadly overlap.

Based on the basic galactic properties and characterization of the data cubes discussed in this section we are satisfied that, though our galaxies may not be 'realistic' by every imaginable metric, the synthetic data cubes are sufficiently similar to those of their observed counterparts to proceed with fitting kinematic models.

4.3   Kinematic modelling

4.3.1   Parameter choices

The de-facto standard tool for kinematic modelling of galaxies is known as a 'tilted ring' model (Rogstad et al., 1974). In such a model, the disc of the galaxy of interest is represented as a series of rings of increasing size. The properties of each ring are described by a set of parameters which can be categorized as geometric (radius, width, thickness, centroid, inclination, position angle, systemic velocity) and physical (surface density, rotation velocity, velocity dispersion). Several routines to fit (a subset of) these parameters exist; we use the publicly available software $^{\text{3D}}$BAROLO[6] (for a detailed description, see Di Teodoro & Fraternali, 2015). Whereas most older tools model only the first few moments of the kinematics – the surface density and velocity fields, and in some cases the velocity dispersion field – $^{\text{3D}}$BAROLO belongs to a class of more recent tools which model the full data cube directly, and therefore nominally utilize all available kinematic information. The software has many configurable parameters; we discuss our choices for several of the most important ones below, and in Table C.3 we summarize the full configuration used.

   The parameter choices with perhaps the greatest influence on the resulting fits are those defining the handling of the geometric parameters for each ring. We adopt a strategy which attempts to minimize the impact of uncertainty in the geometric parameters, which would otherwise distract from the issues we wish to highlight, while still limiting ourselves to information that would be accessible observationally were our sample composed of real rather than simulated galaxies. As described in Sec. 4.2.3, all our synthetic observations are oriented so that the plane of the disc as defined by its angular momentum is inclined $60°$. We make no attempt to measure the inclination either morphologically or kinematically from 'observables'. We instead provide an initial 'correct' guess of $i = 60°$ to the software, but allow this parameter to vary by up to $15°$, allowing for some difference between the 'true' inclination and that which might otherwise be inferred. The handling of the inclination is particularly important in determining the recovered rotation curve since only the projected rotation $V_{\text{rot}}\sin(i)$ is observable, and breaking the degeneracy between V_{rot} and $\sin(i)$ is notoriously difficult. Our choice of $i = 60°$ is also helpful – at higher inclinations the relative impact of uncertainty in i is minimized: $i = 60° \pm 15° \iff \sin(60°)^{+12}_{-18}$ per cent, as

---

[6]`http://editeodoro.github.io/Bbarolo/`, we used the latest version available at the time of writing: 1.3.

compared to e.g. $i = 30° \pm 15° \iff \sin(30°)^{+41}_{-48}$ per cent – without being so high that consecutive rings begin to overlap substantially along the line of sight.

The position angles of the rings are treated similarly to the inclinations: given the construction of our synthetic data cubes, the position angle of the receding side of the galaxy should be 270° counter-clockwise from North. We provide this as an initial guess to the software, and allow for variations of up to 20°, noting that this parameter has much less influence on the recovered rotation curve than the inclination.

We model each galaxy out to the radius enclosing 90 per cent of its H I mass. This typically roughly coincides with the $\log_{10}(\Sigma_{HI}/\text{atoms cm}^{-2}) = 19.5$ isodensity contour, and in all cases is sufficient to reach the asymptotically flat portion of the circular velocity curve, allowing in principle an accurate measurement of the maximum circular velocity. The ring width is fixed at 14.1 arcsec, corresponding to a physical separation of 250 pc at the distance of 3.657 Mpc chosen for our synthetic observations.

We fix the centre of each ring on the peak of the projected stellar distribution in the galaxy, found by calculating the centre of mass of simulated star particles in the plane of the 'sky', removing a fraction of the outermost particles, and iterating. We find that this point corresponds to within a few pixels to the centre of potential defined by the SUBFIND (Springel et al., 2001; Dolag et al., 2009) algorithm and thus, for our galaxies, seems to be a reasonable tracer for the kinematic centre of the system.

For simplicity, the systemic velocity is fixed at 257 km s^{-1}, determined from the distance as $V_{sys} = H_0 D$. While this choice assumes a precision in the distance unavailable for observed galaxies (and no peculiar velocity), we note that the $V - V_{sys} = 0$ km s^{-1} isovelocity contour usually passes through, or very near, the projected peak of the stellar distribution. We therefore believe that deriving the systemic velcoity directly from observables would yield very similar values.

The initial guess for the rotation speed and velocity dispersion of each ring are set to 30 and 8 km s^{-1}, respectively. These initial guesses seem to have little to no impact on the final fit rotation curve and velocity dispersion profile.

We fix the thickness of the rings at 2 arcsec ~ 40 pc. This is much thinner than the actual thicknesses of the simulated gas discs; the height enclosing half the mass is of order 1 kpc. Difficulty modelling thick discs is a well known limitation of tilted ring models. Future codes may be able to better capture the vertical structure of discs (e.g. Iorio et al., 2017), but for the present we are bound by the limitations of current implementations.

4.3.2 Model fitting

Using the parameter choices outlined above (see also Table C.3), the tilted ring model is fit to each galaxy in two stages. In the first stage the free parameters are the rotation speed, velocity dispersion, inclination and position angle of each ring (in ^{3D}BAROLO's 'locally normalized' mode the surface brightness is not explicitly fit). The inclination and position angle profiles are then smoothed (coloured lines in Fig. 4.5 rows 2 & 3). For comparison we show the 'global' inclination and position angles of the systems as determined directly from the simulation data (see Sec. 4.2.3) with thin gray lines.

In the second stage the rotation speeds and velocity dispersions of the rings are fit again with the geometric parameters held fixed at their smoothed values; the result is illustrated by the (thin) coloured lines in Fig. 4.5 rows 1 & 4. The 'true' rotation and dispersion profiles were measured from the simulation particles directly and are shown for comparison with thin gray lines. The rotation profile was measured using the H I mass-weighted mean azimuthal velocity of gas particles in a series of 2 kpc thick, 500 pc wide cylindrical shells aligned along the disc plane. The velocity dispersion profile was measured using the same series of rings. There are two components of the velocity dispersion:

$$\sigma = \sqrt{\frac{1}{3}\left(\frac{k_{\rm B}T}{\mu m_{\rm p}} + \sigma_\phi^2 + \sigma_r^2 + \sigma_z^2\right)} \tag{4.2}$$

where $k_{\rm B}$ is Boltzmann's constant, T is the particle temperature, μ is the mean molecular weight, $m_{\rm p}$ is the proton mass, and σ_ϕ, σ_R and σ_z are the azimuthal, radial and vertical components of the particle velocity dispersion. The first 'thermal' component comes from small scale random motions parameterized by the gas particle temperatures and the second 'bulk' component from the relative motions of the simulation particles. Both components are reflected in the synthetic data cubes (Sec. 4.2.3), though in practice the 'bulk' component always dominates by a factor of > 2.

4.3.3 Correction for pressure support

The equation of gas rotational velocities with circular velocities (i.e. mass profiles):

$$V_{\rm rot} = V_{\rm circ} = \sqrt{\frac{GM(< r)}{r}} \tag{4.3}$$

requires that gravitational forces dominate the dynamics of the system. If the gas disc of a galaxy is supported against collapse in part by a pressure gradient in the

disc, the rotation speed systematically underestimates the circular velocity. Under the assumption that turbulence is the dominant source of pressure, the pressure, density and (radial) velocity dispersion of gas are related as $P = \rho \sigma_R^2$. Adding a term to account for the force due to a pressure gradient in the disc to eq. 4.3 then straightforwardly gives:

$$V_{\rm circ}^2 = V_{\rm rot}^2 - \sigma_R^2 \frac{\mathrm{d}\log(\rho \sigma_R^2)}{\mathrm{d}\log R} \tag{4.4}$$

(The gradient of the pressure is usually negative, yielding a net positive correction.) We calculate this correction for our simulated galaxies directly from the particle information to correct the gas rotation curves in the top row (thin gray lines) of Fig. 4.5 and show the result with the heavy gray lines. We tested the correction on simple models of equilibrium gas disks using the same hydrodynamics scheme and resolution as in APOSTLE and find excellent agreement between the corrected rotation velocity and the circular velocity for radii $\gtrsim 100\,\mathrm{pc}$. That the corrected rotation curves do not agree with the circular velocity curves (heavy black lines) therefore seems to be due to departures from dynamical equilibrium.

Under the additional assumptions that the vertical structure of the disc does not vary with radius and that the velocity dispersion is isotropic ($\sigma = \sigma_r$, with σ the velocity dispersion along the line of sight), eq. 4.4 can be written in terms of observationally accessible quantities as:

$$V_{\rm circ}^2 = V_{\rm rot}^2 - \sigma^2 \frac{\mathrm{d}\log(\Sigma_{\rm HI}\sigma^2)}{\mathrm{d}\log R} \tag{4.5}$$

where $\Sigma_{\rm HI}$ is the surface density of the H I gas. This formulation of the pressure support correction is the one most commonly employed in the rotation curve literature[7]. We measure the surface density along the (projection of) each of the best fitting rings directly from the synthetic data cubes (coloured lines, Fig. 4.5, 5th row). For comparison we also show the H I surface density profiles measured directly from the simulation particle distributions with a thin gray line. In the 6th row of the same figure we show the 'pressure' profile $\Sigma_{\rm HI}\sigma^2$ – the gradient is measured from the best

---

[7]It is often misleadingly called an 'asymmetric drift correction', for a detailed discussion of this and several related topics see sec. 5.5 of Pineda et al. (2017).

fitting parameters (α, R_0) of the function:

$$\frac{\Sigma_{\mathrm{HI}}\sigma^2}{(\Sigma_{\mathrm{HI}}\sigma^2)_0} = \frac{(R_0 + 1)}{R_0 + e^{\alpha R}} \tag{4.6}$$

This is the same functional form used in recent analyses of the THINGS and LIT-TLE THINGS galaxies[8] (Oh et al., 2011, 2015; Iorio et al., 2017).

4.4   The importance of orientation

Examples of the final, pressure support corrected rotation curves of AP-L1-V1-8-0 and AP-L1-V4-8-0 (left and centre columns of Fig. 4.3), in two orientations each, are shown with the heavy red and blue lines in the first row of Fig. 4.5. Instead of the random azimuthal directions used when analyzing our sample en masse, the viewing angles are carefully chosen to highlight the importance of the orientation to the recovered fit. Both projections are at an inclination of 60°, but offset by a 90° rotation about the galactic pole. The rotation curves drawn in blue significantly[9] underestimate the rotation speed of the gas, while those drawn in red overestimate it. These errors in the fits cannot be due to differences in the fit inclination (a difference of 10° at $i = 60°$ only changes V_{rot} by ~ 10 per cent), velocity dispersion (differences of $\lesssim 4\,\mathrm{km\,s^{-1}}$), or pressure support correction profiles. They are rather due the orientation of non-circular motions present in the gas discs relative to the line of sight.

This is illustrated in Fig. 4.6. We select particles within $2\,\mathrm{kpc}$ of the plane of the disc and construct a smooth velocity field in three dimensions, then sample the field in the disc plane. The upper panels show the residual azimuthal motions in the discs after the mean rotation at each radius has been removed. The two projection axes are illustrated by the coloured lines: the red line lies along the direction which, after projection, lies along the major axis of the synthetic observation which, when fit with $^{\mathrm{3D}}$BAROLO, yields the rotation curve drawn in red on Fig. 4.5, and similarly for the blue line. For both galaxies the red line, corresponding to an overestimated rotation

---

[8]de Blok et al. (2008) make no mention of pressure support corrections in their analysis, though for the majority of the galaxies in their sample the correction would be expected to be very small.

[9]The shaded area shows the error as estimated by $^{\mathrm{3D}}$BAROLO: the model parameters are re-sampled around the best fitting values to determine the variations required to change the model residual by 5 per cent. This yields an error similar to what might be derived from differences between the approaching and receding sides of the galaxy (Di Teodoro & Fraternali, 2015).
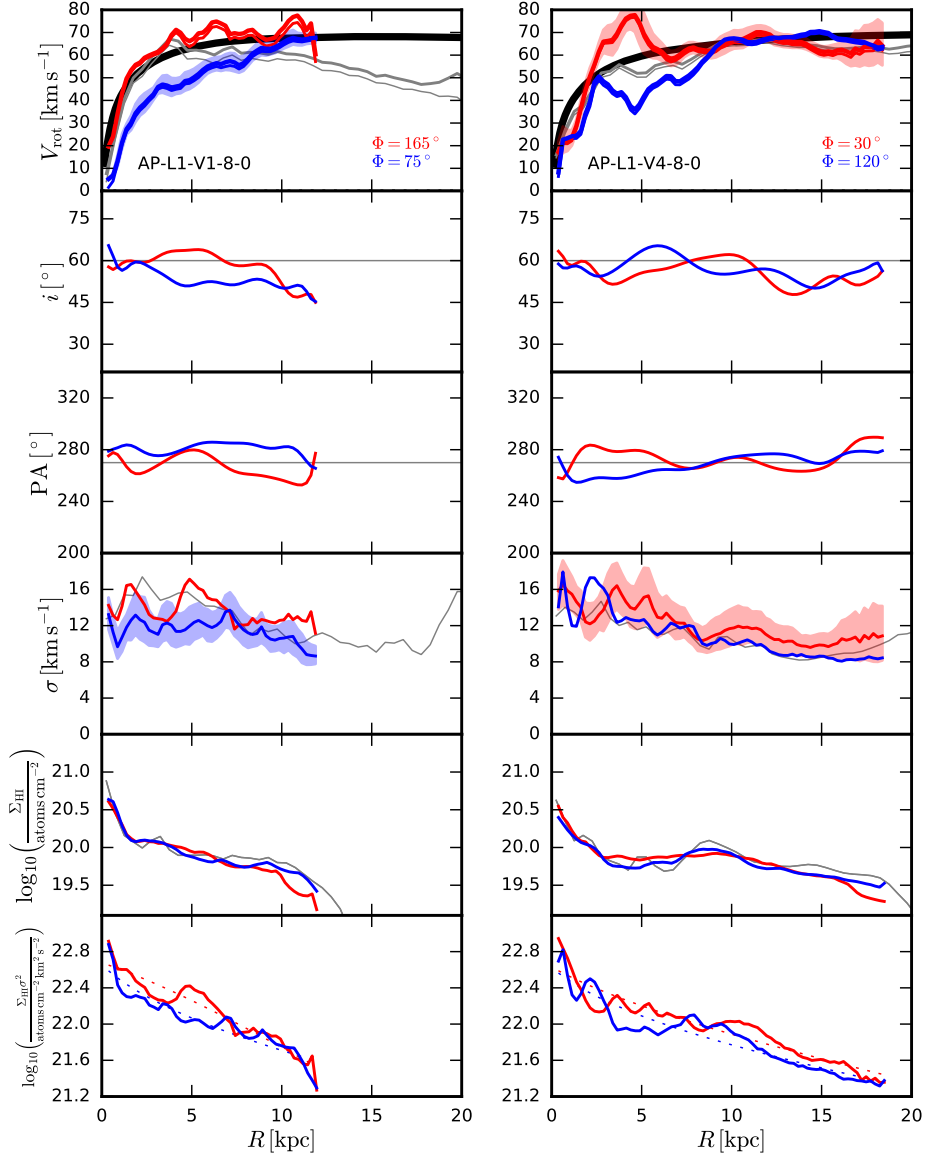
Figure 4.5: Summary of kinematic modelling for two of the galaxies shown in Fig. 4.2 (left and centre columns). Fits for two orientations of each galaxy, labelled by Φ (see Fig. 4.6), are shown by the red and blue curves, offset from each other by a 90° rotation about the galactic pole. *First row:* Rotation curves: circular velocity curve (thick black), gas azimuthal velocity (thin gray), same corrected for pressure support (thick gray), kinematic model with regularized geometric parameters (thin coloured), same corrected for pressure support (thick coloured) with errors estimated by ^{3D}BAROLO (shaded area – for clarity only shown for one orientation). *Second row:* Inclination profiles: nominal inclination (thin gray), regularized inclination profile (coloured). *Third row:* As second row, but for the position angle profile. *Fourth row:* Velocity dispersion profiles: velocity dispersion calculated directly from simulation particle distribution (gray), kinematic model with regularized geometric parameters (coloured) with errors (shaded area). *Fifth row:* Surface density profiles: surface density calculated directly from simulation particle distribution (gray), surface density along the projection of each ring defined by the regularized inclination and position angle profiles (coloured). *Sixth row:* $\Sigma_{HI}\sigma^2$ profiles: the profiles shown with coloured lines in the fourth and fifth rows are combined and fit with a simple function (dotted lines, see Sec. 4.3.3) for use in calculating the pressure support correction for the (thin solid coloured) rotation curves shown in the first row.

curve, lies approximately along a maximum in the azimuthal velocity residual, and the blue line, corresponding to an underestimated rotation curve, along a minimum. This makes intuitive sense: in projection, most of the information about the rotation velocity is contained in sight lines near the major axis – gas rotating faster than average lying on the major axis drives the rotation curve up, and vice versa.

The lower panels of Fig. 4.6 further illustrate the pattern present in the non-circular motions. The black symbols show the rotation velocity as a function of azimuthal angle at a radius of 5 kpc (innermost gray ring in the upper panels). We fit the first three terms of a Fourier series:

$$V(\phi) = \sum_{m=0}^{2} V_m \cos(m(\phi - \phi_m)) \tag{4.7}$$

to these points, and plot each term separately with dashed line styles. In both cases there is an obvious $m = 2$ term whose maxima align with the projection axis drawn in red in the upper panels (red vertical lines in lower panels) and whose minima align with the direction drawn in blue. AP-L1-V1-8-0 also has a significant $m = 1$ term. An $m = 1$ pattern could be introduced if the bulk velocity of the galaxy has a net component in the plane of the disc. We take care to choose a reference frame in which the H I disc has a null bulk motion, so this $m = 1$ pattern is apparently real, but we do not discuss it further and focus instead on the $m = 2$ pattern.

Fig. 4.7 confirms unambiguously the effect of this $m = 2$ pattern on the recovered rotation curve. We fit a tilted ring model and measure the rotation curve for the same two galaxies in a series of projections separated by rotations of $15°$ about the galactic pole. We label the orientations by an angle Φ (as labelled in the upper panels of Fig. 4.6), and choose a reference direction Φ_0 as the maximum of the nominal orientation of the $m = 2$ pattern illustrated by the red lines in the upper panels of Fig. 4.6, i.e. $\Phi_0 = 165°$ for AP-L1-V1-8-0 and $30°$ for AP-L1-V4-8-0. At $\Phi - \Phi_0 = 0°$ and $180°$ we expect the recovered rotation curve to be maximized, and it should be minimized at $90°$ and $270°$. We show the fit rotation velocities (pressure support corrections included, though they are small) at two radii, $R = 2$ kpc and 10 kpc. The fit rotation curves clearly show an $m = 2$ variation as the projection angle is varied. To guide the eye and illustrate phase variations we plot the best fitting $V_0 + V_2 \cos(2((\Phi - \Phi_0) - \Phi'))$, with Φ' allowing freedom in the phase. The phase offsets ($\Phi' \neq 0$) are easily explained: the $m = 2$ pattern is not always exactly aligned with the reference direction Φ_0. For instance, at $R = 2$ kpc in AP-L1-V1-8-0 the azimuthal
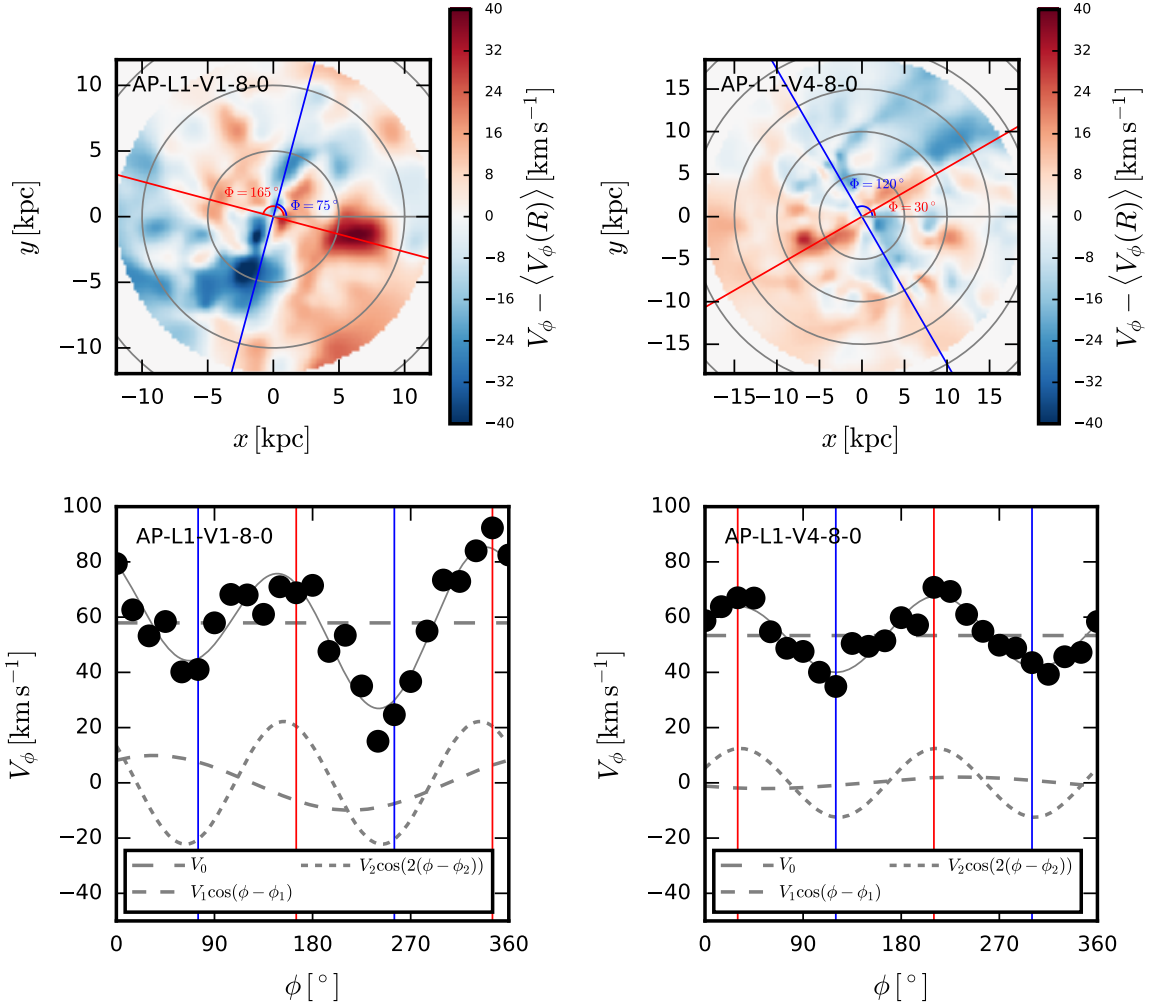
Figure 4.6: *First row:* Face-on maps of the residual azimuthal motions (after subtracting the mean rotation as a function of radius) in the disc plane for the two galaxies shown in Fig. 4.5. The red and blue lines correspond to the directions that lie along the major axis of the projections modeled and shown with the lines of corresponding colour in Fig. 4.5. We label the projection orientation Φ according to its angular offset from the x-axis, as illustrated. The gray circles are drawn at intervals of $5\,\mathrm{kpc}$. *Second row:* Azimuthal velocity at $5\,\mathrm{kpc}$ as a function of azimuth (black symbols). The best fitting first three terms of a Fourier series are shown with broken line styles, the sum of the three with a solid line. The vertical coloured lines correspond to the directions along the lines of the same colours in the upper panels, and coincide approximately with the peaks & troughs of the $m = 2$ mode. This alignment, though imperfect, extends to larger and smaller radii as well.
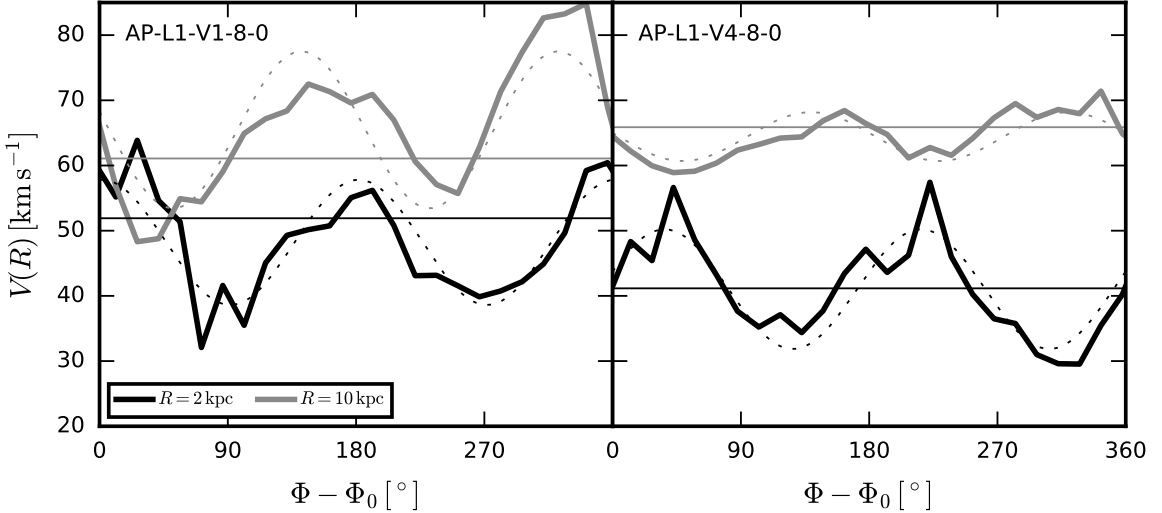
Figure 4.7: Rotation velocity at 2 and 10 kpc as recovered by ^{3D}BAROLO as a function of projection axis Φ, including pressure support corrections. The reference direction Φ_0 is defined as nominal direction of the maximum of the $m = 2$ pattern in the upper quadrants, i.e. the red line in the upper panels of Fig. 4.6. $\Phi_0 = 165°$ and $30°$ for AP-L1-V1-8-0 and AP-L1-V4-8-0, respectively. The horizontal lines shows the mean rotation velocity of the H I gas at the same radii, measured directly from the simulation particles, also corrected for pressure support. We expect the fit rotation speed to vary proportionally to $\cos(2(\Phi-\Phi_0))$; we show the best fitting $V_0+V_2\cos(2((\Phi-\Phi_0)-\Phi'))$ with a dotted line (note the additional freedom Φ' in the phase). In general $\Phi' \neq 0$ because in some cases because the $m = 2$ pattern (Fig. 4.6 upper panels) is, at some radii, not exactly aligned along the direction defined by Φ_0.

velocity residual appears well aligned with the red and blue lines in Fig. 4.6, and the best fitting $\Phi' = 2°$. At $R = 10$ kpc in the same galaxy, on the other hand, the $m = 2$ pattern lags the orientation defined by Φ_0 by perhaps $40°$; this is reflected by the best fitting $\Phi' = -38°$.

4.4.1 Applicability to observed galaxies

Studies of real galaxies are of course not afforded the luxury of examining the 3D velocity field directly; we turn now to the projected signature of the $m = 2$ patterns discussed above. An inclined ring is an ellipse which we parameterize by its semi-major axis length R, equivalent to the radius of the face-on ring, its parametric angle ϕ, equivalent to the polar angle of the face-on ring, and its inclination i. For a ring with a uniform azimuthal velocity V_1 perturbed by an $m = 2$ pattern with amplitude V_2 and phase ϕ_2, the velocity along the line of sight is (assuming for simplicity a ring

centered at the origin and with position angle along $\phi = 0$):

$$V(R, \phi) = V_1 \sin(i) \cos(\phi) \left[1 + \frac{V_2}{V_1} \cos(2(\phi - \phi_2)) \right] \tag{4.8}$$

If $V_2 \ll V_1$ the changes to the velocity field will be subtle, but they can be brought out by subtracting $V_1 \sin(i) \cos(\phi)$ from Eq. 4.8, leaving:

$$V(R, \phi) = V_2 \sin(i) \cos(\phi) \cos(2(\phi - \phi_2)) \tag{4.9}$$

$$= \frac{V_2}{2} \sin(i) \left[\cos(3\phi - 2\phi_2) + \cos(\phi - 2\phi_2) \right] \tag{4.10}$$

If the $m = 2$ pattern is at maximum on the kinematic major axis ($\phi_2 = 0°$ or $180°$) the velocity along the major axis is boosted and the rotation curve is overestimated; if it is at minimum ($\phi_2 = 90°$ or $270°$) the velocities along the major axis are suppressed and the rotation curve is underestimated. These two scenarios are illustrated schematically in Fig. 4.8 – the product of the $\cos(\phi)$ and $\cos(2(\phi - \phi_2))$ components yields a characteristic 3-peaked pattern. As described in detail by Schoenmakers et al. (1997); Spekkens & Sellwood (2007), a harmonic pattern of order m in the azimuthal motions within the disc translates to patterns of order $m \pm 1$ in the projected velocity field. We focus, however, on the $m = 3$ pattern in projection induced by the $m = 2$ pattern in 3D, because the $m = 1$ pattern is easily confused with the stronger pattern due to the bulk rotation of the disc and/or an error in the systemic velocity.

In Fig. 4.9 we examine whether this characteristic pattern is apparent when modelling the same two galaxies, AP-L1-V1-8-0 and AP-L1-V4-8-0. In the left column we show the same four projections which, when modelled by ^{3D}BAROLO, yield the rotation curves shown in Fig. 4.5, and the coloured lines along the major axes correspond to the lines in Fig. 4.6, indicating where the major axes lie in 3D. The second column shows the 1st moment map of the model data cube constructed by ^{3D}BAROLO, and the third column the difference between the data and model (notice the change in colour scale). The gray ellipse marks 2 kpc. The characteristic pattern illustrated in Fig. 4.8 is not readily apparent in any of the four cases illustrated, for several reasons. First, the amplitude of the pattern is expected, in these examples, to be $\lesssim 15\,\mathrm{km\,s^{-1}}$ (keeping in mind that projection introduces a factor of $\sin(i)$), which seems to be comparable to or smaller than other features in the residuals. Second, there are also features in the 3D velocity field in the radial direction which we have thus far neglected since the azimuthal features seem most important in dictating the behavior of the rotation
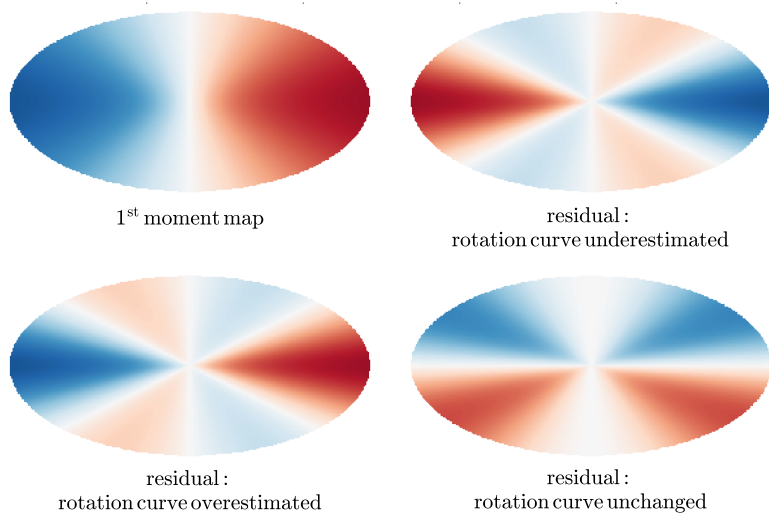
Figure 4.8: Schematic representation of the orientations of the 3-peaked pattern due to an $m = 2$ perturbation of the azimuthal velocity field which correspond to a maximal over- and underestimate of the rotation curve, and the orientation which leaves the rotation curve unchanged.

curve. These features have amplitudes comparable to those in the azimuthal direction and also contribute to the projected velocity field, partially cancelling the signature of the azimuthal residuals (see also Spekkens & Sellwood, 2007). Third, the tilted ring model as implemented by ^{3D}BAROLO (and indeed many other commonly used routines) has no provision for azimuthal variations in velocity along each ring, nor for any radial motions. However, it the algorithm still attempts to minimize the residual between the 'observed' and model data cubes and may spuriously adjust the geometric parameters of the rings to achieve this, which can further mask the expected pattern. It is not surprising, then, that the presence of such important non-circular motions is not necessarily readily apparent in the course of a typical tilted ring analysis of a galaxy. Even when such motions are apparent, their importance is easily underestimated. The azimuthal variations in our galaxies are of order 30 per cent in the central regions, resulting in similar changes of order 30 per cent in the rotation curves, yet in the model residuals the apparent differences are in some cases as small as 10 per cent, which could more easily be neglected as unimportant.

The patterns of Fig. 4.8 may be more apparent in the residual from a simpler kinematic modelling which aims only to remove the first order rotation term in the velocity field, using fewer free parameters. We fit the simple kinematic model described in Sec. 4.2.4 to the same projections of the galaxies illustrated in Fig. 4.9. In one case, the $\Phi = 75°$ projection of AP-L1-V1-8-0, the 3-peaked pattern is rather obvious in the central regions (see the top right panel of Fig. C.2).

What of real galaxies? Though the signature of the $m = 2$ perturbation to the azimuthal velocity field is subtle in projection, we examined the galaxies from the THINGS and LITTLE THINGS surveys with the most pronounced examples of slowly rising rotation curves and found two examples which suggest that inadequately modeled non-circular motions may significantly affect the rotation curves. The 1st moment maps of DDO 47 and DDO 87 are shown in the left column of Fig. 4.10. Iorio et al. (2017) elaborate enough of the details of their modelling process that we were able to accurately reproduce their models for these two galaxies using ^{3D}BAROLO– the model velocity fields are shown in the centre column. The rotation curves of Iorio et al. (2017) for these two galaxies are consistent within the reported errors with those of Oh et al. (2015), despite significant differences in the modelling techniques – in particular, Oh et al. (2015) attempt to account explicitly for non-circular motions in the velocity field.

In the third column of Fig. 4.10 we show the residual after subtracting the
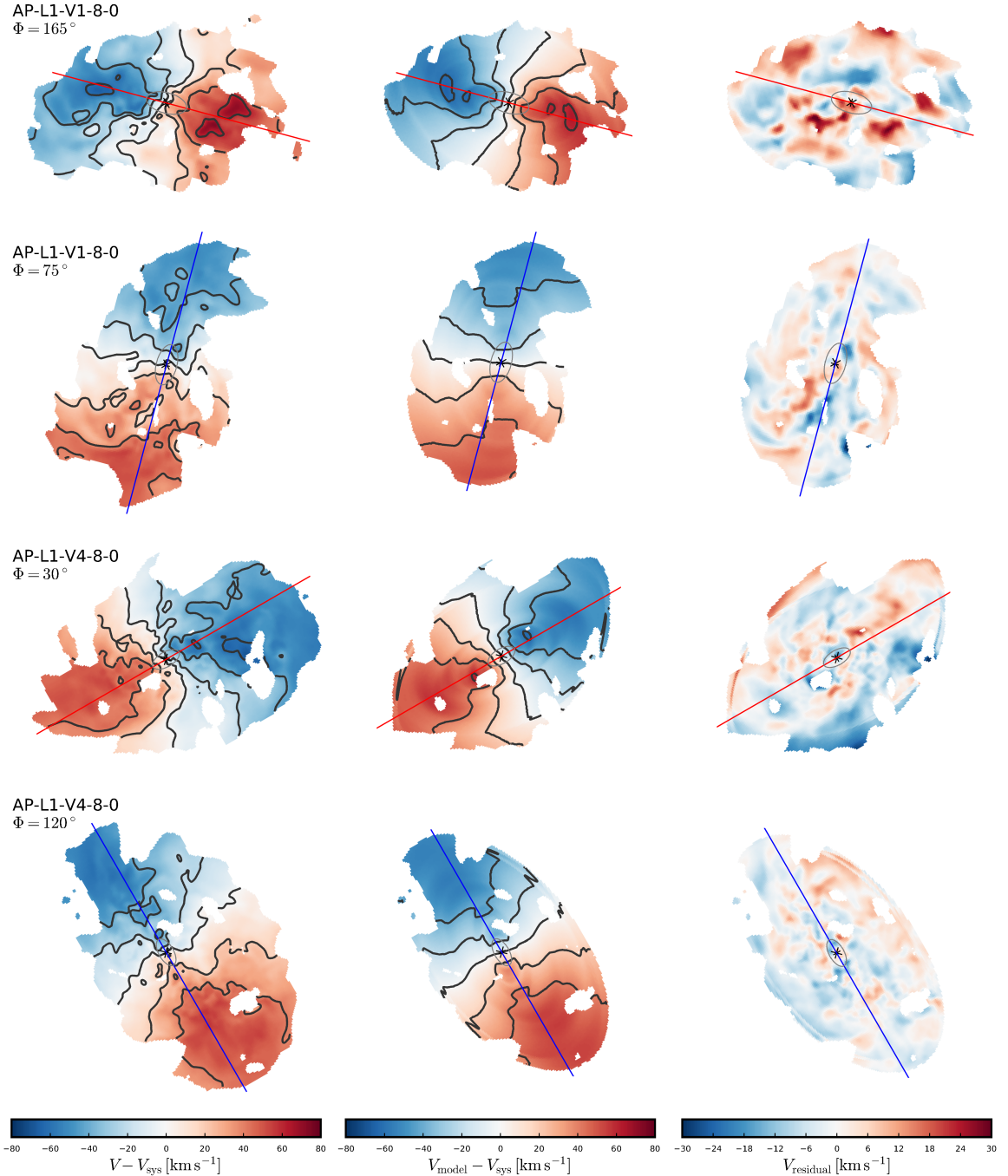
Figure 4.9: *Left column:* Velocity maps for the same two galaxies shown in Figs. 4.5–4.7 along lines lines of sight which place the red (rows 1 & 3, rotation curve systematically overestimated) or blue (rows 2 & 4, rotation curve systematically underestimated) lines from the upper panels of Fig. 4.6 along the major axis. The gray ellipse marks $R = 2\,\mathrm{kpc}$; the isovelocity contours are drawn at the same positions as the tick marks on the colour bars. *Centre column:* Velocity maps extracted from the $^{3\mathrm{D}}$BAROLO model data cubes for the same galaxies and orientations. *Right column:* Difference of the left and centre columns (note that the colour scale is compressed).

^{3D}BAROLO model velocity field. In both cases a 3-peaked pattern is evident in the central regions. We further highlight the presence of the pattern in the lower panels of the figure. In the first row we show the velocity as a function of azimuth ($\phi = 0$ is along the kinematic major axis) along a ring at $2.5\,$kpc, illustrated by a gray ellipse in the upper panels. We fit the function of Eq. 4.8 to these data (we add an additional phase ϕ_1 to the $\cos(\phi)$ term). In the upper panel we show the leading $V_1 \cos(\phi - \phi_1)$ term (the $\sin(i)$ is unimportant here and has been absorbed into V_1). In the second row we show the velocities around the same ring once the $V_1 \cos(\phi - \phi_1)$ component has been removed, and the $V_2 \cos(\phi - \phi_1) \cos(2(\phi - \phi_2))$ term of the fit. We further decompose this term into its two cosine components, shown with dashed lines. Since they are multiplied there is only a single amplitude; for illustration we show both components with amplitude $\sqrt{V_2}$, but this choice is arbitrary. The three peaked pattern is clearly visible in the data. The phase of the pattern, with a peak at $\phi \sim 180°$, corresponds that which we expect to cause an underestimate of the rotation curve. For DDO 47, there is a further, independent hint that we should expect an $m = 2$ symmetric pattern in the velocity field: the stellar distribution shows an apparent bar pattern (Georgiev et al., 1997).

As previously mentioned, DDO 47 and DDO 87 both have slowly rising rotation curves out to radii of $\sim 4\,$kpc. The residual pattern has an amplitude in projection of ~ 7–$10\,$km s^{-1}, or about 30 per cent of the (apparent) mean rotation speed at the same radius. Guided by the analysis illustrated in Figs. 4.5 & 4.6, this could plausibly correspond to a 30 per cent underestimate of the rotation curve in the inner regions, enough to call into question the slowly rising nature of the rotation curves.

4.5   The inner mass deficit problem

The discussion above shows clearly that non-circular motions in the gas of APOSTLE galaxies substantially impacts the rotation curves as recovered using ^{3D}BAROLO, and that there is at least circumstantial evidence to support the idea that modelling of real galaxies may suffer from similar effects. We now examine the impact of such modelling errors on the interpretation of the cusp-core problem. We adopt as our metric for comparison the diagram from fig. 6 of Oman et al. (2015), which characterizes the cusp-core problem as a deficit of mass in the central region (traced by V_{circ} at $2\,$kpc) as compared to the mass expected for a cuspy CDM system of the same total mass (as traced by V_{max}). We present a similar diagram in Fig. 4.11. We adopt the same radius
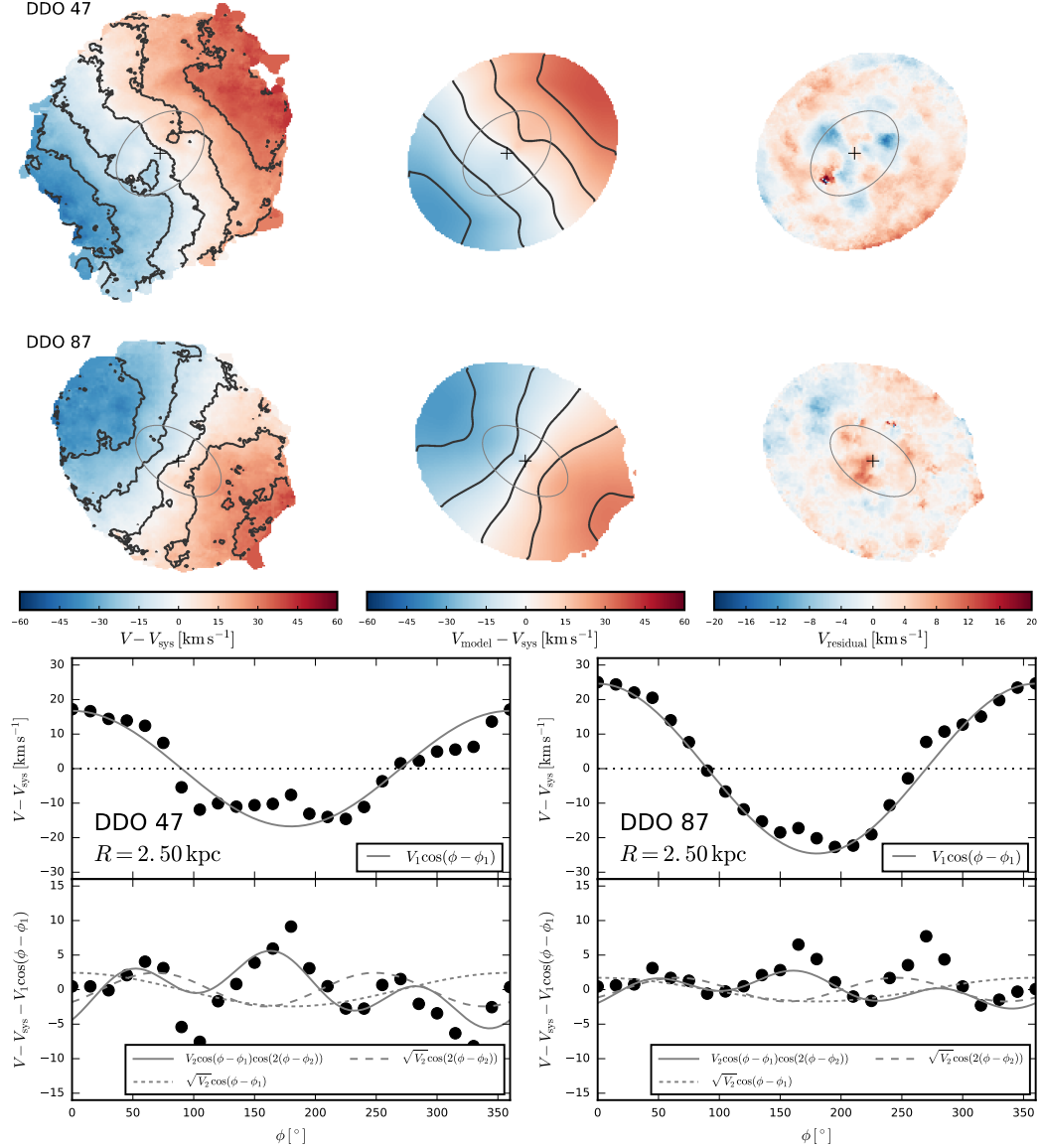
Figure 4.10: *Upper: Left column:* Velocity maps for the LITTLE THINGS galaxies DDO 47 and DDO 87, which have slowly rising rotation curves. The gray ellipse marks $R = 2.5\,\mathrm{kpc}$; the isovelocity contours are drawn at the same positions as the tick marks on the colour bars. *Centre column:* Velocity maps extracted from $^{3\mathrm{D}}$BAROLO model data cubes for the same galaxies. We use the same configuration for $^{3\mathrm{D}}$BAROLO as in Iorio et al. (2017), and confirm that we recover the same rotation curves. *Right column:* Difference of the left and centre columns, notice the '3 petal' pattern near the centre. *Lower: First row:* Velocity as a function of the parametric angle ϕ, and the best-fitting cosine function, at $R = 2.5\,\mathrm{kpc}$ (gray ellipse in upper panels). *Second row:* Residual velocities after removing the main cosine component, and the best-fitting projected $m = 2$ function. Both galaxies have a clear 3-peaked pattern in the residuals, oriented such that the maximum of the $m = 1$ component approximately aligns with a minimum of the $m = 2$ component, and vice versa. This is the signature, in projection, of an $m = 2$ perturbation to a pure rotation field – the combination of the π-period pattern from the perturbation and the usual 2π-period pattern from the line of sight projection of the azimuthal velocity produces a 3-peaked pattern. This orientation corresponds to that which, in our interpretation, would cause a maximal underestimate of the rotation curve (see Fig. 4.8).

of 2 kpc, which is as small as reasonably possible while minimizing concerns regarding the spatial resolution of both the simulations and observations. The relation between the two aforementioned quantities, and associated 1σ scatter, as predicted from the circular velocity profiles of galaxies from the APOSTLE and EAGLE simulations, is shown by the red line and shaded band. Crucially, for the V_{max} range selected for our synthetic observations (60–$120\,\mathrm{km\,s^{-1}}$), 2 kpc is small enough to probe the rising part of the rotation curve. This is not the case for smaller systems, where the rotation curve may already reach the flat part at 2 kpc, for instance e.g. IC 1613, LITTLE THINGS point #19, has a slowly rising rotation curve, yet lies directly on the red line (and the 1:1 line).

Galaxies with slowly rising rotation curves lie below the red line: what is often described as a core in the dark matter profile is, roughly speaking, equivalent to a central mass deficit in this diagram[10]. The broken black lines illustrate the relations obtained by removing fixed amounts of mass from the central 2 kpc of an NFW halo as a function of V_{max}. The red points are derived from the circular velocity curves of the galaxies in our sample (Sec. 4.2.2), omitting those which we have flagged as kinematically disturbed (Sec. 4.2.4; they vertical gray band illustrates our selection in V_{max}). These unsurprisingly lie along the red line and shaded band; these galaxies are drawn from the distribution defining that line. The green points are derived from the gas rotation profiles of the same galaxies, as measured directly from the simulation particle distributions. Because we have removed galaxies which are kinematically disturbed, the green points approximately overlap the red points.

The black points are derived from the rotation curves for the same galaxies as recovered using $^{\mathrm{3D}}$BAROLO. The discrepancy of the model fit with the actual rotation of the gas is, in many cases, striking, and due primarily to the effects of non-circular motions on the rotation curve modelling, as discussed in Sec. 4.4. The points move, substantially, depending on which orientations are chosen for the galaxies: AP-L1-V4-8-0 (point #6), for instance, moves approximately vertically between its plotted position and the 1:1 line, depending which projection is used (e.g. Fig. 4.7). We plot here the result of modelling a single projection for each galaxy, chosen randomly with the constraint that $i = 60°$. For comparison, we also show points derived from the rotation curves of THINGS and LITTLE THINGS galaxies as reported by de Blok

---

[10]Strictly speaking to infer a dark matter core the baryonic contribution to the rotation curve must be subtracted, which we make no attempt to do here. However, the galaxies of most interest in this analysis are expected to be heavily dark matter dominated, so the baryonic contribution is safely ignored to leading order.
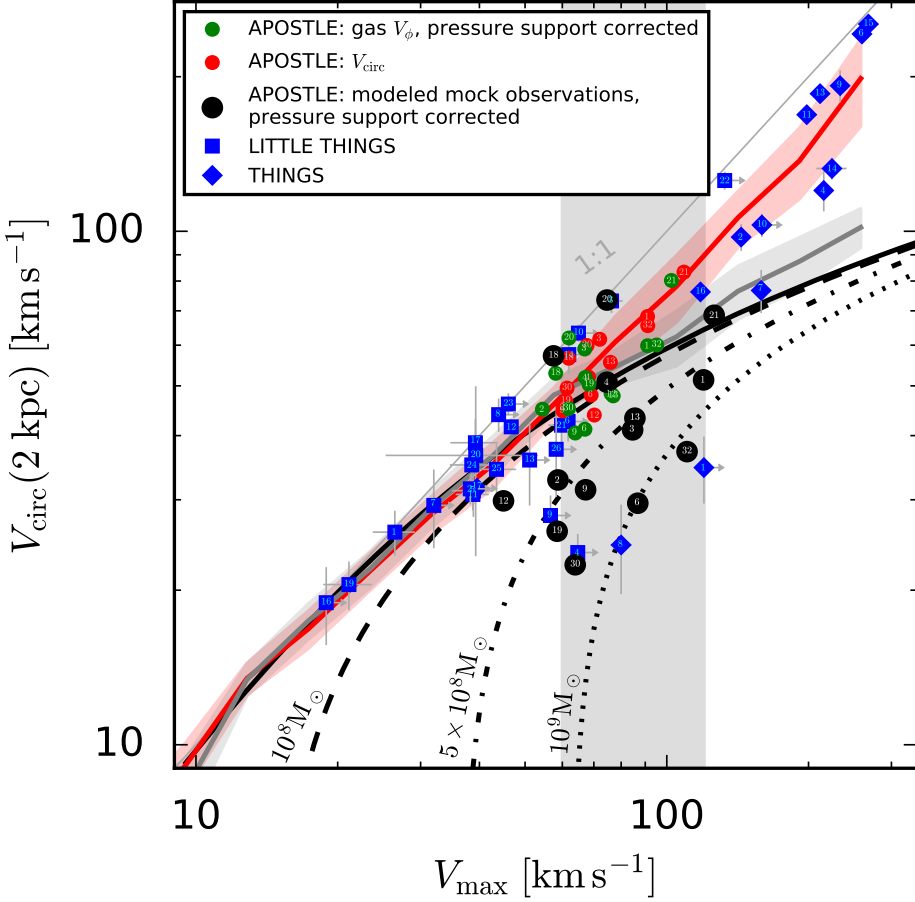
Figure 4.11: Circular velocity at 2 kpc plotted against maximum circular velocity, a measurement of the 'central mass deficit'. The lines are reproduced from fig. 6 of Oman et al. (2015, see their sec. 4.6 for additional details). The solid black line indicates the expected correlation for an NFW (Navarro et al., 1996b, 1997) mass profile and the mass concentration relation of Ludlow et al. (2014); this is well traced by haloes in an N-body simulation (gray line). Values measured from the circular velocity profiles of galaxies from the APOSTLE and EAGLE simulations lie along the red line. The broken lines indicate the correlation for the same (NFW) profile but removing a fixed mass from the central 2 kpc, as labelled. Three points are shown for each of the APOSTLE galaxies in our sample: one each for the circular velocity curve (red), the gas azimuthal speed corrected for pressure support (green) and the ^{3D}BAROLO rotation curve corrected for pressure support (black). Galaxies which we flag as kinematically disturbed (see Fig. 4.3 and Sec. 4.2.4) are omitted. The gray shaded area marks our selection in V_{max}, as in Fig. 4.1. We show measurements from the THINGS (blue diamonds) and LITTLE THINGS (blue squares) collaborations for comparison.

et al. (2008); Oh et al. (2011, 2015). Within the range in V_{max} spanned by our sample of simulated galaxies, we straightforwardly reproduce the full width of the scatter in $V_{\mathrm{circ}}(2\,\mathrm{kpc})$. Furthermore, the scatter we find can be considered a *lower* bound: all of our simulated observations are at a fixed inclination of 60°, approximately the most favourable for tilted ring modelling, and we make reasonable but somewhat optimistic assumptions regarding how well key parameters such as distance and kinematic centre are known (see Sec. 4.3.1). These results suggest that the inner mass deficit diversity, and by extension the cusp-core problem, may simply be due to the inability of current models to properly account for non-circular motions in the gas discs of galaxies.

4.5.1 Diagnosing the influence of non-circular motions

If the large scatter in inner mass deficits for observed galaxies seen in Fig. 4.11 is indeed driven by modelling errors due to non-circular motions in the gas discs of the galaxies, some signature might be expected to appear in the velocity field of the galaxies. This has already been alluded to above in the discussion around Figs. 4.9–4.10; we now return to this point but consider the entire sample of both simulated and observed galaxies. We quantify the strength of the non-circular motions as a function of radius as the rms (about 0) of the residual velocity field after the first-order (rotation) term has been removed:

$$A_{\mathrm{non\text{-}circular}}(R) = \frac{\sqrt{\langle (V(R,\phi) - V_{\mathrm{sys}} - V_1(R)\cos(\phi - \phi_1(R)))^2 \rangle}}{V_1(R)} \qquad (4.11)$$

where the average is over all azimuthal directions ϕ. The result of this measurement for all galaxies in both our observed and simulated samples is shown in Fig. 4.12.

Considering first the simulated sample, it is reassuring that those galaxies which we have flagged as 'kinematically disturbed', i.e. which have gas rotation velocities at 2 kpc which differ by more than 15 per cent from the circular velocity at the same radius, in general have much stronger non-circular motions than those where the gas rotation velocity and circular velocity agree reasonably well. Examining the latter galaxies in more detail, it is interesting that of the 4 galaxies which lie furthest below the NFW curve in Fig. 4.11 (black points #30, 19, 6, 32), 3 are exactly those which have the strongest non-circular motions near 2 kpc: AP-L1-V16-19-0, AP-L1-V11-5-0 and AP-L1-V10-30-0; the fourth (AP-L1-V4-8-0) has apparently weaker $A_{\mathrm{non\text{-}circular}}$. Another interesting system is AP-L1-V6-18-0, which lies nearly on the 1:1 line in
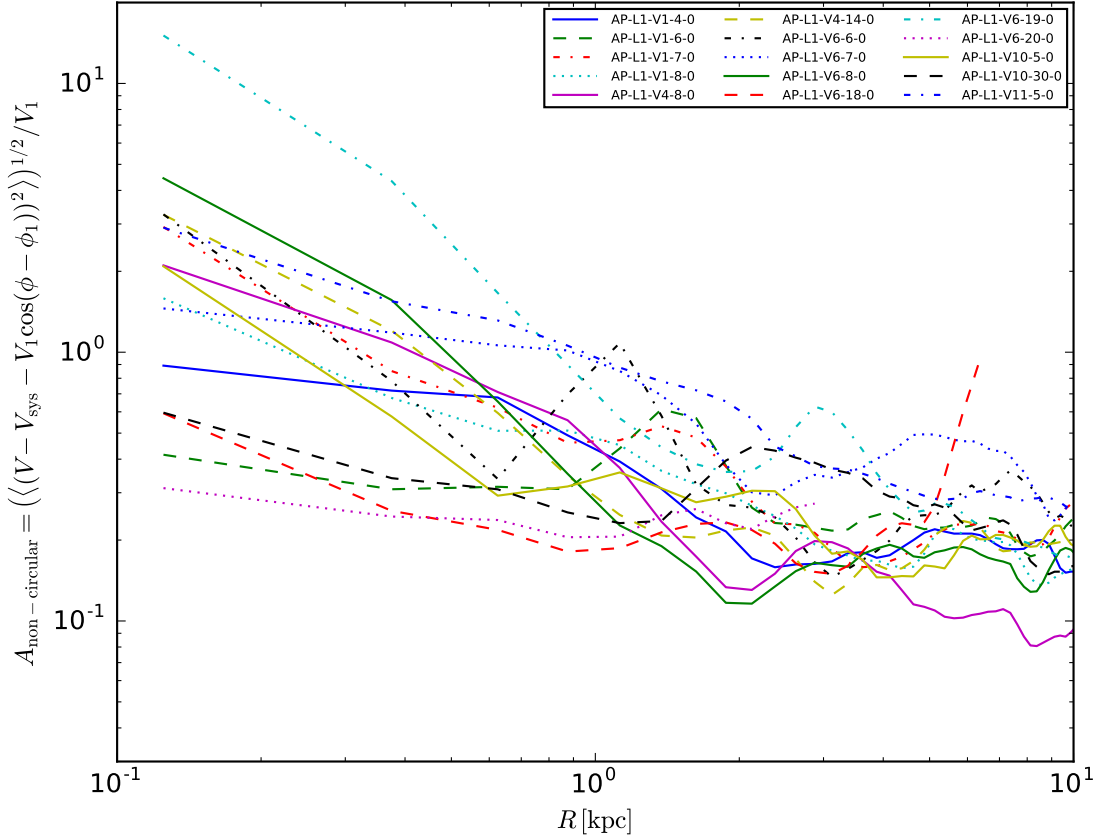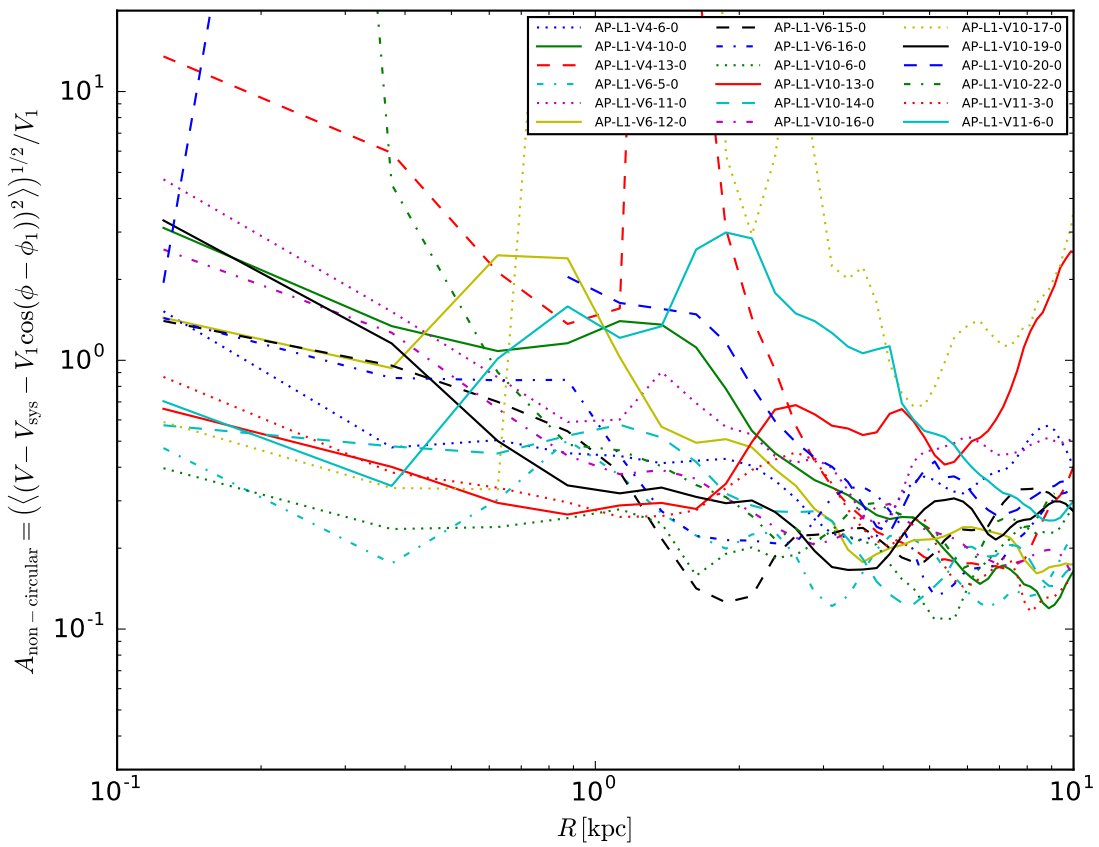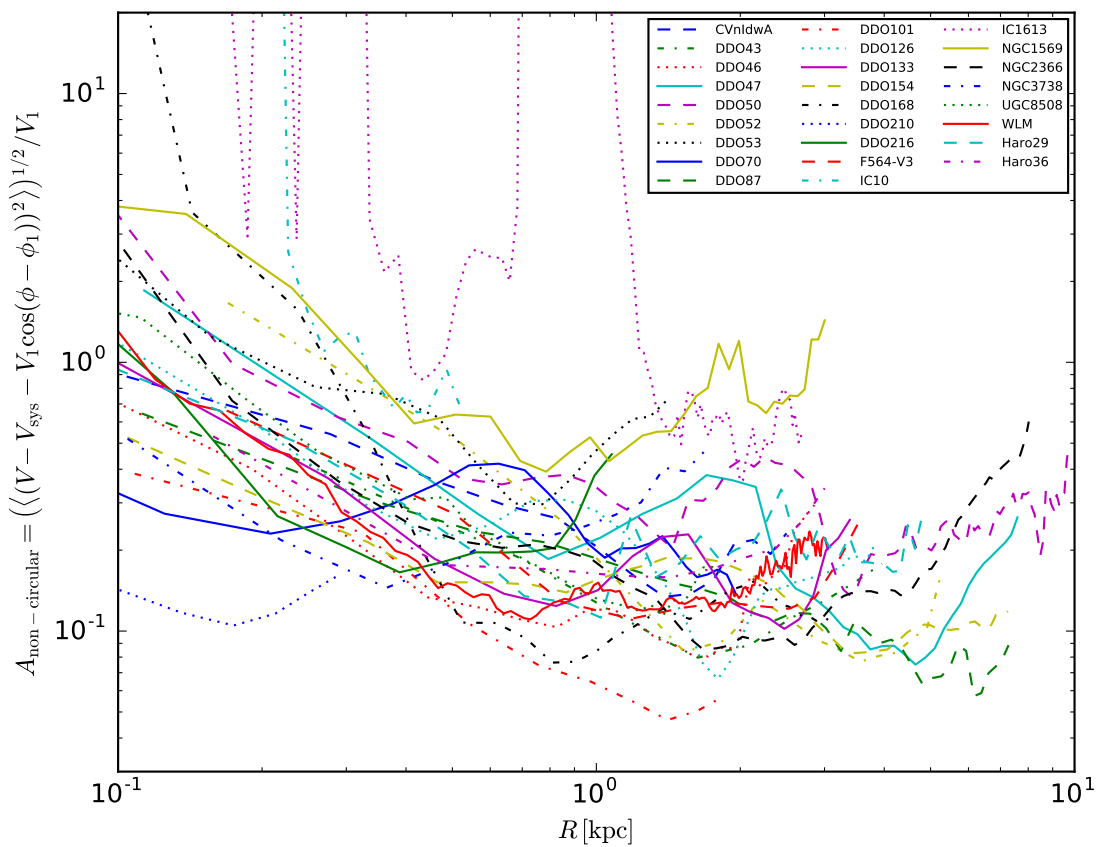
Figure 4.12: The first panel (subsequent panels are shown on subsequent pages) illustrates the strength of non-circular motions (Eq. 4.11) as a function of radius for the simulated galaxies in which the rotation velocity of the gas at $2\,\mathrm{kpc}$ matches the circular velocity at the same radius to within 15 per cent. The non-circular motions in these galaxies are generally weaker than in the 'kinematically disturbed' galaxies shown in the second panel. The identical measurement for galaxies from the LITTLE THINGS and THINGS surveys are shown in the third and fourth panels, respectively. Note that caution is required when interpreting the measurements of $A_{\mathrm{non\text{-}circular}}$ at radii $R \lesssim 1\,\mathrm{kpc}$; these are based on very few measured points, and this region is usually poorly resolved in both simulations and observations.

Figure 4.12: *Continued.*

Figure 4.12: *Continued.*
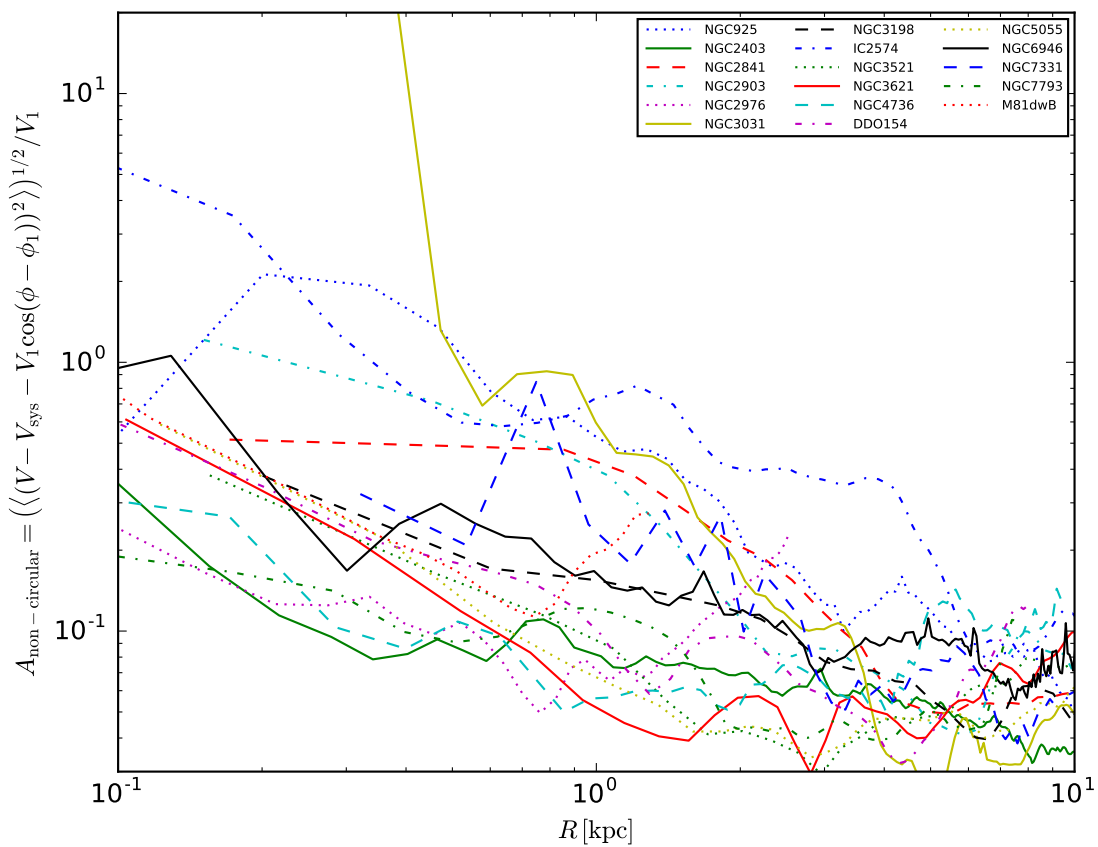
Figure 4.12: *Continued.*

Fig. 4.11 (point #18) and has a large $A_\text{non-circular}$ toward the outskirts of the galaxy.

Turning next to the observed sample of galaxies, it is very intriguing that perhaps the two most extreme examples of cored galaxies, IC 2574 and IC 1613[11], are the two galaxies with the largest values of $A_\text{non-circular}$ in the THINGS and LITTLE THINGS surverys, respectively. Many galaxies well-known to have slowly/linearly-rising rotation curves are amongst those with the strongest non-circular motions (e.g. NGC 925, DDO 168, NGC 1569, DDO 126, DDO 53, NGC 3738, NGC 2366). The correlation is not perfect, however: of DDO 47 and DDO 87, the two examples used in Fig. 4.10, only the former has strong non-circular motions as measured using $A_\text{non-circular}$. One final intriguing system is DDO 50, which was highlighted as a 'missing dark matter' galaxy by Oman et al. (2016), and which also has relatively strong non-circular motions.

While the discussion above is admittedly qualitative, galaxies with slowly rising rotation curves often, though not always, seem to have large values of $A_\text{non-circular}$. This and similar measurements clearly merit further study.

4.6   Discussion

The presence of important $m = 2$ harmonic perturbations to the azimuthal velocity field is evident in our simulated galaxies. The notion that many real galaxies in the circular velocity range spanned by our simulated sample suffer from similarly important perturbations is easily motivated. Estimates of the fraction of galaxies which are barred vary substantially (see, e.g., Algorry et al., 2017, sec. 3.2 for a concise discussion), but there is broad agreement that even morphologically apparent bars are relatively common. From this observation it is reasonable to speculate that if weaker distortions are included in calculating a 'bar-like' fraction, that fraction probably represents a majority of galaxies.

The 'classical' tilted ring model (Rogstad et al., 1974), and many variations thereupon, does not contain any parameters that allow for azimuthal variations in the velocity along each ring, or for radial motions. At best, non-circular motions are small enough that they do not seriously affect the modelling; at worst, the parameters are biased to incorrect values that allow the model to partially 'compensate' the non-circular motions and thus minimize the relevant residual.

---

[11]IC 1613 is intrinsically small and its rotation speed is already maximal at 2 kpc, so it does not appear as an outlier in Fig. 4.11.

Trachternach et al. (2008) and performed harmonic decompositions of the THINGS sample of galaxies. They concluded that typical non-circular motions in these galaxies have amplitudes less than 5 per cent of the rotation velocities, and that they are therefore safely neglected (see also van Eymeren et al., 2009, who reach a similar conclusion for a different sample of galaxies). This is likely correct for several of the THINGS galaxies, though we note that because the decompositions are performed along the rings from a tilted ring model fit some of the non-circular motions are likely masked by spurious variations of the ring parameters. For instance, though the azimuthal variations in our two examples AP-L1-V1-8-0 and AP-L1-V4-8-0 at $R = 5\,\mathrm{kpc}$ have amplitudes of 15–$20\,\mathrm{km\,s^{-1}}$ (Fig. 4.6), harmonic decompositions at the same radius of the projections shown in Fig. 4.10 suggest somewhat smaller (inclination corrected) amplitudes of $\lesssim 12\,\mathrm{km\,s^{-1}}$. In two cases where more pronounced non-circular motions are present, IC 2574 and NGC 2366, Trachternach et al. (2008) refer to Oh et al. (2008), who derive what they dub the BULK velocity field of the galaxies, based on an iterative multiple Gaussian decomposition of the H I line profile. The same method is applied to all of the LITTLE THINGS galaxies analysed in Oh et al. (2015), where lower galaxy masses mean that similarly small non-circular velocities are relatively much more important. This method seems effective in removing the contribution of local non-circular motions to the velocity field, but it is not clear that it can correctly compensate for distortions on the scale of the entire disc. For instance, a pure $m = 2$ harmonic perturbation to the gas azimuthal velocity does not produce multiple peaks in the H I line profile at any location; the BULK velocity field procedure will therefore fail in removing the signature of this perturbation.

The signature of an azimuthal $m = 2$ pattern can be masked in projection by a similar pattern in the radial gas motions, offset $45°$ that in the azimuthal motions (Spekkens & Sellwood, 2007). Our galaxies, in particular AP-L1-V1-8-0 and AP-L1-V4-8-0, have such $m = 2$ patterns in the radial motions as well, offset approximately $45°$ from the pattern in the azimuthal velocities, though we have not shown this in our analysis above. We intend to return to this issue and its effect on the projected velocity fields in a future paper. Spekkens & Sellwood (2007) also emphasize that even if the mean rotation speed of the gas can be recovered by a model, in a general non-axisymmetric potential this is not equivalent to the circular velocity – the correct approach in this case is to attempt to recover the potential directly and then derive the equivalent circular velocity curve (mass profile) from the potential. This may be particularly relevant for systems such as the ones we have flagged as kinematically

distrubed – a selection which is not straightforward for observed galaxies.

Thus far we have not addressed the origin of the $m = 2$ harmonic modes present in our simulated galaxies. Because our simulations are fully cosmological, we can in principle examine a wide variety of perturbation sources, e.g. bar-unstable discs, the shape of the dark matter halo, interactions with other galaxies, mergers, gas accretion, modes in the gas disc driven by supernova explosions, etc. Because of the many possibilities, identifying which source(s) may be dominant clearly requires a reasonably extensive study; we defer the examination of this question to a future paper.

Our analysis supports the idea that non-circular motions are rarely, if ever, small enough to be ignored in the dwarf regime, except perhaps if one is lucky with regard to the orientation of the patterns in a particular galaxy. We find errors in the recovered velocity at $2\,\mathrm{kpc}$ of up to 50 per cent, yet the observable signature of the perturbations driving the errors is subtle. If real galaxies are subject to similar systematic effects, it is unclear whether anything meaningful can be inferred from attempts to measure the dark matter density profile or inner logarithmic slope based on rotation curve measurements. The most promising, though laborious, way forward would seem to be to pursue the development/improvement of models which encode explicitly potentially large, azimuthally variable non-circular motions, in the spirit of Spekkens & Sellwood (2007). After the obligatory initial validation of such models on simple, analytic test cases, unbiased (and ideally large) samples of model galaxies drawn from fully cosmological simulations offer a useful proving ground. We have found the process of examining multiple projections of the same galaxy at fixed inclination to be particularly telling of the systematic uncertainties associated with non-circular motions.

4.6.1   Inclination errors

An error in estimating the inclination when modelling a rotating disc gives rise to a pattern very similar to that due to an $m = 2$ symmetric distortion in the azimuthal velocity field (e.g. Warner et al., 1973); we consider here whether the patterns seen in the velocity fields of DDO 47 and DDO 87 could be due to inclination errors. In both cases the sign of the residual pattern along the major axis is opposite the sign of the velocity field along the major axis, which could be due to an *over*estimate of the inclination. For illustration we use the radius $R = 2.5\,\mathrm{kpc}$ shown in the lower panels

of Fig. 4.10. At this radius the redisual pattern has an amplitude of $\gtrsim$ 20 per cent that of the rotation speed at the same radius. The assumed inclinations for DDO 47 and DDO 87 for the models shown (see Iorio et al., 2017) are 37° and 42°, respectively. To account for the observed pattern exclusively with inclination errors the intrinsic inclinations would need to be $\lesssim$ 28° and $\lesssim$ 32°, respectively, i.e. overestimates by 10–15°. Motivated by difficulty in explaining the existence of outliers well above the BTFR, Oman et al. (2016) recently argued that such large inclination errors may be present in the analysis of similar galaxies. However, the inclination estimates of Iorio et al. (2017) are already lower the values of 46° and 56° found by Oh et al. (2015), and assuming the very low inclinations necessary to explain the residual pattern would revise the maximum circular velocity of the two systems to 99 and 89 $\mathrm{km\,s^{-1}}$, which would move both galaxies well off the BTFR (Fig. 4.1; DDO 47 and DDO 87 are LITTLE THINGS points #4 and #9). This scenario could be avoided by invoking a strong warping of the H I discs, but this begins to seem rather contrived; it seems unlikely that inclination errors are the source of the patterns seen in the residual maps for these two galaxies. Nevertheless, great care must be taken to avoid mistaking inclination effects for a harmonic mode in the gas motion.

4.7 Summary and Conclusions

We have constructed synthetic, spatially and spectrally resolved, H I observations of a selection of galaxies from the APOSTLE simulation project, whose H I properties reproduce well several relevant scaling relations. The characteristics of the synthetic observations are sufficiently similar to those of real observations from the THINGS and LITTLE THINGS surveys as to enable us to proceed with reconstructing their rotation curves via tilted ring modelling and conduct a meaningful comparison with the observed counterparts of our simulated galaxies. We find that the rotation curves obtained for our simulated galaxies depend sensitively on the orientation (at fixed inclination) of the line of nodes of the chosen projection with patterns in the non-circular motions within the gas discs. In particular, gas rotating slower than the average at a particular radius aligned along the major axis of the projection results in an underestimated rotation curve at that radius, and vice versa.

The signature of the relevant non-circular motions becomes much more difficult to discern once projection effects are taken into account. However, for two extreme examples of galaxies with slowly rising rotation curves, DDO 47 and DDO 87, we

show that the tell-tale pattern corresponding to an $m = 2$ bar-like perturbation in the azimuthal velocity field, oriented such as to cause an underestimate of the rotation curve, is present in the data.

All APOSTLE galaxies have central dark matter cusps. The non-circular motions in the gas discs in our simulations have a sufficient influence on the central rotation velocities as recovered by a tilted ring analysis to reproduce unaided the full scatter in central mass deficits highlighted by Oman et al. (2015), without appealing to any mechanism(s) creating dark matter cores.

We have shown that the cusp-core problem may be plausibly explained as an artifact of improperly modelled non-circular motions in the gas discs of galaxies. Put another way, we tentatively suggest that dark matter cores do not exist. Despite the apparent recent consensus that issues surrounding the treatment of non-circular motions in rotation curve modelling are sufficiently well understood to justify constructing relatively complicated models in order to explain the existence of slowly rising rotation curves, we contend that the impact of such non-circular motions on rotation curves is still routinely and severely underestimated. Whether this interpretation can be borne out in full detail remains to be seen.

Chapter 5

Conclusions

5.1 Prospects for the cusp-core problem

Twenty three years after it was posed, the cusp-core problem still stands. In the abstract of Chapter 2, I stated that 'one or more of the following statements must be true: (i) the dark matter is more complex than envisaged by any current model; (ii) current simulations fail to reproduce the effects of baryons on the inner regions of dwarf galaxies; and/or (iii) the mass profiles of 'inner mass deficit' galaxies inferred from kinematic data are incorrect'. Interpreted broadly, this is a perhaps disheartening statement. If the particle physics models, the numerical models and the kinematic models are all suspect, this seems to leave very little space to claim that anything about the problem, beyond its existence, is actually understood. This would, of course, be overlooking the tremendous effort invested in attempting to solve the problem, and the rich literature on the subject, but it begs a question. How should efforts be focussed to maximize the chance of at least narrowing the possible solution space of the cusp-core problem? I have a few thoughts, organized below by topic: simulations, particle physics, and observations.

5.1.1 Numerical galaxy formation models

It is an exciting time to be in the cosmological simulation game. The EAGLE and Illustris projects have revolutionized the field in the past two years by providing the first simultaneously hydrodynamical and cosmological galaxy formation models that produce sets of galaxies which not only seem 'realistic' when considered individually, but actually match at least some of the major scaling relations as a population. For

what is essentially a first attempt, the number of things the models get 'right' is, to be frank, incredible. Conversely, this is the first of what I'm sure will be many generations of similar simulations, and there is ample room for improvement.

Galaxies in the EAGLE and Illustris models all preserve their dark matter cusps, but there are other current and similarly sophisticated models which make galaxies with cores – the FIRE and NIHAO models, in particular, spring to mind. Taken individually, galaxies produced by these models can claim a degree of realism on par with the cuspy ones mentioned above. It is interesting that, at least at our current level of understanding, galaxy formation does not seem to care whether the end result should include a cusp or a core – broadly speaking, the individual galaxies look equally good in both scenarios.

One thing lacking at present from the models which produce cores are realizations of galaxy populations in cosmologically representative volumes. The models have enough freedom that both types – with cusps and with cores – will probably produce equally 'realistic' galaxy populations once the models are appropriately 'calibrated', at least at the level of detail of current comparisons. Still, eventually something must break the degeneracy and invalidate one type of model (or both), and population properties are an important constraint on the models.

'Baryon induced core formation' is only one of many proposed types of solutions to the cusp-core problem. This means that it is difficult to use observations to constrain the scenario directly: there are too many possible alternate interpretations of rotation curves and similar measurements, and all are uncertain. Instead, it may be easier to look to other features of the models. For instance, models which create dark matter cores apparently require very violent stellar feedback prescriptions. These must have testable consequences beyond only the creation of a dark matter core. Making and checking these types of predictions may provide an indirect means of supporting or ruling out the idea of baryon induced cores.

Models are adaptable. Simulations will probably always lack the dynamic range to resolve all scales relevant to galaxy formation, which means the models will always include calibrated prescriptions for some processes, lending them much flexibility to meet the demands of many constraints. The situation is especially dire in the context of the cusp-core problem, where there is still significant disagreement over what the constraint to be satisfied actually is. Understanding the rotation curve measurement, and its correct interpretation, is key.

5.1.2   The particle nature of dark matter

The question underlying the entire discussion around the cusp-core problem is 'what is dark matter?'. To be more optimistic, perhaps it should not be called a problem, but an opportunity – there is here a hint that we can learn something about the physics of dark matter. To be very optimistic: a satisfactory answer to the cusp-core question could help inform the design of an experiment to actually detect the dark matter particle(s).

On the practical side of things, it seems very difficult to make much progress on the cusp-core problem with proposed solutions rooted in the physics of dark matter. Currently, the most promising models in this context are those in which the dark matter can self-scatter. The simplest scenario has just two free parameters: the particle mass and the scattering cross section. It seems theoretically tractable to constrain such a simple model by measuring the density profiles of dark matter haloes, but I start to feel skeptical as soon as the model has any additional complexity, e.g. a velocity dependent scattering cross section. Actually implementing these models in galaxy formation simulations is an additional, and formidable, challenge.

The ability of cusp-core observations to constrain particle physics models is severely hampered by their quality. If the dark matter halo profile is determined by dark matter physics, rather than dynamical coupling to baryons, a useful initial assumption is that haloes of a given mass are similar (though there may be caveats, haloes of fixed mass have varying assembly histories, for instance). The scatter in the shape of halo profiles may then reasonably be expected to be small. As seen in Chapter 2, a large diversity is apparently measured, but is the scatter real, or only a symptom of systematic errors in modelling observations? The discussion in Chapter 4 suggests that systematic errors play a significant role. Until these errors are corrected, or at least understood, what the measurement relevant to particle physics models actually is remains too uncertain to be of much use. Once again: understanding the measurements is key.

5.1.3   Kinematic modelling of observations

As discussed above, it is very difficult to make progress with modelling when the measurements constraining the models are suspect. It is encouraging that the quality of the measurements themselves, i.e. the data cubes coming (primarily) from radio telescopes, now seem to be good enough for the job. However, the translation of a data

cube into a circular velocity curve – a dynamical mass profile – remains uncertain.

I think much of the current difficulty in reaching a consensus on what the data cubes are actually telling us about the centres of galaxies stems from stretching the tilted ring model well beyond its intended purpose: to trace the geometry of a warped, but otherwise undisturbed, thin disc. This is a blunt tool for the task at hand; I'd like to outline a few ways in which it might be sharpened, or perhaps rather set aside and replaced.

Following the analysis of Chapter 4, I think it is clear that an ideal kinematic model should explicitly encode departures from azimuthal symmetry. The presence of such asymmetries is glaringly obvious in the data, and conspicuously absent in most models. The cost of this will be, inevitably, an increase in the number of model parameters, a number which is already not small. To make the computational task even more daunting, it would also be desireable to fit all of the model parameters simultaneously, rather than independently at each radius. Currently, many parameters are treated as independent when they should be correlated; simultaneous fitting at least allows for explicit handling of correlations between any parameters. Given this, a revision of the error estimates is almost implied: simultaneous fitting would allow for much more meaningful statistical error estimates, including quantifying case-by-case the influence of parameter degeneracies.

In this alternative picture, the goal of the modelling could be, instead of a rotation curve, a simultaneous complete description of both the kinematics of the gas and the hydrodynamic forces acting on the gas at each measured position, inferred from the inputs: (i) incomplete kinematic and geometric information, i.e. a data cube, and (ii) additional observations to constrain as much as possible the thermodynamic state of the interstellar medium, and thus the hydrodynamic forces. Assuming, albeit probably incorrectly, an equilibrium system, the gravitational force, or potential, at each position can be extracted from the model, along with robust statistical uncertainties. The remaining step is then to quantify the systematic uncertainties. Techniques using 'realistic' simulated galaxies, such as comparing multiple orientations of the same galaxy as in Chapter 4, are especially useful in this context.

Implementing the ouline above would be no small undertaking. It represents a return to the drawing board in terms of how kinematic modelling is done. The most important aspect, I think, is the unambiguous characterization of the uncertainty in the measurement.

5.2 An explanation for the unexpected diversity of dwarf galaxy rotation curves

In Chapter 2 I proposed a new description of the cusp-core problem, quantified by the 'inner mass deficit' of galaxies. Compared to descriptions based on measuring the inner logarithmic slope of the dark matter density profile, this description sidesteps the need for many uncertain analysis steps while still demonstrating the problem clearly and unambiguously. This is possible primarily because the apparent problem is so severe that it is evident even if the dynamical contribution of the luminous component of galaxies is ignored, at least on the scale of dark matter dominated dwarfs. The problem cast this way appears as a large scatter in the rotation speed of dwarf galaxies which is unexpected in the standard cold dark matter cosmology.

In Chapter 3 I showed based on the ratio of dark and luminous matter measured out to galactic outskirts that, at least for some galaxies, the output of kinematic models is suspect. I cited inclination errors as plausible cause of the discrepancies. In hindsight, I think this conclusion is still basically correct, but armed with the additional insight afforded by the analysis presented in Chapter 4, the effects of non-circular motions should stand alongside inclination errors as a leading probable cause.

Finally, in Chapter 4 I showed that once a sample of simulated galaxies generated with a fully-featured model of galaxy formation, all of which have a dark matter cusp, are 'observed' and analyzed analogously to real galaxies, the full width of the scatter of the unexpectedly diverse rotation curves of dwarfs is reproduced. Many points remain to be followed up, but this is a convincing proof of concept for the idea that non-circular motions and departures from dynamical equilibrium are the source of at least a significant part of the diversity. Until the kinematic models are better understood, it is unclear which models of cosmology and galaxy formation best capture the central structure of galaxies.

APPENDICES

Appendix A

Observed Rotation Curve Compilation

Previously published as an appendix to Kyle A. Oman, Julio F. Navarro, Azadeh Fattahi, Carlos S. Frenk, Till Sawala, Simon D. M. White, Richard Bower, Robert A. Crain, Michelle Furlong, Matthieu Schaller, Joop Schaye, Tom Theuns; The unexpected diversity of dwarf galaxy rotation curves. *Mon Not R Astron Soc* 2015; 452 (4): 3650–3665.

Our sample of galaxy rotation curves is drawn from several sources. We describe each set of observations in Secs. A.1–A.10; the key properties of the individual rotation curves are summarized in Table A.1.

A.1 Kauffmann et al. (2015)

This publication presents 187 rotation curves for galaxies in the GALEX Arecibo Sloan Survey (GASS) with maximum rotation velocities of 90–$350 \, \mathrm{km \, s^{-1}}$. Long slit spectra were measured using the blue-channel spectrograph on the 6.5-m Multi Mirror Telescope and the Dual Imaging Spectrograph on the 3.5-m Apache Point Observatory telescope, with angular resolutions of 1.25 arcsec and 1.5 arcsec respectively. Though long slit spectroscopy offers excellent angular resolution, the main drawback is that the velocity field is measured only along one direction through the galaxy, making possible errors due to, for example, non-circular motions more difficult to quantify. For each spectrum, an attempt was made to produce two rotation curves: one derived from H α emission, and a second from fitting stellar absorption templates. The

stellar absorption based rotation curves are typically in good agreement with the H α curves, but of slightly better quality, so we use these where possible. Of the 187 rotation curves in the sample, we retain 106 in our compilation, the rest being of insufficient quality, resolution or extent for use in our analysis. Of these, 99 are stellar absorption based rotation curves (of which 52 also have good H α rotation curves, which we discard) and 7 are H α based. For brevity, we omit all discarded rotation curves from this source in Table A.1.

A.2 Oh et al. (2015)

This publication presents 26 rotation curves for galaxies in the Local Irregulars That Trace Luminosity Extremes, The H $\textsc{i}$ Nearby Galaxy Survey (LITTLE THINGS) sample. This observing program is closely related to the THINGS survey (see Sec. A.4). The maximum measured rotation velocities of these galaxies range from about 20 to 120 $\mathrm{km\,s^{-1}}$. Observations were taken using the NRAO Very Large Array. The angular resolution of 6 arcsec is a factor of 2 better than that of the THINGS survey. Radio interferometry leads naturally to 2-dimensional velocity maps. H $\textsc{i}$ observations are traditionally better than their optical (usually H α) counterparts at mapping the velocity field in the outskirts of galaxies at the cost of poorer spatial resolution throughout. The LITTLE THINGS sample offers a good compromise, with sufficient resolution to probe the inner kiloparsec. The rotation curves were constructed from the velocity fields using a tilted-ring model, with asymmetric drift corrections applied as needed. We retain all 26 galaxies in our sample.

A.3 Adams et al. (2014)

This publication presents a sample of 7 rotation curves of galaxies with maximum rotation velocities of about 100 $\mathrm{km\,s^{-1}}$. The velocity fields were measured with the VIRUS-W integral field spectrograph on the 2.7-m Harlan J. Smith telescope at McDonald Observatory. The use of an integral field unit (IFU) allows measurement of the velocity field in 2 dimensions, while maintaining the high spatial resolution typical of optical rotation curves: the fibres feeding the spectrograph have diameters of 3.1 arcsec. The velocity field is constructed by simultaneous mapping of the H β line and two O $\textsc{iii}$ lines. The rotation curves were constructed from the velocity fields using a tilted-ring model. We retain all 7 galaxies in our sample.

A.4 de Blok at al. (2008) and Oh et al. (2011)

These two publications are part of the THINGS project. The 19 rotation curves presented in de Blok et al. (2008) are those that are most straightforwardly derived, while seven of those requiring more careful analysis were presented in Oh et al. (2011) (in some cases reanalysing galaxies from de Blok et al., 2008). Maximum measured rotation velocities are 30–$300\,\mathrm{km\,s^{-1}}$. The survey was carried out with the NRAO Very Large Array in B, C and D configurations. The angular resolution of 12 arcsec is substantially better than that of most earlier H I rotation curve measurements. The rotation curves were constructed from the velocity fields using a tilted-ring model. Four galaxies from Oh et al. (2011) – Ho I, Ho II, M81dwB and DDO 53 – required substantial asymmetric drift corrections. We retain 15 of the 19 galaxies from de Blok et al. (2008), discarding three that were reanalyzed by Oh et al. (2011) and NGC 4826, which appears to have a counter-rotating disk component that complicates the interpretation. We discard Ho II (also named DDO 50), DDO 53, DDO 154 and NGC 2366 from the Oh et al. (2011) sample in favour of the higher angular resolution observations of Oh et al. (2015).

A.5 Reyes et al. (2011)

This publication presents a collection of 189 rotation curves with maximum rotation velocities of 100–$400\,\mathrm{km\,s^{-1}}$. All are long slit H α measurements, variously measured using the TWIN spectrograph on the 3.5-m telescope at Calar Alto Observatory (~ 1.5 arcsec resolution), the CCDS spectrograph on the 2.4-m Hiltner telescope at the MDM Observatory (~ 2 arcsec resolution), and the Dual Imaging Spectrograph on the 3.5-m telescope at Apache Point Observatory (~ 1.5 arcsec resolution). We were not able to obtain the full rotation curve dataset, but use instead the parameters of an arctangent model fit (Courteau, 1997) to the rotation curves to estimate the rotation velocity at $2\,\mathrm{kpc}$ and at maximum (the asymptotic value of the model). We retain all 189 rotation curves in our sample, but use an open symbol type in Fig. 2.7 to visually separate these data from the other sources in our compilation for which we have full rotation curves.

A.6 Kuzio de Naray et al. (2008)

This publication presents rotation curves for a selection of 17 galaxies with maximum rotation velocities of 50–100 km s^{-1}. These were measured with the DensePak IFU on the 3.5-m WIYN telescope at the Kitt Peak National Observatory. The instrument has a pixel size of 3 arcsec, and multiple slightly offset exposures of the same region were taken to improve the resolution of the rotation curves to $\sim$ 2 arcsec. The rotation curves were constructed from the velocity fields using a tilted-ring model. No correction for asymmetric drift was applied as the correction is expected to be < 2 km s^{-1} in all cases. We retain 15 galaxies in our sample, discarding UGC 4325 (alternate name NGC 2552) and NGC 959 in favour of more recent observations.

A.7 de Blok et al. (2004)

This publication presents a single, very high resolution rotation curve. Discounting the satellites of the Milky Way, NGC 6822 is the nearest late-type dwarf galaxy to us, at a distance of less than 500 kpc. This allows for a high spatial resolution ($\sim$ 20 pc) H I map even with the modest 8 arcsec angular resolution of the Australia Telescope Compact Array.

A.8 Swaters et al. (2003)

This publication presents 15 rotation curves with maximum measured rotation velocities of about 100–150 km s^{-1}. The double spectrograph on the 200-inch Hale telescope at Mount Palomar Observatory was used to obtain long-slit H α spectra along the major axis of each galaxy. The spectra have a nominal resolution of 0.5 arcsec but, in practice, are limited by seeing of $\sim$ 1–2 arcsec. The galaxies targetted also had existing H I maps, which were used to extend the H α curves to larger radii. We retain 4 galaxies in our sample, discarding UGC 731 that has a counter-rotating component, and UGC 8490, UGC 5721, UGC 4499, UGC 4325, UGC 2259, UGC 11861, UGC 11707, UGC 11557, LSB F568-3 and LSB F563-V2 in favour of more recent observations of the same galaxies.

A.9   de Blok & Bosma (2002)

This publication presents 24 rotation curves of galaxies with maximum measured rotation velocities of about 50–$100 \, \mathrm{km \, s^{-1}}$. Long slit H α spectra were measured using the Carelec spectrograph on the $192 \, \mathrm{cm}$ telescope at the Observatoire de Haute Provence. The angular resolution is seeing-limited to ~ 2 arcsec. These data are supplemented with lower resolution H I velocity maps for all but two of the galaxies, allowing the extension of the rotation curves to larger radii. We exclude UGC 5750, UGC 4325, UGC 1281, UGC 10310, NGC 4395, NGC 3274, NGC 2366, LSB F563-1 and DDO 64 from our sample in favour of more recent observations, retaining 15 galaxies.

A.10   de Blok et al. (2001)

This paper presents 26 rotation curves of galaxies with maximum measured rotation velocities between 40 and 200$\mathrm{km \, s^{-1}}$. The 4-m Kitt Peak and 100-in Las Campanas telescopes were used to obtain long slit H α spectra. The resolution is seeing-limited to ~ 1.5 arcsec. Where available, H I velocity maps supplement the H α data, extending the rotation curves to larger radii. We exclude UGC 5750, UGC 11557, LSB F583-4, LSB F583-1, LSB F568-3 and LSB F563-1 from our sample in favour of more recent observations, retaining 20 rotation curves.

Table A.1: Basic properties of galaxies in our sample. Galaxy names and distances are those used in the publication cited. The observation type specifies the spectral feature(s) used to construct the rotation curve. Resolutions assume the distance in column 3, based on angular resolution as quoted by the cited publication. $V_{\mathrm{circ}}(2\ \mathrm{kpc})$ and V_{max} are the quantities plotted in Fig. 2.7. Explanation of notes: (1) stellar absorption-derived rotation curve preferred to H α-derived rotation curve (see Sec. A.1); (2) galaxy excluded from our sample in favour of a more recent observation; (3) excluded due to a counter-rotating component in the rotation curve.

Galaxy	Reference	Distance (Mpc)	Observation type	Observation resolution (kpc)	$V_{\mathrm{circ}}(2\mathrm{kpc})$ ($\mathrm{km\,s^{-1}}$)	V_{max} ($\mathrm{km\,s^{-1}}$)	Notes
GASS 9891	Kauffmann et al. (2015)	110.5	stellar abs.	0.8	122.3	≥ 353.0	(1)
GASS 9463	Kauffmann et al. (2015)	152.5	H α	1.1	127.6	≥ 239.9	—
GASS 8096	Kauffmann et al. (2015)	147.8	stellar abs.	0.9	122.7	≥ 187.4	(1)
GASS 7286	Kauffmann et al. (2015)	115.2	stellar abs.	0.7	85.3	141.2	(1)
GASS 7031	Kauffmann et al. (2015)	141.8	stellar abs.	0.9	99.7	171.2	—
GASS 6583	Kauffmann et al. (2015)	206.9	stellar abs.	1.2	88.3	≥ 152.9	—
GASS 57017	Kauffmann et al. (2015)	138.3	H α	1.0	96.2	≥ 178.0	—
GASS 56612	Kauffmann et al. (2015)	124.2	stellar abs.	0.7	128.6	≥ 156.6	—
GASS 52297	Kauffmann et al. (2015)	140.5	stellar abs.	0.8	84.1	≥ 116.5	—
GASS 51899	Kauffmann et al. (2015)	165.7	stellar abs.	1.0	93.9	139.8	(1)
GASS 51416	Kauffmann et al. (2015)	190.6	stellar abs.	1.1	77.8	118.3	—
GASS 51351	Kauffmann et al. (2015)	125.5	stellar abs.	0.9	240.1	280.0	(1)
GASS 48356	Kauffmann et al. (2015)	122.9	stellar abs.	0.9	124.4	139.0	(1)
GASS 47221	Kauffmann et al. (2015)	136.2	stellar abs.	0.8	77.0	≥ 140.4	(1)
GASS 42402	Kauffmann et al. (2015)	197.0	stellar abs.	1.2	66.0	≥ 259.1	—

Continued on next page.

Galaxy	Reference	Distance (Mpc)	Observation type	Observation resolution (kpc)	$V_{\text{circ}}(\text{2kpc})$ (km s^{-1})	V_{max} (km s^{-1})	Notes
GASS 42141	Kauffmann et al. (2015)	154.2	stellar abs.	1.1	55.6	214.1	–
GASS 42140	Kauffmann et al. (2015)	195.7	stellar abs.	1.2	89.2	$\geq$ 240.9	–
GASS 42025	Kauffmann et al. (2015)	157.2	stellar abs.	0.9	86.1	$\geq$ 224.3	(1)
GASS 41783	Kauffmann et al. (2015)	158.9	stellar abs.	1.1	177.4	254.3	(1)
GASS 4137	Kauffmann et al. (2015)	190.6	stellar abs.	1.1	66.5	$\geq$ 127.3	–
GASS 41323	Kauffmann et al. (2015)	188.4	stellar abs.	1.1	41.3	96.4	–
GASS 4130	Kauffmann et al. (2015)	191.9	stellar abs.	1.4	102.8	233.8	–
GASS 4094	Kauffmann et al. (2015)	118.2	stellar abs.	0.7	116.4	193.3	–
GASS 4057	Kauffmann et al. (2015)	170.0	stellar abs.	1.0	138.9	$\geq$ 192.0	–
GASS 4048	Kauffmann et al. (2015)	177.3	stellar abs.	1.1	100.3	$\geq$ 182.1	(1)
GASS 4040	Kauffmann et al. (2015)	115.2	stellar abs.	0.7	122.7	140.6	–
GASS 4038	Kauffmann et al. (2015)	178.6	stellar abs.	1.1	71.5	$\geq$ 248.4	(1)
GASS 40317	Kauffmann et al. (2015)	174.7	stellar abs.	1.0	153.8	195.4	(1)
GASS 40257	Kauffmann et al. (2015)	168.3	stellar abs.	1.0	75.3	$\geq$ 150.0	–
GASS 40247	Kauffmann et al. (2015)	167.9	stellar abs.	1.2	162.6	267.4	–
GASS 3971	Kauffmann et al. (2015)	182.4	stellar abs.	1.3	106.8	228.4	(1)
GASS 39595	Kauffmann et al. (2015)	186.3	stellar abs.	1.1	182.0	$\geq$ 208.0	(1)
GASS 39567	Kauffmann et al. (2015)	133.6	stellar abs.	0.8	145.4	$\geq$ 182.9	(1)
GASS 38964	Kauffmann et al. (2015)	137.9	stellar abs.	1.0	110.2	297.9	(1)
GASS 38758	Kauffmann et al. (2015)	124.6	stellar abs.	0.9	132.9	233.7	(1)
GASS 38472	Kauffmann et al. (2015)	113.1	stellar abs.	0.7	89.7	139.1	–

Galaxy	Reference	Distance (Mpc)	Observation type	Observation resolution (kpc)	V_{circ}(2kpc) (km s^{-1})	V_{max} (km s^{-1})	Notes
GASS 3819	Kauffmann et al. (2015)	194.0	stellar abs.	1.2	60.6	86.3	(1)
GASS 3817	Kauffmann et al. (2015)	192.7	stellar abs.	1.2	71.8	$\geq$ 114.3	(1)
GASS 3777	Kauffmann et al. (2015)	169.6	stellar abs.	1.0	107.8	$\geq$ 134.1	(1)
GASS 3645	Kauffmann et al. (2015)	131.5	stellar abs.	0.8	115.2	211.9	(1)
GASS 3524	Kauffmann et al. (2015)	162.7	stellar abs.	1.0	114.1	237.9	(1)
GASS 3524	Kauffmann et al. (2015)	162.7	H α	1.0	122.4	$\geq$ 199.9	—
GASS 3509	Kauffmann et al. (2015)	207.3	stellar abs.	1.2	187.4	244.8	(1)
GASS 3439	Kauffmann et al. (2015)	165.3	stellar abs.	1.0	113.0	158.3	—
GASS 3261	Kauffmann et al. (2015)	160.6	stellar abs.	1.0	39.5	$\geq$ 58.2	—
GASS 3189	Kauffmann et al. (2015)	164.5	H α	1.0	54.7	$\geq$ 168.3	—
GASS 30811	Kauffmann et al. (2015)	209.4	stellar abs.	1.3	103.4	$\geq$ 316.1	—
GASS 30479	Kauffmann et al. (2015)	131.9	stellar abs.	0.8	121.1	$\geq$ 137.8	(1)
GASS 30338	Kauffmann et al. (2015)	179.0	stellar abs.	1.1	134.1	$\geq$ 227.4	(1)
GASS 29892	Kauffmann et al. (2015)	156.7	stellar abs.	0.9	118.1	268.5	(1)
GASS 29842	Kauffmann et al. (2015)	146.0	stellar abs.	1.1	138.0	215.3	(1)
GASS 29555	Kauffmann et al. (2015)	135.3	stellar abs.	0.8	44.2	$\geq$ 97.1	(1)
GASS 27167	Kauffmann et al. (2015)	162.7	stellar abs.	1.0	134.6	175.1	(1)
GASS 26822	Kauffmann et al. (2015)	161.0	stellar abs.	1.2	97.2	206.0	(1)
GASS 25214	Kauffmann et al. (2015)	133.2	stellar abs.	0.8	46.8	86.4	—
GASS 24496	Kauffmann et al. (2015)	180.3	stellar abs.	1.1	121.2	$\geq$ 198.2	(1)
GASS 24366	Kauffmann et al. (2015)	176.0	stellar abs.	1.1	123.7	$\geq$ 191.7	—

Continued on next page.

Galaxy	Reference	Distance (Mpc)	Observation type	Observation resolution (kpc)	$V_{\mathrm{circ}}(2\mathrm{kpc})$ (km s^{-1})	$V_{\max}$ (km s^{-1})	Notes
GASS 24168	Kauffmann et al. (2015)	111.4	stellar abs.	0.7	86.3	≥ 240.5	(1)
GASS 24094	Kauffmann et al. (2015)	184.6	stellar abs.	1.1	149.5	≥ 183.1	–
GASS 23450	Kauffmann et al. (2015)	203.9	stellar abs.	1.2	92.9	207.5	–
GASS 23315	Kauffmann et al. (2015)	140.9	stellar abs.	0.8	101.0	≥ 133.6	(1)
GASS 22999	Kauffmann et al. (2015)	194.9	stellar abs.	1.2	63.5	≥ 218.1	(1)
GASS 21842	Kauffmann et al. (2015)	192.7	stellar abs.	1.2	100.7	227.4	–
GASS 20292	Kauffmann et al. (2015)	128.1	stellar abs.	0.8	93.7	166.6	–
GASS 20133	Kauffmann et al. (2015)	209.4	stellar abs.	1.3	73.1	≥ 151.5	–
GASS 20041	Kauffmann et al. (2015)	132.3	stellar abs.	0.8	55.4	≥ 109.4	(1)
GASS 18900	Kauffmann et al. (2015)	194.0	stellar abs.	1.2	151.0	≥ 241.4	–
GASS 18335	Kauffmann et al. (2015)	184.6	stellar abs.	1.1	111.5	≥ 281.8	–
GASS 17684	Kauffmann et al. (2015)	154.6	stellar abs.	0.9	91.1	≥ 256.2	(1)
GASS 17640	Kauffmann et al. (2015)	149.5	stellar abs.	0.9	39.8	≥ 153.1	–
GASS 15257	Kauffmann et al. (2015)	123.3	stellar abs.	0.7	59.8	≥ 75.4	–
GASS 15181	Kauffmann et al. (2015)	200.4	stellar abs.	1.2	74.5	≥ 219.8	–
GASS 14831	Kauffmann et al. (2015)	190.2	stellar abs.	1.1	77.2	265.2	(1)
GASS 14247	Kauffmann et al. (2015)	141.3	stellar abs.	1.0	75.8	≥ 318.3	–
GASS 14017	Kauffmann et al. (2015)	169.6	stellar abs.	1.0	129.3	≥ 207.2	–
GASS 12460	Kauffmann et al. (2015)	211.6	stellar abs.	1.3	136.9	≥ 343.4	(1)
GASS 12069	Kauffmann et al. (2015)	166.2	stellar abs.	1.2	86.3	≥ 138.6	(1)
GASS 12002	Kauffmann et al. (2015)	157.2	stellar abs.	0.9	142.7	208.3	–

Continued on next page.

Galaxy	Reference	Distance (Mpc)	Observation type	Observation resolution (kpc)	$V_{\mathrm{circ}}(2\mathrm{kpc})$ ($\mathrm{km\,s^{-1}}$)	V_{max} ($\mathrm{km\,s^{-1}}$)	Notes
GASS 11956	Kauffmann et al. (2015)	169.2	stellar abs.	1.0	81.1	≥ 176.6	(1)
GASS 11845	Kauffmann et al. (2015)	155.5	stellar abs.	1.1	95.7	167.9	(1)
GASS 11824	Kauffmann et al. (2015)	162.7	H α	1.0	72.2	≥ 196.7	–
GASS 11808	Kauffmann et al. (2015)	205.1	stellar abs.	1.2	122.3	≥ 194.9	–
GASS 11514	Kauffmann et al. (2015)	183.3	stellar abs.	1.1	106.0	164.9	(1)
GASS 11437	Kauffmann et al. (2015)	113.1	stellar abs.	0.7	83.6	≥ 183.0	(1)
GASS 11386	Kauffmann et al. (2015)	197.9	stellar abs.	1.2	96.3	148.1	–
GASS 11349	Kauffmann et al. (2015)	109.6	stellar abs.	0.7	98.5	≥ 144.0	(1)
GASS 11270	Kauffmann et al. (2015)	169.2	H α	1.0	50.6	54.5	–
GASS 11223	Kauffmann et al. (2015)	152.0	stellar abs.	1.1	117.5	≥ 184.3	–
GASS 11120	Kauffmann et al. (2015)	116.1	stellar abs.	0.8	165.7	≥ 197.8	(1)
GASS 11087	Kauffmann et al. (2015)	161.0	stellar abs.	1.0	116.1	191.8	(1)
GASS 11019	Kauffmann et al. (2015)	154.2	stellar abs.	0.9	87.6	≥ 133.4	(1)
GASS 10949	Kauffmann et al. (2015)	112.2	stellar abs.	0.7	94.1	144.1	–
GASS 10948	Kauffmann et al. (2015)	110.5	stellar abs.	0.7	96.2	≥ 142.5	(1)
GASS 10943	Kauffmann et al. (2015)	117.8	stellar abs.	0.7	105.7	152.3	(1)
GASS 10942	Kauffmann et al. (2015)	107.5	stellar abs.	0.6	42.0	≥ 101.4	–
GASS 10884	Kauffmann et al. (2015)	110.1	stellar abs.	0.7	93.6	171.1	(1)
GASS 10850	Kauffmann et al. (2015)	152.0	stellar abs.	0.9	114.2	≥ 204.7	(1)
GASS 10841	Kauffmann et al. (2015)	115.6	stellar abs.	0.7	165.9	166.0	–
GASS 10831	Kauffmann et al. (2015)	116.9	H α	0.7	127.1	158.9	–

Continued on next page.

Galaxy	Reference	Distance (Mpc)	Observation type	Observation resolution (kpc)	$V_{\mathrm{circ}}(2\mathrm{kpc})$ (km s^{-1})	V_{max} (km s^{-1})	Notes
GASS 10827	Kauffmann et al. (2015)	128.9	stellar abs.	0.8	108.5	≥ 166.2	–
GASS 10813	Kauffmann et al. (2015)	114.8	stellar abs.	0.7	117.6	149.5	–
GASS 10447	Kauffmann et al. (2015)	201.7	stellar abs.	1.2	57.1	≥ 127.2	–
GASS 10404	Kauffmann et al. (2015)	154.6	stellar abs.	0.9	110.2	≥ 166.0	–
GASS 10358	Kauffmann et al. (2015)	158.5	stellar abs.	1.0	52.2	≥ 133.3	–
GASS 10218	Kauffmann et al. (2015)	198.7	stellar abs.	1.2	81.2	≥ 117.5	(1)
GASS 10019	Kauffmann et al. (2015)	131.9	stellar abs.	0.8	117.2	≥ 177.2	(1)
WLM	Oh et al. (2015)	1.0	H I	< 0.1	35.1	38.5	–
UGC 8508	Oh et al. (2015)	2.6	H I	0.1	46.1	≥ 46.1	–
NGC 3738	Oh et al. (2015)	4.9	H I	0.1	125.6	≥ 132.7	–
NGC 2366	Oh et al. (2015)	3.4	H I	0.1	41.9	59.8	–
NGC 1569	Oh et al. (2015)	3.4	H I	0.1	36.6	39.3	–
LSB F564-V3	Oh et al. (2015)	8.7	H I	0.3	38.7	39.2	–
IC 1613	Oh et al. (2015)	0.7	H I	< 0.1	20.5	21.1	–
IC 10	Oh et al. (2015)	0.7	H I	< 0.1	–	≥ 36.4	–
Haro 36	Oh et al. (2015)	9.3	H I	0.3	37.6	≥ 58.2	–
Haro 29	Oh et al. (2015)	5.9	H I	0.2	34.4	43.5	–
DDO 87	Oh et al. (2015)	7.7	H I	0.2	28.0	≥ 56.6	–
DDO 70	Oh et al. (2015)	1.3	H I	< 0.1	43.9	≥ 43.9	–
DDO 53	Oh et al. (2015)	3.6	H I	0.1	29.2	≥ 32.0	–
DDO 52	Oh et al. (2015)	10.3	H I	0.3	42.6	≥ 61.7	–

Galaxy	Reference	Distance (Mpc)	Observation type	Observation resolution (kpc)	$V_{\text{circ}}(2\text{kpc})$ (km s^{-1})	V_{max} (km s^{-1})	Notes
DDO 50	Oh et al. (2015)	3.4	H I	0.1	31.2	38.8	–
DDO 47	Oh et al. (2015)	5.2	H I	0.1	23.7	≥ 64.7	–
DDO 46	Oh et al. (2015)	6.1	H I	0.2	73.2	76.3	–
DDO 43	Oh et al. (2015)	7.8	H I	0.2	31.5	≥ 38.3	–
DDO 216	Oh et al. (2015)	1.1	H I	< 0.1	18.9	≥ 18.9	–
DDO 210	Oh et al. (2015)	0.9	H I	< 0.1	–	≥ 12.0	–
DDO 168	Oh et al. (2015)	4.3	H I	0.1	57.5	61.9	–
DDO 154	Oh et al. (2015)	3.7	H I	0.1	35.8	≥ 51.1	–
DDO 133	Oh et al. (2015)	3.5	H I	0.1	41.6	46.7	–
DDO 126	Oh et al. (2015)	4.9	H I	0.1	30.7	38.7	–
DDO 101	Oh et al. (2015)	6.4	H I	0.2	63.3	≥ 64.9	–
CVnIdwA	Oh et al. (2015)	3.6	H I	0.1	25.9	26.4	–
UGC 2259	Adams et al. (2014)	9.9	H β+O III	0.1	74.0	≥ 93.4	–
UGC 11707	Adams et al. (2014)	15.0	H β+O III	0.2	51.6	≥ 103.7	–
NGC 959	Adams et al. (2014)	9.9	H β+O III	0.1	78.6	≥ 84.1	–
NGC 5949	Adams et al. (2014)	14.3	H β+O III	0.2	92.2	≥ 111.2	–
NGC 5204	Adams et al. (2014)	3.2	H β+O III	< 0.1	83.2	≥ 89.4	–
NGC 2976	Adams et al. (2014)	3.6	H β+O III	0.1	74.8	≥ 76.8	–
NGC 2552	Adams et al. (2014)	11.4	H β+O III	0.2	57.9	≥ 96.1	–
NGC 2366	Oh et al. (2011)	3.4	H I	0.2	43.2	≥ 66.7	(2)
M81 dw B	Oh et al. (2011)	5.3	H I	0.3	31.6	≥ 39.5	–

Continued on next page.

Galaxy	Reference	Distance (Mpc)	Observation type	Observation resolution (kpc)	V_{circ}(2kpc) (km s^{-1})	V_{max} (km s^{-1})	Notes
IC 2574	Oh et al. (2011)	4.0	H I	0.2	24.5	80.0	–
Ho II	Oh et al. (2011)	3.4	H I	0.2	27.9	37.5	(2)
Ho I	Oh et al. (2011)	3.8	H I	0.2	28.3	37.2	–
DDO 53	Oh et al. (2011)	3.6	H I	0.2	32.4	32.5	(2)
DDO 154	Oh et al. (2011)	4.3	H I	0.2	34.5	≥ 50.0	(2)
UGC 5750	Kuzio de Naray et al. (2008)	56.1	H α	0.5	19.0	≥ 73.4	–
UGC 477	Kuzio de Naray et al. (2008)	35.5	H α	0.3	41.3	≥ 111.7	–
UGC 4325	Kuzio de Naray et al. (2008)	10.1	H α	0.1	82.4	≥ 110.7	(2)
UGC 191	Kuzio de Naray et al. (2008)	17.6	H α	0.2	78.0	≥ 97.2	–
UGC 1551	Kuzio de Naray et al. (2008)	20.2	H α	0.2	42.4	≥ 82.5	–
UGC 1281	Kuzio de Naray et al. (2008)	5.5	H α	0.1	37.8	≥ 45.8	–
UGC 128	Kuzio de Naray et al. (2008)	60.0	H α	0.6	46.1	144.9	–
UGC 11820	Kuzio de Naray et al. (2008)	13.3	H α	0.1	80.1	96.9	–
NGC 959	Kuzio de Naray et al. (2008)	7.8	H α	0.1	76.7	79.2	(2)
NGC 7137	Kuzio de Naray et al. (2008)	22.5	H α	0.2	53.4	≥ 71.6	–
NGC 4395	Kuzio de Naray et al. (2008)	3.5	H α	< 0.1	–	≥ 32.7	–
LSB F583-4	Kuzio de Naray et al. (2008)	49.0	H α	0.5	42.1	≥ 95.8	–
LSB F583-1	Kuzio de Naray et al. (2008)	32.0	H α	0.3	42.0	≥ 72.4	–
LSB F568-3	Kuzio de Naray et al. (2008)	77.0	H α	0.7	41.4	≥ 114.3	–
LSB F563-V2	Kuzio de Naray et al. (2008)	61.0	H α	0.6	52.9	≥ 103.8	–
LSB F563-1	Kuzio de Naray et al. (2008)	45.0	H α	0.4	51.7	≥ 146.4	–

Galaxy	Reference	Distance (Mpc)	Observation type	Observation resolution (kpc)	$V_{\text{circ}}(2\text{kpc})$ (km s^{-1})	V_{max} (km s^{-1})	Notes
DDO 64	Kuzio de Naray et al. (2008)	6.1	H α	0.1	59.8	≥ 59.8	–
NGC 925	de Blok et al. (2008)	9.2	H I	0.5	34.7	≥ 119.9	–
NGC 7793	de Blok et al. (2008)	3.9	H I	0.2	76.2	117.9	–
NGC 7331	de Blok et al. (2008)	14.7	H I	0.8	253.2	268.1	–
NGC 6946	de Blok et al. (2008)	5.9	H I	0.3	132.5	224.3	–
NGC 5055	de Blok et al. (2008)	10.1	H I	0.6	185.3	211.6	–
NGC 4826	de Blok et al. (2008)	7.5	H I	0.4	-166.7	180.2	(3)
NGC 4736	de Blok et al. (2008)	4.7	H I	0.3	168.7	198.3	–
NGC 3627	de Blok et al. (2008)	9.3	H I	0.5	178.0	207.1	–
NGC 3621	de Blok et al. (2008)	6.6	H I	0.4	102.9	≥ 159.2	–
NGC 3521	de Blok et al. (2008)	10.7	H I	0.6	192.1	233.4	–
NGC 3198	de Blok et al. (2008)	13.8	H I	0.8	76.7	158.7	–
NGC 3031	de Blok et al. (2008)	3.6	H I	0.2	242.2	259.8	–
NGC 2976	de Blok et al. (2008)	3.6	H I	0.2	75.0	≥ 86.2	(2)
NGC 2903	de Blok et al. (2008)	8.9	H I	0.5	120.1	215.5	–
NGC 2841	de Blok et al. (2008)	14.1	H I	0.8	–	323.9	–
NGC 2403	de Blok et al. (2008)	3.2	H I	0.2	97.4	143.9	–
NGC 2366	de Blok et al. (2008)	3.4	H I	0.2	43.2	≥ 66.7	(2)
IC 2574	de Blok et al. (2008)	4.0	H I	0.2	20.6	≥ 78.5	(2)
DDO 154	de Blok et al. (2008)	4.3	H I	0.2	34.5	≥ 50.0	(2)
NGC 6822	de Blok et al. (2004)	0.5	H I	< 0.1	41.8	≥ 56.3	–

Galaxy	Reference	Distance (Mpc)	Observation type	Observation resolution (kpc)	$V_{\mathrm{circ}}(2\mathrm{kpc})$ (km s^{-1})	V_{max} (km s^{-1})	Notes
UGC 8490	Swaters et al. (2003)	20.5	H I+H α	0.1	30.0	80.1	(2)
UGC 731	Swaters et al. (2003)	8.0	H I+H α	< 0.1	61.5	≥ 74.0	(3)
UGC 5721	Swaters et al. (2003)	6.7	H I+H α	< 0.1	76.2	80.4	(2)
UGC 4499	Swaters et al. (2003)	13.0	H I+H α	0.1	46.2	≥ 74.2	(2)
UGC 4325	Swaters et al. (2003)	10.1	H I+H α	0.1	77.0	104.6	(2)
UGC 2259	Swaters et al. (2003)	9.8	H I+H α	0.1	78.8	93.7	(2)
UGC 12732	Swaters et al. (2003)	13.2	H I+H α	0.1	45.8	≥ 98.0	–
UGC 11861	Swaters et al. (2003)	25.1	H I+H α	0.1	80.4	164.0	(2)
UGC 11707	Swaters et al. (2003)	15.9	H I+H α	0.1	51.3	≥ 99.9	(2)
UGC 11557	Swaters et al. (2003)	23.8	H I+H α	0.1	35.1	≥ 84.5	(2)
LSB F574-1	Swaters et al. (2003)	96.0	H I+H α	0.5	57.9	≥ 104.2	–
LSB F568-V1	Swaters et al. (2003)	80.0	H I+H α	0.4	67.0	124.9	–
LSB F568-3	Swaters et al. (2003)	77.0	H I+H α	0.4	32.5	111.2	(2)
LSB F568-1	Swaters et al. (2003)	85.0	H I+H α	0.4	67.9	≥ 130.7	–
LSB F563-V2	Swaters et al. (2003)	61.0	H I+H α	0.3	87.7	≥ 113.1	(2)
UGC 711	de Blok & Bosma (2002)	26.4	H α	0.3	27.8	≥ 91.6	–
UGC 5750	de Blok & Bosma (2002)	56.0	H I+H α	0.5	20.0	≥ 49.6	(2)
UGC 5005	de Blok & Bosma (2002)	52.0	H I+H α	0.5	29.6	≥ 100.0	–
UGC 4325	de Blok & Bosma (2002)	10.1	H I+H α	0.1	73.8	≥ 122.6	(2)
UGC 4173	de Blok & Bosma (2002)	16.8	H I+H α	0.2	22.8	≥ 57.0	–
UGC 3371	de Blok & Bosma (2002)	12.8	H I+H α	0.1	33.9	≥ 85.7	–

Continued on next page.

Galaxy	Reference	Distance (Mpc)	Observation type	Observation resolution (kpc)	$V_{\mathrm{circ}}(2\mathrm{kpc})$ $(\mathrm{km\,s^{-1}})$	V_{max} $(\mathrm{km\,s^{-1}})$	Notes
UGC 3137	de Blok & Bosma (2002)	18.4	H I+H α	0.2	45.6	106.9	–
UGC 1281	de Blok & Bosma (2002)	5.5	H I+H α	0.1	37.7	≥ 56.9	(2)
UGC 1230	de Blok & Bosma (2002)	51.0	H I+H α	0.5	50.5	112.7	–
UGC 10310	de Blok & Bosma (2002)	15.6	H I+H α	0.1	38.9	≥ 75.0	(2)
NGC 5023	de Blok & Bosma (2002)	4.8	H I+H α	< 0.1	64.9	≥ 84.4	–
NGC 4455	de Blok & Bosma (2002)	6.8	H I+H α	0.1	44.9	≥ 64.4	–
NGC 4395	de Blok & Bosma (2002)	3.5	H I+H α	< 0.1	57.0	≥ 84.2	(2)
NGC 3274	de Blok & Bosma (2002)	6.7	H I+H α	0.1	82.5	82.6	(2)
NGC 2366	de Blok & Bosma (2002)	3.4	H I+H α	< 0.1	54.0	55.5	(2)
NGC 1560	de Blok & Bosma (2002)	3.0	H I+H α	< 0.1	42.6	≥ 77.5	–
NGC 100	de Blok & Bosma (2002)	11.2	H α	0.1	60.0	≥ 91.2	–
LSB F563-1	de Blok & Bosma (2002)	45.0	H I+H α	0.4	57.1	≥ 114.1	(2)
IC 2233	de Blok & Bosma (2002)	10.5	H I+H α	0.1	40.8	≥ 92.8	–
DDO 64	de Blok & Bosma (2002)	6.1	H I+H α	0.1	46.3	≥ 46.9	(2)
DDO 52	de Blok & Bosma (2002)	5.3	H I+H α	0.1	43.1	≥ 50.0	(2)
DDO 47	de Blok & Bosma (2002)	4.0	H I+H α	< 0.1	44.0	≥ 67.0	(2)
DDO 189	de Blok & Bosma (2002)	12.6	H I+H α	0.1	47.6	≥ 65.7	–
DDO 185	de Blok & Bosma (2002)	5.1	H I+H α	< 0.1	43.3	≥ 49.6	–
UGC 6614	de Blok et al. (2001)	85.0	H α	0.6	120.2	≥ 205.2	–
UGC 5750	de Blok et al. (2001)	56.0	H α	0.4	23.2	≥ 78.9	(2)
UGC 4115	de Blok et al. (2001)	3.2	H I+H α	< 0.1	–	≥ 39.8	–

Galaxy	Reference	Distance (Mpc)	Observation type	Observation resolution (kpc)	$V_{\mathrm{circ}}(2\mathrm{kpc})$ (km s^{-1})	$V_{\max}$ (km s^{-1})	Notes
UGC 11819	de Blok et al. (2001)	60.0	H I+H α	0.4	73.0	$\geq$ 154.7	–
UGC 11748	de Blok et al. (2001)	73.0	H I+H α	0.5	198.9	250.0	–
UGC 11648	de Blok et al. (2001)	48.0	H I+H α	0.3	74.3	$\geq$ 144.6	–
UGC 11616	de Blok et al. (2001)	73.0	H I+H α	0.5	87.8	$\geq$ 142.8	–
UGC 11583	de Blok et al. (2001)	5.0	H I+H α	< 0.1	35.6	$\geq$ 35.6	–
UGC 11557	de Blok et al. (2001)	22.0	H I+H α	0.2	34.5	$\geq$ 80.4	(2)
UGC 11454	de Blok et al. (2001)	91.0	H I+H α	0.7	85.8	$\geq$ 152.2	–
LSB F730-V1	de Blok et al. (2001)	144.0	H α	1.0	87.3	$\geq$ 145.3	–
LSB F583-4	de Blok et al. (2001)	49.0	H I+H α	0.4	44.5	$\geq$ 69.9	(2)
LSB F583-1	de Blok et al. (2001)	32.0	H I+H α	0.2	40.7	$\geq$ 86.9	(2)
LSB F579-V1	de Blok et al. (2001)	85.0	H I+H α	0.6	93.5	$\geq$ 114.4	–
LSB F571-8	de Blok et al. (2001)	48.0	H I+H α	0.3	68.1	$\geq$ 143.9	–
LSB F568-3	de Blok et al. (2001)	77.0	H I+H α	0.6	41.0	$\geq$ 101.1	(2)
LSB F563-1	de Blok et al. (2001)	23.6	H I+H α	0.2	84.0	112.4	(2)
ESO 4880490	de Blok et al. (2001)	22.0	H α	0.2	62.3	$\geq$ 97.1	–
ESO 4250180	de Blok et al. (2001)	86.0	H α	0.6	–	$\geq$ 144.5	–
ESO 3050090	de Blok et al. (2001)	11.0	H α	0.1	34.6	$\geq$ 54.6	–
ESO 3020120	de Blok et al. (2001)	69.0	H α	0.5	48.3	$\geq$ 86.3	–
ESO 2060140	de Blok et al. (2001)	60.0	H α	0.4	83.6	$\geq$ 118.0	–
ESO 1870510	de Blok et al. (2001)	18.0	H α	0.1	36.3	$\geq$ 39.9	–
ESO 1200211	de Blok et al. (2001)	15.0	H α	0.1	21.8	$\geq$ 25.4	–

Galaxy	Reference	Distance (Mpc)	Observation type	Observation resolution (kpc)	$V_{\mathrm{circ}}(2\mathrm{kpc})$ $(\mathrm{km\,s^{-1}})$	V_{max} $(\mathrm{km\,s^{-1}})$	Notes
ESO 0840411	de Blok et al. (2001)	80.0	H α	0.6	19.7	≥ 61.3	−
ESO 0140040	de Blok et al. (2001)	212.0	H α	1.5	120.3	≥ 272.7	−

Appendix B

Additional rotation curve examples

Previously published as an appendix to Kyle A. Oman, Julio F. Navarro, Laura V. Sales, Azadeh Fattahi, Carlos S. Frenk, Till Sawala, Matthieu Schaller, Simon D. M. White; Missing dark matter in dwarf galaxies?. *Mon Not R Astron Soc* 2016; 460 (4): 3610–3623.

In Fig. B.1 we show the rotation curves of all observed galaxies whose rotation curves extend to at least $2r_h^{st}$, i.e. the same galaxies as appear in Fig. 3.4 and Table 3.2. This serves to illustrate the striking diversity in rotation curve shapes, in addition to the scatter in $V_{\rm circ}(2r_h^{st})$, relative to the results from simulations. We note rotation curves in reasonable agreement with our simulations at all radii (e.g. Haro 29, WLM, DDO 154, NGC 2366, NGC 2403), rotation curves which agree with our simulated rotation curves at $2r_h^{st}$ but have very different shapes (e.g. CVnIdwA, UGC 8508, DDO 126, IC 2574, DDO 87, NGC 4736), rotation curves with shapes similar to those in our simulations but with systematically high (NGC 5204) or low (NGC 1569, DDO 50) velocities at all radii, and rotation curves that have neither shapes nor velocities at $2r_h^{st}$ consistent with our simulations (e.g. IC 1613, UGC 11707, NGC 7793).
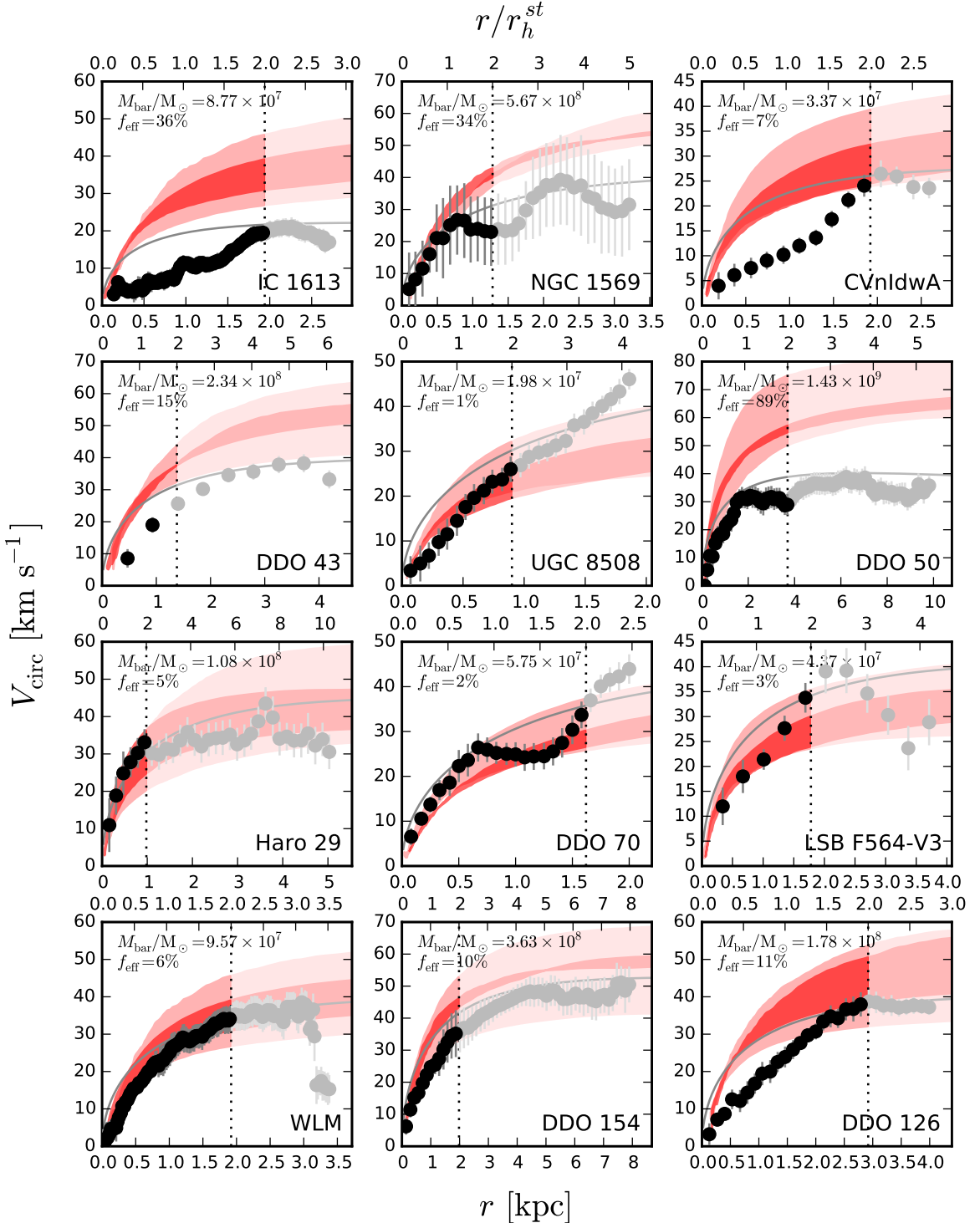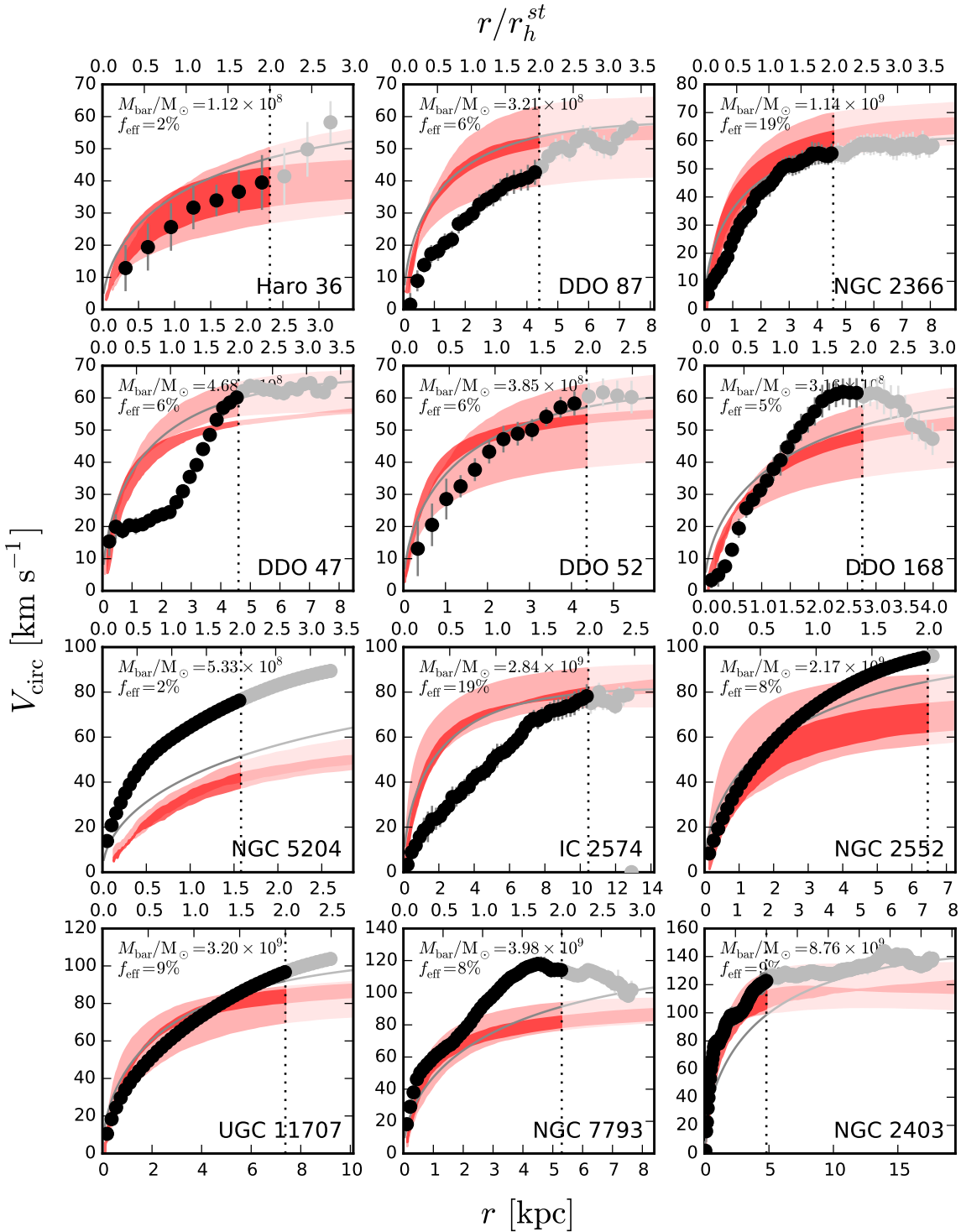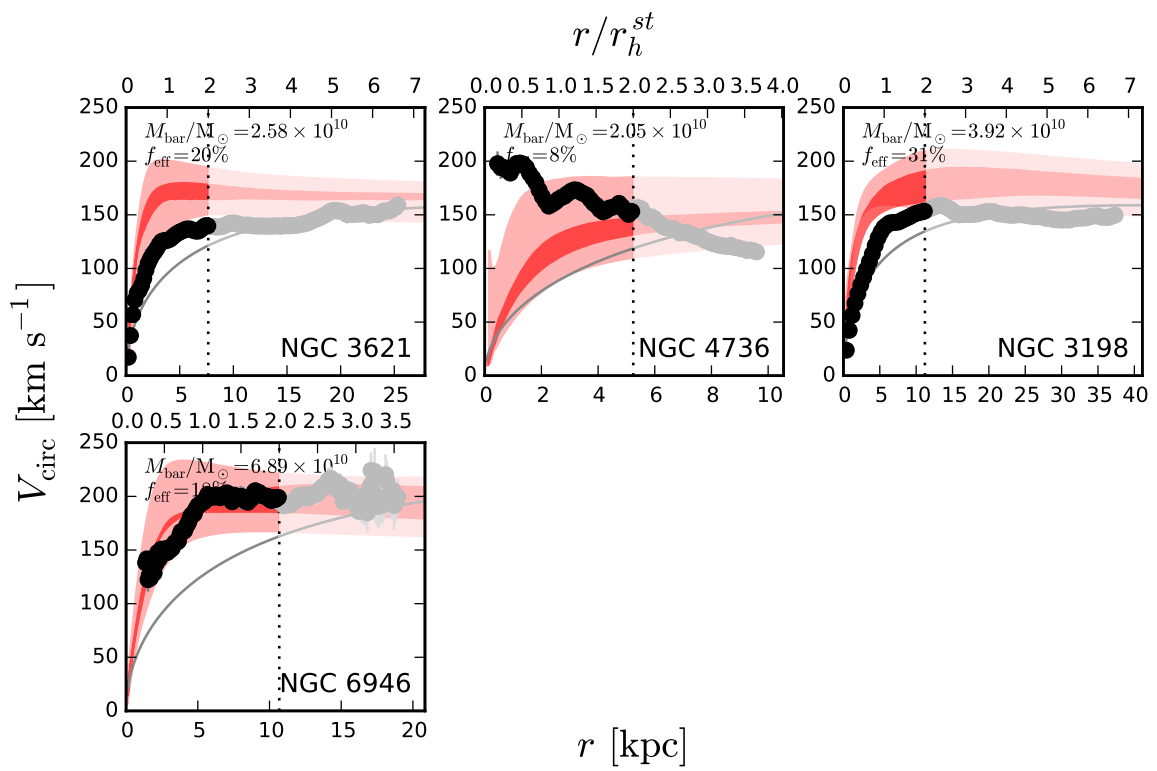
Figure B.1: Rotation curves for all galaxies with rotation curves that extend to at least $2r_h^{st}$ (see also Table 3.2). The panels are in order of increasing $V_{\mathrm{circ}}(2r_h^{st})$. Symbols, lines and shading are as in Fig. 3.3.

Figure B.1: *Continued.*

Figure B.1: *Continued.*

Appendix C

Additional properties of mock-observed simulated galaxies and observed comparison sample

C.1 Properties of simulated and observed galaxies

In Tables C.1 & C.2 we collect some key properties of our sample of simulated galaxies and the THINGS (Walter et al., 2008) and LITTLE THINGS (Hunter et al., 2012) galaxies, respectively, including the key to the numeric labels used in Figs. 4.1, 4.4 & 4.11.

Not all galaxies in these surveys are amenable to kinematic analysis. We select the THINGS galaxies analysed in de Blok et al. (2008) and Oh et al. (2011). In cases where the same galaxy is analysed in both studies, we use the more recent analysis. We exclude some of the galaxies:

- NGC 4826 has two counter-rotating discs, making the interpretation of the rotation curve as a circular velocity curve less certain.

- Ho II is the same galaxy as DDO 50, which appears in the LITTLE THINGS sample.

- We omit DDO 53, DDO 154 and NGC 2366 which are included as part of the LITTLE THINGS sample.

- Ho I has a particularly small inclination of $\lesssim 14°$ (Oh et al., 2011), which makes the necessary inclination correction unacceptably large and uncertain.

We select all of the LITTLE THINGS galaxies analysed in Oh et al. (2015).

Table C.1: Selected properties of the synthetically observed APOSTLE galaxies in our sample. Columns: **(1)** Number corresponding to labels in Figs. 4.1, 4.4 & 4.11; **(2)** Object label as described in Sec. 4.2.1; **(3)** Neutral hydrogen mass (the gas mass used in the BTFR is $M_{\rm bar} = M_\star + 1.4M_{\rm HI}$); **(4)** Stellar masses; **(5)** H I sizes defined as the radius where $\Sigma_{\rm HI}$ drops to $1\,{\rm M_\odot\,pc^{-2}}$, measured from the $0^{\rm th}$ moment maps; **(6)** Maximum circular velocity ($V_{\rm circ} = \sqrt{GM(<r)/r}$); **(7)** Circular velocity at $2\,{\rm kpc}$; **(8)** Maximum H I gas azimuthal velocity; **(9)** H I gas azimuthal velocity at $2\,{\rm kpc}$; **(10)** Maximum rotation velocity as fit with $^{\rm 3D}$BAROLO; **(11)** Rotation velocity at $2\,{\rm kpc}$.

Symbol Number	Object	$M_{\rm HI}$ ($\rm M_\odot$)	$M_\star$ ($\rm M_\odot$)	$R_{\rm HI}$ (kpc)	$\max(V_{\rm circ})$ ($\rm km\,s^{-1}$)	$V_{\rm circ}(2\,{\rm kpc})$ ($\rm km\,s^{-1}$)	$\max(V_{\rm gas})$ ($\rm km\,s^{-1}$)	$V_{\rm gas}(2\,{\rm kpc})$ ($\rm km\,s^{-1}$)	$\max(V_{\rm rot})$ ($\rm km\,s^{-1}$)	$V_{\rm rot}(2\,{\rm kpc})$ ($\rm km\,s^{-1}$)
1	AP-L1-V1-4-0	2.6×10^9	2.6×10^9	23.4	91.0	68.2	91.1	59.9	119.7	51.4
2	AP-L1-V1-6-0	1.2×10^8	8.8×10^8	3.3	60.2	45.5	54.4	45.0	58.7	32.8
3	AP-L1-V1-7-0	3.0×10^8	6.7×10^8	4.2	72.0	61.6	66.9	59.0	84.6	41.0
4	AP-L1-V1-8-0	2.9×10^8	7.7×10^8	1.5	68.2	52.0	67.2	51.9	74.7	50.8
5	AP-L1-V4-6-0	4.4×10^8	1.4×10^9	7.5	86.4	74.8	97.6	62.1	102.2	25.2
6	AP-L1-V4-8-0	6.1×10^8	8.1×10^8	2.0	69.1	48.0	67.0	41.2	86.8	29.5
7	AP-L1-V4-10-0	2.2×10^9	4.9×10^8	17.7	66.2	45.5	62.6	25.0	77.7	25.0
8	AP-L1-V4-13-0	3.9×10^8	2.7×10^8	7.3	64.8	53.3	58.5	34.8	97.5	31.2
9	AP-L1-V4-14-0	1.0×10^9	4.2×10^8	11.4	60.2	44.7	63.9	40.5	67.2	31.4
10	AP-L1-V6-5-0	1.3×10^9	2.3×10^9	11.9	89.5	72.4	93.9	54.5	118.6	71.1
11	AP-L1-V6-6-0	2.1×10^9	7.6×10^8	8.9	68.0	46.4	66.5	39.3	86.5	31.1
12	AP-L1-V6-7-0	1.5×10^9	5.1×10^8	13.3	70.2	43.9	76.2	48.3	45.0	29.9
13	AP-L1-V6-8-0	2.8×10^9	8.4×10^8	21.2	75.9	55.6	76.9	47.8	85.6	43.3
14	AP-L1-V6-11-0	3.1×10^8	7.5×10^8	5.4	60.3	49.8	50.1	32.3	60.4	16.8
15	AP-L1-V6-12-0	1.7×10^9	1.5×10^9	16.2	76.6	61.8	81.4	50.9	88.7	38.8
16	AP-L1-V6-15-0	6.3×10^8	3.4×10^8	8.5	61.6	46.0	64.9	31.6	66.5	52.5
17	AP-L1-V6-16-0	4.1×10^8	5.3×10^8	7.6	65.5	55.0	66.4	43.6	102.8	58.8
18	AP-L1-V6-18-0	1.9×10^8	3.0×10^8	4.4	61.9	56.6	58.1	52.9	57.5	57.2
19	AP-L1-V6-19-0	6.5×10^8	5.2×10^8	9.4	61.0	46.7	68.4	50.3	58.5	26.0
20	AP-L1-V6-20-0	2.3×10^7	3.8×10^8	1.7	67.7	59.9	62.0	62.0	74.6	73.5

Symbol Number	Object	M_{HI} (M$_\odot$)	$M_\star$ (M$_\odot$)	R_{HI} (kpc)	max(V_{circ}) (km s^{-1})	$V_{\mathrm{circ}}(2\,\mathrm{kpc})$ (km s^{-1})	max(V_{gas}) (km s^{-1})	$V_{\mathrm{gas}}(2\,\mathrm{kpc})$ (km s^{-1})	max(V_{rot}) (km s^{-1})	$V_{\mathrm{rot}}(2\,\mathrm{kpc})$ (km s^{-1})
21	AP-L1-V10-5-0	2.0×10^9	6.1×10^9	12.1	108.8	83.3	102.3	80.2	126.1	68.6
22	AP-L1-V10-6-0	2.1×10^9	4.0×10^9	13.5	103.9	71.2	92.0	59.6	125.0	30.8
23	AP-L1-V10-13-0	6.0×10^8	2.0×10^9	4.3	83.6	74.9	75.5	58.9	120.7	50.1
24	AP-L1-V10-14-0	1.4×10^9	9.7×10^8	13.7	66.3	51.0	64.0	42.7	73.9	28.5
25	AP-L1-V10-16-0	1.1×10^9	9.6×10^8	5.6	75.5	51.6	68.6	35.1	93.1	43.2
26	AP-L1-V10-17-0	4.4×10^8	7.6×10^8	6.1	67.4	48.5	51.9	38.4	58.2	20.5
27	AP-L1-V10-19-0	4.9×10^8	4.9×10^8	9.1	67.2	48.2	70.3	26.7	74.3	20.9
28	AP-L1-V10-20-0	3.0×10^8	7.0×10^8	2.0	73.5	62.3	74.1	42.4	80.9	47.4
29	AP-L1-V10-22-0	3.9×10^8	7.6×10^8	7.2	65.5	48.0	66.6	31.1	68.0	22.4
30	AP-L1-V10-30-0	6.4×10^8	3.6×10^8	9.7	61.4	49.5	61.8	45.1	63.9	22.4
31	AP-L1-V11-3-0	4.6×10^9	9.5×10^9	27.7	118.4	94.6	123.6	79.3	136.2	81.3
32	AP-L1-V11-5-0	4.7×10^9	3.2×10^9	24.4	91.1	65.5	95.2	60.1	110.4	37.2
33	AP-L1-V11-6-0	4.1×10^9	1.4×10^9	26.1	88.5	67.6	95.5	46.9	108.0	43.2

Table C.2: Selected properties of the THINGS and LITTLE THINGS galaxies. Columns: **(1)** Number corresponding to labels in Figs. 4.1, 4.4 & 4.11; **(2)** Galaxy name used in survey publications; **(3)** Survey; **(4)** Distance; **(5)** Average inclination; **(6)** Average position angle; **(7)** Neutral hydrogen mass (the mass used in the BTFR is $M_{\mathrm{bar}} = M_\star + 1.4 M_{\mathrm{HI}}$); **(8)** Stellar mass (galaxies with no reported measurement marked '–'); **(9)** H I sizes defined as the radius where Σ_{HI} drops to $1\,\mathrm{M}_\odot\,\mathrm{pc}^{-2}$ (galaxies with surface density profiles that do not cross this value marked '–'); **(10)** Maximum rotation velocity; **(11)** Rotation velocity at $2\,\mathrm{kpc}$ (rotation curves with no measurements near $2\,\mathrm{kpc}$ marked '–'). **References** for all quantities are Walter et al. (2008); Oh et al. (2011, 2015), except column (7) which is drawn from Walter et al. (2008); Hunter et al. (2012) and column (9) which we measure directly from the moment maps provided by the survey teams.

Symbol Number	Object	Survey	D (Mpc)	Incl. (°)	PA (°)	M_{HI} ($\mathrm{M}_\odot$)	$M_\star$ ($\mathrm{M}_\odot$)	R_{HI} (kpc)	$\max(V_{\mathrm{rot}})$ (km s^{-1})	$V_{\mathrm{rot}}(2\,\mathrm{kpc})$ (km s^{-1})
1	CVnIdwA	LITTLE THINGS	3.6	66	48	4.7×10^7	4.9×10^6	1.5	26.4	25.9
2	DDO43	LITTLE THINGS	7.8	41	294	1.7×10^8	–	2.8	38.7	31.5
3	DDO46	LITTLE THINGS	6.1	28	274	1.9×10^8	–	–	76.3	73.2
4	DDO47	LITTLE THINGS	5.2	46	312	3.9×10^8	–	5.0	64.7	23.7
5	DDO50	LITTLE THINGS	3.4	50	176	7.1×10^8	1.1×10^8	6.3	38.8	31.2
6	DDO52	LITTLE THINGS	10.3	43	8	2.7×10^8	5.4×10^7	4.4	61.7	42.6
7	DDO53	LITTLE THINGS	3.6	27	132	5.2×10^7	9.8×10^6	–	32.0	29.3
8	DDO70	LITTLE THINGS	1.3	50	44	4.1×10^7	1.9×10^7	1.6	43.9	43.9
9	DDO87	LITTLE THINGS	7.7	56	235	2.5×10^8	3.2×10^7	2.4	56.6	28.0
10	DDO101	LITTLE THINGS	6.4	51	287	2.3×10^7	6.6×10^7	–	64.9	63.3
11	DDO126	LITTLE THINGS	4.9	65	138	1.4×10^8	1.6×10^7	3.1	38.7	30.7
12	DDO133	LITTLE THINGS	3.5	43	360	1.0×10^8	3.0×10^7	2.7	46.7	41.6
13	DDO154	LITTLE THINGS	3.7	68	226	2.9×10^8	8.3×10^6	3.4	51.1	35.8

Symbol Number	Object	Survey	D (Mpc)	Incl. (°)	PA (°)	$M_{\rm HI}$ ($M_\odot$)	$M_\star$ ($M_\odot$)	$R_{\rm HI}$ (kpc)	$\max(V_{\rm rot})$ (km s^{-1})	$V_{\rm rot}(2\,{\rm kpc})$ (km s^{-1})
14	DDO168	LITTLE THINGS	4.3	46	276	3.0×10^8	5.9×10^7	–	61.9	57.5
15	DDO210	LITTLE THINGS	0.9	67	65	2.0×10^6	6.0×10^5	0.3	12.0	–
16	DDO216	LITTLE THINGS	1.1	64	134	5.6×10^6	1.5×10^7	–	18.9	18.9
17	F564-V3	LITTLE THINGS	8.7	56	12	4.1×10^7	–	0.4	39.2	38.7
18	IC10	LITTLE THINGS	0.7	47	56	6.0×10^7	–	–	36.4	–
19	IC1613	LITTLE THINGS	0.7	48	74	3.4×10^7	2.9×10^7	0.0	21.1	20.5
20	NGC1569	LITTLE THINGS	3.4	69	122	2.5×10^8	3.6×10^8	2.9	39.3	36.6
21	NGC2366	LITTLE THINGS	3.4	63	39	6.9×10^8	6.9×10^7	5.6	59.8	41.9
22	NGC3738	LITTLE THINGS	4.9	23	292	1.1×10^8	4.7×10^8	–	132.7	125.6
23	UGC8508	LITTLE THINGS	2.6	82	126	1.9×10^7	7.8×10^6	0.7	46.1	46.1
24	WLM	LITTLE THINGS	1.0	74	174	7.1×10^7	1.6×10^7	1.8	38.5	35.1
25	Haro29	LITTLE THINGS	5.9	61	214	6.3×10^7	1.4×10^7	1.2	43.5	34.4
26	Haro36	LITTLE THINGS	9.3	70	248	1.4×10^8	–	2.4	58.2	37.6
1	NGC925	THINGS	9.2	66	287	4.6×10^9	1.0×10^{10}	–	119.9	34.7
2	NGC2403	THINGS	3.2	63	124	2.6×10^9	5.1×10^9	12.3	143.9	97.4
3	NGC2841	THINGS	14.1	74	153	8.6×10^9	1.3×10^{11}	22.2	323.9	–
4	NGC2903	THINGS	8.9	65	204	4.4×10^9	1.6×10^{10}	17.2	215.5	120.1
5	NGC2976	THINGS	3.6	64	334	1.4×10^8	1.8×10^9	2.3	86.2	74.9
6	NGC3031	THINGS	3.6	59	330	3.6×10^9	7.9×10^{10}	–	259.8	242.2
7	NGC3198	THINGS	13.8	72	215	1.0×10^{10}	2.5×10^{10}	26.9	158.7	76.7
8	IC2574	THINGS	4.0	53	56	1.5×10^9	1.0×10^9	9.3	80.0	24.5

Symbol Number	Object	Survey	D (Mpc)	Incl. (°)	PA (°)	M_{HI} ($\mathrm{M}_\odot$)	$M_\star$ ($\mathrm{M}_\odot$)	R_{HI} (kpc)	$\max(V_{\mathrm{rot}})$ ($\mathrm{km\,s^{-1}}$)	$V_{\mathrm{rot}}(2\,\mathrm{kpc})$ ($\mathrm{km\,s^{-1}}$)
9	NGC3521	THINGS	10.7	73	340	8.0×10^9	1.0×10^{11}	19.9	233.4	192.1
10	NGC3621	THINGS	6.6	65	345	7.1×10^9	1.6×10^{10}	22.5	159.2	102.9
11	NGC4736	THINGS	4.7	41	296	4.0×10^8	2.0×10^{10}	3.4	198.3	168.7
12	DDO154	THINGS	4.3	66	230	3.6×10^8	2.6×10^7	4.5	50.0	34.6
13	NGC5055	THINGS	10.1	59	102	9.1×10^9	1.3×10^{11}	16.4	211.6	185.3
14	NGC6946	THINGS	5.9	33	243	4.2×10^9	6.3×10^{10}	15.3	224.3	132.5
15	NGC7331	THINGS	14.7	76	168	9.1×10^9	1.6×10^{11}	22.7	268.1	253.2
16	NGC7793	THINGS	3.9	50	290	8.9×10^8	2.8×10^9	6.7	117.9	76.2
17	M81dwB	THINGS	5.3	44	311	2.5×10^7	3.0×10^7	0.9	39.5	31.6

C.2 Velocity field symmetry diagnostics

The centre and right panels of Fig. 4.4 show the results of measurements diagnosing the symmetry of the galaxy velocity fields which are most clearly explained graphically. In Fig. C.1 we illustrate the rotational symmetry diagnostic shown in the centre panel of Fig. 4.4, and in Fig. C.2 we illustrate the azimuthal symmetry diagnostic shown in the right panel of Fig. 4.4.

C.3 ^{3D}BAROLO configuration

In Table C.3 we summarize the full configuration used for the ^{3D}BAROLO software. We omit parameters which do not affect the result of the calculation (e.g. flags to enable or disable additional diagnostic output, file path definitions, etc.).
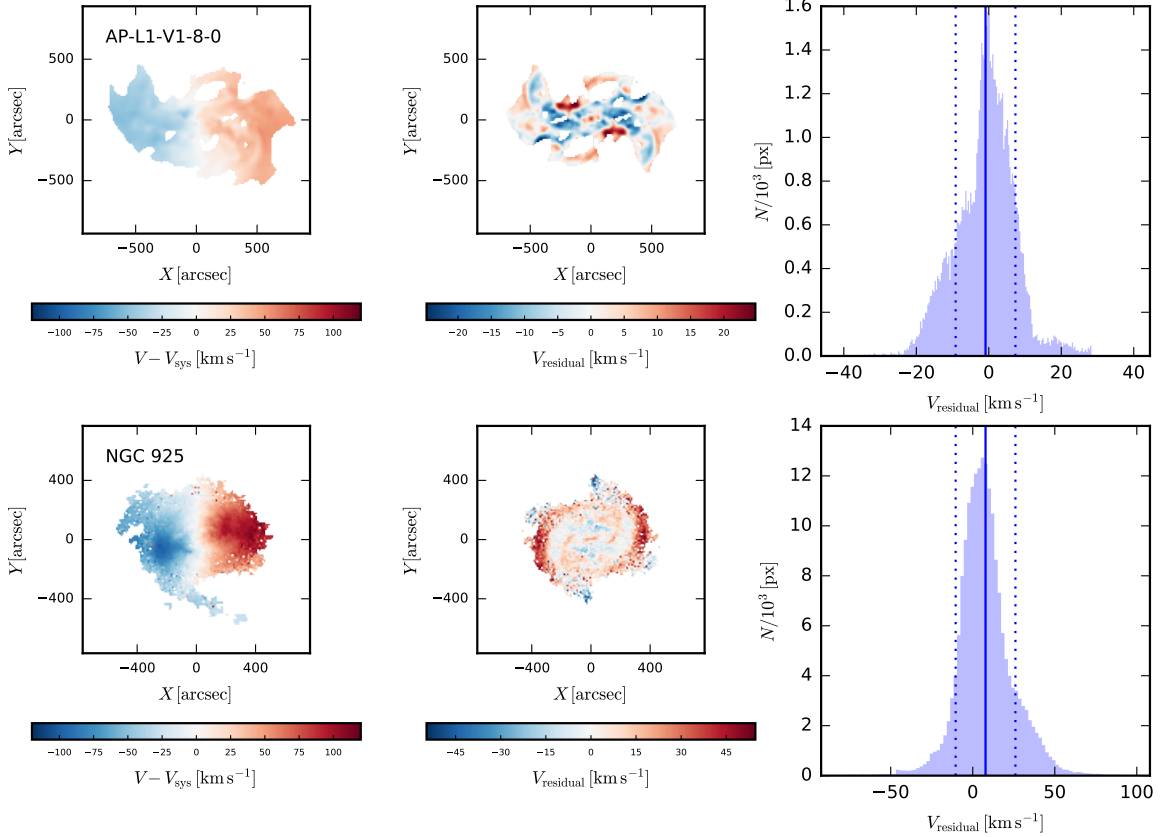
Figure C.1: Illustration of the measurements plotted in the centre panel of Fig. 4.4. *Left column:* 1$^{\text{st}}$ moment map for one simulated galaxy AP-L1-V1-4-0 (above) and one THINGS galaxy NGC 4736 (below). *Centre column:* The velocity field from the left column is rotated 180° and aligned with the unrotated field by superimposing the galactic centre in each field. The two fields are then subtracted (with a sign change applied to the rotated field) to give the residual shown. *Right column:* Histogram of the pixel values of the residual in the centre column. A perfectly rotationally symmetric velocity field would yield a sharp peak at $0\,\mathrm{km\,s^{-1}}$. If one side of the galaxy has systematically higher $|V - V_{\mathrm{sys}}|$ than the other the mean (vertical solid line) moves away from 0; local asymmetries increase the rms width (vertical dotted lines) of the distribution.
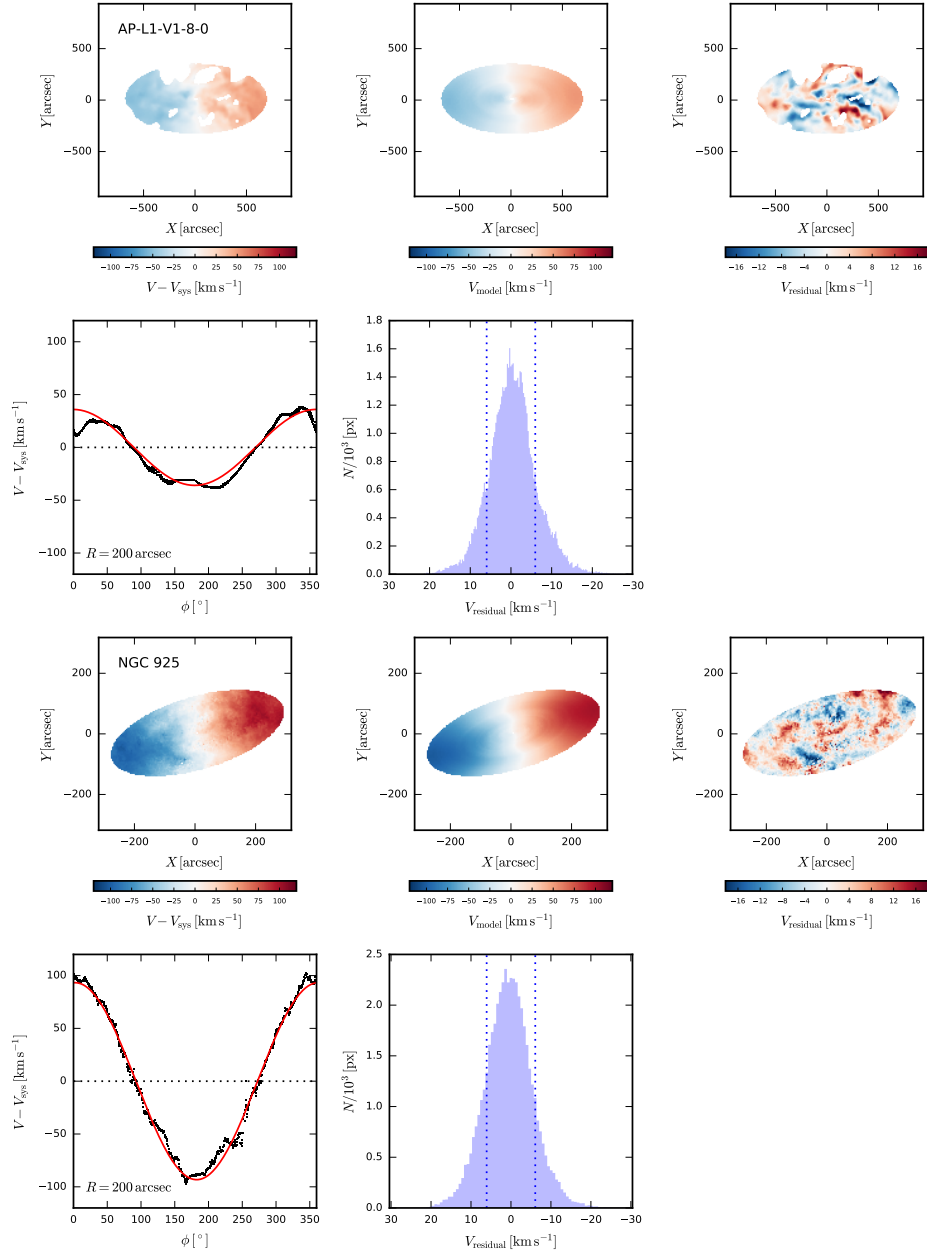
Figure C.2: Illustration of the measurement plotted in the right panel of Fig. 4.4. There are two sets of five panels; the upper five correspond to the simulated galaxy AP-L1-V1-4-0, the lower five to the THINGS galaxy NGC 4736. *Panel 1:* The velocity field of the galaxy, cropped to the radius enclosing 90 per cent of the H I mass (simulated galaxy) or the maximum radius modeled in de Blok et al. (2008, or Oh et al., 2011, 2015, as appropriate). The orientation and aspect ratio of the ellipse are set by the global inclination and position angle of the galaxy. $(i, \mathrm{PA}) = (60°, 270°)$ for APOSTLE, for observed galaxies see Table C.2. *Panel 2:* A simple kinematic model constructed by fitting a cosine to the velocities in a series of rings (illustrated in panel 4). The inclinations and position angles are held fixed at the global values. *Panel 3:* Residual after subtraction of the velocity fields in panels 1 & 2. *Panel 4:* Example of cosine fit to one ring at $R = 300\,\mathrm{arcsec}$. The phase and amplitude are free parameters, but the vertical offset is fixed at $0\,\mathrm{km\,s^{-1}}$. *Panel 5:* Histogram of the pixel values of the residual in panel 3. Azimuthal asymmetries increase the rms width (vertical dotted lines) of the distribution; note that the width is the rms scatter from 0.

Table C.3: Parameters used to configure the ³ᴰʙᴀʀᴏʟᴏ software, omitting parameters which have no impact on the result of the calculation. Our parameter choices where they differ from the default values are inspired by the choices made by Iorio et al. (2017). These authors model the LITTLE THINGS galaxies; given that we mimic the observing setup of this survey and our simulated galaxies of interest are broadly similar to those in this sample, many of their parameter choices are applicable here. The most significant change we make is to restrict the inclination and position angles somewhat closer to their 'true' values.

Parameter	Value	Units	Description & comments
CHECKCHANNELS	FALSE	–	Check for bad channels in the data cube?
FLAGROBUSTSTATS	TRUE	–	Use robust statistics?
FLAGSEARCH	FALSE	–	Search for sources in the data cube?
FLAGRING	FALSE	–	Fit velocity field with a ring model?
SMOOTH	FALSE	–	Smooth the data cube?
GALFIT	TRUE	–	Fit a 3D model to the data cube?
BOX	NONE	px	Select a sub-region of the cube?
NRADII	*varies*	–	Number of rings to use; we use enough rings to reach the radius enclosing 90 per cent of the H I mass of the galaxy.
RADSEP	14.101	arcsec	Separation of rings.
XPOS	*varies*	px	Centre of rings, set individually for each galaxy at the projected centre of the stellar light distribution.
YPOS	*varies*	px	As XPOS.
VSYS	257.4528	km s^{-1}	Systemic velocity.

Continued on next page.

Parameter	Value	Units	Description & comments
VROT	30	km s^{-1}	Initial guess for rotation velocity.
VDISP	8	km s^{-1}	Initial guess for velocity dispersion.
INC	60	degrees	Initial guess for inclination.
DELTAINC	15	degrees	Allowed deviation of inclination from initial guess.
PA	270	degrees	Initial guess for position angle.
DELTAPA	20	degrees	Allowed deviation of position angle from initial guess.
Z0	2.136	arcsec	Disc scale height.
DENS	−1	atoms cm^{-2}	Global column density of gas (unused when NORM LOCAL is set).
FREE	VROT VDISP INC PA	–	Parameters to fit for each ring.
MASK	SMOOTH	–	The data cube is smoothed by a factor of 2 and a signal-to-noise cut is used to define a mask.
BLANKCUT	2.5	–	Signal-to-noise threshold for mask construction.
SIDE	B	–	The entire galaxy is modeled; the approaching and receding sides can also be fit separately.
NORM	LOCAL	–	The model is normalized pixel by pixel, i.e. the surface brightness is not explicitly fit.
LTYPE	1	–	Layer type along z is gaussian.
FTYPE	2	–	Minimization function is |model − observed|
WFUNC	1	–	Azimuthal weighting function is $\|\cos\theta\|$
TOL	0.001	–	Minimization tolerance.

Parameter	Value	Units	Description & comments
TWOSTAGE	TRUE	–	Two stage fitting, i.e. geometric parameters are regularized and rotation velocity is fit again.
POLYN	bezier	–	Degree of polynomial fitting INC and PA.
FLAGERRORS	*varies*	–	Errors are estimated only for those galaxies we use for illustrative purposes.
BWEIGHT	1	–	Exponent of weight for blank pixels.
LINEAR	0.424	channels	Instrumental spectral broadening (standard deviation).
CDENS	10	–	Number of clouds to use in building the ring model.
NV	200	–	Number of sub-clouds used within each cloud (see CDENS) to populate the spectral axis of the ring model.

Bibliography

Adams, J. J., Gebhardt, K., Blanc, G. A., Fabricius, M. H., Hill, G. J., Murphy, J. D., van den Bosch, R. C. E., & van de Ven, G. 2012, ApJ, 745, 92

Adams, J. J., Simon, J. D., Fabricius, M. H., van den Bosch, R. C. E., Barentine, J. C., Bender, R., Gebhardt, K., Hill, G. J., Murphy, J. D., Swaters, R. A., Thomas, J., & van de Ven, G. 2014, ApJ, 789, 63

Alcubierre, M., Guzmán, F. S., Matos, T., Núñez, D., Ureña-López, L. A., & Wiederhold, P. 2002, Classical and Quantum Gravity, 19, 5017

Algorry, D. G., Navarro, J. F., Abadi, M. G., Sales, L. V., Bower, R. G., Crain, R. A., Dalla Vecchia, C., Frenk, C. S., Schaller, M., Schaye, J., & Theuns, T. 2017, MNRAS, 469, 1054

Begeman, K. G. 1989, A&A, 223, 47

Behroozi, P. S., Wechsler, R. H., & Conroy, C. 2013, ApJ, 770, 57

Benítez-Llambay, A., Navarro, J. F., Abadi, M. G., Gottlöber, S., Yepes, G., Hoffman, Y., & Steinmetz, M. 2013, ApJ, 763, L41

Benson, A. J., Lacey, C. G., Baugh, C. M., Cole, S., & Frenk, C. S. 2002, MNRAS, 333, 156

Bertone, G., Hooper, D., & Silk, J. 2005, Phys. Rep., 405, 279

Binney, J. & Tremaine, S. 2008, Galactic Dynamics: Second Edition (Princeton University Press)

Blitz, L. & Rosolowsky, E. 2006, ApJ, 650, 933

Bode, P., Ostriker, J. P., & Turok, N. 2001, ApJ, 556, 93

Bond, J. R. & Szalay, A. S. 1983, ApJ, 274, 443

Bosma, A. 1978, PhD thesis, PhD Thesis, Groningen Univ., (1978)

—. 2017, in Outskirts of Galaxies, ed. J. H. Knapen, J. C. Lee, & A. Gil de Paz (Astrophysics and Space Science Library, Springer), 362

Boyarsky, A., Lesgourgues, J., Ruchayskiy, O., & Viel, M. 2009a, Physical Review Letters, 102, 201304

Boyarsky, A., Ruchayskiy, O., & Shaposhnikov, M. 2009b, Annual Review of Nuclear and Particle Science, 59, 191

Boylan-Kolchin, M., Bullock, J. S., & Kaplinghat, M. 2011, MNRAS, 415, L40

—. 2012, MNRAS, 422, 1203

Brook, C. B. 2015, MNRAS, 454, 1719

Brook, C. B., Stinson, G., Gibson, B. K., Wadsley, J., & Quinn, T. 2012, MNRAS, 424, 1275

Brooks, A. M. & Zolotov, A. 2014, ApJ, 786, 87

Bullock, J. S., Kravtsov, A. V., & Weinberg, D. H. 2000, ApJ, 539, 517

Bureau, M. & Carignan, C. 2002, AJ, 123, 1316

Campbell, D. J. R., Frenk, C. S., Jenkins, A., Eke, V. R., Navarro, J. F., Sawala, T., Schaller, M., Fattahi, A., Oman, K. A., & Theuns, T. 2017, MNRAS, 469, 2335

Chan, T. K., Kereš, D., Oñorbe, J., Hopkins, P. F., Muratov, A. L., Faucher-Giguère, C.-A., & Quataert, E. 2015, MNRAS, 454, 2981

Cole, D. R., Dehnen, W., & Wilkinson, M. I. 2011, MNRAS, 416, 1118

Cole, S., Percival, W. J., Peacock, J. A., Norberg, P., Baugh, C. M., Frenk, C. S., Baldry, I., Bland-Hawthorn, J., Bridges, T., Cannon, R., Colless, M., Collins, C., Couch, W., Cross, N. J. G., Dalton, G., Eke, V. R., De Propris, R., Driver, S. P., Efstathiou, G., Ellis, R. S., Glazebrook, K., Jackson, C., Jenkins, A., Lahav, O., Lewis, I., Lumsden, S., Maddox, S., Madgwick, D., Peterson, B. A., Sutherland, W., & Taylor, K. 2005, MNRAS, 362, 505

Courteau, S. 1997, AJ, 114, 2402

Courteau, S., Cappellari, M., de Jong, R. S., Dutton, A. A., Emsellem, E., Hoekstra, H., Koopmans, L. V. E., Mamon, G. A., Maraston, C., Treu, T., & Widrow, L. M. 2014, Reviews of Modern Physics, 86, 47

Crain, R. A., Schaye, J., Bower, R. G., Furlong, M., Schaller, M., Theuns, T., Dalla Vecchia, C., Frenk, C. S., McCarthy, I. G., Helly, J. C., Jenkins, A., Rosas-Guevara, Y. M., White, S. D. M., & Trayford, J. W. 2015, MNRAS, 450, 1937

Creasey, P., Sameie, O., Sales, L. V., Yu, H.-B., Vogelsberger, M., & Zavala, J. 2017, MNRAS, 468, 2283

Dalcanton, J. J. & Stilp, A. M. 2010, ApJ, 721, 547

Dalcanton, J. J., Williams, B. F., Seth, A. C., Dolphin, A., Holtzman, J., Rosema, K., Skillman, E. D., Cole, A., Girardi, L., Gogarten, S. M., Karachentsev, I. D., Olsen, K., Weisz, D., Christensen, C., Freeman, K., Gilbert, K., Gallart, C., Harris, J., Hodge, P., de Jong, R. S., Karachentseva, V., Mateo, M., Stetson, P. B., Tavarez, M., Zaritsky, D., Governato, F., & Quinn, T. 2009, ApJS, 183, 67

Dalla Vecchia, C. & Schaye, J. 2012, MNRAS, 426, 140

Davis, M., Efstathiou, G., Frenk, C. S., & White, S. D. M. 1985, ApJ, 292, 371

de Bernardis, P., Ade, P. A. R., Bock, J. J., Bond, J. R., Borrill, J., Boscaleri, A., Coble, K., Crill, B. P., De Gasperis, G., Farese, P. C., Ferreira, P. G., Ganga, K., Giacometti, M., Hivon, E., Hristov, V. V., Iacoangeli, A., Jaffe, A. H., Lange, A. E., Martinis, L., Masi, S., Mason, P. V., Mauskopf, P. D., Melchiorri, A., Miglio, L., Montroy, T., Netterfield, C. B., Pascale, E., Piacentini, F., Pogosyan, D., Prunet, S., Rao, S., Romeo, G., Ruhl, J. E., Scaramuzzi, F., Sforna, D., & Vittorio, N. 2000, Nature, 404, 955

de Blok, W. J. G. 2010, Advances in Astronomy, 2010, 789293

de Blok, W. J. G. & Bosma, A. 2002, A&A, 385, 816

de Blok, W. J. G., Bosma, A., & McGaugh, S. 2003, MNRAS, 340, 657

de Blok, W. J. G. & McGaugh, S. S. 1996, ApJ, 469, L89

—. 1997, MNRAS, 290, 533

de Blok, W. J. G., McGaugh, S. S., & Rubin, V. C. 2001, AJ, 122, 2396

de Blok, W. J. G., Walter, F., Brinks, E., Trachternach, C., Oh, S.-H., & Kennicutt, Jr., R. C. 2008, AJ, 136, 2648

de Blok, W. J. G., Weldrake, D. T. F., & Walter, F. 2004, in IAU Symposium, Vol. 220, Dark Matter in Galaxies, ed. S. Ryder, D. Pisano, M. Walker, & K. Freeman, 373

Del Popolo, A. 2009, ApJ, 698, 2093

Del Popolo, A. & Le Delliou, M. 2017, Galaxies, 5, 17

Del Popolo, A. & Pace, F. 2016, Ap&SS, 361, 162

Di Cintio, A., Brook, C. B., Dutton, A. A., Macciò, A. V., Stinson, G. S., & Knebe, A. 2014, MNRAS, 441, 2986

Di Teodoro, E. M. & Fraternali, F. 2015, MNRAS, 451, 3021

Dolag, K., Borgani, S., Murante, G., & Springel, V. 2009, MNRAS, 399, 497

Dubinski, J. & Carlberg, R. G. 1991, ApJ, 378, 496

Duffy, A. R., Schaye, J., Kay, S. T., & Dalla Vecchia, C. 2008, MNRAS, 390, L64

Dutton, A. A., Courteau, S., de Jong, R., & Carignan, C. 2005, ApJ, 619, 218

Dutton, A. A., Macciò, A. V., Frings, J., Wang, L., Stinson, G. S., Penzo, C., & Kang, X. 2016, MNRAS, 457, L74

Efstathiou, G. 1992, MNRAS, 256, 43P

Einasto, J. 1965, Trudy Astrofizicheskogo Instituta Alma-Ata, 5, 87

Eisenstein, D. J., Zehavi, I., Hogg, D. W., Scoccimarro, R., Blanton, M. R., Nichol, R. C., Scranton, R., Seo, H.-J., Tegmark, M., Zheng, Z., Anderson, S. F., Annis, J., Bahcall, N., Brinkmann, J., Burles, S., Castander, F. J., Connolly, A., Csabai, I., Doi, M., Fukugita, M., Frieman, J. A., Glazebrook, K., Gunn, J. E., Hendry, J. S., Hennessy, G., Ivezić, Z., Kent, S., Knapp, G. R., Lin, H., Loh, Y.-S., Lupton,

R. H., Margon, B., McKay, T. A., Meiksin, A., Munn, J. A., Pope, A., Richmond, M. W., Schlegel, D., Schneider, D. P., Shimasaku, K., Stoughton, C., Strauss, M. A., SubbaRao, M., Szalay, A. S., Szapudi, I., Tucker, D. L., Yanny, B., & York, D. G. 2005, ApJ, 633, 560

El-Zant, A., Shlosman, I., & Hoffman, Y. 2001, ApJ, 560, 636

El-Zant, A. A., Hoffman, Y., Primack, J., Combes, F., & Shlosman, I. 2004, ApJ, 607, L75

Elbert, O. D., Bullock, J. S., Garrison-Kimmel, S., Rocha, M., Oñorbe, J., & Peter, A. H. G. 2015, MNRAS, 453, 29

Fattahi, A., Navarro, J. F., Sawala, T., Frenk, C. S., Oman, K. A., Crain, R. A., Furlong, M., Schaller, M., Schaye, J., Theuns, T., & Jenkins, A. 2016, MNRAS, 457, 844

Ferrarese, L., Ford, H. C., Huchra, J., Kennicutt, Jr., R. C., Mould, J. R., Sakai, S., Freedman, W. L., Stetson, P. B., Madore, B. F., Gibson, B. K., Graham, J. A., Hughes, S. M., Illingworth, G. D., Kelson, D. D., Macri, L., Sebo, K., & Silbermann, N. A. 2000, ApJS, 128, 431

Ferrero, I., Abadi, M. G., Navarro, J. F., Sales, L. V., & Gurovich, S. 2012, MNRAS, 425, 2817

Flores, R. A. & Primack, J. R. 1994, ApJ, 427, L1

Fry, A. B., Governato, F., Pontzen, A., Quinn, T., Tremmel, M., Anderson, L., Menon, H., Brooks, A. M., & Wadsley, J. 2015, MNRAS, 452, 1468

Furlong, M., Bower, R. G., Theuns, T., Schaye, J., Crain, R. A., Schaller, M., Dalla Vecchia, C., Frenk, C. S., McCarthy, I. G., Helly, J., Jenkins, A., & Rosas-Guevara, Y. M. 2015, MNRAS, 450, 4486

Garnavich, P. M., Kirshner, R. P., Challis, P., Tonry, J., Gilliland, R. L., Smith, R. C., Clocchiatti, A., Diercks, A., Filippenko, A. V., Hamuy, M., Hogan, C. J., Leibundgut, B., Phillips, M. M., Reiss, D., Riess, A. G., Schmidt, B. P., Schommer, R. A., Spyromilio, J., Stubbs, C., Suntzeff, N. B., & Wells, L. 1998, ApJ, 493, L53

Garrison-Kimmel, S., Boylan-Kolchin, M., Bullock, J. S., & Lee, K. 2014, MNRAS, 438, 2578

Geha, M., Blanton, M. R., Masjedi, M., & West, A. A. 2006, ApJ, 653, 240

Gentile, G., Angus, G. W., Famaey, B., Oh, S.-H., & de Blok, W. J. G. 2012, A&A, 543, A47

Gentile, G., Famaey, B., & de Blok, W. J. G. 2011, A&A, 527, A76

Georgiev, T. B., Karachentsev, I. D., & Tikhonov, N. A. 1997, Astronomy Letters, 23, 514

Giovanelli, R. & Haynes, M. P. 1988, in Galactic and Extragalactic Radio Astronomy, ed. K. I. Kellermann & G. L. Verschuur (Springer-Verlag), 522

Gnedin, O. Y. & Ostriker, J. P. 2001, ApJ, 561, 61

Gnedin, O. Y. & Zhao, H. 2002, MNRAS, 333, 299

Gottlöber, S., Hoffman, Y., & Yepes, G. 2010, in High Performance Computing in Science and Engineering, Garching/Munich 2009, ed. S. Wagner, M. Steinmetz, A. Bode, & M. M. Müller, 309

Governato, F., Brook, C., Mayer, L., Brooks, A., Rhee, G., Wadsley, J., Jonsson, P., Willman, B., Stinson, G., Quinn, T., & Madau, P. 2010, Nature, 463, 203

Governato, F., Zolotov, A., Pontzen, A., Christensen, C., Oh, S. H., Brooks, A. M., Quinn, T., Shen, S., & Wadsley, J. 2012, MNRAS, 422, 1231

Haardt, F. & Madau, P. 2001, in Clusters of Galaxies and the High Redshift Universe Observed in X-rays, ed. D. M. Neumann & J. T. V. Tran, 64

Halverson, N. W., Leitch, E. M., Pryke, C., Kovac, J., Carlstrom, J. E., Holzapfel, W. L., Dragovan, M., Cartwright, J. K., Mason, B. S., Padin, S., Pearson, T. J., Readhead, A. C. S., & Shepherd, M. C. 2002, ApJ, 568, 38

Hanany, S., Ade, P., Balbi, A., Bock, J., Borrill, J., Boscaleri, A., de Bernardis, P., Ferreira, P. G., Hristov, V. V., Jaffe, A. H., Lange, A. E., Lee, A. T., Mauskopf, P. D., Netterfield, C. B., Oh, S., Pascale, E., Rabii, B., Richards, P. L., Smoot, G. F., Stompor, R., Winant, C. D., & Wu, J. H. P. 2000, ApJ, 545, L5

Hayashi, E. & Navarro, J. F. 2006, MNRAS, 373, 1117

Hayashi, E., Navarro, J. F., Power, C., Jenkins, A., Frenk, C. S., White, S. D. M., Springel, V., Stadel, J., & Quinn, T. R. 2004, MNRAS, 355, 794

Hernquist, L. 1990, ApJ, 356, 359

Hoessel, J. G., Saha, A., & Danielson, G. E. 1998, AJ, 115, 573

Holwerda, B. W., Pirzkal, N., de Blok, W. J. G., Bouchard, A., Blyth, S.-L., van der Heyden, K. J., & Elson, E. C. 2011, MNRAS, 416, 2401

Hopkins, P. F. 2013, MNRAS, 428, 2840

Hu, W. & Dodelson, S. 2002, ARA&A, 40, 171

Hu, W. & Sugiyama, N. 1995, ApJ, 444, 489

Hunter, D. A. & Elmegreen, B. G. 2006, ApJS, 162, 49

Hunter, D. A., Ficut-Vicas, D., Ashley, T., Brinks, E., Cigan, P., Elmegreen, B. G., Heesen, V., Herrmann, K. A., Johnson, M., Oh, S.-H., Rupen, M. P., Schruba, A., Simpson, C. E., Walter, F., Westpfahl, D. J., Young, L. M., & Zhang, H.-X. 2012, AJ, 144, 134

Iorio, G., Fraternali, F., Nipoti, C., Di Teodoro, E., Read, J. I., & Battaglia, G. 2017, MNRAS, 466, 4159

Jenkins, A. 2013, MNRAS, 434, 2094

Johansson, P. H., Naab, T., & Ostriker, J. P. 2009, ApJ, 697, L38

Józsa, G. I. G., Kenn, F., Klein, U., & Oosterloo, T. A. 2007, A&A, 468, 731

Kamphuis, P., Józsa, G. I. G., Oh, S.-. H., Spekkens, K., Urbancic, N., Serra, P., Koribalski, B. S., & Dettmar, R.-J. 2015, MNRAS, 452, 3139

Kaplinghat, M., Tulin, S., & Yu, H.-B. 2016, Physical Review Letters, 116, 041302

Kauffmann, G., Huang, M.-L., Moran, S., & Heckman, T. M. 2015, MNRAS, 451, 878

Kirby, E. N., Bullock, J. S., Boylan-Kolchin, M., Kaplinghat, M., & Cohen, J. G. 2014, MNRAS, 439, 1015

Klypin, A., Kravtsov, A. V., Valenzuela, O., & Prada, F. 1999, ApJ, 522, 82

Kolb, E. W. & Turner, M. S. 1990, The early universe., Front. Phys. 69 (Westview Press)

Komatsu, E., Smith, K. M., Dunkley, J., Bennett, C. L., Gold, B., Hinshaw, G., Jarosik, N., Larson, D., Nolta, M. R., Page, L., Spergel, D. N., Halpern, M., Hill, R. S., Kogut, A., Limon, M., Meyer, S. S., Odegard, N., Tucker, G. S., Weiland, J. L., Wollack, E., & Wright, E. L. 2011, ApJS, 192, 18

Krajnović, D., Cappellari, M., de Zeeuw, P. T., & Copin, Y. 2006, MNRAS, 366, 787

Kroupa, P. 2012, PASA, 29, 395

Kuzio de Naray, R. & Kaufmann, T. 2011, MNRAS, 414, 3617

Kuzio de Naray, R., McGaugh, S. S., & de Blok, W. J. G. 2008, ApJ, 676, 920

Kuzio de Naray, R., McGaugh, S. S., & Mihos, J. C. 2009, ApJ, 692, 1321

Larson, R. B. 1974, MNRAS, 169, 229

Lelli, F., Fraternali, F., & Verheijen, M. 2013, MNRAS, 433, L30

Lelli, F., McGaugh, S. S., & Schombert, J. M. 2016a, AJ, 152, 157

—. 2016b, ApJ, 816, L14

Lelli, F., McGaugh, S. S., Schombert, J. M., & Pawlowski, M. S. 2017, ApJ, 836, 152

Lovell, M. R., Eke, V., Frenk, C. S., Gao, L., Jenkins, A., Theuns, T., Wang, J., White, S. D. M., Boyarsky, A., & Ruchayskiy, O. 2012, MNRAS, 420, 2318

Lovell, M. R., Frenk, C. S., Eke, V. R., Jenkins, A., Gao, L., & Theuns, T. 2014, MNRAS, 439, 300

Ludlow, A. D., Navarro, J. F., Angulo, R. E., Boylan-Kolchin, M., Springel, V., Frenk, C., & White, S. D. M. 2014, MNRAS, 441, 378

Macciò, A. V., Dutton, A. A., & van den Bosch, F. C. 2008, MNRAS, 391, 1940

Macciò, A. V., Paduroiu, S., Anderhalden, D., Schneider, A., & Moore, B. 2012a, MNRAS, 424, 1105

Macciò, A. V., Stinson, G., Brook, C. B., Wadsley, J., Couchman, H. M. P., Shen, S., Gibson, B. K., & Quinn, T. 2012b, ApJ, 744, L9

Madau, P. & Dickinson, M. 2014, ARA&A, 52, 415

Madau, P., Shen, S., & Governato, F. 2014, ApJ, 789, L17

Mashchenko, S., Couchman, H. M. P., & Wadsley, J. 2006, Nature, 442, 539

Mashchenko, S., Wadsley, J., & Couchman, H. M. P. 2008, Science, 319, 174

McGaugh, S. S. 2012, AJ, 143, 40

McGaugh, S. S. & de Blok, W. J. G. 1998, ApJ, 499, 41

McGaugh, S. S., de Blok, W. J. G., Schombert, J. M., Kuzio de Naray, R., & Kim, J. H. 2007, ApJ, 659, 149

McGaugh, S. S., Lelli, F., & Schombert, J. M. 2016, Physical Review Letters, 117, 201101

Milgrom, M. 1983, ApJ, 270, 371

Miralda-Escudé, J. 2002, ApJ, 564, 60

Mo, H., van den Bosch, F. C., & White, S. 2010, Galaxy Formation and Evolution (Cambridge University Press)

Mo, H. J., Mao, S., & White, S. D. M. 1998, MNRAS, 295, 319

Moore, B. 1994, Nature, 370, 629

Moore, B., Ghigna, S., Governato, F., Lake, G., Quinn, T., Stadel, J., & Tozzi, P. 1999, ApJ, 524, L19

Navarro, J. F., Benítez-Llambay, A., Fattahi, A., Frenk, C. S., Ludlow, A. D., Oman, K. A., Schaller, M., & Theuns, T. 2016, preprint (arXiv:1612.06329)

Navarro, J. F., Eke, V. R., & Frenk, C. S. 1996a, MNRAS, 283, L72

Navarro, J. F., Frenk, C. S., & White, S. D. M. 1996b, ApJ, 462, 563

—. 1997, ApJ, 490, 493

Neto, A. F., Gao, L., Bett, P., Cole, S., Navarro, J. F., Frenk, C. S., White, S. D. M., Springel, V., & Jenkins, A. 2007, MNRAS, 381, 1450

Oñorbe, J., Boylan-Kolchin, M., Bullock, J. S., Hopkins, P. F., Kereš, D., Faucher-Giguère, C.-A., Quataert, E., & Murray, N. 2015, MNRAS, 454, 2092

Ogiya, G. & Mori, M. 2014, ApJ, 793, 46

Oh, S.-H., de Blok, W. J. G., Brinks, E., Walter, F., & Kennicutt, Jr., R. C. 2011, AJ, 141, 193

Oh, S.-H., de Blok, W. J. G., Walter, F., Brinks, E., & Kennicutt, Jr., R. C. 2008, AJ, 136, 2761

Oh, S.-H., Hunter, D. A., Brinks, E., Elmegreen, B. G., Schruba, A., Walter, F., Rupen, M. P., Young, L. M., Simpson, C. E., Johnson, M. C., Herrmann, K. A., Ficut-Vicas, D., Cigan, P., Heesen, V., Ashley, T., & Zhang, H.-X. 2015, AJ, 149, 180

Oman, K. A., Navarro, J. F., Fattahi, A., Frenk, C. S., Sawala, T., White, S. D. M., Bower, R., Crain, R. A., Furlong, M., Schaller, M., Schaye, J., & Theuns, T. 2015, MNRAS, 452, 3650

Oman, K. A., Navarro, J. F., Sales, L. V., Fattahi, A., Frenk, C. S., Sawala, T., Schaller, M., & White, S. D. M. 2016, MNRAS, 460, 3610

Papastergis, E., Giovanelli, R., Haynes, M. P., & Shankar, F. 2015, A&A, 574, A113

Papastergis, E. & Shankar, F. 2016, A&A, 591, A58

Pasetto, S., Grebel, E. K., Berczik, P., Spurzem, R., & Dehnen, W. 2010, A&A, 514, A47

Paturel, G., Petit, C., Prugniel, P., Theureau, G., Rousseau, J., Brouty, M., Dubois, P., & Cambrésy, L. 2003, A&A, 412, 45

Pence, W. D., Chiappetti, L., Page, C. G., Shaw, R. A., & Stobie, E. 2010, A&A, 524, A42

Perlmutter, S., Aldering, G., Goldhaber, G., Knop, R. A., Nugent, P., Castro, P. G., Deustua, S., Fabbro, S., Goobar, A., Groom, D. E., Hook, I. M., Kim, A. G., Kim, M. Y., Lee, J. C., Nunes, N. J., Pain, R., Pennypacker, C. R., Quimby, R., Lidman, C., Ellis, R. S., Irwin, M., McMahon, R. G., Ruiz-Lapuente, P., Walton, N., Schaefer, B., Boyle, B. J., Filippenko, A. V., Matheson, T., Fruchter, A. S., Panagia, N., Newberg, H. J. M., Couch, W. J., & Project, T. S. C. 1999, ApJ, 517, 565

Pineda, J. C. B., Hayward, C. C., Springel, V., & Mendes de Oliveira, C. 2017, MNRAS, 466, 63

Planck Collaboration. 2014, A&A, 571, A16

Planck Collaboration, Ade, P. A. R., Aghanim, N., Arnaud, M., Ashdown, M., Aumont, J., Baccigalupi, C., Banday, A. J., Barreiro, R. B., Bartlett, J. G., & et al. 2016, A&A, 594, A13

Pontzen, A. & Governato, F. 2012, MNRAS, 421, 3464

—. 2014, Nature, 506, 171

Power, C., Navarro, J. F., Jenkins, A., Frenk, C. S., White, S. D. M., Springel, V., Stadel, J., & Quinn, T. 2003, MNRAS, 338, 14

Prada, F., Klypin, A. A., Cuesta, A. J., Betancort-Rijo, J. E., & Primack, J. 2012, MNRAS, 423, 3018

Rahmati, A., Pawlik, A. H., Raičevicc̀, M., & Schaye, J. 2013, MNRAS, 430, 2427

Read, J. I. & Gilmore, G. 2005, MNRAS, 356, 107

Read, J. I., Iorio, G., Agertz, O., & Fraternali, F. 2016, MNRAS, 462, 3628

Reyes, R., Mandelbaum, R., Gunn, J. E., Pizagno, J., & Lackner, C. N. 2011, MNRAS, 417, 2347

Rhee, G., Valenzuela, O., Klypin, A., Holtzman, J., & Moorthy, B. 2004, ApJ, 617, 1059

Richards, E. E., van Zee, L., Barnes, K. L., Staudaher, S., Dale, D. A., Braun, T. T., Wavle, D. C., Dalcanton, J. J., Bullock, J. S., & Chandar, R. 2016, MNRAS, 460, 689

Rix, H.-W. & Bovy, J. 2013, A&A Rev., 21, 61

Rocha, M., Peter, A. H. G., Bullock, J. S., Kaplinghat, M., Garrison-Kimmel, S., Oñorbe, J., & Moustakas, L. A. 2013, MNRAS, 430, 81

Rogstad, D. H., Lockhart, I. A., & Wright, M. C. H. 1974, ApJ, 193, 309

Romano-Díaz, E., Shlosman, I., Hoffman, Y., & Heller, C. 2008, ApJ, 685, L105

Rubin, V. C., Ford, Jr., W. K., & Thonnard, N. 1980, ApJ, 238, 471

Rubin, V. C., Thonnard, N., & Ford, Jr., W. K. 1978, ApJ, 225, L107

Sales, L. V., Navarro, J. F., Oman, K., Fattahi, A., Ferrero, I., Abadi, M., Bower, R., Crain, R. A., Frenk, C. S., Sawala, T., Schaller, M., Schaye, J., Theuns, T., & White, S. D. M. 2017, MNRAS, 464, 2419

Sánchez-Salcedo, F. J., Hidalgo-Gámez, A. M., & Martínez-García, E. E. 2014, Rev. Mexicana Astron. Astrofis., 50, 225

Sancisi, R. 2004, in IAU Symposium, Vol. 220, Dark Matter in Galaxies, ed. S. Ryder, D. Pisano, M. Walker, & K. Freeman, 233

Sanders, R. H. 1990, A&A Rev., 2, 1

Santos-Santos, I. M., Brook, C. B., Stinson, G., Di Cintio, A., Wadsley, J., Domínguez-Tenreiro, R., Gottlöber, S., & Yepes, G. 2016, MNRAS, 455, 476

Sawala, T., Frenk, C. S., Fattahi, A., Navarro, J. F., Bower, R. G., Crain, R. A., Dalla Vecchia, C., Furlong, M., Helly, J. C., Jenkins, A., Oman, K. A., Schaller, M., Schaye, J., Theuns, T., Trayford, J., & White, S. D. M. 2016a, MNRAS, 457, 1931

Sawala, T., Frenk, C. S., Fattahi, A., Navarro, J. F., Bower, R. G., Crain, R. A., Dalla Vecchia, C., Furlong, M., Jenkins, A., McCarthy, I. G., Qu, Y., Schaller, M., Schaye, J., & Theuns, T. 2015, MNRAS, 448, 2941

Sawala, T., Frenk, C. S., Fattahi, A., Navarro, J. F., Theuns, T., Bower, R. G., Crain, R. A., Furlong, M., Jenkins, A., Schaller, M., & Schaye, J. 2016b, MNRAS, 456, 85

Schaller, M., Frenk, C. S., Bower, R. G., Theuns, T., Jenkins, A., Schaye, J., Crain, R. A., Furlong, M., Dalla Vecchia, C., & McCarthy, I. G. 2015, MNRAS, 451, 1247

Schaye, J. 2004, ApJ, 609, 667

Schaye, J., Crain, R. A., Bower, R. G., Furlong, M., Schaller, M., Theuns, T., Dalla Vecchia, C., Frenk, C. S., McCarthy, I. G., Helly, J. C., Jenkins, A., Rosas-Guevara, Y. M., White, S. D. M., Baes, M., Booth, C. M., Camps, P., Navarro, J. F., Qu, Y., Rahmati, A., Sawala, T., Thomas, P. A., & Trayford, J. 2015, MNRAS, 446, 521

Schaye, J. & Dalla Vecchia, C. 2008, MNRAS, 383, 1210

Schoenmakers, R. H. M. 1999, PhD thesis, University of Groningen

Schoenmakers, R. H. M., Franx, M., & de Zeeuw, P. T. 1997, MNRAS, 292, 349

Shao, S., Gao, L., Theuns, T., & Frenk, C. S. 2013, MNRAS, 430, 2346

Sievers, J. L., Bond, J. R., Cartwright, J. K., Contaldi, C. R., Mason, B. S., Myers, S. T., Padin, S., Pearson, T. J., Pen, U.-L., Pogosyan, D., Prunet, S., Readhead, A. C. S., Shepherd, M. C., Udomprasert, P. S., Bronfman, L., Holzapfel, W. L., & May, J. 2003, ApJ, 591, 599

Simon, J. D., Bolatto, A. D., Leroy, A., & Blitz, L. 2003, ApJ, 596, 957

Simon, J. D., Bolatto, A. D., Leroy, A., Blitz, L., & Gates, E. L. 2005, ApJ, 621, 757

Spekkens, K., Giovanelli, R., & Haynes, M. P. 2005, AJ, 129, 2119

Spekkens, K. & Sellwood, J. A. 2007, ApJ, 664, 204

Spergel, D. N. & Steinhardt, P. J. 2000, Physical Review Letters, 84, 3760

Spergel, D. N., Verde, L., Peiris, H. V., Komatsu, E., Nolta, M. R., Bennett, C. L., Halpern, M., Hinshaw, G., Jarosik, N., Kogut, A., Limon, M., Meyer, S. S., Page, L., Tucker, G. S., Weiland, J. L., Wollack, E., & Wright, E. L. 2003, ApJS, 148, 175

Springel, V. 2005, MNRAS, 364, 1105

Springel, V., Frenk, C. S., & White, S. D. M. 2006, Nature, 440, 1137

Springel, V., White, S. D. M., Tormen, G., & Kauffmann, G. 2001, MNRAS, 328, 726

Steigman, G. 2007, Annual Review of Nuclear and Particle Science, 57, 463

Swaters, R. A., Madore, B. F., van den Bosch, F. C., & Balcells, M. 2003, ApJ, 583, 732

Swaters, R. A., Sancisi, R., van Albada, T. S., & van der Hulst, J. M. 2009, A&A, 493, 871

Swaters, R. A., Sancisi, R., van der Hulst, J. M., & van Albada, T. S. 2012, MNRAS, 425, 2299

Teyssier, R., Pontzen, A., Dubois, Y., & Read, J. I. 2013, MNRAS, 429, 3068

Tollet, E., Macciò, A. V., Dutton, A. A., Stinson, G. S., Wang, L., Penzo, C., Gutcke, T. A., Buck, T., Kang, X., Brook, C., Di Cintio, A., Keller, B. W., & Wadsley, J. 2016, MNRAS, 456, 3542

Trachternach, C., de Blok, W. J. G., McGaugh, S. S., van der Hulst, J. M., & Dettmar, R.-J. 2009, A&A, 505, 577

Trachternach, C., de Blok, W. J. G., Walter, F., Brinks, E., & Kennicutt, Jr., R. C. 2008, AJ, 136, 2720

Tully, R. B., Rizzi, L., Shaya, E. J., Courtois, H. M., Makarov, D. I., & Jacobs, B. A. 2009, AJ, 138, 323

Valenzuela, O., Rhee, G., Klypin, A., Governato, F., Stinson, G., Quinn, T., & Wadsley, J. 2007, ApJ, 657, 773

van den Bosch, F. C., Robertson, B. E., Dalcanton, J. J., & de Blok, W. J. G. 2000, AJ, 119, 1579

van den Bosch, F. C. & Swaters, R. A. 2001, MNRAS, 325, 1017

van Eymeren, J., Trachternach, C., Koribalski, B. S., & Dettmar, R.-J. 2009, A&A, 505, 1

Vera-Ciro, C. A., Helmi, A., Starkenburg, E., & Breddels, M. A. 2013, MNRAS, 428, 1696

Verheijen, M. A. W. 2001, ApJ, 563, 694

Viel, M., Becker, G. D., Bolton, J. S., & Haehnelt, M. G. 2013, Phys. Rev. D, 88, 043502

Vogelsberger, M., Genel, S., Springel, V., Torrey, P., Sijacki, D., Xu, D., Snyder, G., Nelson, D., & Hernquist, L. 2014a, MNRAS, 444, 1518

Vogelsberger, M., Zavala, J., Cyr-Racine, F.-Y., Pfrommer, C., Bringmann, T., & Sigurdson, K. 2016, MNRAS, 460, 1399

Vogelsberger, M., Zavala, J., & Loeb, A. 2012, MNRAS, 423, 3740

Vogelsberger, M., Zavala, J., Simpson, C., & Jenkins, A. 2014b, MNRAS, 444, 3684

Walker, M. G., Mateo, M., Olszewski, E. W., Peñarrubia, J., Wyn Evans, N., & Gilmore, G. 2009, ApJ, 704, 1274

Walter, F., Brinks, E., de Blok, W. J. G., Bigiel, F., Kennicutt, Jr., R. C., Thornley, M. D., & Leroy, A. 2008, AJ, 136, 2563

Wang, J., Frenk, C. S., Navarro, J. F., Gao, L., & Sawala, T. 2012, MNRAS, 424, 2715

Wang, W., Han, J., Cooper, A. P., Cole, S., Frenk, C., & Lowing, B. 2015, MNRAS, 453, 377

Warner, P. J., Wright, M. C. H., & Baldwin, J. E. 1973, MNRAS, 163, 163

Weinberg, D. H., Davé, R., Katz, N., & Kollmeier, J. A. 2003, in American Institute of Physics Conference Series, Vol. 666, The Emergence of Cosmic Structure, ed. S. H. Holt & C. S. Reynolds, 157

Wendland, H. 1995, Adv. Comp. Math., 4, 389

White, S. D. M. & Frenk, C. S. 1991, ApJ, 379, 52

White, S. D. M., Navarro, J. F., Evrard, A. E., & Frenk, C. S. 1993, Nature, 366, 429

White, S. D. M. & Rees, M. J. 1978, MNRAS, 183, 341

Wiersma, R. P. C., Schaye, J., & Smith, B. D. 2009a, MNRAS, 393, 99

Wiersma, R. P. C., Schaye, J., Theuns, T., Dalla Vecchia, C., & Tornatore, L. 2009b, MNRAS, 399, 574

Wolf, J., Martinez, G. D., Bullock, J. S., Kaplinghat, M., Geha, M., Muñoz, R. R., Simon, J. D., & Avedo, F. F. 2010, MNRAS, 406, 1220

Wu, X. & Kroupa, P. 2015, MNRAS, 446, 330

Zavala, J., Vogelsberger, M., & Walker, M. G. 2013, MNRAS, 431, L20

Zhao, D. H., Jing, Y. P., Mo, H. J., & Börner, G. 2009, ApJ, 707, 354

Zwicky, F. 1933, Helvetica Physica Acta, 6, 110